On-Treatment Image-Guided Radiotherapy for Central Lung Tumours



Louise Susan Helen Bendall
St Catherine's College
University of Oxford

A thesis submitted for the degree of
Doctor of Philosophy

Trinity 2019

Abstract

On-Treatment Image-Guided Radiotherapy for Central Lung Tumours. Louise Bendall, St Catherine's College, submitted for the degree of Doctor of Philosophy, Trinity 2019.

Central lung tumours are notoriously difficult to treat with conventional or high dose per fraction radiotherapy regimens due to abutting and overlapping radiosensitive organs-at-risk. Using two patient cohorts, this thesis explores the scope of isotoxic dose escalation possible for central lung tumours due to new techniques now technically feasible on magnetic resonance (MR) linear accelerators (linacs), for locally-advanced (LA), and early-stage stereotactic radiotherapy, non-small cell lung cancer patients.

Real-time MR imaging of orthogonal slice pairs or radiographically imaged fiducial markers allow target tracking during radiotherapy treatment delivery. In-silico modelling of a tracking technique based on primary tumour centroids was performed, using varying clinical target volume (CTV) to planning target volume (PTV) margins based on ideal, accurate and less accurate tracking. The resulting accumulated dose distributions were assessed for both target coverage and dose to surrounding critical structures, to fully quantify the level of gains that real-time tracked lung radiotherapy on MR-linacs may provide.

A clinically significant increase in mean isotoxically prescribed tumour dose of 3.2 - 12.4 Gy was achieved for LA patients, resulting from the increased separation of target volumes and surrounding critical structures through the use of reduced target volume margins.

Whilst reduced target margins resulted in larger reductions in minimum target volume doses compared to the standard internal target volume (ITV) approach when accumulated across the respiratory cycle, due to the large dose escalations achieved during isotoxic planning, an increase in absolute target doses still prevailed. Surrounding critical structures experienced small increases in maximum doses, causing planning tolerance violations. However these were of a similar magnitude ($\sim$0.5 Gy) and

frequency as measured for the standard technique. Thus the tolerance violations were not clinically relevant, demonstrating the potential for safe implementation of the presented technique.

Assessment of plans produced on images acquired 7 - 22 days prior to treatment delivery demonstrate notably reduced target coverage compared to plans created on the day of treatment, suggesting that daily plan adaption would result in optimal treatment plans. However, for 40% of patients, a higher target dose was achievable using "old" experimental plans compared to the standard ITV technique on up-to-date imaging, demonstrating a benefit of the proposed technique for some patients.

In-silico modelling predicts that tracked delivery of isotoxically dose escalated plans will result in a clinically meaningful increase in two-year disease-free survival for central locally-advanced NSCLC, while respecting current normal tissue dose-limits even allowing for movement effects.

Acknowledgements

Thank you to my supervisors John Fenwick, Maria Hawkins and Bartłomiej Papież for their time, support and guidance over the years, and to Frank Van den Heuvel for his useful comments during the DPhil journey. I'm also grateful to the patients and Hugo et al. for making their data available for research, and to the radiotherapy physics group for their support. I'd like to gratefully acknowledge the funding provided by CRUK and the MRC.

Thank you to my parents for their eternal support and encouragement throughout the years. Dad, I hope this helps convince you that physics is more interesting than mathematics. To my brother, thank you for the academic chats, encouragement, advice and motivation!

Chris, Flash and Jennie, thank you for confirming that not all physicists are 'physicists', and making studying physics so much fun - I wouldn't have studied further without this positive start. I'm deeply grateful to my friends, near and far, for providing some tonic to the DPhil life - particularly Sindu and Tessa for ensuring my time in Oxford was suitably

lively and hydrated.

Finally, a mammoth thank you to my fusband Matthew. For making the adventures all the more fun by doing them together, and being there through it all. Your unwavering support, profound belief in me, and most importantly, much needed distraction helped me more than you'll ever know.

Contents

1 Introduction **1**

1.1 Lung Cancer 1

1.2 NSCLC Radical Radiotherapy 2

1.2.1 Routine Radiotherapy Process 3

1.2.1.1 Pre-Treatment 4

1.2.1.2 Target Definition 6

1.2.1.3 Image Guidance 7

1.2.1.4 Motion Management 9

1.2.2 Conventional Radiotherapy 11

1.2.3 Stereotactic Ablative Radiotherapy 11

1.2.4 Limitations of Current Treatments 13

1.2.5 MR-Linacs 14

2 MRI and MR-Linacs **17**

2.1 Magnetic Resonance Imaging 17

2.1.1 MR Image Formation 18

2.1.2 MRI Sequences 19

2.1.3 Geometric Distortion 20

2.1.4 MRI in Lung 23
2.2 MR-Linacs 24
2.2.1 Technical Considerations 25
2.2.2 Additional Considerations 26
2.2.3 Current Models and Capabilities 28
2.2.3.1 ViewRay^{TM} MR-radiotherapy system 28
2.2.3.2 Elekta Unity MR-linac 32
2.2.3.3 Inline configurations - Aurora RT (Alberta) and Australian 33
2.2.4 MR only planning/electron density 34
2.3 Margin Calculations 36
2.3.1 Random and Systematic Uncertainties 36
2.3.2 van Herk Margin Recipe 37
2.3.3 Real-time Tracking on MR-linacs: Margin Calculation 38
2.4 Summary 44

3 Dosimetric Evaluation **46**

3.1 Respiratory Motion 46
3.2 Treatment Simulation 47
3.3 Target and OAR Coverage 48
3.4 Dose Accumulation 50
3.4.1 Methods: Point Modelling 53
3.4.2 Results: Point Modelling 55

3.4.3 Methods: Airway Modelling 56
3.4.4 Results: Airway Modelling 60
3.5 Discussion 60

4 Dose Escalation **62**

4.1 Patients 62
4.2 Planning Methods 64
4.2.1 Locally Advanced 64
4.2.2 Stereotactic Ablative Radiotherapy 67
4.3 LA Results 69
4.3.1 PTV Volume 69
4.3.2 Isotoxically Prescribed Dose 70
4.3.3 Predicted Survival 74
4.4 SABR Results 80
4.4.1 PTV Volume 80
4.4.2 Isotoxically Prescribed Dose 80
4.4.3 Predicted Survival 82
4.5 Discussion 88
4.6 Conclusion 90

5 Tracking Based on Baseline Imaging **92**

5.1 The Respiratory Cycle 92
5.2 Methods - Accumulation over the Respiratory Cycle 93
5.2.1 Deformable Image Registration 94

5.2.2 Dose Metric Averaging 96
5.2.3 Tracking Technique 97
5.3 Results - Accumulation over Respiratory Cycle 98
5.3.1 Magnitude of Required Tracking 98
5.3.2 Deformable Image Registration Results 98
5.3.3 Accumulation Results 102
5.3.3.1 OAR Accumulation results 102
5.3.3.2 Target Coverage Accumulation Results 112
5.4 Discussion 120
5.5 Conclusion 122

6 Potential Technique Pitfalls **124**

6.1 Tracking Limitations 124
6.2 DIR Limitations 133
6.3 Limitations of Baseline Accumulation 137
6.4 Summary 140

7 Tracking Based on Repeat Imaging **142**

7.1 Introduction 142
7.2 Methods 143
7.3 Results 145
7.3.1 Target Volume Changes 145
7.3.2 Accumulation Results 145
7.3.2.1 Target Coverage Results 145

7.3.2.2 OAR Accumulation Results 153

7.4 Conclusion 155

8 Conclusions **158**

8.1 Limitations of Study 163

8.1.1 Dose Calculation 163

8.1.2 Plan Type 164

8.1.3 Image Artefacts 165

8.1.4 Image Type 166

8.1.5 Image Acquisition Time Points 166

8.2 Further Work 167

8.2.1 Summary of Further Work 169

8.3 Summary 169

Bibliography **177**

List of Figures

1.1 Central tumour and surrounding critical structures 3

1.2 ICRU target volume expansions 8

1.3 Proposed MR-linac workflow 16

2.1 ViewRay^{TM} schematic 29

2.2 Elekta MR-Linac design 34

2.3 Inline and perpendicular orientation of MR-linac schematic 35

3.1 Lung tumour motion 47

3.2 Bifurcation point positions 54

3.3 Bifurcation point motion 57

3.4 Bifurcation point motion in individual directions 58

3.5 Pairing of bifurcation points 59

3.6 Transformation of airways 61

4.1 LA PTV Volumes 71

4.2 LA Isotoxic prescribed doses 72

4.3 LA Increase in prescribed dose 73

4.4 LA Example of high dose escalation 75

4.5 LA Example of low dose escalation 76
4.6 LA Predicted two year disease-free survival 78
4.7 LA dose response model 79
4.8 SABR PTV volumes 81
4.9 SABR Isotoxic prescribed doses 83
4.10 SABR Increase in prescribed dose 84
4.11 SABR Example of high dose escalation 85
4.12 SABR Example of poor dose escalation 85
4.13 SABR BEDs 87

5.1 DIR method schematic 95
5.2 Example of LA tumour motion 99
5.3 DIR DVF 100
5.4 Determinant of Jacobian histogram 103
5.5 Example of poor GTV overlap 106
5.5 Localisation of OAR tolerance breach 111
5.5 Example of good accumulated target coverage 115
5.5 Example of poor target coverage 119

6.1 Example of the effect of tracking on GTV alignment 127
6.2 3D target shapes 128
6.3 Example of GTV and ITV volumes 129
6.4 Example of a single phase with good target coverage 131
6.4 Example of a single phase with poor target coverage 132

6.5 Poor superior/inferior coverage DMA 134

6.6 DVH results for poor/good phase DMA results 135

6.7 Difference in manual vs DIR GTV contours 138

6.8 Example of poor target coverage using DIR accumulation 139

7.1 Example of primary and lymph node relative position change 151

7.2 Dose distribution showing lack of nodal coverage 152

7.3 Example of primary and lymph node relative position change 154

8.1 Example of 4D image artefact 166

List of Abbreviations

3D	Three dimensions
4D	Four dimensions
4DCT	Four dimensional computed tomography
ART	Adaptive radiotherapy
BED	Biologically effective dose
BP	Bifurcation point
CBCT	Conebeam computed tomography
COM	Centre of mass
CT	Computed tomography
CTV	Clinical target volume
DFS	Disease-free survival
DLOAR	Dose limiting organ at risk
DIR	Deformable image registration
DMA	Dose Metric Averaging
DSC	Dice similarity coefficient
DVF	Deformation vector field
EPID	Electronic portal imaging device
GTV	Gross tumour volume
HD	Hausdorff distance
ICRU	International Commission on Radiation Units and Measurements

IGRT	Image-guided radiotherapy
IMRT	Intensity modulated radiotherapy
ITV	Internal target volume
LA	Locally advanced
Linac	Linear accelerator
MLC	Multileaf collimator
MR	Magnetic resonance
MRI	Magnetic resonance imaging
MV	Megavoltage
NTCP	Normal tissue complication probability
NSCLC	Non-small cell lung cancer
OAR	Organ at risk
PBT	Proximal bronchial tree
PET	Positron emission tomography
PRV	Planning organ at risk volume
PTV	Planning target volume
QA	Quality assurance
RF	Radiofrequency
RO	Radiation oncologist

ROI	Region of interest
SABR	Stereotactic ablative radiotherapy
SAR	Specific absorption rate
SBRT	Stereotactic body radiotherapy
TCP	Tumour control probability
TPS	Treatment planning system
VMAT	Volumetric modulated arc therapy
WHO	World Health Organization

Publications

- L.S.H. Bendall, M. Partridge, M.A. Hawkins, J.D. Fenwick. Towards predicting motion of normal tissue and tumours using incomplete real-time data during lung radiotherapy. 4th CRUK/MRC Oxford Institute for Radiation Oncology Symposium, 2016. (Best poster prize.)

  Abstract

  Background: Non-small cell lung cancer (NSCLC) survival is poor at less than 25% at three years. To increase survival using radiotherapy it is suggested that an increase in tumour dose is required. Target motion has been extensively investigated, but motion of surrounding organs at risk (OARs) remains relatively uncharacterised. For accurate, high precision radiotherapy to be delivered the extent of this motion needs to be measured and accounted for. This study aims to predict the movement of the whole structure of OARs using motion models created from pre-treatment imaging combined with the subset of information acquired during real-time imaging.

  Methods: 4DCT pre-treatment scans of ten NSCLC patients were used to assess the degree of respiratory motion of the bronchial tree in order to determine the minimum set of transformations necessary to describe the motion.

  Results: The largest respiratory motion of the airways was found to be in the superior-inferior direction, with motion exceeding 2 cm. Affine transformations were able to reduce the mis-registration errors of bifurcation points to within 0.2 cm. When the corresponding transformations were applied to the airway structure, an improvement in Dice co-efficient (0.2399 to 0.6078) and Hausdorff

distance (2.00 to 0.57 cm) was observed.

Conclusion: Affine transformations have successfully been used to align bifurcation points within the bronchus, and improve the registration of the bronchus walls. The motion model created using the bifurcation points as a subset of geometrical data may be fused with real-time imaging used during treatment to increase the safety of radiotherapy treatment.

- L.S.H. Bendall, M. Partridge, M.A. Hawkins, J.D. Fenwick. EP-1626: Predicting motion of normal tissue using incomplete real-time data during lung radiotherapy. *Radiotherapy and Oncology.* 123(S1), S880-S881, 2017.

Abstract

Purpose or Objective: Imaging during radiotherapy treatment has the potential to increase the accuracy and precision of radiotherapy. MR-linacs can produce high quality images during treatment delivery. However, for image acquisition and analysis to be performed in real-time, fast registration techniques based on incomplete data is required.

Target motion in lung radiotherapy has been extensively investigated but motion of surrounding organs at risk (OARs) remain relatively uncharacterised. Consequences of irradiating nearby OARs to high doses can be fatal. We have investigated the bronchial tree with the aim of characterising the motion of the whole structure throughout the respiratory cycle on the basis of an imaged subspace.

Material and Methods: 4DCT pre-treatment scans of ten NSCLC patients were used to assess the motion of the bronchial tree in order to determine the minimum set of transformations necessary to describe the motion across the respiratory cycle. The bifurcation points (BPs) of the main airways were initially used to characterise the respiratory motion and determine the minimum

number of BPs required to be monitored to accurately infer the position of all BPs.

The accuracy of using the transformations resulting from the BP investigation to account for the respiratory motion of the airway sub-structures between the BPs was assessed using the Dice similarity index, maximum Hausdorff distance and the percentage of data points within the structure that are within 0.2/0.5 cm from the baseline structure. Further investigation into the optimal transformation required to minimise the mis-registration of the airway sub-structures throughout the respiratory cycle was performed including aligning the centre of mass of subsections of airways between the BPs.

Results: It was found that when the BPs were regionally paired and a single transformation applied to both BPs, the mis-registration errors were reduced from 2.19 to 0.18 cm, suggesting small differential motion between regionally paired BPs. This may also indicate that the transform may reduce the mis-registration of the airway sub-structures between the BPs.

The BP transformations did not always improve the registration of the airway sub-structure in terms of maximum Hausdorff distance. The optimal method found to minimise the maximum Hausdorff distance was by aligning the centre of mass of the sub-structures.

Registration technique	Dice similarity index	Max. Hausdorff distance (cm)	Percentage of points within 0.2 cm	Percentage of points within 0.5 cm
Baseline (no registration)	0.33-0.59	0.62-1.14	51.3-94.7	84.2-99.6
BP transformations applied to sub-structures	0.47-0.64	0.73-0.83	73.8-81.4	96.8-98.3
Centre of mass of sub-structures aligned	0.54-0.58	0.50-0.56	85.6-89.9	99.8-99.9

Table 1: Range of results from registration techniques.

Conclusion: Affine transformations have successfully been used to align paired bifurcation points within the bronchus to within 0.18 cm. This demonstrates that it is possible to describe the motion of all the BPs on the basis of a spatial subset of data. Similarly, improvements in the registration of the airway structure has also been achieved, reducing the maximum Hausdorff distance from 1.14 cm to 0.56 cm by using a small subset of information - the centre of mass of sub-structures - at different phases of the respiratory cycle.

- L.S.H Bendall, J.D. Fenwick, B.W. Papież, M.A. Hawkins. Normal Tissue Doses During Isotoxically Dose Escalated Lung Radiation Therapy Using MR-Linacs. *International Journal of Radiation Oncology, Biology and Physics*, 102 (3), S207, 2018.

  Abstract

  Purpose/Objective(s): Real-time imaging using MR-Linac during lung radiotherapy may allow PTV margin reduction, permitting increased isotoxically prescribed doses. However, this may affect the doses received by nearby critical organs at risk (OARs) when respiratory motion is considered. It is hypothesized that surrounding OARs may require monitoring to ensure dose tolerances are not exceeded during treatment over the respiratory cycle.

  Materials/Methods: Isotoxic plans with a range of PTV margins based on MR-Linac tracking accuracies were generated on the mid-ventilation phase of a 4DCT image for 10 patients with locally advanced NSCLC. The dose-distributions were time-integrated over the respiratory cycle of the planning scan (CT1), using a deformable registration algorithm to map distributions back to the mid-ventilation phase. For 5 patients with repeat 4DCT scans, the time-integration was performed on 2 further image sets acquired at a range of 7-22 days (CT2) and 27-50 days (CT3) after CT1 to investigate the effects of

changes in respiration/anatomy.

Results: Planning CT results show that for approximately 50% of plans, small volumes of a single OAR (heart, trachea, pulmonary artery, esophagus) may exceed the dose tolerance. 17/18 of these OARs were the dose limiting structure at planning; the remaining OAR lay at 99.7% of tolerance but over the respiratory cycle received a small increase of 0.4 Gy. For later image sets, the number of plans with OARs exceeding tolerance ranged from 75-90% of plans, and the maximum number of OARs per plan increased from 1 (CT1), to up to 4 (CT2) or 5 (CT3). The dose violations also increased in magnitude, up to 4.8 and 9.2% of tolerance for CT2 and CT3. The regions of overdose within OARs were small (median volume of 1.72 cm3 for CT1), and generally located at or near areas of PTV and OAR overlap.

Conclusion: These results show that for MRI-Linac LA-NSCLC plans created on the mid-ventilation phase of that day's 4DMR image, and delivering high prescribed doses using tight PTV margins, OAR tolerance violations in doses considered over the whole breathing cycle are small and occur at predictable locations. However, these violations grow when dose-distributions are time-integrated over 4D-CT images acquired 1-7 weeks after the planning scan, indicating that frequent re-imaging and plan re-optimization is required to minimize tolerance violations.

Abstract 1101; Table 1 Results across whole respiratory cycle for OARs that exceeded tolerance.

Structure	Structure composition	Number of OARs exceeding tolerance across all plans (max % above tolerance)		
		CT1	CT2	CT3
PTVstandard	ITV + 5 mm (CTV) + 5 mm (PTV)	4/120 (+2.5%)	6/60 (+4.0%)	10/60 (+8.9%)
$PTV_{MRtrack_lo_acc}$	GTV_{midV} + 5 mm (CTV) + 5 mm (PTV)	4/120 (+2.4%)	7/60 (+4.8%)	10/60 (+9.2%)
$PTV_{MRtrack_hi_acc}$	GTV_{midV} + 5 mm (CTV) + 2 mm (PTV)	5/120 (+3.2%)	8/60 (+3.1%)	10/60 (+6.3%)
$PTV_{MRtrack_ideal}$	GTV_{midV} + 5 mm (CTV) + 0 mm (PTV)	5/120 (+2.4%)	11/60 (+3.1%)	16/60 (+8.2%)

ITV – internal target volume, GTV_{midV} – gross tumor volume on mid-ventilation phase of 4DCT.

Table 2: Results across whole respiratory cycle for OARs that exceeded tolerance. ITV – internal target volume, GTVmidV – gross tumor volume on mid-ventilation phase of 4DCT.

- L.S.H. Bendall, B.W. Papież, M.A. Hawkins, J.D. Fenwick. Isotoxic Dose Escalation with Real-Time Imaging on an MR-Linac in Lung Radiation Therapy, *International Journal of Radiation Oncology, Biology and Physics*, 102(3), S207, 2018.

  Abstract Purpose/Objective(s): Lung cancer survival is poor with only 5% survival at 10 years. Recent studies suggest that dose escalation in chemoradiotherapy is required to increase survival. However, dose escalation can be limited by dose constraints placed on surrounding organs as risk to limit potentially fatal side effects. MR-Linac offer real-time imaging during radiotherapy. It is hypothesized that MR-Linac tracking techniques may allow PTV margin reduction, leading to a meaningful dose escalation with no expected increase in toxicity.

  Materials/Methods: To calculate a range of CTV-PTV margins required for real-time tracking on an MR-Linac, MR systematic tracking errors were taken from literature, combined with contouring errors (1 mm) and random per-fraction localization errors (1 mm) as per van Herk et al. An ideal case of 0 PTV margin and the standard clinical margin were also used for comparison. 4DCT scans from 10 locally advanced NSCLC patients were used to create a range of isotoxic plans based on the mid-ventilation phase and varying PTV margins. Planning aims and constraints were taken from standard clinical practice and the UK IDEAL-CRT trial, and the PTV dose per fraction was increased until one or more OAR constraint-level was reached. The planned doses were used to estimate the expected two-year disease free survival (DFS) using a radiobiological model in lung cancer by Partridge et al. An increase of $\geq$ 5% DFS was considered clinically useful.

  Results: MR systematic tracking errors of 0.2 mm and 1.35 mm were used for $\text{PTV}_{\text{MRtrack_hi_acc}}$ and $\text{PTV}_{\text{MRtrack_lo_acc}}$. Median isotoxically-prescribed doses of

72.8, 74.8 and 76.5 Gy could be delivered to $PTV_{MRtrack_lo_acc}$, $PTV_{MRtrack_hi_acc}$ and $PTV_{MRtrack_ideal}$ leading to modelled gains in DFS of 4.2, 9.0 and 14.0% respectively when compared to $PTV_{standard}$ median dose of 71.0 Gy. Depending on tumor location and proximity of nearby OARs, prescribed doses were limited by constraints on the heart, pulmonary artery, esophagus, aorta and trachea in 11, 9, 9, 7 and 4 cases respectively.

Conclusion MR-Linacs with the capability of real-time tracking potentially allow the PTV margin to be reduced, leading to notable increases in isotoxically-prescribed doses, and useful gains in modelled two-year disease free survival.

Chapter 1

Introduction

1.1 Lung Cancer

Lung cancer is the third most common cancer in the UK with over 47,000 cases per year on average in the UK alone in 2014 - 2016 [1], accounting for 13% of total cancer cases [2]. Lung cancers are 85-90% non-small cell lung cancer (NSCLC) which includes squamous cell carcinoma, adenocarcinoma and large cell carcinoma [3]. Lung cancer causes the most cancer deaths: 23% and 21% of cancer deaths for men and women respectively [2]. Lung cancer incidence is strongly related to age, with the peak rate of lung cancer cases at 85-89 years. Lung cancer has poor survival which is strongly linked with the stage of disease; one-year survival falls from 35 to 6% when comparing stage I and stage IV respectively, and around 75% of patients are diagnosed with late stage disease (stage III or IV) [4]. Overall five-year survival rates are just 8.4% and 11.6% for men and women respectively [5].

Lung cancer patients are classified into stages based upon the anatomical extension of the tumour. The TNM staging system includes information about the tumour size and location, T, the nodal involvement, N, and the absence or presence of metastasis,

(spread from the primary tumour), M. The stages are further grouped based on their predicted survival into stage I-IV [6]. The WHO performance status categorises patients based upon their ability to perform daily activities, ranging from 0 (fully active, no restriction) to 5 (dead) [7]. The disease staging and patient performance status are used to determine the treatments most suitable for patients considering their likely efficacy and tolerability.

Primary treatment options for NSCLC include radiotherapy (27%), chemotherapy (25%) and surgery (16%) [8], which are often used in combination. The remaining patients receive supportive care and other palliative treatments. Surgery is the standard of care for operable early-stage disease, with around 50% of stage I and II patients undergoing surgery, whereas only 1.5% receive surgery for stage IV disease [1, 9].

1.2 NSCLC Radical Radiotherapy

The aim of radiotherapy is to deliver a lethal dose of radiation to the tumour cells, whilst minimising the dose to surrounding healthy tissues to ensure toxicities are minimised. The therapeutic ratio describes this compromise between the probability of tumour control (TCP) and the probability of normal tissue complications (NTCP) [10]. Dose to normal tissues cannot be completely avoided due to the close proximity of the tumour and normal tissues, as shown in Figure 1.1, and the physical dose deposition characteristics of the radiation used. New techniques aim to improve the therapeutic ratio of treatments, by reducing the dose to surrounding organs at risk (OARs), increasing the dose to the target, or both.

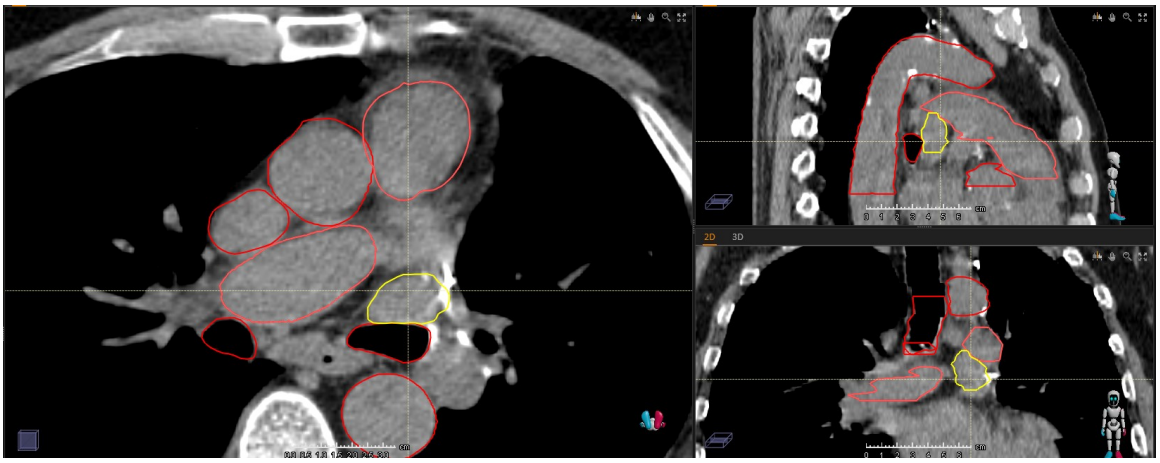

Figure 1.1: Example of central tumour (yellow) and some surrounding critical structures (red). The close proximity of critical structures often limits the achievable target dose for central lung tumours.

1.2.1 Routine Radiotherapy Process

The routine radiotherapy process will be discussed in more detail in the following sections, but will now be briefly summarised. When a patient is diagnosed with cancer, they will first undergo a range of tests to establish the stage of the disease. This will help the multi-disciplinary team decide the optimal treatment for the specific patient and disease. If this is radiotherapy, and the patient agrees to treatment, preparation can begin with a radiotherapy planning scan, which can also be used for motion assessment of the tumour. The planning scan consists of a contrast-enhanced 3DCT, 4DCT, or both. Delineation of target and surrounding avoidance structures is performed on the scan to enable generation and optimisation of the planned dose distribution. These are produced in a treatment planning system, which models the treatment beam interactions within the patient. Quality assurance (QA) is performed on the treatment plan prior to delivery to ensure the integrity of the treatment plan. Volumetric imaging may be further used to assess the patient set-up prior to the

treatment delivery, allowing for corrections to be made if required. This imaging may be used throughout treatment, along with other methods to assess how the patient is responding to treatment and whether any changes to the plan are required. Follow-up of the patient after treatment is important to monitor any toxicities, and to ensure any further treatment that is necessary for optimal outcome is received.

1.2.1.1 Pre-Treatment

Prior to radiotherapy treatment, a volumetric three-dimensional (3D) computed tomography (CT) image is acquired. This allows the target and healthy surrounding organs at risk (OARs) to be visualised and delineated [11]. The resulting greyscale image is made up of the varying electron densities which are also used to calculate dose deposition from the radiation beams used in radiotherapy [12]. Four-dimensional computed tomography (4DCT) imaging can also be used to quantify and account for the respiratory motion of the target and OARs [13–17].

Other imaging modalities may also be used to obtain additional information. For example, magnetic resonance (MR) imaging may be used due to it's exceptional soft tissue contrast to aid target and OAR delineation [18], and functional imaging [19] such as positron emission tomography (PET) is used during staging of the patient, and often fused with the planning CT to aid GTV and nodal definition [20, 21].

Treatment planning systems (TPS) are used to model the beams that are produced by radiotherapy treatment machines, linear accelerators (linacs). The pre-treatment imaging and structure delineations are used to determine the optimal beam configurations which are modelled by the TPS, which calculates the dose deposition within

the patient.

Radiotherapy treatments have improved in their conformality to the target shape as discussed by Bucci et al. [22]. Multiple fields are used to take full advantage of the dose deposition characteristics of the radiation through tissue; the fields intersect at the tumour to combine to a lethal dose to the tumour, whilst the relatively high dose near the entry of each beam are spread around the body.

The shape of beams produced by modern linacs can be modified by the linac jaws and multi-leaf collimators (MLCs), and conventionally the intensity of the beams can be altered by placing a physical wedge into the beam during delivery. Intensity modulated radiotherapy (IMRT) has been shown to have favourable results in lung radiotherapy in terms of both planned dose distribution and patient outcomes [23,24]. IMRT allows for increased shaping of the radiation beams by subdividing each beam into segments. Varying levels of dose can be delivered to each segment, resulting in an inhomogeneous intensity across the field when the segments are combined. This potentially allows a more conformal 3D dose distribution to envelope the target structure, and better spare the surrounding OARs.

Arc based techniques such as volumetric modulated arc therapy (VMAT) are extensions of IMRT which can improve the conformality of the radiation even further, whilst potentially reducing the treatment delivery time [25]. This can be achieved by continuously delivering the treatment whilst the gantry rotates around the patient and the linac jaws and MLCs move simultaneously to create highly conformal dose distributions.

1.2.1.2 Target Definition

The International Commission on Radiation Units (ICRU) has released several reports describing systems for radiotherapy prescription, recording and reporting of radiotherapy treatment delivery, which aim to standardise processes across the globe.

Target volumes are defined for radiotherapy treatment in ICRU 50 (1993) [26]. The gross tumour volume, GTV, is defined as "the gross palpable or visible/demonstrable extent and location of malignant growth". The GTV is expanded to the clinical target volume, CTV, to include any sub-clinical microscopic malignant disease. The CTV is the volume that requires treatment to achieve the aim of treatment, whether it be cure or palliation. Due to limitations in treatment delivery accuracy and anatomical variations that may occur during treatment, a geometrical margin is used around the CTV to produce the planning target volume, or PTV. The purpose of the PTV is to ensure that the prescribed dose is delivered to the entire CTV, and so aims to account for any internal organ and patient motion, inaccuracies such as patient set-up and treatment delivery limitations. Organs at risk, OARs, are also identified as normal tissues that may affect treatment planning and/or the prescribed dose.

Respiratory motion is a concern with regards to lung radiotherapy treatments, as the delivery of radiotherapy occurs over many respiratory cycles. Respiration results in tumour and surrounding tissues undergoing both motion and deformation. Conventional treatments tackled this issue by using large PTV margins. However, this can create large treatment volumes including significant amounts of healthy tissue, which can lead to radiation induced toxicities or limit the tumour dose prescription.

ICRU 62 (1999) [27] further breaks down the PTV margin into an internal margin that accounts for any physiological variation in CTV, and the set-up margin that accounts for uncertainties in the set-up of the patient and radiation beams during planning and treatment delivery. The internal target volume (ITV) is the combination of the CTV and the internal margin. In lung radiotherapy, the ITV is often produced by combining the CTV volumes on each of the 4DCT phases, which ensures the ITV encompasses all positions of the tumour throughout the respiratory cycle. The PTV is thus described by the CTV expanded to include the internal margin and the set-up margin. The expansions of target volumes are depicted in Figure 1.2.

Analogous to the CTV to PTV margin, a planning organ at risk volume (PRV) is defined for the OAR to account for any geometrical uncertainties in the position of the OAR during treatment. The OAR is expanded by a geometrical margin to form the PRV. ICRU Report 83 [29] introduces new concepts to extend the current recommendations to include the more complex IMRT treatment plans.

1.2.1.3 Image Guidance

As technological improvements have driven an increase in the conformality of treatments, the consequences of discrepancies between planned and delivered dose distributions have become more important. Sharper dose gradients encompassing the target volumes result in larger dose differences when deviations occur. Image guided radiotherapy (IGRT) aims to minimise these dose deviations by utilising imaging prior to and during treatment delivery.

Traditionally, portal films or EPIDs (electronic portal imaging devices) were used

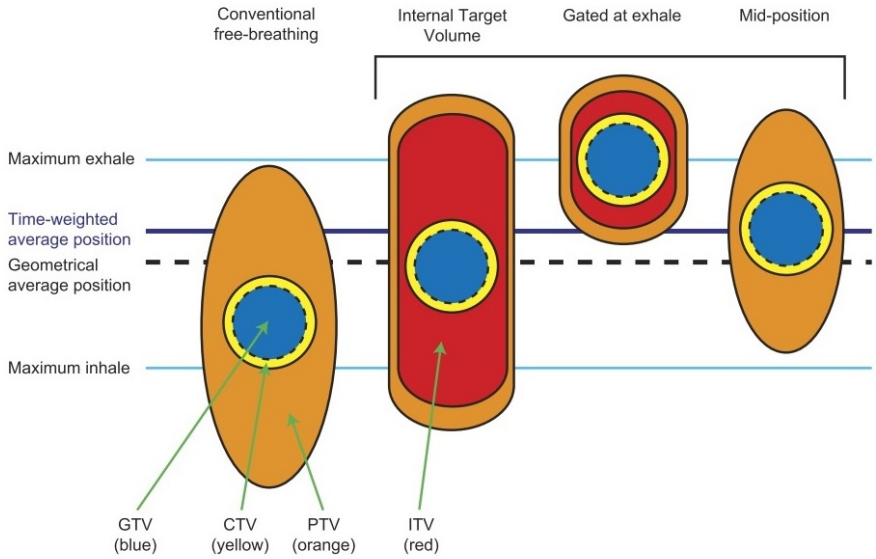

Figure 1.2: Schematic of ICRU volume expansions [28].

to verify patient set-up prior to treatment. These devices oppose the treatment head and use the treatment beam to create the images as discussed by Boyer et al. [30]. However, the mega-voltage (MV) energy of the beams produce images with poor contrast, and so the anatomical sites for which they can be accurately used are limited [31].

Three dimensional images of the patient can now be acquired immediately before each radiotherapy fraction, in the treatment position, through the use of kilovoltage conebeam computed tomography (CBCT) which is now commonly integrated within modern linacs [32–35]. The improved contrast compared to MV imaging and the three-dimensional nature of the images can help to ensure that patient set-up is optimal prior to treatment delivery, and can monitor any inter-fractional changes that may affect the dose distribution. However, soft tissue contrast is often poor, and artefacts are often present in the images, so patient set-up using CBCT is often based

on the bony anatomy rather than the tumour position.

Whilst CBCT is currently the optimal and most readily available technique to reduce set-up errors in lung radiotherapy [36], it should be noted that imaging duration is longer for CBCT, at approximately 2 minutes compared to just 15 seconds for CT imaging [37]. 4D CBCT has been shown to improve the image quality compared to 3D CBCT when motion is involved such as respiratory motion during lung radiotherapy [38].

The acquisition of CBCT requires an additional dose of radiation to the patient, which, as with the delivery of any radiation, must be optimised particularly when used for multiple fractions throughout the treatment course. A balance between the dose received by the patient and the image quality of the image needs to be struck, and will depend upon the task for which the images will be used [39].

1.2.1.4 Motion Management

Several papers discuss in detail the methods used to measure, minimise and mitigate respiratory motion during lung radiotherapy [40–45]. It has been recommended that respiratory motion management techniques are used when the target is seen to move more than 5 mm, or if clinically important OAR sparing can be gained [40]. Motion management methods include;

- 4DCT imaging can be used during treatment planning to minimise image artefacts that may effect target and OAR delineation. Imaging is correlated with the respiratory cycle, and the 4DCT dataset is split into several (usually 10) phases, with each phase made up of a 3D image showing the anatomy in a par-

ticular part of the respiratory cycle. This allows for the extent of any motion and deformation to be visualised and considered during radiotherapy treatment planning and delivery [28].

- Tracking techniques aim to synchronise the treatment delivery with the respiratory motion by moving the treatment beam during delivery [46, 47].

- Gating methods monitor the position of the target, and turn off the radiation beam if/when the target moves out of a pre-defined volume [48].

- Deep inspiration breath-hold techniques limit imaging/treatment to during a patient breath-hold, aiming to minimise any motion and deformation [49].

- Audio-visual feedback to the patient, which aims to help the patient maintain a periodic breathing motion [50].

- Abdominal compression physically restricts the motion of the abdomen, which has been found to reduce lung tumour motion, particularly in tumours located in the lower lobes [51].

- Continuous positive airway pressure provides a constant supply of pressurised air to the lungs, minimising the need for diaphragm motion [52].

- "Plan of the day" IGRT uses multiple CTV to PTV margins to create multiple plans; the most optimal plan is selected at each fraction based on imaging immediately prior to treatment [53].

- "Anatomy of the day" extends the "plan of the day" approach to create a new plan for each fraction based on the days anatomy [54].

- Mechanical ventilation which controls the frequency and depth of respiration [55].

Each technique has its own uncertainties and challenges; for example, tracking methods require the accurate localisation of the target in real-time. This is particularly difficult in cases where tumours border surrounding healthy tissue, resulting in poor contrast between the two.

1.2.2 Conventional Radiotherapy

Conventional radiotherapy regimens typically deliver 5 daily fractions each week, for several weeks. The standard regimen used in the UK for treatment of NSCLC is 60-66 Gy in 30-33, 2 Gy fractions over 6-6.5 weeks, or 55 Gy in 20, 2.75 Gy fractions over 4 weeks [56].

1.2.3 Stereotactic Ablative Radiotherapy

Stereotactic body radiotherapy (SBRT), also known as stereotactic ablative radiotherapy (SABR), is used for early stage, localised NSCLC; clinical stage T1 N0 M0 or T2/T3 ($\leq$ 5 cm) N0 M0 patients, who are medically inoperable or who have refused surgery and have a WHO performance status of 0-2. SABR is currently only considered to tumours outside a 2 cm radius of the main airways and proximal bronchial tree to limit any potential toxicity [57]. A standard fractionation regime of 54 Gy delivered in 3, 18 Gy fractions, with an inter-fraction interval of at least 40 hours is used [58]. More central tumours can be treated using a more fractionated regimen,

of lower dose per fraction. The smaller target volumes, combined with the increased use of pre-treatment and on-treatment imaging allow for a safe increase in dose per fraction compared to conventional radiotherapy.

A small phase I trial with 6 month follow-up has shown that treating ultra-central NSCLC is safe and effective on the MR-Linac [59]. "Ultra-central" tumours were defined as those with GTVs directly abutting the main-stem bronchi, carina or contents of the mediastinum. Five patients were treated with 50 Gy in 5 fractions (a biologically effective dose, BED, of 100 Gy^{-10}), with a goal of 95% of the PTV receiving 95% of prescription dose, with strict OAR doses. Cine-gating was used on each fraction, and the planned dose distribution was calculated on each fractions' image prior to treatment and assessed by comparison with the planned dose distribution. Adaption was used in 10 of 25 plans; to ensure optimal target coverage (3 plans), and to limit the doses received by OARs (7 plans) including the uninvolved lung, trachea, bronchial tree, oesophagus, heart, spinal cord and stomach. Good local control was reported with 100% response at 3 and 6 months, and no toxicity grade $\geq$3 acute (within 6 months of treatment) were observed.

There is also an active debate about whether patients who are fit to undergo surgery should be offered SABR as discussed by Weder et al. [60], and several ongoing clinical trials such as SABRTooth [61] and STABLEMATES [62] aim to answer this question.

1.2.4 Limitations of Current Treatments

There are some limitations in the motion management strategies used today. Methods such as tracking and gating require an accurate knowledge of tumour position in real-time. Often a surrogate of respiratory motion, such as the the chest wall position as used by the Varian Real-time Position Management^{TM} (RPM) system is used, or fiducial markers are placed within/near the tumour - however this in an invasive procedure and not without risk. Care has to be taken to ensure an accurate correlation between tumour and surrogate motion. Uncertainties in this correlation, as well as those in IGRT images used to accurately identify the tumour require consideration during treatment.

The time taken for treatment delivery can also have an impact on the accuracy of delivery. For SABR patients, it has been found that if treatments exceed 34 minutes, a shift from the original set-up position of greater than 5 mm can be occur [63]. For this reason, VMAT treatments may be preferable to IMRT and conventional treatments, particularly for SABR cases where a high dose per fraction is delivered.

It has been suggested by multiple analyses and clinical studies that to increase survival of lung cancer radiotherapy patients, an increase in delivered dose to the tumour is required [64–67]. Several studies have suggested a minimum biologically effective dose (BED_{10}) of at least 100 Gy^{-1} [68–70]. The BED can be used to compare dose regimens, and represents the biological dose received by specific tissues when delivered a specific dose per fraction and total dose. However, dose escalation is limited due to the proximity and radiosensitivity of surrounding structures. This is particularly

true of central tumours which can be near/abut the proximal bronchial tree, trachea, oesophagus, heart and large blood vessels. Advancements in technology, particularly imaging improvements and delivery techniques such as tracking and gating may allow for target margin reduction, which effectively increases the separation between the target and the surrounding OARs.

Although overall survival is strongly linked with the dose delivered to the tumour, several studies have also recently found that it may also linked to the dose received by surrounding OARs. Vivekanandan et al. [71] found a link between all cause death rate and volumes of the heart and left atrial walls receiving >63 Gy respectively. Similarly, Ramroth et al. found for patients treated with concurrent chemotherapy and radiotherapy, higher radiotherapy doses resulted in poorer survival, which they suggest may at least partly be a result of the high toxicity of treatments [67]. This suggests that techniques that are able to reduce the dose to surrounding OARs may increase patient survival even without dose escalation.

1.2.5 MR-Linacs

Many of the current limitations of radiotherapy treatments can potentially be improved through the use of MR-linacs. These are linacs which replace the conventional MV or CBCT imaging with that of magnetic resonance imaging [72–75]. Although a simple idea, it is a feat of engineering to combine the equipment required for the MR imaging, including strong magnetic fields, with the complex equipment required by the linac to produce accurate, reliable treatment beams.

Improved MR soft tissue contrast compared with CT/MV/CBCT imaging may

increase the accuracy of delineation [76–78] and IGRT techniques [79], particularly when it can be hard to visualise the border between target and surrounding OARs. The increase in accuracy may allow for margin reduction, with the potential for a reduction in dose to OARs, and/or a dose escalation to the target.

MR imaging does not use ionising radiation, which obviously will be of benefit to the patient in terms of reducing the total dose delivered to healthy tissues. This also means that it is justifiable to use imaging more frequently during the treatment delivery, potentially prior to, during and after treatment to confirm the treatment delivery. This again has the potential to increase the accuracy of the treatment delivery.

In particular, real-time imaging and tumour tracking/gating may allow for on-line adaptive radiotherapy to be performed on an MR-linac. Practically, this may allow for an MR image to be taken, a plan produced and delivered using real-time tracking/gating during every treatment fraction. This technique is likely to minimise inter-fraction variability and intra-fraction discrepancies. Bainbridge et al. [80] have proposed a potential patient pathway for radical radiotherapy on an MR-linac for locally advanced NSCLC (Figure 1.3), which suggests that adaptive radiotherapy may be beneficial for lung cancer treatment. This has already begun in other anatomical sites [81]. Magnetic resonance imaging (MRI) and MR-linacs will be discussed in more detail in Chapter 2.

The aim of this thesis is to explore in detail how an MR-linac may be used to treat NSCLC, and to gauge the feasibility and possible advantages of the technique.

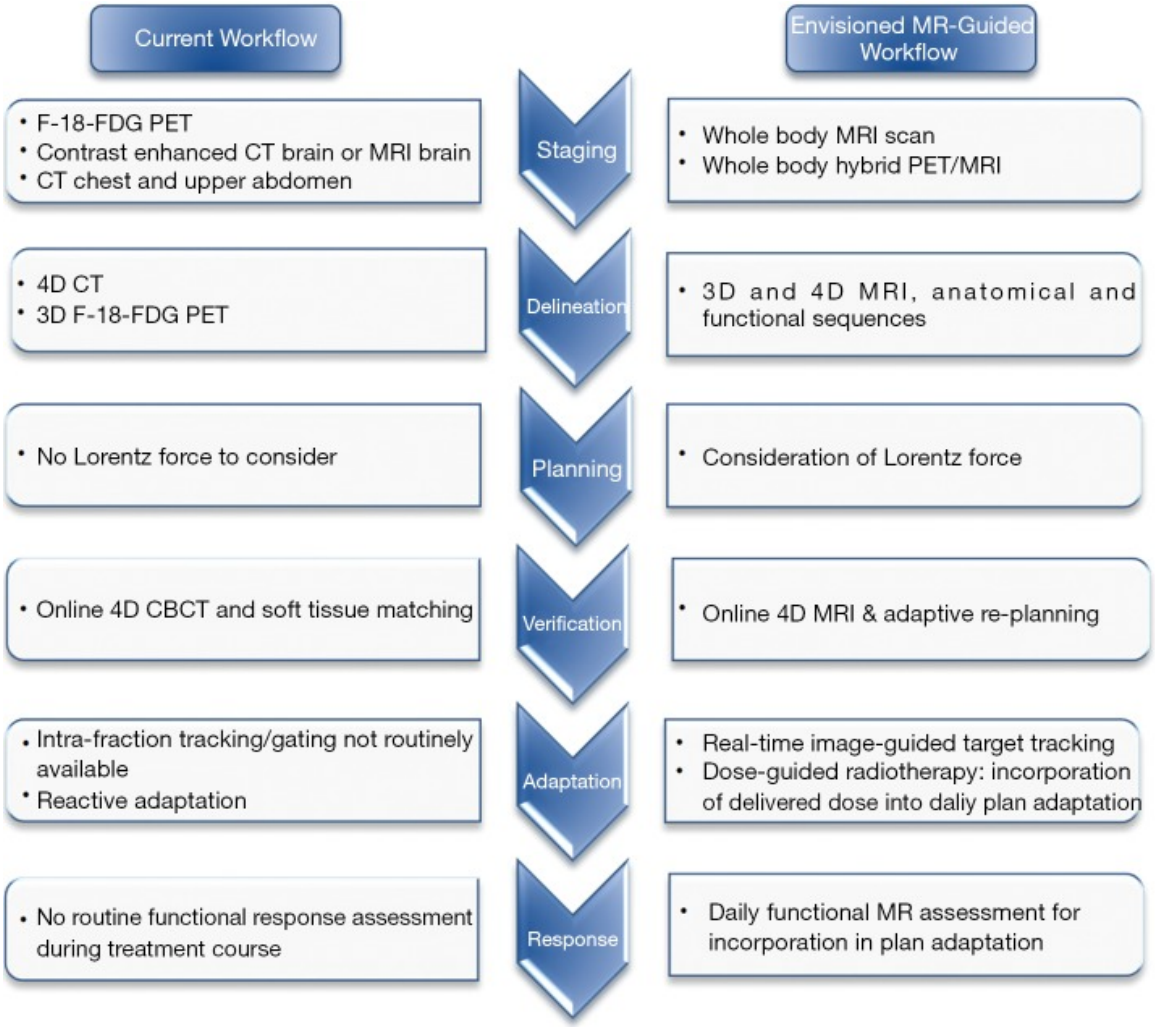

Figure 1.3: A proposed MR-linac workflow for lung radiotherapy [80].

Chapter 2

MRI and MR-Linacs

2.1 Magnetic Resonance Imaging

MRI produces 3D images with excellent image contrast and high spatial resolution. The information contained in the images can be changed by employing different imaging parameters (sequences), allowing a range of physical and physiological characteristics to be displayed and quantified. The contrast in the images can demonstrate the proton density, T1 and T2 relaxation times, tissue susceptibility variations, tissue perfusion and oxygenation of tissues among many other properties.

MR images are produced using strong magnetic fields, B_0. It is a non-invasive imaging technique that does not use ionising radiation, allowing for long scans which are able to be repeated with no radiation protection concerns. Due to the application of radiowaves, there may be some heating of patient tissues during imaging, described by the specific absorption rate (SAR). However, this can be managed effectively through careful choice of imaging sequence and patient positioning. SAR limits have been introduced across the US and Europe as discussed by Bottomley [82]. Whilst SAR may be an issue in diagnostic imaging, particularly for scanners with a magnetic

field of ≥3 T, to date all available MR-linacs have a maximum magnetic field of 1.5 T. Care also needs to be taken around metal objects that may be affected by the magnetic fields associated with MRI. For example, patients with pacemakers, metal clips etc. are unsuitable for MRI as the magnetic field may cause the devices to move within the body [83].

2.1.1 MR Image Formation

MRI was first successfully demonstrated independently by Purcell [84] and Bloch [85]. The majority of MR imaging is based upon the nucleus of hydrogen (a single proton), which exhibits a spin and is abundant within the body, primarily as water and fat. The proton can be considered a tiny bar magnet with angular momentum which causes it to precess at a particular frequency, known as the Lamour frequency, ω, which is dictated by the strength of the applied magnetic field, B_0, and the gyromagnetic ratio, γ.

In the absence of a magnetic field the spin axes of protons within tissue will be randomly distributed, and the associated dipole moments will effectively cancel each other out. When a magnetic field is applied, the spins axes partially align, creating a net magnetic dipole.

Additional energy is introduced in the form of radiowaves (a radiofrequency, (RF) pulse), which deflects the magnetic dipole. When the radiofrequency source is switched off, the magnetic vector will return to its original orientation and energy will be emitted. This energy is detected by receiver coils placed around the patient, and reconstructed to produce the image.

Different tissues have varying relaxation times. That is, the time taken for the magnetic dipole to return to its original orientation when the RF pulse stops varies between different tissues. The characteristic time taken for the longitudinal magnetic dipole moment to decay to its equilibrium value (prior to RF pulse) is called T1, a spin-lattice relaxation, due to interactions between the spins and surrounding environment. The characteristic time taken for the axial component of the deflected dipole to return to it's equilibrium value (zero) is known as T2; a spin-spin relaxation process driven by the de-phasing of spins. T2* is the "observed" value of "true" T2, which includes the effect of magnetic field inhomogeneities. T2* is always less than or equal to T2.

2.1.2 MRI Sequences

There are many different pulse sequences available to image varying properties of the same subject. For example, a "fat suppression" pulse sequence will remove the fat signal from the image. "Longitudinal", or T1-weighted images generally have the best anatomical information, whereas "transverse" or T2-weighted images are used to obtain biological characteristics that may present pathological information. Several studies have thoroughly discussed the role of MRI in radiotherapy, including the choice of sequences available [18, 86, 87]. A selection of MRI sequences used specifically for lung cancer imaging are listed in Table 2.1.

Steady state free precession (SSFP) sequences are known to be geometrically robust, whilst also able to be acquired quickly and with high resolution [88]. However, these sequences are susceptible to banding artefacts due to magnetic field inhomo-

geneities. Fast spin echo (FSE) sequences are intrinsically correct for magnetic field inhomogeneities, but have longer acquisition times, and thus often include some blurring. Diffusion weighted imaging (DWI) creates images based on the movement of water molecules, and so can demonstrate the diffusion of water through tissues. This can be used to highlight tumours due to the restriction of water molecule motion due to their increased cellularity compared with healthy tissues [18].

2.1.3 Geometric Distortion

The three-dimensional spatial fidelity of images used during radiotherapy is vital to ensure accurate treatments. Any residual geometric distortion of images used during IGRT has the potential to result in incorrect beam placement and delivery, which may compromise the dose to the target as well as surrounding healthy tissues. The occurrence and severity of any distortion will depend upon a number of factors. System/scanner-related factors can for the most part be accounted for during post-processing of the image [89]. Patient-related factors, such as magnetic susceptibility and chemical shift are patient dependent and so harder to account for.

System distortions result from magnetic field, B_0, inhomogeneities and gradient non-linearities. These distortions are generally negligible at imaging isocentre, but increase in magnitude with distance, up to around a couple of centimetres for large fields of view [90]. MRI depends upon the use of Fourier transforms to relate the spatially encoded time-domain data to the frequency-domain data. Spatially varying linear gradients are used to encode the spatial information. Any deviations in the linearity of these gradients will cause distortion as the spatial encoding will be incor-

Sequence	Strength	Acquisition type	Spatial resolution	Distortion risk	Variants	Comments
Volumetric T1w GRE	Nodules	Breath-hold	High	Low	Dixon, 4D	Low contrast
T2w single-shot FSE	Infiltrative disease	Breath-hold	Low-moderate	Low	Cine	
T2w gated FSE	Mediastinal structures, infiltrative disease	Respiratory gated	Moderate-high	Moderate	Dixon, volumetric	Long acquisitions
T2/T1w bSSFP	Lung function	Free-breathing	Moderate-high	Moderate	Cine, 4D	Banding artefacts
T1w FSE	Mediastinal lymph nodes	Multiple breath-hold	Moderate	Moderate	DCE	
DWI	Dose painting	Multiple breath-hold	Low	High		Distortion risk reduction possible

Table 2.1: MRI sequences for lung cancer imaging. Abbreviations: GRE = gradient echo; DCE = dynamic contrast-enchanced; FSE = fast spin echo; T1w/T2w = T1/T2 weighted; bSSFP = balanced steady-state free precession; DWI = diffusion-weighted imaging [86].

rect. In super-conducting MRI systems, it is the gradient field inhomogeneity that contributes most to the geometric distortion, particularly for new scanners which use shorter gradient coils to allow fast-switching gradients [91, 92].

Correction for system-induced geometric distortion is often performed during post-processing. The system distortion is measured using uniform phantoms and can be corrected for by using a transformation in a similar process to deformable image registration; a global or local transformation is used to transform from the measured system, to an undistorted one [88]. Spherical harmonics [93], tri-linear interpolations [94], splines [95] and polynomials [96] have all been previously investigated as correction methods. Post-processing techniques are able to minimise these errors down to a few millimetres [89, 90, 97].

Patient-induced distortions are caused by variations in the magnetic susceptibility of varying tissues within the patient. These arise at interfaces between tissues that have significantly different susceptibilities, particularly between soft-tissue and air or bone. Tissue magnetic susceptibility-induced effects are patient-dependant and are difficult to assess and predict. The effect is larger for stronger magnetic fields. For the lung, simulations have shown it to be a maximum of 0.56 and 3.34 mm for a magnetic field strength of 0.5 T and 3.0 T respectively [98]. Chemical shift artefacts are produced due to molecules having different compositions. For example, protons within fat are partially shielded from the magnetic field as the electron orbit is close to the nucleus. Conversely, protons in water undergo less shielding as the electron cloud is further from the nucleus. This causes the fat proton to experience a slightly weaker field, and to precess at a slightly lower frequency than the water proton. This

can lead to the mis-mapping of pixels, as the fat proton will be assumed to be located somewhere the magnetic field strength is lower than is really the case. The resulting white and dark banding of structures is mostly seen around structures that contain water and are surrounded by fat, such as the liver, kidneys etc.

2.1.4 MRI in Lung

The lungs are traditionally a difficult site for MR imaging due to their low density and susceptibility differences between soft tissue and air. Healthy lung tissue has a density of just 0.1 g/cm^3, roughly ten fold lower than other tissues [99]. As the MR signal is directly proportional to the tissue proton density, this results in an MR signal for lung that will be ten times weaker.

Oxygen in air is paramagnetic, whereas tissue is diamagnetic, leading to bulk magnetic susceptibility differences at lung-air interfaces. This creates a static local field gradient, which can result in rapid de-phasing in gradient echo imaging. As the local field gradients will be dependant upon the strength of a scanner's main magnetic field, low-field MRI at B_0=0.5 T has shown some advantages for lung imaging [100]. However, low-field MRI requires signal averaging to improve the signal-to-noise ratio, and so may lead to longer imaging times.

To reduce the effect of respiratory motion and improve image characteristics, the image can be captured during breath-hold. This can be done using bellows to measure the change in volume in the abdomen, which is considered a surrogate for the respiratory cycle. An alternative, MR-specific technique is the use of MR-navigators. These measure the breathing motion directly from the MR signal as discussed by Stam

et al. [101], who determined an accuracy of 0.5 mm and a time lag of less than 30 ms when using 1D pencil-beam navigators to measure phantom motion. A 2D navigator tracking technique based on a kidney was found to be accurate to within 1.5 mm. A dedicated 90-180° spin echo excitation, or a pencil beam readout is used to measure the MR signal, usually orthogonal to the base of the diaphragm. This approach can also be used for retrospective gating of scans during free-breathing imaging.

Small solid or soft tissue lesions in the lungs are well identified with MRI. The sensitivity of MRI for lung nodules larger than 4 mm is around 85%, and reaches 100% for nodules greater than 8 mm [102]. It has been shown that MRI can be used to accurately evaluate a patient's TNM staging [103]. MRI can be particularly useful in cases where the excellent soft tissue contrast can help identify the tumour boundary within regions of atelectasis and pleural effusion.

Hyperpolarized xenon gas MRI has also been investigated in NSCLC patients to assess the functional ventilation of the lungs. A clinical trial to determine if respiratory tolerance to radiotherapy can be predicted, and it's use as a tool to assess radiation-induced lung injury has been recently undertaken [104].

2.2 MR-Linacs

There are several different models of MR-linac, whose current use range from those that are in clinical use (ViewRay^{TM} MRIdian), those that are being used for research (Elekta Unity), and those that are still being developed.

2.2.1 Technical Considerations

Both MRI scanners and radiotherapy linacs are complicated machinery, and so combining the two modalities is not a simple task. There are three main issues that need to be considered in the design of an MR-linac: the magnetic interference, the radiofrequency interference and the radiotherapy beam transmission through the MRI scanner.

MRI uses three electromagnetic fields for imaging; the strong static magnetic field, B_0, to orientate the hydrogen nuclei; the weaker gradient field for image generation; and the weak RF field to produce the measurable signal. These fields may be affected by the close proximity of the linac. The strong B_0 field may interact with the electron beam used in the linac to produce the treatment beam, causing it to miss the target affecting the photon beam output. The presence and rotation of the linac may affect the gradient fields which reduces the spatial integrity of the MR images [105].

To minimise these effects, and for optimal imaging and treatment delivery, passive and active shielding is required. Different designs of MR-linacs have slightly different techniques for doing this.

Radiotherapy treatment beam transmission through MR machinery results in beam attenuation, scatter and field heterogeneities and so needs to be considered and minimised.

The presence of the magnetic field for MR imaging will affect the treatment beam. When the treatment beam photons interact in the patient, secondary electrons are produced. During conventional treatments (no magnetic field) these electrons will

continue forwards on their path, resulting in a build-up region of lower dose at the entrance of the beam, and a reduction of dose near the exit. However, within an MR-linac, these secondary electrons will be affected by the Lorentz force from the magnetic field. This causes a spiralling of the electrons, resulting in a decreased build-up dose (by around 5 mm for a 6 MV beam in a field of 1.5 T [72]), an increase in exit surface dose as the electrons may re-enter the tissue (the electron return effect) and a small shift in the resulting dose distribution. These effects are dependent on the energy of the electrons, and increase with increasing magnetic field (B_0). The effect is most pronounced at air:tissue interfaces, which are prevalent in lung radiotherapy treatments. However, this change in the dose deposition due to the induced curvature of the electrons can be modelled and accounted for during treatment planning [106].

2.2.2 Additional Considerations

The current models of MR-linacs that are available have a limited imaging and treatment field of view due to technical restrictions. For example the Elekta Unity is limited to 22 cm in the cranial-caudal direction, and 57 cm in the lateral direction [107]. However, when Chuter et al. [108] analysed 1,223 previous lung treatments, including a 1 cm margin for plan adaption, it was found that 95.8% of plans would have had plans small enough to be treatable on the MR-linac.

The positioning of patients on a diagnostic MR scanner is generally different to that of a patient during radiotherapy treatment delivery. Care is taken to ensure there are minimal gaps between the coil and patient which minimises the loss of signal-to-noise ratio. However, during radiotherapy treatment, immobilisation devices and/or

the limited bore size of MR-linacs may alter patient and MR coil positioning, and so need to be considered. Due to the strong magnetic fields used in the MR-linac, all radiotherapy treatment devices used on the MR-linac must be "MR-safe", i.e. compatible for use in the strong magnetic fields associated with the MR scanner.

On a conventional linac, the couch on which the patient lies during treatment is able to move in at least four-dimensions by translating in the cranial-caudal, anterior-posterior and left-direction direction, and rotating from the head of the couch. An extension of this is rotation within the pitch and roll axes, for example by the six degrees of freedom couch by Varian, as discussed by Schmidhalter et al. [109]. This ability to move the couch (and patient) allows any inter-fraction variation in patient set-up to be quickly and easily minimised. The couch motion of the MR-linac however is often limited to the superior-inferior direction, as the couch passes through the bore of the MR machinery. However, practically this is not expected to be an issue due to the anticipated workflow on the MR-linac of creating a "plan of the day" based on the patient's current position, hence removing the need to align the patient to the previous pre-treatment position.

To date, no MR-linac is able to perform the complex requirements of VMAT delivery. However, it is expected that in the fullness of time this will become feasible, allowing the more conformal dose distributions provided by VMAT to be delivered on the MR-linac.

2.2.3 Current Models and Capabilities

There are several MR-linac designs currently available as discussed by Ménard and van der Heide [110] and shown in Table 2.2. The static magnetic fields, B_0, range from 0.35-1.5 T. The geometrical accuracy of the images will increase with falling B_0 due to a reduction in geometrical distortions. Wachowicz et al. [111] have investigated the optimal magnetic field strength in terms of contrast-to-noise ratio for use on MR-linacs. The image contrast depends upon B_0 and the tissue-specific relaxation properties, and it was found for some anatomical sites (glioma, kidney and liver tumours), a lower magnetic field resulted in an improved contrast-to-noise ratio.

2.2.3.1 ViewRay™ MR-radiotherapy system

The first MR-radiotherapy system with FDA clearance that was commercially available, and in routine clinical use is the ViewRay™ MRIdian system [74] (ViewRay Inc., Cleveland, OH, USA). The ViewRay™ system uses a double doughnut, 0.35 T whole-body MRI, a schematic of which can be seen in Figure 2.1. The vertical gap in the magnet is used to deliver the radiation beam. The system has a 50 cm diameter spherical imaging field of view. The radiotherapy delivery system consists of a robotic, 3-headed ^{60}Co source, that delivers a dose rate of 550 cGy/min from three, up to 10.5x10.5 cm^2 fields. The use of three cobalt sources, equally spaced 120° apart provides a similar dose-rate to conventional linear accelerators. Conventional or "step and shoot" IMRT plans are currently deliverable on the ViewRay.

Real-time MR imaging can be used during treatment on the ViewRay™ to allow for the tracking of tumours or target tissues that are imaged within a single sagittal

Authors	Mutic et al. (ViewRay) [74]	Lagendijk et al. (Elekta) [112]	Fallone et al. (Alberta) [113, 114]	Keall et al. (Australia) [75, 115]
Field Strength	0.35 T	1.5 T	0.56 T	1.0 T
Radiation source	Co-60	7 MV	6 MV	6 MV
Clearance	70 cm bore	70 cm bore	85 cm open bore	82 cm open bore
Source to isocentre	105 cm	150 cm	130 cm	180 - 330 cm
Max field size at isocentre	27.3 x 27.3 cm	22 x 57 cm	Unknown	40 x 40 cm
MLC width	10.5 mm at isocentre	7.1 mm at isocentre	Unknown	5 mm centre/ 10 mm peripheral

Table 2.2: Comparison of systems combining MRI and linacs.

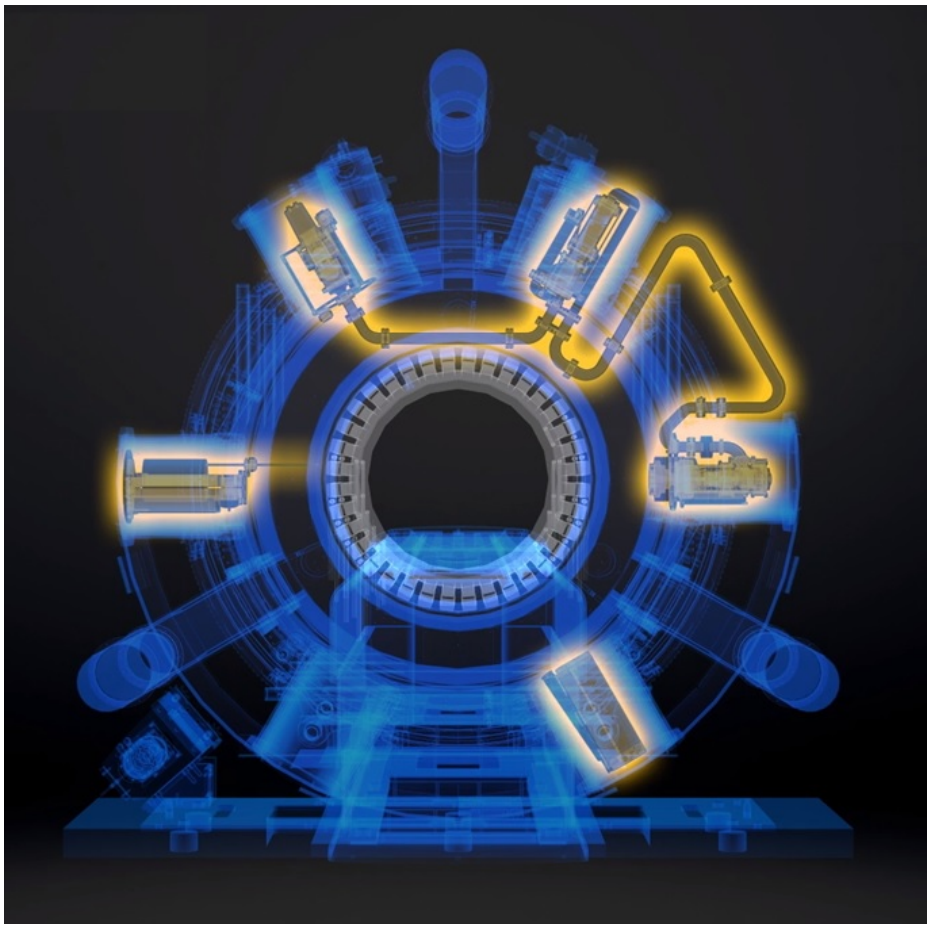

Figure 2.1: ViewRay^{TM} schematic, showing MR components in blue, linac components in orange. Reproduced with the permission of ViewRay Technologies, Inc. All rights reserved.

plane at 4 frames-per-second, or in 3 parallel sagittal planes at 2 frames-per-second. A system latency of 300 ms has been measured [74]. The geometric distortion of the ViewRay^{TM} system has been found to be within 1 mm within a spherical volume of diameter 200 mm [116].

ViewRay^{TM} incorporates adaptive radiotherapy (ART) by providing integrated software that is able to auto-contour and perform dose calculations for 3D-conformal or IMRT treatments. The TPS can complete optimisation and calculate required MLC motion and resulting dose distributions within 30 seconds, making ART treatments based on the image of the day a realistic option. Initial use of the ViewRay^{TM} has been discussed by Lamb et al. [117], which noted the time taken for an adaptive, gated protocol treating abdominal/pelvic SABR of approximately 90 minutes. The median time to beam commencement was 54 minutes (range 34-99 minutes).

There are a few disadvantages of the ViewRay^{TM} design. The use of cobalt sources are known to provide beams with a lower output, less penetration, larger penumbra and higher surface doses than a linac [118, 119]. However, the use of double-focussed MLCs results in a penumbra similar to that achieved on a linac for small fields of a few centimetres. The surface dose from the cobalt sources is also reduced by the introduction of the magnetic field and the resulting increase in build-up region.

The low magnetic field strength of 0.35 T is also known to reduce the signal-to-noise ratio when compared to a higher field strength. Conversely, the low magnetic field strength is known to reduce magnetic susceptibility artefacts, which will minimise distortions of the patient to within 0.3 mm [120].

The ViewRay^{TM} system has been used to quantify the difference in intra- and

inter-observer variability of GTV delineation for lung SABR cases compared with the gold-standard of 4DCT imaging. Whilst the ViewRay^{TM} was found to have acceptable inter-observer agreement between two radiation oncologists (ROs), it was recommended that more experience should be accumulated to improve the results. An increase in inter-observer error was also highlighted for tumours < 5 cm^3, potentially limiting the use of the MR-linac to larger tumours [121].

Noel et al. [79] compared the imaging available on the ViewRay^{TM} system with the CBCT/MVCT available on linacs and used in standard clinical protocols. Three radiation oncologists (ROs) reviewed images, including for two thorax patients, and were asked to select the image with better visualisation of the targets and 46 surrounding OARs. Whilst agreement of the ROs was poorest for the thorax cases, 63% of structures were better visualised by the MR-linac images than the conventional CBCT/MVCT images. However, RO consensus was not reached for one structure; the trachea, but the target and pulmonary structures were never better visualised by the CBCT/MVCT compared to the MR imaging.

Imaging prior to treatment and used for planning on the ViewRay^{TM} system uses the TrueFISP sequence, which is a balanced steady-state free precession (bSSFP) sequence. With the low field of 0.35 T, TrueFISP results in images with a high contrast-to-noise ratio, short repetition time and a lower specific absorption rate (SAR) allowing frequent/continual imaging. However, this sequence is vulnerable to field inhomogeneities that may be caused by placing the patient inside the magnetic field. Saenz et al. [122] discuss the characterisation of the MR imaging parameters. The ViewRay^{TM} system was found to be consistent and passed all criteria previously

set by the American College of Radiology for MRI. For real-time imaging, an alternative sequence is used: a segmented echo planar imaging sequence, which provides imaging at 4 frames per second [123].

ViewRay^{TM} have extended their offering to include a new system using a linac rather than the three cobalt sources, which uses a similar split-magnet design.

2.2.3.2 Elekta Unity MR-linac

The Elekta Unity MR-linac (Elekta AB, Stockholm, Sweden) is based on a 1.5 T Philips Achieva MRI scanner, which produces diagnostic quality images, and an Elekta linac. It is a joint effort between Elekta (linac), Philips (MR) and the Radiotherapy Department in Utrecht as described by Ladendijk et al. [124], which received CE marking in June 2018 [125].

Unlike the ViewRay^{TM} system, a closed bore magnet is used and surrounded by an Elekta accelerator that produces a 7 MV flattening filter free beam as shown in Figure 2.2. The alterations to the linac/MRI that were required have been previously discussed [126]. The characterisation of the Unity system was performed by Woodings et al. [127] prior to the first clinical IMRT treatments of lumbar spine metastases in 2017 [107] using three or five beam IMRT. Active shielding is used to minimise the effects of the magnetic fields on the linac and treatment beam production. The arrangement allows for the stronger magnet, but requires the treatment beam to traverse through the MRI cryostat as well as the MRI body coil. The field size at isocentre is limited to 22 cm in the cranial caudal direction, and 57 cm in the lateral direction, with MLCs 7.1 mm wide at isocentre. Practical considerations include the

limitation of couch motion to the cranial-caudal direction only. However, this is not considered problematic as it is expected that treatments will be re-planned at every fraction based on the specific patient set-up [107].

Active magnetic shielding is used to minimise the magnetic field from the MR at the sensitive parts of the linac. The gun of the accelerator experiences no magnetic field; the field is minimised for the accelerator tube. By magnetically decoupling the MR and linac devices, the effect of the linac on the accuracy of the MR images is reduced. The introduction of additional magnets can be used to ensure the combined magnetic field is independent of the linac position during gantry rotation.

To reduce the effect of treatment beam transmission through the magnet, the MRI design has been altered to move the super-conducting coils and split the gradient coils. The magnet thickness was also minimised and made homogeneous.

To overcome the issue of RF interference, synchronisation of the imaging and radiation delivery allow intra-fractional imaging by very quickly alternating imaging and treatment [124].

2.2.3.3 Inline configurations - Aurora RT (Alberta) and Australian

The Alberta [113, 128] and Australian [75] MR-linacs use an inline orientation, where the linac is aligned with the main magnetic field, B_0 rather than perpendicular to it as per the ViewRay^{TM}/Elekta Unity design, as shown in Figure 2.3. There are several advantages to this design, including no beam attenuation and a smaller effect of the magnetic field on the electron gun and waveguide within the linac machinery. A sharper penumbra and no electron return effect is experienced due to the reduced

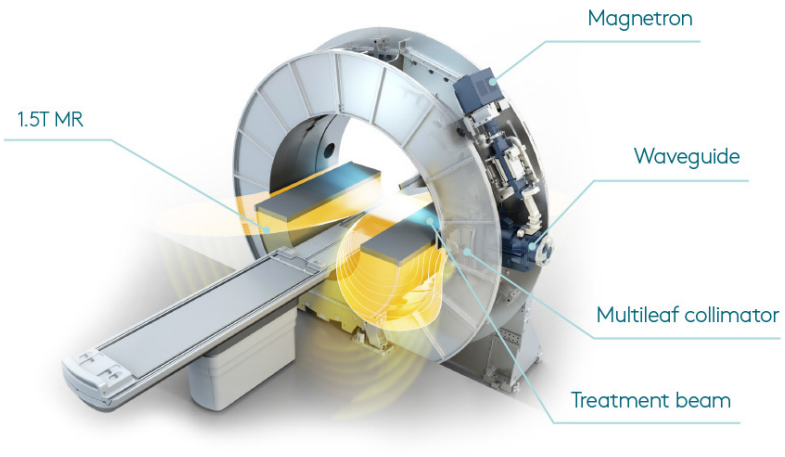

Figure 2.2: Elekta MR-Linac design. Image courtesy of Elekta.

effects of the magnetic field on the electron transport within the patient.

The Alberta system combines a bi-polar rotating 0.5 T MR system with a 6 MV linac. The set-up of the machine can be altered to allow the treatment radiation field to be positioned perpendicular or parallel to the main magnetic field [113]. Kirkby et al. [129] used Monte Carlo simulations to investigate the optimal position of the treatment beam in relation to the magnetic field. It is known that the magnetic field will have an impact on the dose distribution of delivered treatment plans, particularly for lung plans. It was found that the in-line geometry was preferable to the perpendicular set-up in terms of calculated dose distributions.

The Australian MR-Linac system combines a Siemens Magnetom Avanto, 1 T MRI system, with a 6 MV Linatron MP industrial linac [75].

2.2.4 MR only planning/electron density

Unlike CT images conventionally used for radiotherapy treatment planning, MR image intensity is not directly related to the electron density. The problem is highlighted

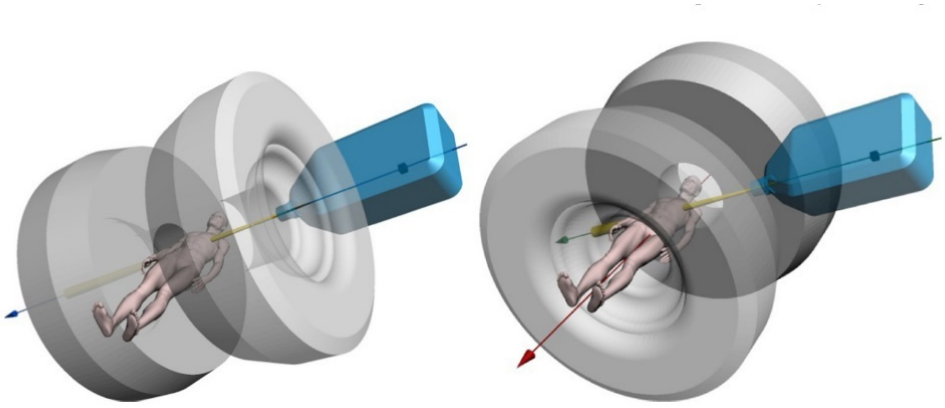

Figure 2.3: (Left) Inline and (Right) perpendicular orientation of MR-linacs with B_0 [75].

when considering bone and air within MR images - both will appear dark (low signal), but have vastly different attenuation coefficients and resulting photon dose deposition.

For MR images to be used for dose calculations in radiotherapy, a technique to assign electron densities to the image is required; a CT Atlas and non-rigid registration or segmentation and bulk Hounsfield unit (HU) overrides have been used. The resulting images are often referred to as "synthetic CT", "substitute CT" or "pseudo-CT". Any inaccuracies within the synthetic CT will lead to uncertainties in the dose calculation and so need to be carefully considered. As described in a literature review by Edmund and Nyholm [130], the majority of studies have investigated the use of techniques to obtain synthetic CT in the brain and prostate [131, 132]. Wang et al. [133] discuss the use of an atlas based method for creating synthetic CT data for use in lung radiotherapy planning. The plans produced on the synthetic CT datasets were copied to the corresponding CTs for eleven patients, and the resulting changes in dose received by PTV and OARs was investigated. No significant differences were observed in the dose-volume metrics, except for maximum spinal cord dose when the

PTV was located in the lung apex. This demonstrates the feasibility of potentially using an MR-only workflow for lung radiotherapy treatments.

2.3 Margin Calculations

2.3.1 Random and Systematic Uncertainties

As discussed in Section 1.2.1.2, CTV to PTV margins are used to ensure the entirety of the CTV is treated to the appropriate dose when taking into account inaccuracies in the imaging, treatment planning and delivery of radiotherapy treatment plans. Hence, the margins required will depend upon the particular equipment and techniques used, and should be calculated for specific MR-linac configurations and delivery techniques [134].

Geometric uncertainties in radiotherapy have been defined as systematic: "any deviation that occurs in the same direction and is of a similar magnitude for each fraction throughout the treatment course", or random: "a deviation that can vary in direction and magnitude for each delivered treatment fraction" [135].

Systematic errors may be introduced at localisation, planning or treatment delivery; for example, uncertainties in the initial delineation of the target structures, beam modelling or imaging and treatment beam isocentre alignment. Random errors are associated with the execution of the treatment, such as patient set-up errors which vary fraction to fraction. When accumulated over several fractions, random uncertainties result in a blurring of the dose distribution, whereas systematic uncertainties result in a shift of the dose distribution relative to the CTV.

IGRT techniques aim to minimise the uncertainties in radiotherapy treatments.

However, an offline strategy will not be able to predict the random uncertainties in future fractions, and so larger PTV-CTV margins will be required to ensure adequate coverage of the CTV. Conversely, an online technique will be able to account for both the systematic and random uncertainties of each fraction.

2.3.2 van Herk Margin Recipe

An analytical description of the required CTV-PTV margins, including both systematic and random uncertainties is provided by van Herk et al. [136]. The probability of the CTV receiving a particular dose is calculated by combining the quadratic sum of the standard deviation of systematic and random errors and the penumbral uncertainty as per equation 2.1.

$$M = \alpha\Sigma + \beta\sqrt{\sigma^2 + {\sigma_\mathrm{p}}^2} - \beta\sigma_\mathrm{p} \tag{2.1}$$

where M is the required margin, Σ is the quadratic sum of the standard deviations of all systematic errors, σ is the quadratic sum of the standard deviations of all random variations, σ_p is the standard deviation describing the penumbra uncertainty. For the particular case of the margins required for 90% of the patient population to receive a minimum dose to the CTV of 95% of the nominal dose, $\alpha = 2.5$ (for 3D consideration), and $\beta = 1.64$ is required [136].

The van Herk formula has been experimentally verified for 3D conformal radiotherapy and IMRT in lung cancer by Eccelstone et al. [137]. The formula was found to be "robust against variations in tumour size and motion, treatment technique, plan conformity, as well as low tissue density". The study also considered target motion effects, an increase in which was found to reduce the plan conformity, but not beyond

clinically acceptable levels.

This margin recipe only considers translational errors, and excludes rotational errors and shape deviations. Thus, practically the margins used clinically are likely to be larger than those calculated via this method.

2.3.3 Real-time Tracking on MR-linacs: Margin Calculation

This project aims to simulate a potential radiotherapy treatment as may be delivered on the MR-linac. It is suggested that real-time imaging may be used to identify the primary tumour centre of mass (COM) and to track the radiotherapy treatment delivery based on this position. Thus the random uncertainties present in conventional (untracked) radiotherapy are largely eliminated. Random uncertainties are reduced to a component of the delineation error; systematic uncertainties include delineation errors, the coincidence of imaging and treatment beam isocentres and any uncertainties in the tracking technique.

The delineation of the target volume during both pre-treatment planning and in real-time as part of the tracking technique leads to uncertainties due to the limited resolution of the images, distortion in the image (see Section 2.1.3) and the method for performing the contouring. The gold-standard of imaging in lung cancer is currently 4DCT. However, the improved soft tissue contrast of MR images compared with CT, advancements in MRI such as new sequences, and the opportunity for increased imaging on the MR-linac suggest that MRI has the potential to become important in lung radiotherapy imaging [18, 138]. The delineation of target volumes and OARs for lung cancer using MR images is currently being investigated in a clinical trial based at

The Christie [139]. Patient-specific geometric distortions will vary patient to patient, but for a single patient are considered to be systematic throughout treatment as the anatomy will be largely similar, and so is likely to have a similar effect on the magnetic field. A previous study has found tissue magnetic susceptibility-induced distortions of up to 0.56 mm for lungs imaged with a 0.5 T scanner [98]. The uncertainty in the real-time delineation of lung tumours on cine-MR as part of the tracking technique has been estimated to be 1 mm, which is similar to the in-plane pixel size for some cine-MR imaging [140]. As the delineation will be required throughout the respiratory cycle, over many fractions, it is considered to be partly a systematic uncertainty as the conditions for delineation will be broadly consistent for each patient throughout the respiratory cycle and fractions.

A further systematic uncertainty lies in the coincidence of the imaging and treatment beam isocentres. As the imaging is used to align the target and treatment beam, any residual difference in the isocentres will result in a systematic shift of treatment to that planned. The ViewRay^{TM} system specification claims incidence to within 1 mm [123].

The time taken for image acquisition and the tracking system latencies due to the time required for processing and implementation of tracking will obviously limit the accuracy of the tracking. For example, during the time for the image to be acquired and processed, the position of the tumour will continue to change, and so the treatment delivery beam will lag behind the tumour motion. When considering a 1D target motion in the superior direction, this systematic uncertainty will result in the top edge of the target receiving a reduced dose, and the tissue immediately

inferior to the target will receive a higher dose than expected. The reverse will be true when the tumour is moving in the inferior direction. This systematic uncertainty will occur in each direction of motion, and is considered a patient-specific systematic uncertainty. The level of geometric uncertainty, i.e. the distance between the true position and the tracked position at a specific time point will depend upon the system latency and the speed of motion, which will vary patient-to-patient. It is assumed that a patient will breathe at a similar rate and amplitude throughout treatment and so the error will be similar for each fraction.

Prediction models have been investigated with the aim of reducing the resulting geometric uncertainties due to the lag in tracking. Seregni et al. [141] have proposed several algorithms, and tested them across a range of acquisition periods (250 to 750 ms) and system latencies (50 to 300 ms). The latency on the ViewRay^{TM} system is currently 300 ms. Six lung cancer patients were imaged on a 3 T MR scanner using a cine-MRI sequence (balanced steady-state free precession, TrueFISP). Five patients were imaged under free-breathing; one patient used audio-visual feedback. Two patients had repeat imaging and so a total of 8 scans were assessed. The imaging consisted of the interleaved acquisition of 512 coronal and 512 sagittal slices, with an acquisition period of 250 ms per slice - two coronal and two sagittal slices per second. The MR imaging parameters were: repetition time 3.03 ms, echo time 1.32 ms, flip angle 45°, bandwidth 1500 Hz per pixel, scan matrix 256 x 256 pixels with 1.48 x 1.48 mm spacing, slice thickness 5 mm, k-space percentage sampling 65% and acceleration factor 2. The tracking error was calculated as the Euclidean distance between the predicted and ground truth tumour position (Radiation Oncologist con-

tours on the reference image) for each of the remaining 1022 frames. The accuracy varied across the five patients who were imaged during free-breathing, but use of the novel algorithm enabled a reduction in the patient-specific tracking root mean square error to 0.2-1.2 mm depending on the acquisition period and system latency investigated. Although current MR-linac systems use 0.5-1.5 T, the reduction in magnetic field strength is not expected to reduce the tracking accuracy.

Other studies have investigated the accuracy of tracking techniques based both on the MR-linac and conventional linacs, with similar results to Seregni et al [141]. A similar interleaved real-time imaging approach was also investigated for tracking of the kidney by Bjerre et al. [140]. A translational error of 1.15 mm was found for a kidney motion of 39.9 mm, during simulation of tracked radiotherapy treatment delivery on the MR-linac. Ravkilde et al. [142] have investigated the geometrical accuracy of dynamic MLC tracking using an implantable transponder, on a conventional linac. The phantom study that performed tracking based on a 3 mm tungsten sphere simulated 8 real patient target trajectories, including 4 lung cases. The tracking system latency was found to be 140 ms, which led to a mean root-mean-square error of 0.54 mm for lung trajectories. In the proof of concept study investigating the use of tracking on the MR-linac, Crijns et al. [143] measured a system latency of approximately 200 ms, consisting of an acquisition time of 50 ms, and a tracking time of 150 ms. It was found that compensation for motion using tracking could nearly fully restore the sharpness of dose distribution from delivery to a static target. The auto-contouring of lung tumours in "real-time" on cine-MR images has been investigated. Yun et al. [144] degraded bSSFP images acquired on a 3 T scanner to the

image parameters expected for low-field imaging; 0.2 and 0.5 T. An increase in the root mean squared error of tracked tumour position with an decrease in magnetic field strength from 0.5 (<0.55 mm) to 0.2 T (<0.92 mm) was reported, with an auto-contouring speed of 5 ms. The accuracy of the auto-contouring of lung tumours has also been investigated with comparison to the intra- and inter-observer variability of radiation oncologists, the gold standard. It was found the algorithm could produce contours within 20 ms, and the contours produced had a similar agreement with manual contours when comparing intra- and inter-observer variability [145].

As the uncertainties in real-time tracking on the MR-linac have been estimated, the van Herk formula [136] can be used to determine the CTV to PTV margins required to account for these uncertainties (see Section 2.3.2). Two margin calculations were performed; one considered "high accuracy", and one considered "low accuracy". The constituent uncertainties can be seen in Table 2.3.

The van Herk margin recipe assumes that dose is delivered in an infinite number of fractions, delivering infinitesimally small dose per fraction. Whilst this is an appropriate approximation for conventional treatments (i.e. delivered over 20/30/33 fractions), for hypofractionated treatments, the margin recipe may be more problematic. Several authors [146,147] have suggested the use of "effective" values for random and systematic uncertainties to account for the reduction in the number of fractions. Thus small increases in the calculated margin sizes were calculated using equations 2.2 and 2.3, as shown in Table 2.3 for a reduction to 3 fractions.

$$\Sigma' = \sqrt{\Sigma^2 + \sigma^2/n} \tag{2.2}$$

$$\sigma' = \sqrt{((n-1)/n)\sigma} \tag{2.3}$$

where Σ' is the modified systematic uncertainty, σ' is the modified random uncertainty, and n is the number of fractions.

The systematic and random uncertainties have been combined with a beam penumbra of 8.0 mm [148] to calculate the margins required for a tracking technique on an MR-linac [136]. This resulted in a range of required margins of 2.65 and 4.74 mm (3.00 and 4.91 mm for 3 fraction SABR), to ensure that 95% of the CTV would be treated to the prescription dose for 90% of the population. This was rounded to 2 and 5 mm for use in the planning system, to allow a pragmatic view of the implementation and future developments of the technique.

The assumption that the remaining uncertainties are predominantly systematic rather than random is a conservative assumption, and so an ideal CTV to PTV margin of zero was also investigated. The results were compared to the standard conventional clinical technique of ITV + 5 mm (CTV) + 5 mm (PTV) (with no tracking).

Bainbridge et al. [148] undertook a similar calculation to investigate lung treatments on the MR-linac. However, their study is quite different to that of this thesis, as it is simulating the use of an ITV approach with no tracking. The only adjustment to the conventional planning technique was to consider the creation of a plan at every fraction immediately prior to treatment (thus reducing the difference in observed 4D tumour motion between planning and fraction to zero), and to image with MR rather than CBCT (which they have assumed will reduce the contouring error and per-fraction localisation error from 2 mm to 1 mm). As no tracking is simulated, an expected intrafractional baseline drift was included in their margin calculation, which is not required in this study. The uncertainty in the incidence of the MR and radiotherapy isocentre was not considered by Bainbridge et al.

Uncertainty	High accuracy	Low accuracy
Random uncertainties:		
Delineation [148]	1 mm	1 mm
Effective random uncertainty	0.816 mm	0.816 mm
Systematic uncertainties:		
Delineation (distortion)	1 mm	1 mm
Imaging and treatment coincidence [123]	0 mm	1 mm
Tracking uncertainty [141]	0.2 mm	1.2 mm
Total systematic uncertainty	1.02 mm	1.85 mm
Effective total systematic uncertainty	1.172 mm	1.938 mm
Penumbra [148]	8 mm	8 mm
Total margin	2.65 mm	4.74 mm
Total margin (SABR)	3.00 mm	4.91 mm

Table 2.3: Breakdown of uncertainties used in margin calculation.

2.4 Summary

MR-linacs have the potential to provide more frequent imaging during image-guided radiotherapy, as well as an improvement in soft-tissue contrast of images acquired. The feasibility of four-dimensional real-time imaging and tracking techniques based on the real-time anatomy rather than surrogates has been demonstrated. This is currently being investigated on the MR-linac for use in the thorax.

The elimination of the potential for changes in the tumour position and motion between treatment delivery and planning (or daily set-up imaging) through the combination of high contrast, real-time imaging and tracking is predicted to allow for target margin reduction as described and calculated in Section 2.3.3.

Central lung tumours are notoriously difficult to treat with conventional or high dose per fraction radiotherapy regimens due to the abutting/overlapping radio-sensitive organs at risk. The reduced margins applicable for use on the MR-linac may allow an isotoxic dose escalation for central lung tumours, with the aim of improving the therapeutic ratio of treatments by increasing the dose to the target volume whilst maintaining a clinically acceptable dose to the OARs.

This project aims to explore the scope of dose escalation possible for central lung

tumours due to new techniques now technically feasible on the MR-linac. The effect of any predicted margin reduction on both the target and OAR doses will be investigated using dose accumulation throughout the respiratory cycle to fully quantify the level of gains that the implementation of real-time tracked lung radiotherapy on MR-linacs may provide.

Chapter 3

Dosimetric Evaluation

3.1 Respiratory Motion

Respiratory motion is a concern during lung radiotherapy, which has been discussed extensively since the mid-1980s, as reviewed in detail by Korreman [149] and Yoganathan [44]. The pattern of respiratory motion of tumours and organs is known to depend upon their volume, location and fixation to other organs. Motion is predominately in the superior-inferior (cranial-caudal) direction, followed by the anterior-posterior direction, with least motion in the left-right direction [13, 40, 44, 150, 151]. A 3D lung tumour motion of greater than 3 cm has been reported, however some tumours are known to move very little. When assessing the motion of 21 lung cancer tumours, Seppenwoolde et al. [150] concluded that "the average amplitude of the tumour motion was greatest (12 +/- 2 mm) in the cranial-caudal direction, for tumours situated in the lower lobes and not attached to rigid structures such as the chest wall or vertebrae". The average motion of these tumours can be seen in Figure 3.1.

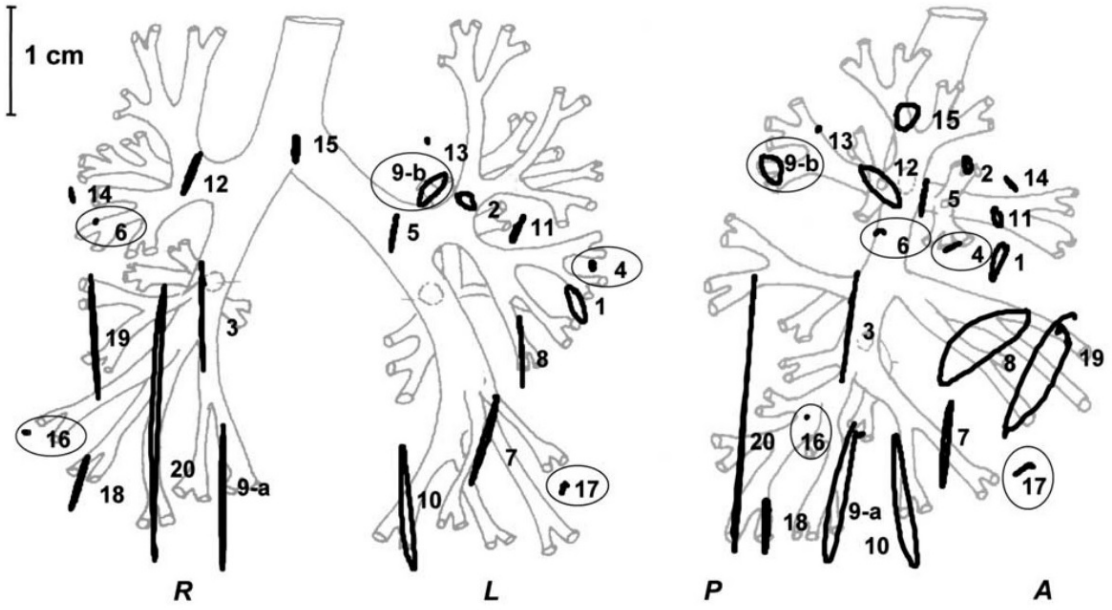

Figure 3.1: Orthogonal projections of the trajectories of 21 tumours as per Seppenwolde et al. [150]. Left image depicts coronal view, right image sagittal view. The tumours are displayed at the approximate positions, those attached to bony anatomy are circled.

3.2 Treatment Simulation

Radiotherapy plans are generally produced on a single image, which is a snapshot of the anatomy at a single time-point. However, if the treatment is delivered throughout the respiratory cycle, any residual motion may cause variations in the planned dose distribution.

The in-silico modelling performed in this thesis is based upon the expected use of MR-linacs, as discussed in detail in Chapter 2. Radiotherapy treatment plans were produced on the mid-ventilation phase. The mid-ventilation phase is the 4DCT phase in which the tumour position is most similar to its time-averaged position throughout the respiratory cycle, as first suggested by Wolthaus et al. [152]. Due to asymmetry in respiratory motion, the mid-ventilation position is not the geometrical midpoint of ventilation, but the time-averaged position, which is usually closer to exhale than inhale. The centre of mass positions of the primary GTV across each phase was

averaged, and the phase with the primary GTV centre of mass position closest to this average was identified as the mid-ventilation phase.

Tracking techniques are used in radiotherapy to mitigate tumour motion by aligning the treatment beam with the target at all times. A technique has been simulated that tracks the primary tumour centre of mass (COM) and repositions the treatment fields accordingly for each phase. In this dataset, the respiratory cycle is divided into ten phases and so the treatment delivery is adapted ten times. More frequent adaptions may be possible in the future using interleaved orthogonal MR imaging, where multiple slices can be acquired every second.

The methods investigated are also directly relevant to the use of implanted fiducial markers for tracking. Once inserted in or close to the tumour, fiducial markers can be used as surrogates of tumour position during treatment delivery [153]. Localisation of radio-opaque fiducial markers can be obtained through fluoroscopic imaging, although this can result in significant radiation doses [154]. Alternatively, the insertion of electromagnetic transponders can be used to wirelessly (and without imaging dose) localise the markers as a surrogate of tumour motion, such as the commercially available Calypso device as described by Shah et al. [46].

3.3 Target and OAR Coverage

To fully assess the doses received by the target and surrounding healthy tissues, dose accumulation over the respiratory cycle was performed and compared to planned doses. The reduced margins that were used, as calculated in Section 2.3.3, have the potential to reduce the target coverage compared to planning techniques using larger, standard margins when the respiratory motion is considered. However, it is predicted that the use of tracking will recover target coverage to similar levels achieved by standard techniques. The tracking technique only considers a rigid translation to

align the primary GTV COM, and does not account for any rotations or tumour deformation during respiration.

As the tracking technique simulated will be based on the primary GTV COM, patients with involved lymph nodes used in this study may suffer with reduced coverage if any differential motion between the primary tumour and lymph nodes exists. This motion has been investigated by Schaake et al. [155] in 51 patients using gold markers implanted into the lymph nodes and daily 4D CBCT. Considerable differential motion between tumour and lymph nodes was found. For twelve patients, Jan et al. [156] concluded that the primary tumour is a comparable surrogate for lymph node position. Future developments on the MR-linac may allow the lymph nodes to be identified and so more complicated tracking or adaption techniques may be possible. However, this is considered beyond the scope of this project, but may suggest that this simulated technique is a pessimistic estimate of achievable coverage on the MR linac.

It was unknown what effect the tracking would have on the surrounding healthy structures. If the relative position between target centre and OAR remained constant, a similar coverage to that at planning would be expected. However, it is known that there is a potential for differential motion, and since the tracking is based solely on the primary target COM, the resulting dose to the OAR could change. An increased dose is expected when the separation between the target and OAR narrows; a decreased OAR dose is expected when the separation widens. Both these scenarios may occur throughout the respiratory cycle, and so the effects may be largely cancelled out. As the plans were produced isotoxically, at least one OAR was at tolerance at planning, so even a small increase in dose may result in OAR(s) breaching dose tolerance(s). The use of smaller margins was predicted to allow a meaningful dose escalation. This coupled with the tracking technique may result in a larger increase in OAR dose from planned doses, than occurs for standard treatments when considered throughout

the respiratory cycle. Therefore this is an important safety consideration in the implementation of dose-escalated tracking techniques.

3.4 Dose Accumulation

For accurate dose accumulation, there are three main requirements as described in detail by Jaffray et al. [157]: a time dependant description of the anatomy and treatment parameters, a method to calculate the dose at each time point, and the ability to accurately accumulate the dose across each time point for each sub-volume. 4DCT images provide the opportunity for the delineation of the target and surrounding structures throughout the respiratory cycle. Modern treatment planning systems allow plans to be accurately calculated on each phase. The difficulty in the process is how to combine the doses received by the sub-volumes across the different 4DCT phases, and perform the dose accumulation.

Deformable image registration (DIR) methods are available to provide the mapping between images required to allow dose accumulation. A subsequent image is warped to the same reference conditions as the reference image, allowing the dose distributions from both images to be accumulated. In this study, each phase will be deformed to the mid-ventilation phase on which the plan was produced. DIR algorithms aim to balance the trade-off between optimising the similarity between images, whilst maintaining a realistic deformation. Commercial DIR software is often included in image processing software and radiotherapy treatment planning systems.

DIR software uses a model to perform the registration and so there will be some limitations. Sarrat et al. [158] discuss the use of DIR in lung radiotherapy and the challenges and limitations that exist. The validation of different DIR software, for different clinical scenarios has been investigated by many authors, for many different DIR systems, using a range of test data. Results vary and while some studies demon-

strate a distance to agreement similar to the image voxel size, others have reported a difference in lung GTV dose of greater than 5% [159–165]. As the registrations can be used in clinical decision making, it is important that the DIR systems have been properly assessed for specific clinical use. Algorithms used in commercial DIR can be very involved and are often supplied as "black boxes" where the user has little control over the settings, and so careful validation of DIR system accuracy is important. The American Association of Physicists in Medicine (AAPM) recently produced a report on the use of image registration and fusion algorithms and techniques [166], which aims to both describe available systems and suggest recommended quality assurance and quality control procedures.

The ANAtomically CONstrained Deformation Algorithm (ANACONDA) is one such DIR system used in radiotherapy within the RayStation TPS (RaySearch Laboratories, Stockholm, Sweden). This combines the use of image intensities with anatomical information. The objective function aims to maximise the image similarity whilst maintaining a regular and invertible grid, and anatomically relevant registrations using delineations as discussed by Weistrand et al. [161]. The RayStation DIR has been validated in thoracic cases and found to have an average target registration error of 1.17 +/- 0.87 mm for 16 thoracic cases, which is similar to delineation uncertainties. Good conformality was also demonstrated through very high Dice similarity coefficient of 0.98 for the two lungs.

As there are known limitations to the accuracy of dose accumulation using DIR methods, an alternative method was also used by averaging the coverage results from each phase incorporating the entire respiratory cycle. However, this is likely to be a pessimistic measure of dose accumulation. If one considers the minimum point dose to a target volume, if the point in each phase that receives the minimum dose is in the exact same point of the structure, the average dose will be accurate. However, it is likely that the point of minimum dose will change between phases due to variations in

the dose distribution and so simply averaging the minimum dose across all phases will result in the minimum possible value. In reality, the "true" value will likely be greater than the averaged minimum estimate, but cannot be less than this. The converse is true for the normal structures. The maximum point dose is likely to be in a different position in each phase, and so the "true" maximum dose is likely to be less than the averaged maximum estimate, but will not exceed it.

Thus, for both target and OAR coverage, the dose metric average (DMA) estimate is the "worst-case" estimate, and the reality will be the same or better.

Both the DIR and average technique will be used to calculate the accumulated dose in the following work. The known limitations in validating DIR algorithms suggest the simplistic average of phases approach is still relevant to give an estimation of the "worst case" dose accumulation. Due to the limitations of both the DIR and average approach to dose accumulation, the feasibility of an alternative method was investigated.

Initial work was undertaken to assess the motion of the proximal bronchial tree (PBT), with the aim of determining whether a simple motion model could be used to accurately accumulate the dose throughout the respiratory cycle. The PBT is a central structure that is known to be a dose-limiting structure during radiotherapy for central lung tumours, and also undergo reasonable respiratory motion. Weckesser et al. have previously measured the respiratory motion of central structures for 24 patients using a two CT images (expiration and inspiration); the airways were found to move up to 14 mm [167]. The dose to the PBT is known to be particularly problematic for central lung tumours, and the "excessive toxicity" experienced in a previous dose-escalation study [57], has led to suggestions of a "no fly zone", effectively limiting treatment of tumours abutting the proximal bronchial tree to lower doses per fraction [168–170]. The PBT is a structure of concern during lung radiotherapy, but also contains clearly visible anatomical landmarks in the form of the bifurcation points.

Visible landmarks have been used in previous studies investigating the accuracy of DIR algorithms, such as in the EMPIRE10 challenge [171] and in the framework suggested by Castillo et al. [172].

3.4.1 Methods: Point Modelling

The bifurcation points (BPs) were initially used as an accurate anatomical point that is easily visualised throughout the respiratory cycle. The carina is also used extensively in radiotherapy treatments for localisation and patient set-up. Ten lung cancer patients who had previously received lung radiotherapy at The Churchill Hospital, Oxford, and had given their written consent for the use of their scans for research purposes were investigated. 4DCT scans acquired on an Optima 580 CT scanner (GE Medical Systems Ltd.) were retrospectively binned into 10 respiratory phases using the integrated Varian Real-time Position Management^{TM} (RPM) system. The RPM system is a non-invasive imaging system that allows the chest motion to be used as a surrogate for respiratory motion. The location of the carina and seven main BPs were identified in Eclipse^{TM} V13 (Varian Medical Systems, Inc.) in each 4DCT phase. A trachea point was also added near a reproducible point, such as a high density spot of cartilage. All point analysis was done in relation to the carina point, which was labelled as the origin, (0,0,0), in each phase. The point positions can be seen in Figure 3.2, and the patient characteristics can be seen in Table 3.1.

A rotation was performed with the aim of minimising the impact of any patient motion or rotation during the scan, by ensuring the angle between the carina point and trachea point was the same for each phase of the image set. Affine transformations were used to register the position of the points on each phase to those at baseline (phase 0, end inspiration).

The number of transformations used to model the seven BP motions with respect to the carina was varied from 7 (where each BP had it's own transformation, and so

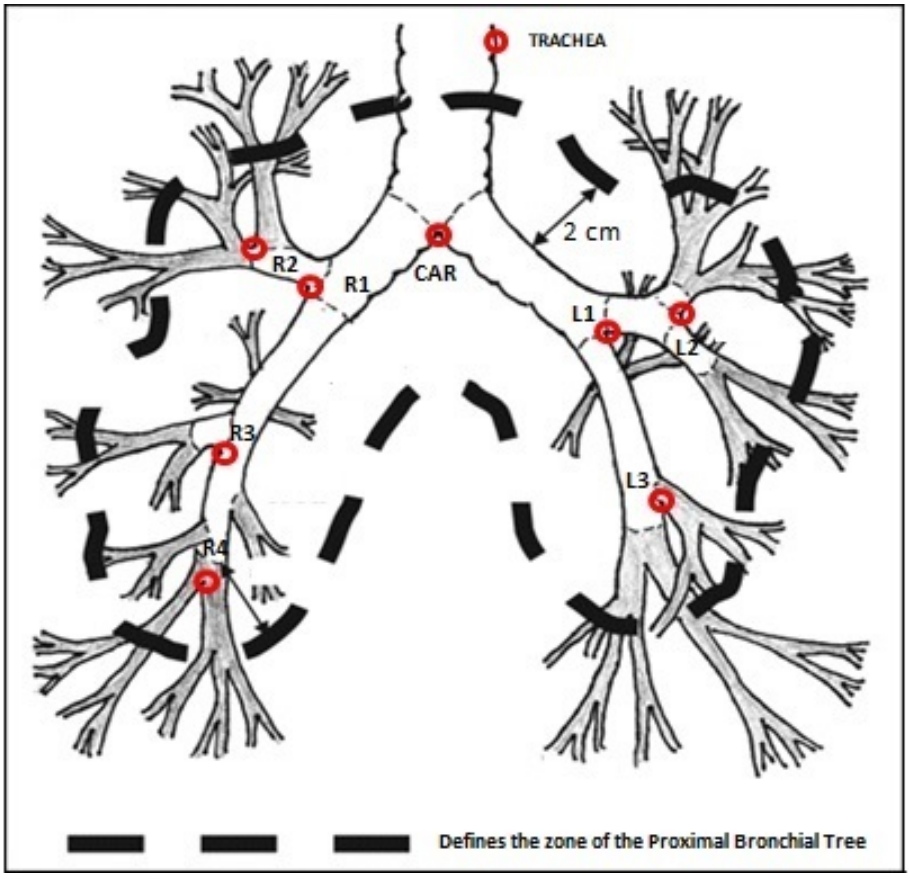

Figure 3.2: Bifurcation point positions, adapted from Timmerman et al. [57]. Car = carina, R1,R2/L1,L2 etc. = right/left hand bifurcation points

Patient Number	TNM Stage	Tumour location	Stage
1	T2aN0M0	Right Lower	I B
2	T4N0M0	Right Middle	III A
3	Mets from colorectal primary	Lower Upper	
4	T1aN2M0	Left Middle	III A
5	T1aN0M0	Right Upper	I A
6	T2bN0M0	Right Upper	II A
7	T1aN0M0	Right Lower	I A
8	T1aN0M0	Right Upper	I A
9	T3N2M0	Right Middle	III A
10	T3N0M0	Right Lower	II B

Table 3.1: Patient characteristics for PBT motion investigation

perfect agreement was expected), to 1 (a single, global transformation for all BPs). As the number of transformations reduced, it was expected that the accuracy of the models would decrease. The transformations were optimised on a range of subsets of the BPs and applied to all BPs to determine if their position could be inferred from their position in phase 0, and the rotation/scaling factors obtained from the subset of points. The residual maximum absolute distance between points at baseline and in each phase was used as a measure of the accuracy of using affine transformations to map the BPs throughout the respiratory cycle.

Code was written in MatLab R2015b (The MathWorks Inc.) and used for all optimisations, using the "fminunc" minimisation optimisation function. A transformation matrix containing a rotation angle and scaling factor for each direction was optimised to minimise the sum square error, or maximum 3D distance between the BPs in phase X and baseline. Several metrics were used to assess the differences between the different BPs motion; average distance, average absolute difference, standard deviation of distance and the sum square error of distances between BPs at phase X and baseline.

The robustness of the registration models were investigated by re-optimising a single phase from each patient with a slight deviation on the starting parameters of 0-0.2 radians for rotations, and 0.95-1.2 for scaling factors.

3.4.2 Results: Point Modelling

The BPs were identified in 650/700 cases (7 BPs per phase, per patient). BPs were unable to be identified due to tumour involvement or more frequently due to the motion or volume averaging that takes place in between CT slices. If a point was unable to be visualised, the point was ignored in all optimisations.

The location of the BPs did not appear to correlate with the amplitude of motion, similar to previous findings that the extent of tumour motion cannot be predicted from their size, position within lungs or pulmonary function by Stevens et al. [173].

The largest motion measured was for point R3, which demonstrated an absolute maximum motion of 2.2 cm in the superior/inferior direction. The range of motion varied considerably between patients. Maximum motion of points ranged from 0.15 (patient 1) to 2.2 cm (patient 10). The absolute maximum motion values can be seen in Figure 3.3. Results for each direction can be seen in Figure 3.4.

As expected, an increased variability of scaling factors were found across BPs in the superior-inferior direction (standard deviation 0.111) compared with lateral (0.047) or anterior-posterior (0.014). The optimisations were found to be very robust, resulting in the same transformations to within 5 decimal places. This suggests the global minimum value had been found by the optimisation.

When the BPs were regionally paired, as in Figure 3.5 and a single transformation applied to both points, the maximum misalignment of BPs was 1.8 mm across the 10 patients and 10 respiratory phases. This suggests that the motion of the airways between the BPs may also be predictable to a reasonable accuracy through the application of this transformation.

3.4.3 Methods: Airway Modelling

The BPs were used as a surrogate for the airway structure position to assess if the registration models based on the BPs would be useful in modelling the airway structures. This was investigated by applying the resulting point transformations to the airway structures.

The airways were contoured on each phase for 5 patients, who had a range of respiratory motion. The contours produced a 3D array of points making up the contour of the airways on a slice by slice basis. The transformations were interpolated between the BPs, and applied to the length of the airways. Metrics commonly used in radiotherapy, the Dice similarity coefficient (DSC) [174, 175] and distance to agreement, including Hausdorff distance [176] were used to compare the contours.

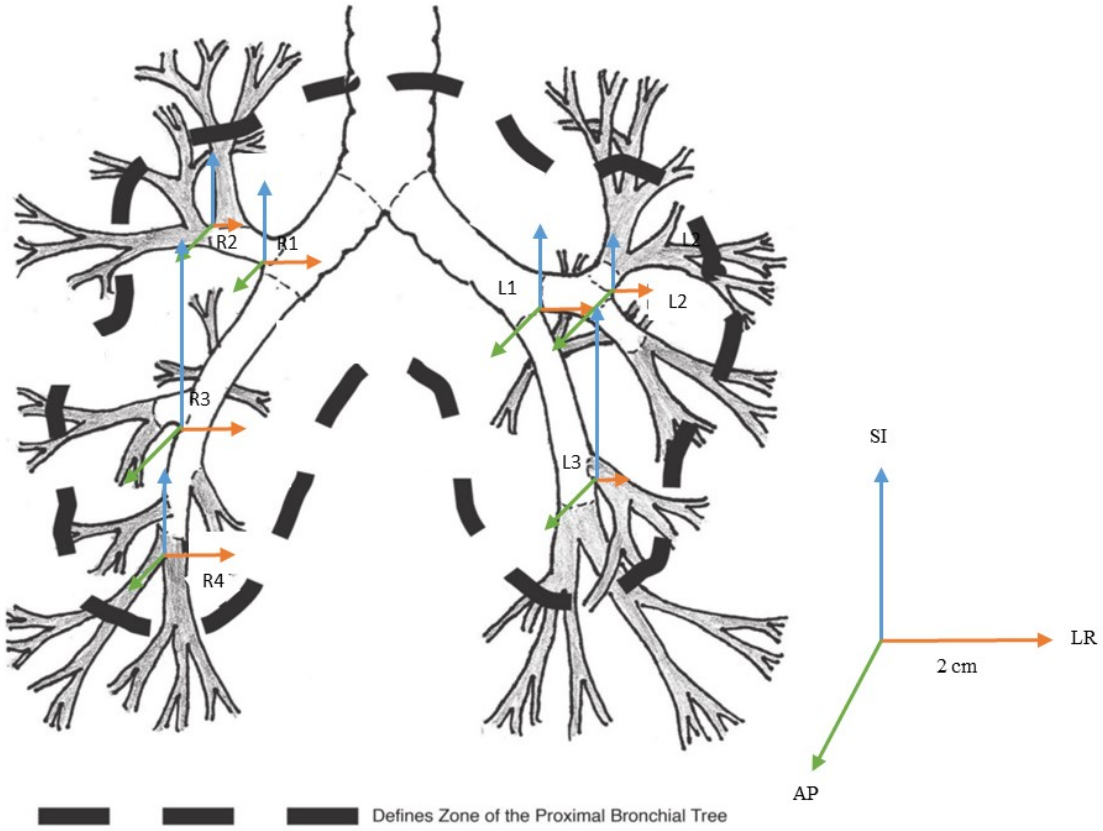

Figure 3.3: Motion of bifurcation point positions, adapted from Timmerman et al. [57]. Arrows show the relative size of motion in each direction.

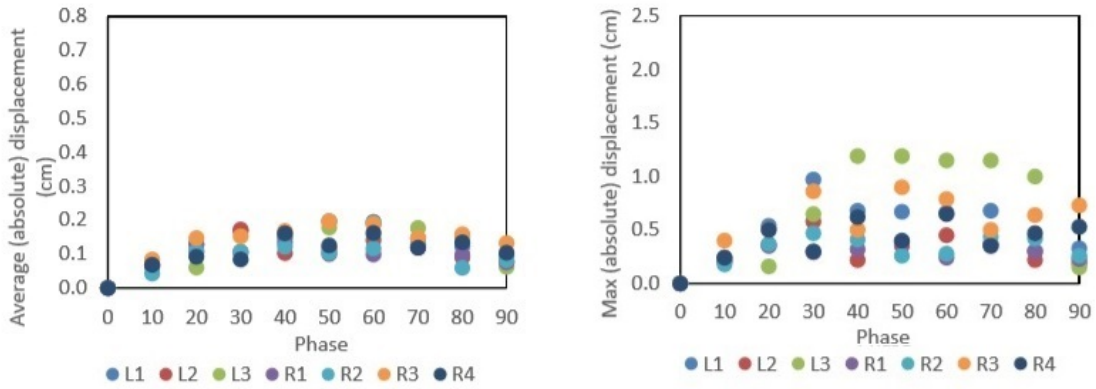

(a) Left-right direction

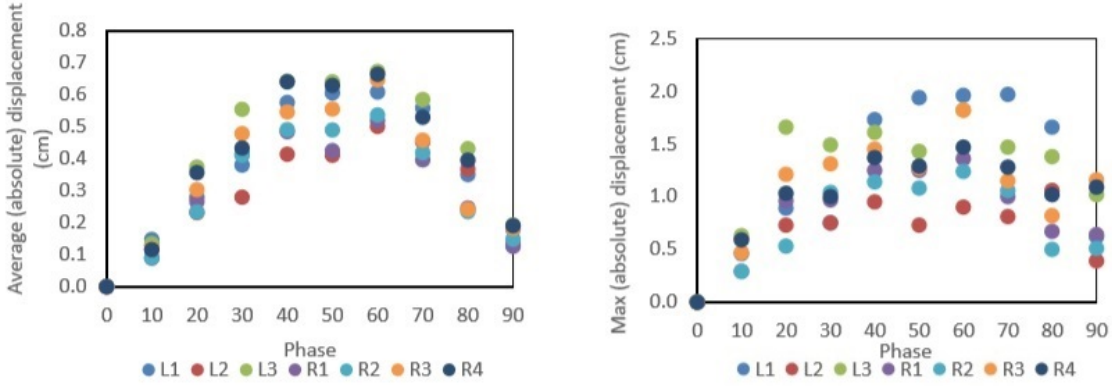

(b) Superior-inferior direction

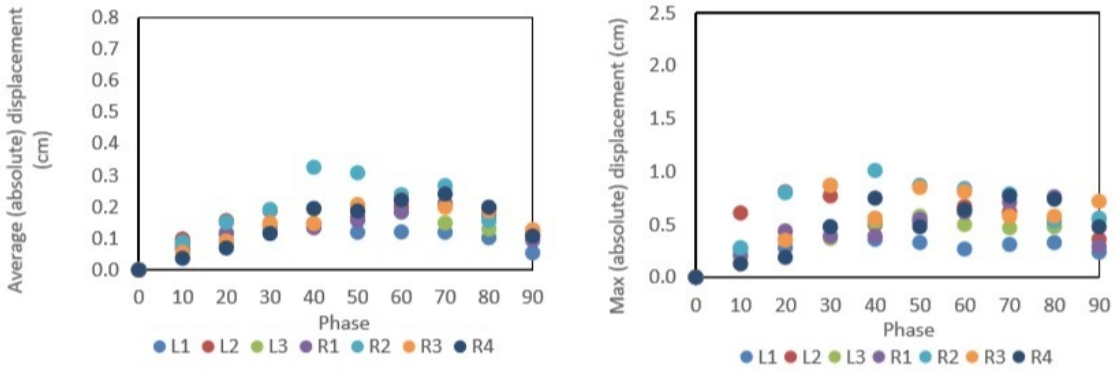

(c) Poserior-anterior direction

Figure 3.4: Bifurcation point motions; (L) Average absolute displacement, (R) Maximum absolute displacement for each individual direction of motion.

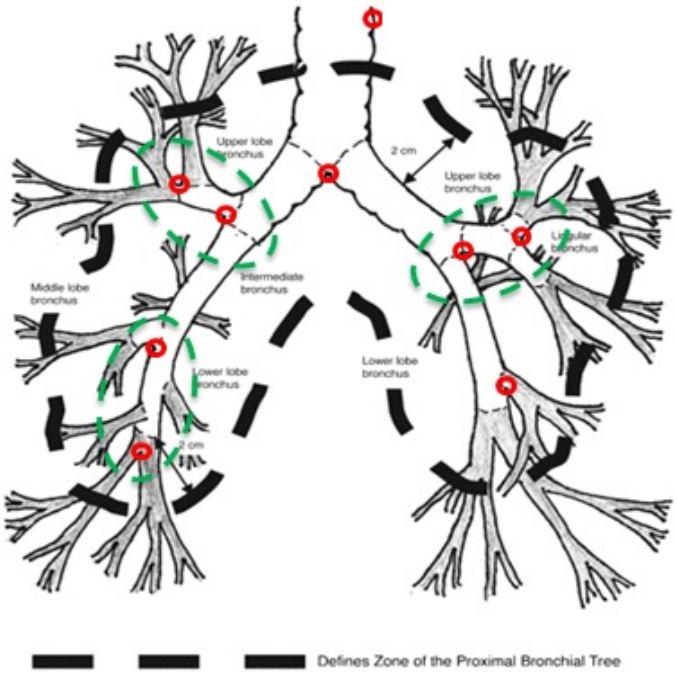

Figure 3.5: Pairing of points shown in green.

The DSC is a measure of the overlap of volumes, calculated using Equation (3.1) [174], for which a minimum value of 0.8-0.9 [166] has been suggested for adequate contour similarity in radiotherapy.

$$DSC = \frac{2|V_{\text{reference}} \cap V_{\text{transformed}}|}{V_{\text{reference}} \cup V_{\text{transformed}}} \tag{3.1}$$

where DSC is equal to the ratio of twice the volume of intersection of the reference volume and the transformed volume to the sum of the two volumes. DSCs range from 0 to 1; volumes which have no overlap will have a DSC of 0, perfectly overlapping volumes will have a DSC of 1.

The Hausdorff distance is a measure of the maximum distance between two structures [176], calculated by taking the maximum value of the smallest distance for every point of a structure to any point of the other structure. The modified Hausdorff distance (average of all calculated distances between two structures) has also been shown

to be a useful measure of image similarity [177].

3.4.4 Results: Airway Modelling

The transformations obtained from the BPs were successfully used to increase the overlap of the airway structures throughout the respiratory cycle. When the BP transformation for each end of the bronchial airway were used throughout that particularly branch of the bronchial tree, the Dice similarity coefficient was increased from 0.24 to 0.61, and a decrease in maximum Hausdorff distance from 2.0 to 0.5 cm was measured. An example of the improvement seen in a single slice is shown in Figure 3.6.

3.5 Discussion

The use of bifurcation point motion models to transform the airway structures throughout the respiratory cycle has demonstrated the difficulties in using simple models to predict the respiratory motion of a complicated structure that undergoes reasonable respiratory motion. Whilst an increase in conformity metrics was seen, the max DSC achieved was 0.61, and a Hausdorff distance of 0.5 cm between the structures remained. The AAPM suggest a DSC of at least 0.8-0.9 for use in image registration, based upon contouring uncertainty [166]. Thus, it was concluded that the error in the registration using the simple localised affine transformations of structures is too large for reliable dose accumulation. The full evaluation of target and OAR coverage across the respiratory cycle for ten locally advanced, and ten SABR NSCLC patients will be performed using DIR and dose metric averaging across the 10 respiratory phases.

The accuracy of the modelling performed could potentially be improved, for example by using more points within the airway structures, or through the use of artificial intelligence or machine learning. As other techniques for dose accumulation are avail-

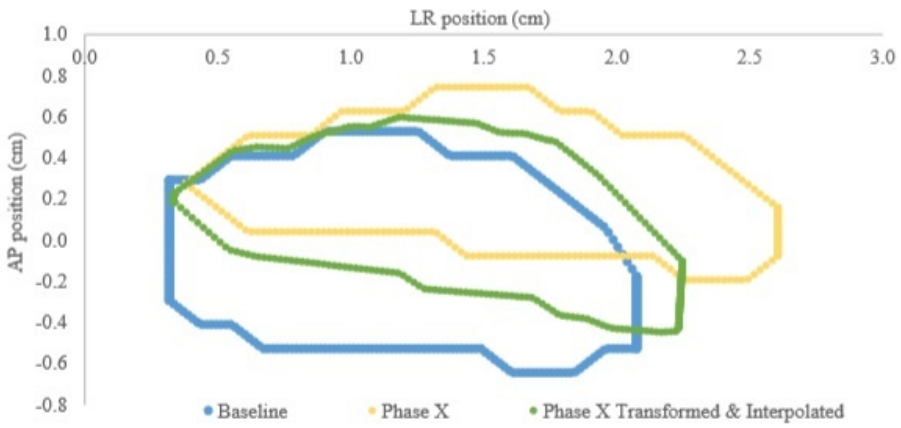

Figure 3.6: Example of a single slice transformation of airways.

able, it was beyond the scope of this thesis to further explore the motion modelling.

Chapter 4

Dose Escalation

4.1 Patients

The dose escalation made possible using the MR-linac and a tracking technique for central NSCLC tumours has been investigated in this thesis. Ten locally advanced patients and ten early stage SABR patients who had undergone 4DCT scans were used in this study. Scans of five locally advanced patients were taken from a publicly available dataset described by Hugo et al. [178], for which multiple 4DCT image sets were available. The remaining 15 patients were retrospectively analysed after receiving treatment at The Churchill Hospital, Oxford. All patients were selected based on the central position of their tumour(s), and had given their consent for their images to be used for research purposes.

The 4DCT images acquired were binned into 10 3D image sets, each representing a single phase (phase 0 to phase 90) of the respiratory cycle. It has been shown that 4DCT image sets can adequately capture the motion of lung tumours [17, 179–181] throughout respiration. All patients were imaged on a 16-slice helical CT scanner, with a slice thickness of 2.5 mm (Oxford) or 3 mm (Hugo et al. patients [178]).

The derivation of the margins used has been discussed in Section 2.3.3. Briefly, the

mid-ventilation 4DCT phase was used for planning, with a GTV to CTV margin of 5/0 mm for locally advanced/early stage patients, as per standard clinical practice. Mid-ventilation CTV to PTV margins of 0, 2 and 5 mm were used to simulate a "perfect", "high accuracy" and "low accuracy" tracking technique, calculated using the uncertainties listed in Table 4.1. The "high accuracy" margin was rounded down to 2 mm (from 2.65 and 3.00 mm), to allow for future developments in the treatment delivery/tracking techniques.

Plans were also produced using the conventional ITV technique (PTV_{ITV}), based on the ITV (sum of all CTVs) plus a 5 mm setup margin, which did not include tracking, for comparison with the experimental plans. PTV_{ITV} and $PTV_{\text{Low Accuracy}}$, both of which had an ITV/CTV to PTV margin of 5 mm would be of equal volume if there was no tumour motion during respiration. When motion occurs, the ITV approach results in a larger PTV as it envelopes the position of the tumour throughout the respiratory cycle, as opposed to accounting for the motion by tracking.

This resulted in a range of required margins of 2.65 and 4.74 mm (3.00 and 4.91 mm for 3 fraction SABR), to ensure that 95% of the CTV would be treated to the prescription dose for 90% of the population. This was rounded to 2 and 5 mm for use in the planning system, to allow a pragmatic view of the implementation and future developments of the technique.

Uncertainty	High Accuracy	Low Accuracy
Random uncertainties:		
Delineation [148]	1 mm	1 mm
Systematic uncertainties:		
Delineation (distortion)	1 mm	1 mm
Imaging and treatment coincidence [123]	0 mm	1 mm
Tracking uncertainty [141]	0.2 mm	1.2 mm
Total systematic	1.02 mm	1.85 mm
Penumbra [148]	8 mm	8 mm
Total margin	2.65 mm	4.74 mm
Total margin (SABR)	3.00 mm	4.91 mm

Table 4.1: Breakdown of uncertainties used in margin calculation.

4.2 Planning Methods

An in-silico modelling study was undertaken to assess the potential dose escalation that may be possible due to reduced margins as a result of treating central lung tumours on an MR-linac with a tracking technique.

Delineation of the GTV was performed by a radiation oncologist on a minimum of the two extreme 4DCT phases, and often on all phases. On phases where the GTV had not been contoured by a radiation oncologist, the GTV contours were copied from the nearest phase where it had been delineated and then edited as required. All delineations and contour margin expansions were performed in the Eclipse (version 13) treatment planning system (TPS), and organs as risk were delineated following guidance from the consensus atlas by Kong et al. [182].

The RayStation (version 7) TPS was used to produce dual-arc VMAT plans using 6 MV photons, based upon an Elekta Agility standard linac, with MLCs 5 mm wide at isocentre. Although VMAT plans are currently not used on MR-linacs, it is anticipated that this will come into clinical practice in the near future. In-silico modelling of 7-field IMRT plans were also completed for two patients to investigate whether similar levels of dose escalation could be achievable using IMRT.

Isotoxic plans were produced for each PTV. Normal tissue tolerances were taken from clinical trials and current clinical practice.

4.2.1 Locally Advanced

The planning aims and OAR dose tolerances for the locally advanced (LA) patients were largely taken from the UK-based IDEAL-CRT trial, and thus have been tested in a phase I-II trial and shown to result in acceptable toxicity levels [183]. IDEAL-CRT aimed to deliver an escalated range of dose per fraction, ranging from 63 to 73 Gy in 30 once-daily fractions over 40 days with two concurrent cycles of cisplatin

and vinorelbine. Isotoxic plans were delivered to 82 patients to investigate the ideal fractionation regimen in terms of survival and acceptable toxicity. As the safety of delivered doses was observed, the prescribed dose and dose limits of the oesophagus were increased. Toxicity levels were found to be acceptable, and the trial concluded that the maximum tolerated dose to 1 cm^3 of oesophagus was 68 Gy. Two-year overall survival was 68.0% (95% confidence intervals 57.8-78.1%), and the mean overall survival was 36.9 months.

A recent further evaluation of the results from IDEAL-CRT by Vivekanandan et al. [71] found an association between all-cause death rate and the dose received by small volumes of heart receiving between 63 and 69 Gy. Thus an additional heart constraint of maximum dose to 2% of heart of 66 Gy (the mid point of 63 and 69 Gy) was used. Additional constraints on other surrounding OARs were added to limit the doses received at planning, because the upper limit of tumour prescription dose of 73 Gy used within IDEAL-CRT was removed in this study, and so higher OAR doses otherwise may have occurred. These extra constraints were selected by analysing the planned doses to these structures for 24 IDEAL-CRT patients. The 24 patients were selected based on the tumour location and prescription dose, aiming to include the plans expected to have the highest OAR doses;

- All 10 patients with "upper" tumour locations.
- 10 patients with "upper-mid" tumour location, with a range of prescribed doses.
- Any additional patients with the maximum prescribed dose of 73 Gy (4 additional "upper-mid" tumour location patients).

The OAR planned doses for these 24 patients were considered safe limits as no unacceptable toxicities were found in the IDEAL-CRT study. The patient characteristics can be seen in Table 4.2, and the planning constraints used are shown in Table 4.3.

Patient	Stage	TNM	Tumour Location
1	IIIA	T3N2M0	Left-Mid/Hilar
2	IA	T1aN0M0	Left-Middle
3	**IIIA**	**T3N2M0**	**Right-Upper**
4	**IIIA**	**T2N2M0**	**Left-Upper**
5	IIA	T2aN1M0	Right-Hilar
6	**IIIB**	**T2N3M0**	**Right-Lower**
7	IIA	T2aN1M0	Left-Middle
8	**IIA**	**T1N1M0**	**Left-Upper**
9	IIB	T3N0M0	Right-Middle
10	**IIA**	**T2N2M0**	**Right-Lower**

Table 4.2: LA-NSCLC Patient characteristics. Patients highlighted in bold are those which had audio-visual feedback to minimise breathing irregularity during image acquisition as per Hugo et al. [178].

Volume	Constraint	Origin
PTV	90% isodose to cover 98% of PTV	IDEAL-CRT
Lung	$EQD2_{mean}$ 18.2 Gy	IDEAL-CRT
Heart	$D_{100\%} < 45$ Gy	IDEAL-CRT
	$D_{67\%} < 53$ Gy	IDEAL-CRT
	$D_{33\%} < 60$ Gy	IDEAL-CRT
	$D_{2\%} < 66$ Gy	Vivekanandan et al.
Spinal Cord	$D_{0.1cc} \leq 47$ Gy	IDEAL-CRT
Brachial Plexus	$D_{30\%} \leq 60$ Gy	IDEAL-CRT
	$D_{0.1cc} \leq 65$ Gy	IDEAL-CRT
Oesophagus	$D_{1cc} \leq 68$ Gy	IDEAL-CRT
Pulmonary artery, aorta, vena cava	$D_{1cc} \leq 75$ Gy	Analysis of IDEAL-CRT doses
Proximal bronchial tree	$D_{1cc} \leq 75$ Gy	Analysis of IDEAL-CRT doses
Trachea	$D_{1cc} \leq 75$ Gy	Analysis of IDEAL-CRT doses

Table 4.3: Constraints used during LA-NSCLC isotoxic radiotherapy treatment planning. "IDEAL-CRT" constraints as per trial protocol [183], findings from a heart dose investigation by "Vivekanandan et al." [71], and post-hoc "Analysis of IDEAL-CRT doses" as part of this thesis.

The clinical relevance of any increase in prescribed dose obtained through the reduced margins was predicted by calculating the estimated two year disease-free survival from a radiobiological model. Partridge et al. [66] performed a review of sixteen clinical trials of dose escalation for locally-advanced NSCLC. The results of 29 different "standard" (2.0-2.3 Gy/fraction, 1 fraction, 5 days per week), hyperfractionated (more than one fraction per day) and hypofractionated (3.5-26 Gy per fraction) treatment regimens were analysed. Actuarial local disease-free survival (DFS) at two years was used as the primary efficacy endpoint. The dose-response described by the resulting model can be seen in Figure 4.7.

The resulting doses for each PTV were converted into biologically effective dose (BED_{10}) using Equation (4.1) and then to two Gray equivalent dose (EQD_2) using Equation (4.2). This allowed the two year disease-free survival to be estimated from the Partridge model, and the experimental PTV results to be compared to the standard PTV_{ITV} results. An increase of at least 5% in two year disease-free survival was considered clinically meaningful.

4.2.2 Stereotactic Ablative Radiotherapy

The stereotactic ablative radiotherapy (SABR) planning constraints were based on those used in the EORTC-22113-08113-LungTech trial, as discussed by Adebahr et al. [185]. LungTech is investigating the safety and efficacy of using SABR for central

$$BED_{\alpha/\beta} = Nd\Big[1 + \frac{d}{\alpha/\beta}\Big] - k(T - T_{\text{delay}}) \tag{4.1}$$

$$EQD_2 = BED_{\alpha/\beta}\Big/\Big(1 + \frac{2}{\alpha/\beta}\Big) \tag{4.2}$$

where N is the number of fractions of size d, T is the overall treatment time, T_{delay} is the delay until the onset of repopulation (21 days), and k is the biological dose needed to compensate each day for repopulation (0.6 Gy/day) as calculated by Van Baardwijk et al. [184]. A tumour α/β of 10 Gy was used, as commonly used for lung cancer.

early stage inoperable lung tumours with 8 fractions of 7.5 Gy (BED_{10} of 105 Gy^{-1}). The patient characteristics can be seen in Table 4.4, and the planning constraints are listed in Table 4.5.

The dose-response model used for the locally-advanced patients as discussed in Section 4.2.1 was not used for the SABR investigation as the data used in the model at high doses, around the SABR prescription dose, are very dispersed, and it appears the model is driven by data at lower doses. Therefore, alternative models specific to SABR patients have been used.

SABR for early-stage lung cancer is known to be very effective, with local control rates greater than 90% when biologically effective doses of at least 100 Gy^{-1} are delivered to the tumour [186–188]. Many dose escalation studies have concluded there is a significant improvement in survival if targets receive a BED_{10} of at least 100 Gy^{-1}. To assess the clinical relevance of any dose escalation found to be possible through the use of an MR-linac tracking technique, the increase in the number of plans able to achieve a BED_{10} of at least 100 Gy^{-1} was compared to the standard technique.

Zhang et al. [189] studied the correlation between planned BED and pooled estimates of two-year overall survival using 34 observational studies that included a total of 2,587 patients. The doses were split into four dose groups; "low" (<83.2 Gy),

Patient	Stage	Tumour Location
S1	I	Mid-right
S2	I	Mid-left
S3	I	Mid-left
S4	I	Mid-right
S5	I	Mid-right
S6	I	Mid-right
S7	I	Mid-right
S8	I	Mid-left
S9	I	mid-right
S10	I	Mid-left

Table 4.4: SABR patient characteristics.

Volume	Constraint	Origin
PTV	100% isodose to cover 95% of PTV 90% isodose to cover 99% of PTV 110% $\leq$ max dose $\leq$ 130% of prescribed dose	LungTech
Lungs-GTV	V20$\leq$ 10%	SABR Consortium
Heart	$D_{1cc} < 50$ Gy	SABR Consortium
Spinal Cord	$D_{0.1cc} \leq 32$ Gy	LungTech
Brachial Plexus	$D_{1cc} \leq 38$ Gy	LungTech
Oesophagus	$D_{1cc} \leq 40$ Gy	LungTech
Body-PTV	$D_{1cc} \leq 60$ Gy	LungTech
Chest wall	$D_{1cc} \leq 39$ Gy $D_{30cc} \leq 35$ Gy	SABR Consortium
Great vessels	$D_{1cc} \leq 60.5$ Gy	Clinical practice
Trachea and main bronchus	$D_{1cc} \leq 44$ Gy	LungTech

Table 4.5: Planning constraints used for SABR patients taken from SABR Consortium guidelines [58], LungTech trial protocol [185], and clinical practice used in clinic.

"medium" (83.2-106 Gy), "medium to high" (106-146 Gy) and "high" (>146 Gy), and it was found that the two-year overall survival was superior for the "medium" and "medium-high" groups compared with the "low" and "high" groups. The study also highlighted a trend towards more adverse events with a higher dose, which may help explain the decreased survival for the "high" dose group. The isotoxically escalated prescribed doses from this study will also be classified into the dose groups from Zhang et al., to investigate the predicted outcome for each experimental PTV.

4.3 LA Results

4.3.1 PTV Volume

The PTV volumes calculated for each patient are shown in Table 4.6 and Figure 4.1. The PTV volumes for the (standard) ITV technique ranged from 73.7 to 660.4 cm^3, with a median/mean volume of 239.5/279.8 cm^3. The tracking approaches based on a single phase GTV, as discussed in detail in Section 2.3, were found to reduce the size of the PTV volume compared with the standard technique. Statistical tests could be used to assess significance, although as the margins have been reduced, the re-

sults are somewhat obvious; $P<.05$ ($PTV_{\text{Low Accuracy}}$) and $P<.001$ ($PTV_{\text{High Accuracy}}$, PTV_{Perfect}) were calculated when a two-tailed, paired t-test was performed, comparing the experimental PTVs to the standard PTV. The "low accuracy" tracking technique was found to reduce the PTV volume to a median/mean (range) of 187.2/225.5 (46.3-556.9) cm^3. The "high accuracy" tracking was found to reduce this further to a median/mean (range) of 131.8/163.4 (31.0-425.8) cm^3, and the consideration of "perfect tracking" reduced this to less than 50% of the standard volume to a median/mean of 103.9/126.9 (21.3-356.3) cm^3.

4.3.2 Isotoxically Prescribed Dose

The isotoxically prescribed doses achievable for each PTV and patient can be seen in Table 4.7 and Figure 4.2. The dose escalation achieved by the experimental PTVs was found to be dosimetrically relevant compared to the doses achieved for the standard PTV, as shown in Figures 4.3. The increase in prescribed dose was found to be statistically significant when a two-sided, paired t-test was used ($P<.05$). The specific organ at risk constraints that limited the possible dose escalations depended on tumour location, and were: maximum dose to 2% of heart, maximum dose to 1 cm^3 of pulmonary artery, aorta, trachea and oesophagus.

Large degrees of escalation were achievable for two patients in particular. However, when removing these two patients from the data set and considering the remaining eight patients, the increase in prescribed dose was still found to be dosimetrically relevant. The level of dose escalation achievable was found to be dependent on the tumour position relative to the surrounding dose limiting OARs. Importantly, overlap of the CTV with an OAR with a maximum dose constraint was found to restrict the possible dose escalation. Patients 2 and 9 were able to receive a large dose escalation, and had minimal overlap of CTV and OARs (0.7 and 0.9 cm^3), whereas the remaining patients had more significant overlaps ranging from 3.5 to 18.3 cm^3.

Patient	PTV Volume (cm^3) - LA NSCLC			
	PTV_{ITV}	$PTV_{Low\ Accuracy}$	$PTV_{High\ Accuracy}$	$PTV_{Perfect}$
1	73.7	46.3	31.0	21.3
2	106.6	75.9	50.6	33.6
3	119.8	97.7	62.0	45.5
4	143.7	131.3	85.4	63.7
5	169.7	131.4	93.2	72.5
6	309.2	243.0	170.4	135.3
7	366.7	327.8	249.3	183.5
8	414.4	342.2	235.6	182.4
9	434.4	302.7	230.8	175.5
10	660.4	556.9	425.8	356.3
Median	239.5	187.2	131.8	103.9
Mean	279.8	225.5	163.4	126.9
Minimum	73.7	46.3	31.0	21.3
Maximum	660.4	556.9	425.8	356.3

Table 4.6: PTV volumes (cm^3) for each locally NSCLC advanced PTV. PTV_{ITV} is the standard ITV approach with clinically used CTV to PTV margins of 5 mm. $PTV_{Low\ Accuracy}$, $PTV_{High\ Accuracy}$, and $PTV_{Perfect}$ are the experimental PTV volumes created using a single phase GTV and a range of CTV to PTV margins (5, 2, 0 mm) based on estimated uncertainties in the tracking process as previously discussed.

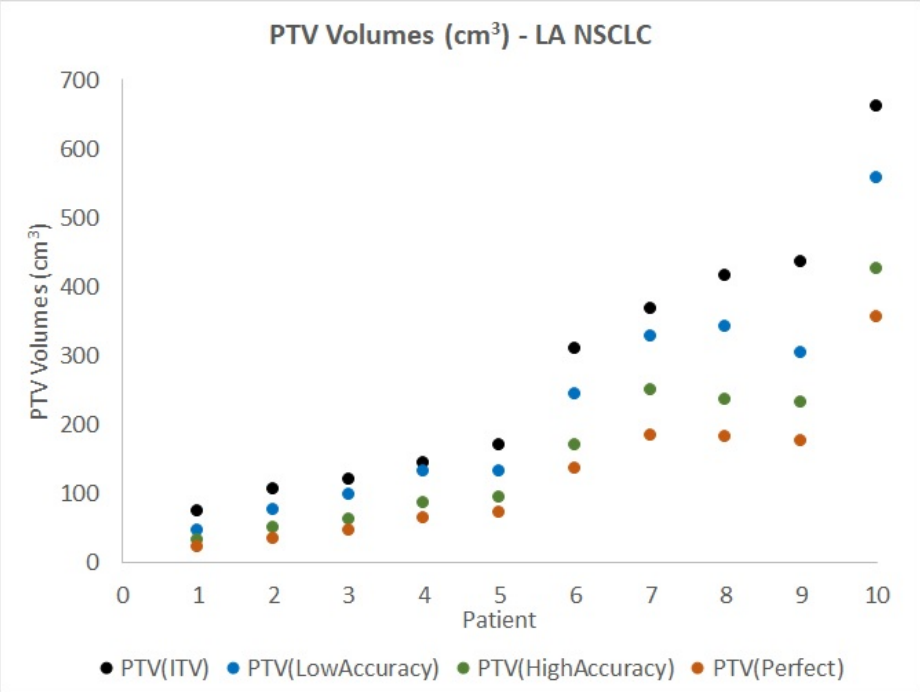

Figure 4.1: LA-NSCLC PTV Volumes

Patient	Prescribed dose (Gy) - LA NSCLC				Limiting OAR
	PTV_{ITV}	$PTV_{Low\ Acc}$	$PTV_{High\ Acc}$	PTV_{Perf}	
1	70.4	71.2	71.8	72.2	Heart
2	90.0	92.6	109.9	131.5	Pulmonary artery
3	75.8	77.5	77.5	78.9	Aorta/trachea
4	71.6	73.2	75.4	76.4	Oesophagus
5	73.6	74.5	76.7	78.5	Pulmonary artery
6	65.9	69.8	71.8	76.5	Heart/pulmonary artery
7	67.5	68.2	69.7	70.0	Aorta
8	64.1	66.7	69.7	72.0	Aorta/trachea
9	72.6	88.3	102.8	113.4	Heart
10	70.2	72.4	74.1	76.5	Oesophagus
Median	71.0	72.8	74.8	76.5	
Mean	72.2	75.4	80.0	84.6	
Minimum	64.1	66.7	69.7	70.0	
Maximum	90.0	92.6	109.9	131.5	
		P=0.049	P=0.03	P=0.03	

Table 4.7: Prescribed doses (Gy) for each locally advanced NSCLC PTV. PTV_{ITV} is the standard ITV approach with clinically used CTV to PTV margins of 5 mm. $PTV_{Low\ Acc}$, $PTV_{High\ Acc}$, and PTV_{Perf} are the experimental PTV volumes created using a single phase GTV and a range of CTV to PTV margins (5, 2, 0 mm) based on estimated uncertainties in the tracking process as previously discussed.

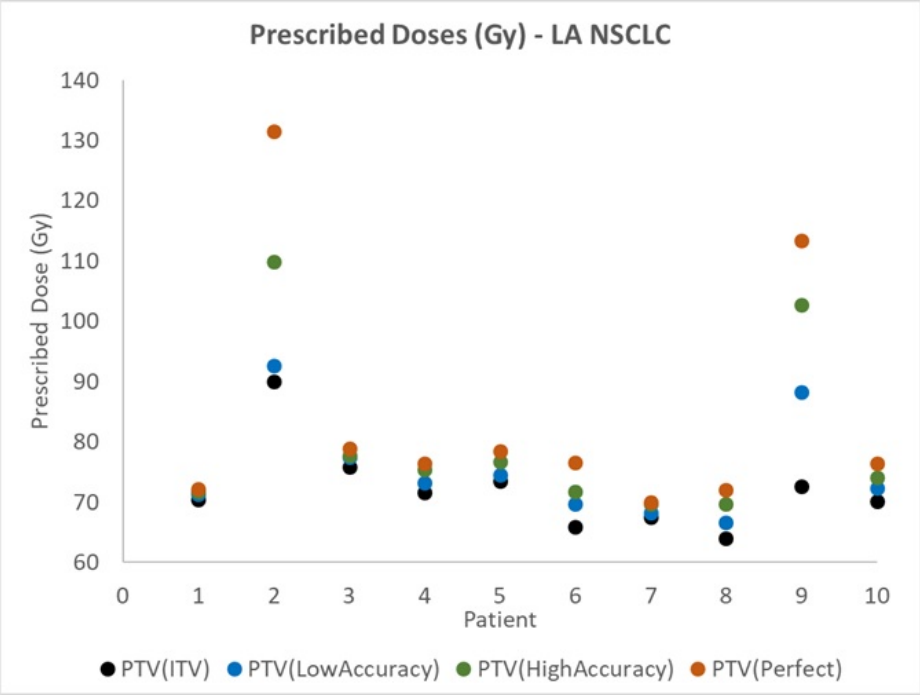

Figure 4.2: LA-NSCLC Prescribed doses

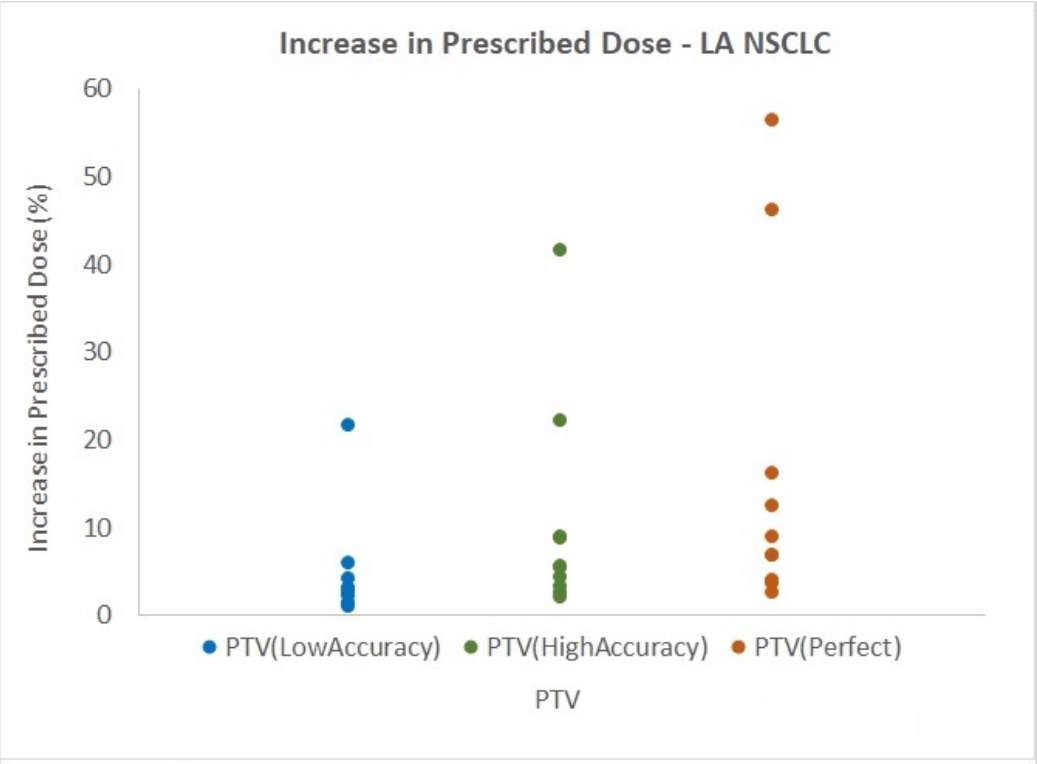

(a) LA-NSCLC Increase in prescribed doses, as a percentage of PTV_{ITV}

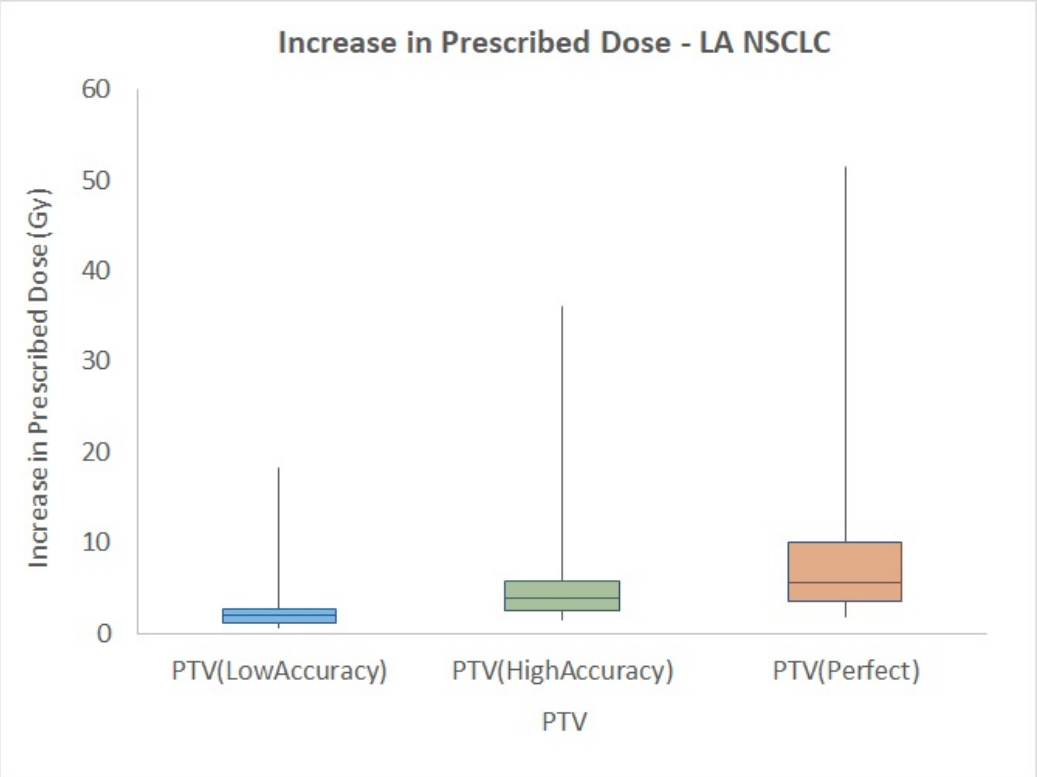

(b) LA-NSCLC Box plot of increase in prescribed doses, compared to PTV_{ITV}

Figure 4.3: LA-NSCLC Increase in prescribed doses compared to PTV_{ITV} for each experimental PTV.

For Patients 2 and 9, the reduction in CTV to PTV margin resulted in a proportionally large decrease in the overlap of PTV and dose-limiting OARs, allowing a large increase in target dose, with no increase in dose to OARs. Conversely, patients 1 and 3 who had very limited dose escalation, had a large degree of PTV and OAR overlap even for the smallest PTV (which is the same volume as the CTV). Thus for these patients, no technique will be able to increase the dose to the tumour volume without compromising the dose to surrounding OARs which may result in increased toxicity, or accepting a less homogeneous dose to the tumour, with the regions of CTV/OAR overlap receiving a reduced dose. This can be easily visualised by comparing Patients 2 and 9 in Figure 4.4, where a small overlap of CTV and OARs in seen, and a large dose escalation was achieved, with Figure 4.5 where a reasonable CTV and OAR overlap is seen, resulting in only a small dose escalation.

The results suggest that patients who would benefit most from treatment on the MR-linac can easily be identified during the radiotherapy planning stage, using the planning 4D image set based upon the region of overlap between CTV and surrounding OARs.

The IMRT plans resulted in similar levels of dose escalation compared with the VMAT plans as can be seen in Table 4.8. Generally the IMRT prescribed doses were lower than the VMAT plans, which has been attributed to the reduced conformality of the IMRT technique. Only two patients were used to confirm that similar levels of dose escalation were achievable for IMRT (currently technically feasible on the MR-linac) compared to VMAT (as used in this study), as it is anticipated that this will become available in the near future.

4.3.3 Predicted Survival

The increased prescribed doses for the experimental PTVs resulted in increased biological effective doses (BED), calculated using an α/β of 10 Gy. A median BED_{10} of

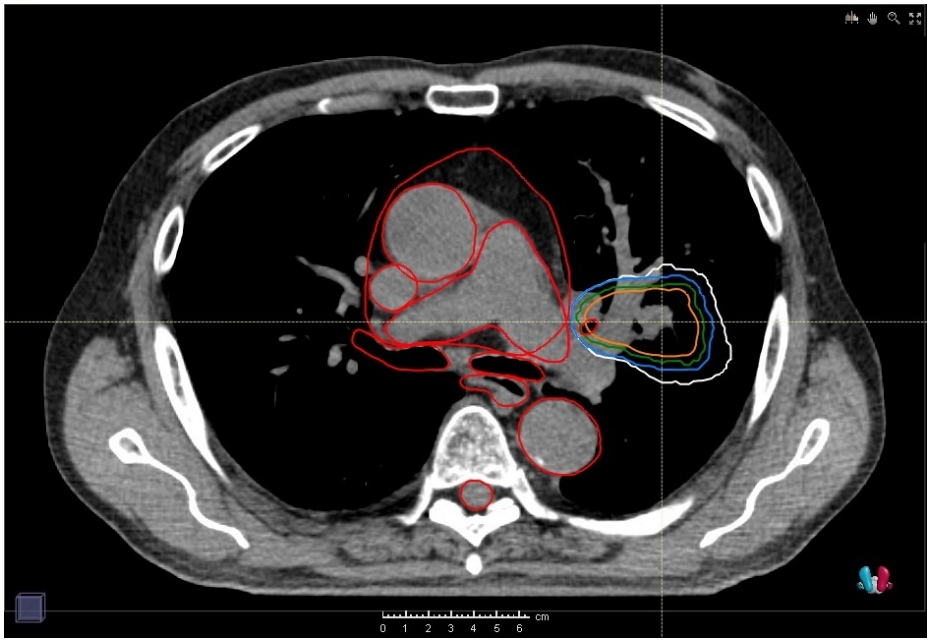

(a) LA-NSCLC Patient 2

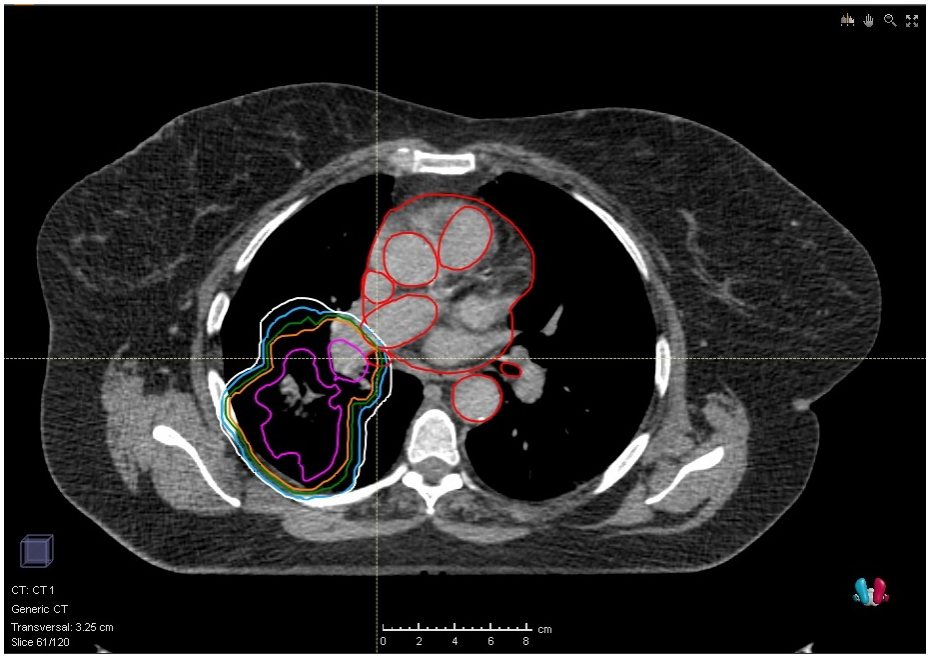

(b) LA-NSCLC Patient 9

Figure 4.4: LA-NSCLC - High dose escalation achieved due to minimal overlap of tumour and OAR. OARs shown in red, PTV_{ITV} in white, $PTV_{Low\ Accuracy}$ in blue, $PTV_{High\ Accuracy}$ in green, $PTV_{Perfect}$/CTV in orange, GTV in purple.

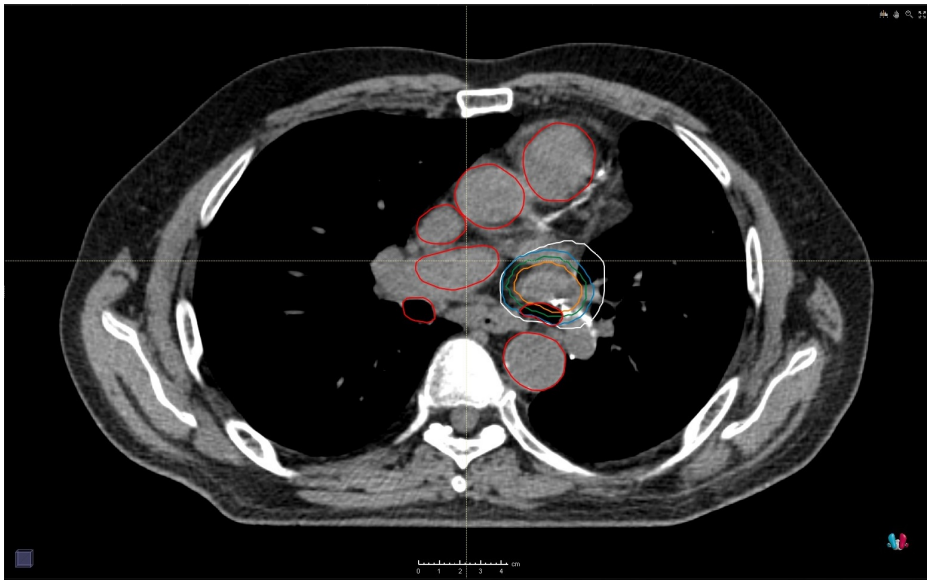

(a) LA-NSCLC Patient 1

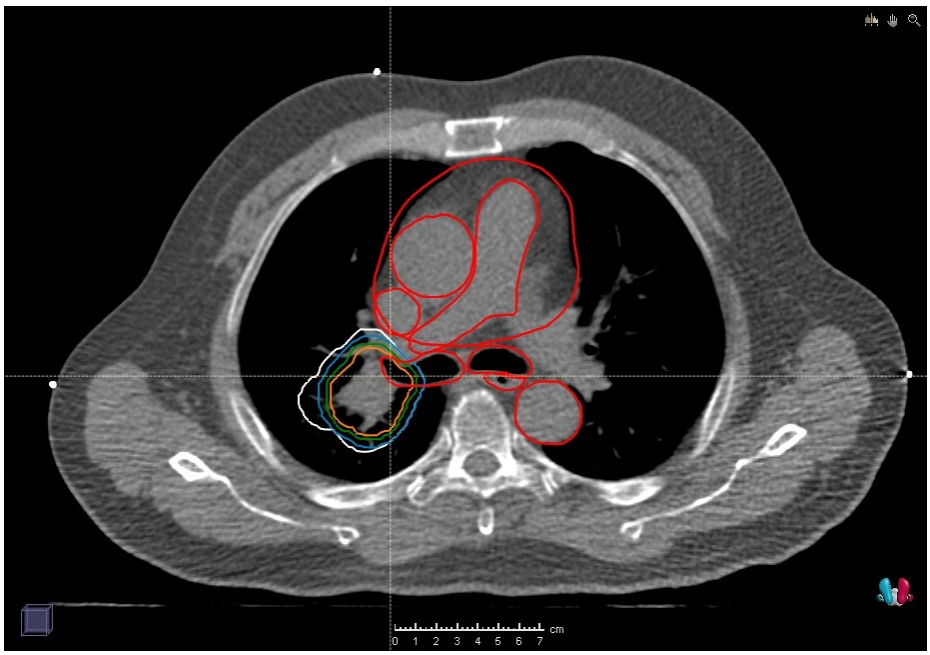

(b) LA-NSCLC Patient 3

Figure 4.5: LA-NSCLC - Low dose escalation achieved due to moderate overlap of tumour and OAR. OARs shown in red, PTV_{ITV} in white, $PTV_{\text{Low Accuracy}}$ in blue, $PTV_{\text{High Accuracy}}$ in green and PTV_{Perfect}/CTV in orange.

Patient	Increase in prescribed dose (Gy) compared to PTV_{ITV}		
	$PTV_{Low\ Accuracy}$	$PTV_{\ High\ Accuracy}$	$PTV_{Perfect}$
2-VMAT	2.6	19.9	41.5
2-IMRT	6.9	8.4	18.8
8-VMAT	2.6	5.6	7.9
8-IMRT	3.2	8.1	8.7
Patient	Increase in prescribed dose (%) compared to PTV_{ITV}		
	$PTV_{Low\ Accuracy}$	$PTV_{\ High\ Accuracy}$	$PTV_{Perfect}$
2-VMAT	2.9%	22.1%	46.1%
2-IMRT	7.9%	9.6%	21.3%
8-VMAT	4.1%	8.7%	12.4%
8-IMRT	4.8%	12.2%	13.2%

Table 4.8: Increase in prescribed doses for VMAT and IMRT plans

87.8 Gy^{-1} for the standard technique using PTV_{ITV} was increased to 90.5, 93.4 and 96.0 Gy^{-1} for $PTV_{Low\ Accuracy}$, $PTV_{High\ Accuracy}$ and $PTV_{Perfect}$ respectively.

When using the calculated BEDs and a radiobiological model from a previous study [66], the median of predicted two year disease-free survival increased from 36.2% for the PTV_{ITV} to 40.5, 45.2 and 50.2% for $PTV_{Low\ Accuracy}$, $PTV_{High\ Accuracy}$ and $PTV_{Perfect}$ respectively. Individual patient results can be seen in Table 4.9 and Figure 4.6. The increase in predicted survival was statistically significant, with $P<.05$ for each experimental PTVs for a paired t-test.

As an increase of at least 5% of two year disease-free survival was considered clinically relevant, from Table 4.9 it is clear that the "low accuracy" technique may not be beneficial enough to warrant use of an MR-linac for the majority of patients. The minimal increase in dose and resulting estimated two year disease-free survival is not a wholly surprising result as both PTV_{ITV} and $PTV_{LowAccuracy}$ use the same microscopic spread margin of 5 mm, and the same "set-up" margin of a further 5 mm. The difference in these two PTVs is that the PTV_{ITV} accounts for any tumour motion by increasing the target volume to envelope the tumour throughout the respiratory cycle, whereas $PTV_{Low\ Accuracy}$ accounts for any tumour motion using tracking. Thus for patients with small motion, there would be little difference between these PTV

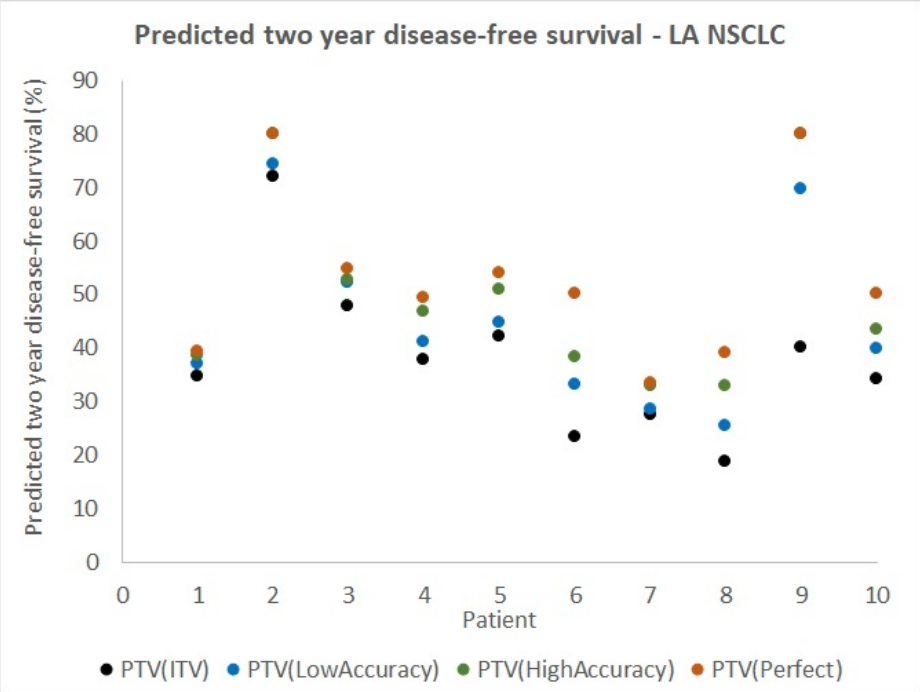

Figure 4.6: LA-NSCLC Predicted two year disease-free survival.

Patient	Increase in predicted two year disease-free survival (%)			Max motion (mm)
	$PTV_{Low\ Accuracy}$	$PTV_{High\ Accuracy}$	$PTV_{Perfect}$	
1	2.4	3.9	4.7	6.8
2	2.4	8.0	8.0	5.8
3	4.3	4.8	6.8	3.4
4	3.4	9.0	11.4	1.6
5	2.5	8.7	11.9	5.2
6	9.7	14.9	26.7	5.9
7	1.1	5.5	6.0	3.0
8	6.8	14.1	20.3	2.7
9	29.6	39.8	39.8	7.9
10	5.7	9.4	16.0	6.1
Median	3.9	8.9	11.7	5.5
Mean	6.8	11.8	15.2	4.8
Minimum	1.1	3.9	4.7	1.6
Maximum	29.6	39.8	39.8	7.9

Table 4.9: Increase in predicted two year disease-free survival for each locally advanced PTV (%). Values in red are those that did not reach a 5% increase in predicted two year disease-free survival. Max motion is the largest of the 3D change in position of the GTV COM from mid-ventilation position across respiratory cycle.

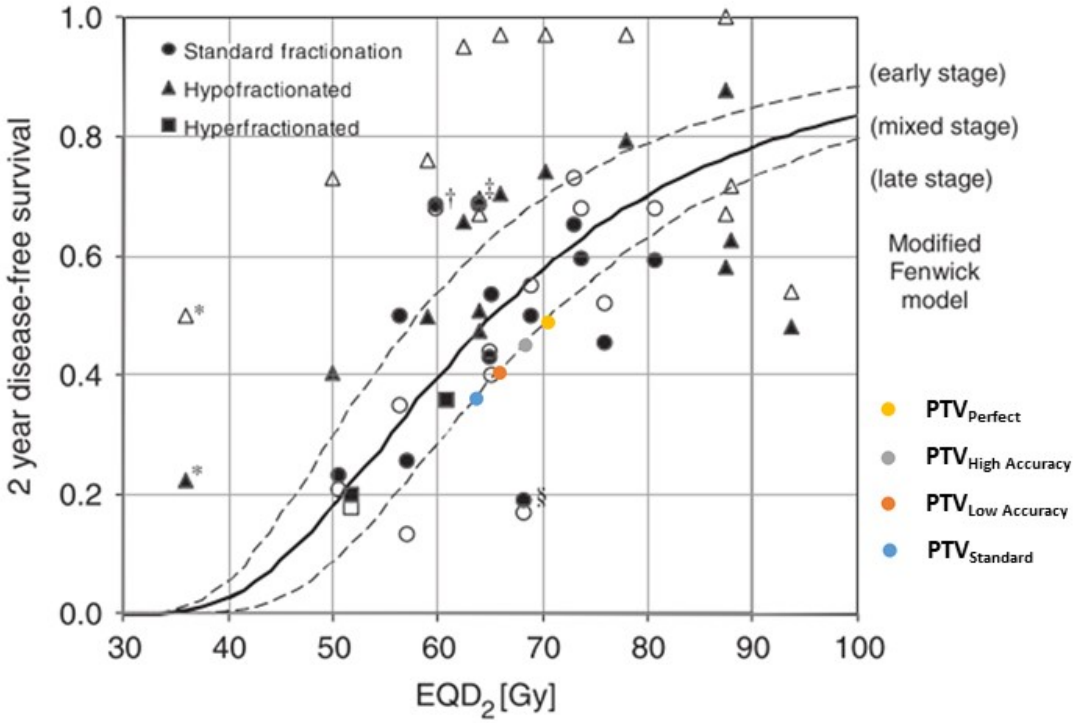

Figure 4.7: Adapted from Partridge et al.'s dose-response model [66]. Open symbols show raw non-stage-corrected 2-year survival, solid symbols show disease-free survival for a population composed of 44% early and 56% late stage. Solid colours show resulting predicted 2 year disease-free survival for each PTV.

sizes, and so a similar isotoxic dose would be expected. The ten patients had a median/mean (range) of maximum 3D motion of 5.5/4.8 (1.6-7.9) mm.

4.4 SABR Results

4.4.1 PTV Volume

Similar to the locally-advanced results, the experimental SABR PTVs were found to be statistically significantly smaller than the clinically used PTV_{ITV} ($P<.001$), as can be seen in Table 4.10 and Figure 4.8.

The difference between the PTVs was proportionally larger than the LA-NSCLC results, due to the smaller CTV sizes, with $PTV_{\text{High Accuracy}}$ and PTV_{Perfect} margins resulting in PTVs with approximately a half and a quarter of the volume of PTV_{ITV}. Patient S10, which had the largest total PTV volumes consisted of two separate lesions.

4.4.2 Isotoxically Prescribed Dose

The dose escalation achieved for each PTV can be seen in Table 4.11 and Figures 4.9 and 4.10. Due to the central location of the tumours selected, the increase in prescribed dose was small in absolute terms. The dose limiting OARs were the proximal bronchial tree, trachea and oesophagus in 8, 1 and 1 cases respectively.

Similar to the locally-advanced results, two patients (S1 and S5) were able to receive higher increases in prescribed dose. Both of these patients had no overlap between CTV and OARs (see Figure 4.11), and the reduction in CTV to PTV margin increased the separation between target and OARs, allowing higher dose escalation. Patients S6, S7, S9 and S10 had some overlap of CTV and OAR, which limited the possible dose escalation. Patients S9 and S10 had particularly low doses. This is due to the position of the tumours, which directly abut the apex of the proximal bronchial

Patient	PTV Volume (cm^3) - SABR NSCLC			
	PTV_{ITV}	$PTV_{Low\ Accuracy}$	$PTV_{High\ Accuracy}$	$PTV_{Perfect}$
S1	13.5	10.5	5.3	2.4
S2	17.5	10.3	5.2	2.2
S3	34.1	20.5	11.7	6.5
S4	44.1	32.8	20.2	11.9
S5	44.4	38.6	24.6	15.1
S6	48.6	32.3	18.6	9.6
S7	57.9	40.5	25.0	14.5
S8	62.5	40.2	24.9	14.5
S9	81.9	60.0	41.1	28.2
S10	129.1	101.6	64.5	38.7
Median	46.5	35.7	22.4	13.2
Mean	53.4	38.7	24.1	14.4
Minimum	13.5	10.3	5.2	2.2
Maximum	129.1	101.6	64.5	38.7

Table 4.10: PTV volumes (cm^3) for each early stage, SABR PTV. PTV_{ITV} is the standard ITV approach with clinically used CTV to PTV margins of 5 mm. $PTV_{Low\ Accuracy}$, $PTV_{High\ Accuracy}$, and $PTV_{Perfect}$ are the experimental PTV volumes created using a single phase GTV and a range of CTV to PTV margins (5, 2, 0 mm) based on estimated uncertainties in the tracking process as previously discussed.

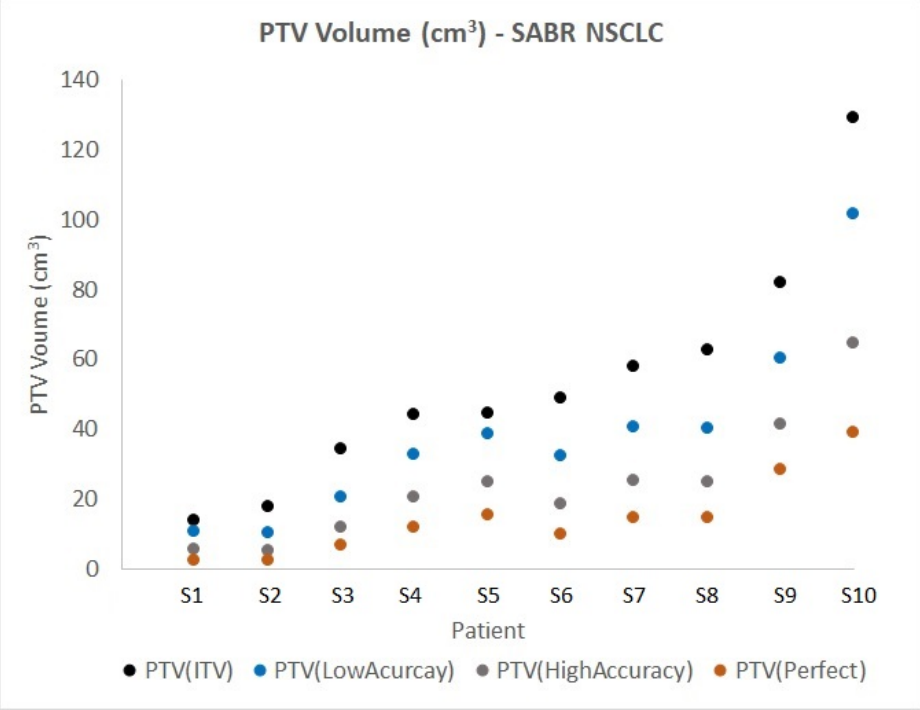

Figure 4.8: SABR PTV volumes.

tree, as depicted in Figure 4.12.

4.4.3 Predicted Survival

The number of plans able to achieve a biologically effective dose of at least 100 Gy^{-1} was increased from just 3 plans for PTV_{ITV} to 5, 7 and 8 of 10 plans for $PTV_{Low\ Accuracy}$, $PTV_{High\ Accuracy}$, and $PTV_{Perfect}$ respectively, as shown in Table 4.12 and Figure 4.13. This suggests that the use of the MR-linac with a tracking technique may be clinically useful. The remaining two patients (S9 and S10) which did not reach a BED_{10} of 100 Gy^{-1} for any PTV, had larger amounts of overlap of PTV and the proximal bronchial tree; for PTV_{ITV}, the region of overlap was 9.5 and 7.1 cm^3, which can be seen in Figure 4.12. There was some PTV/proximal bronchial tree overlap even with the smallest experimental PTV which limited the dose escalation. These patients were also the patients with the largest PTV volumes, which suggests there may be a limit on the size of central PTVs that can adequately be treated with isotoxically dose escalated SABR. This has been found in other studies, such as Parker et al. [190], which concluded that increased local control for SABR patients was associated with smaller GTV volume and PTV volume

Each plan was classified into a dose level based on those suggested by Zhang et al. [189]; "low" (<83.2 Gy), "medium" (83.2-106 Gy), "medium to high" (106-146 Gy) and "high" (>146 Gy). The meta-analysis results from Zhang et al. estimate a three year overall survival rate of 0.494, 0.611, 0.627 and 0.468 for "low", "medium", "medium-high" and "high" dose classifications respectively. The two patients with the large increase in prescribed dose received a "high" dose for $PTV_{Perfect}$, with BEDs of 160.9 and 187.9 Gy^{-1} respectively. Zhang et al. reported a grade 3-5 adverse event occurrence rate of 0.093 for "high" dose, compared with 0.073/0.078 for "medium"/"medium-high" dose. However, as this study simulates isotoxic dose escalation, the toxicity that may have contributed to the reduced overall survival for

Patient	Prescribed Dose (Gy) - SABR NSCLC			
	PTV_{ITV}	$PTV_{Low\ Accuracy}$	$PTV_{High\ Accuracy}$	$PTV_{Perfect}$
S1	64.8	69.7	75.1	80.3
S2	57.3	59.2	60.8	61.8
S3	58.5	59.1	59.8	64.6
S4	55.0	58.8	67.8	70.9
S5	61.3	65.3	74.2	89.0
S6	54.6	57.3	62.3	66.0
S7	45.9	50.4	55.9	59.3
S8	54.9	57.8	58.5	59.2
S9	42.3	42.9	45.7	48.5
S10	38.7	52.9	53.0	54.6
Median	55.0	58.3	60.3	63.2
Mean	53.3	57.3	61.3	65.4
Minimum	38.7	42.9	45.7	48.5
Maximum	64.8	69.7	75.1	89.0
		P=.01	P<.001	P<.001

Table 4.11: Prescribed doses (Gy) for each SABR PTV. PTV_{ITV} is the standard ITV approach with clinically used CTV to PTV margins of 5 mm. $PTV_{Low\ Accuracy}$, $PTV_{High\ Accuracy}$, and $PTV_{Perfect}$ are the experimental PTV volumes created using a single phase GTV and a range of CTV to PTV margins (5, 2, 0 mm) based on estimated uncertainties in the tracking process as previously discussed.

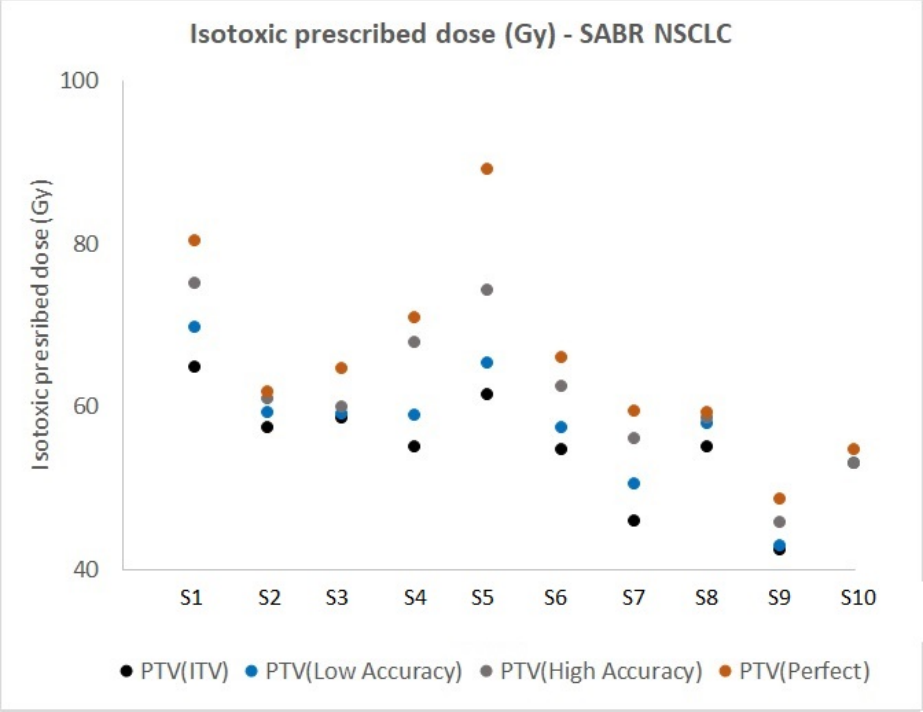

Figure 4.9: SABR Isotoxic prescribed doses

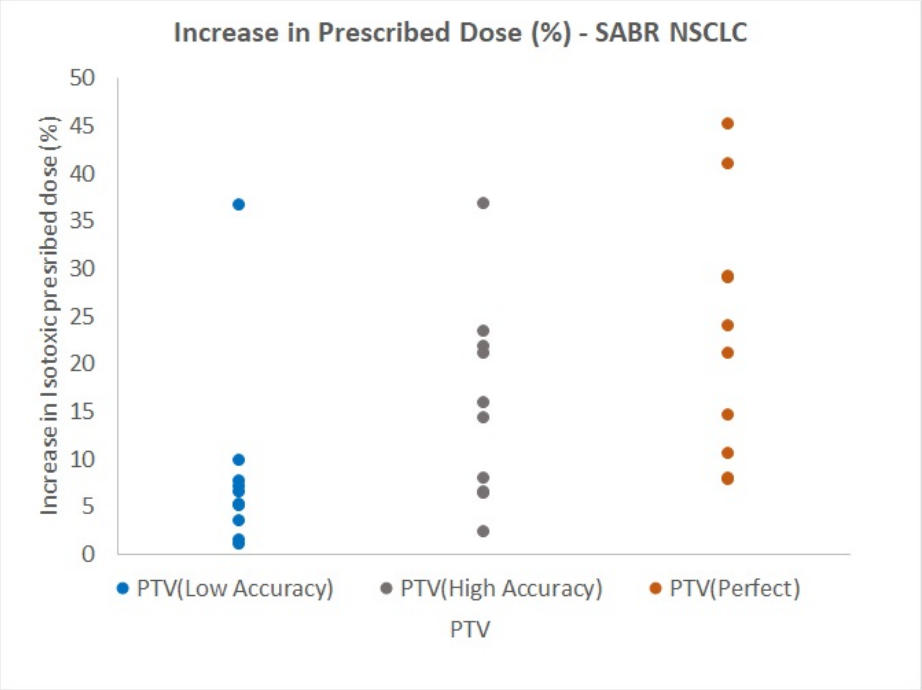

(a) SABR Increase in prescribed dose

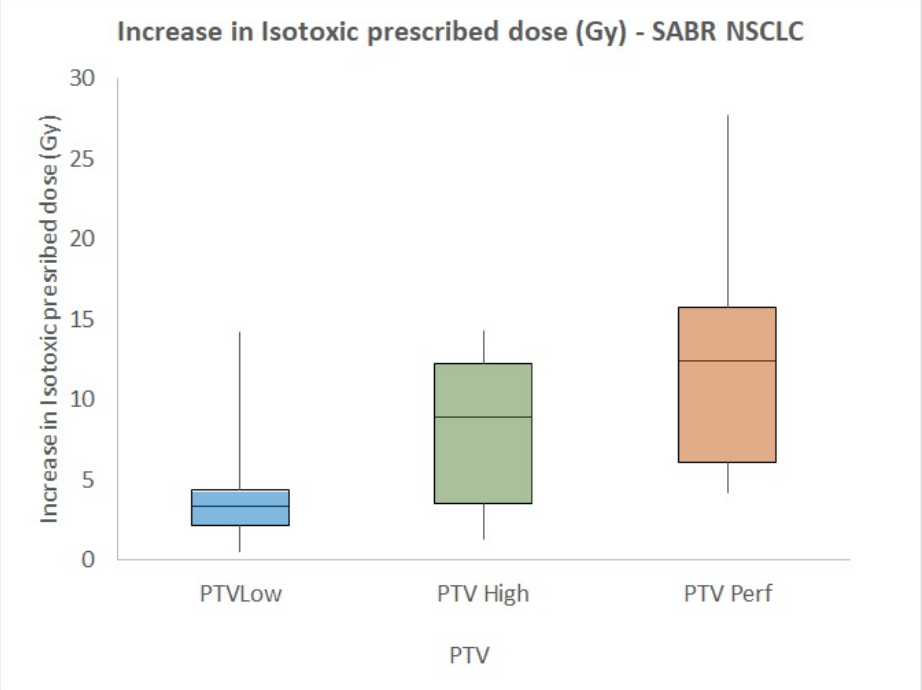

(b) SABR Box plot of increase in presrcibed dose

Figure 4.10: SABR Increase in prescribed dose, relative to PTV_{ITV}

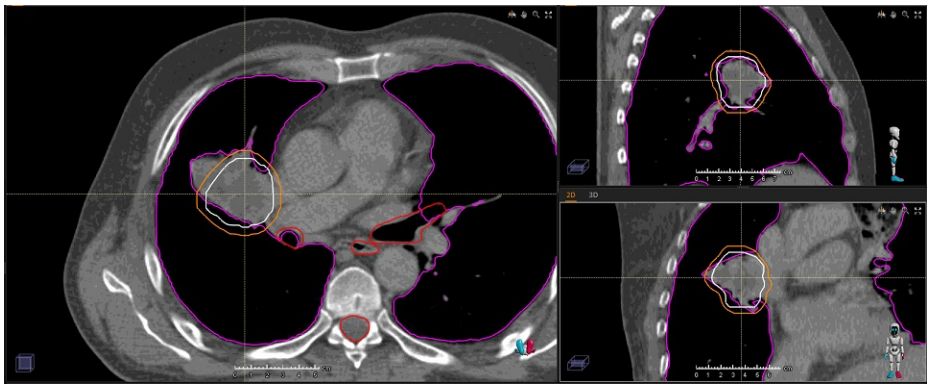

Figure 4.11: SABR Patient 5 - Good escalation achievable as no immediately abutting OAR. PTV_{ITV} in white, and $PTV_{Perfect}$/CTV in orange.

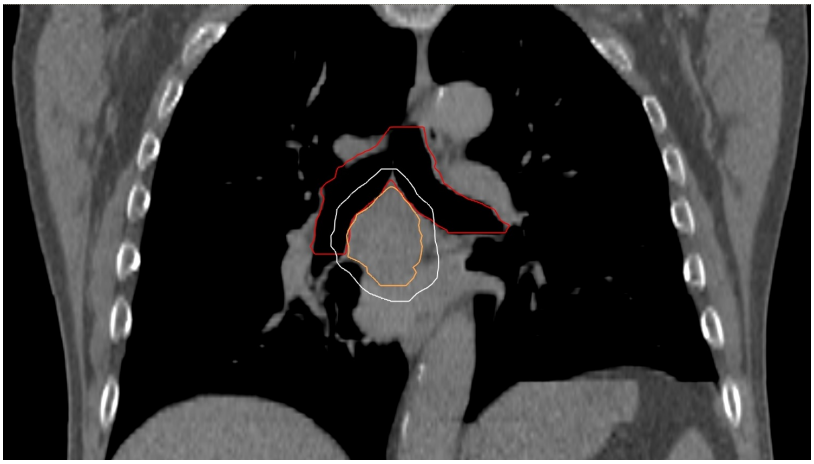

(a) SABR Patient 9 - poor dose escalation achieved.

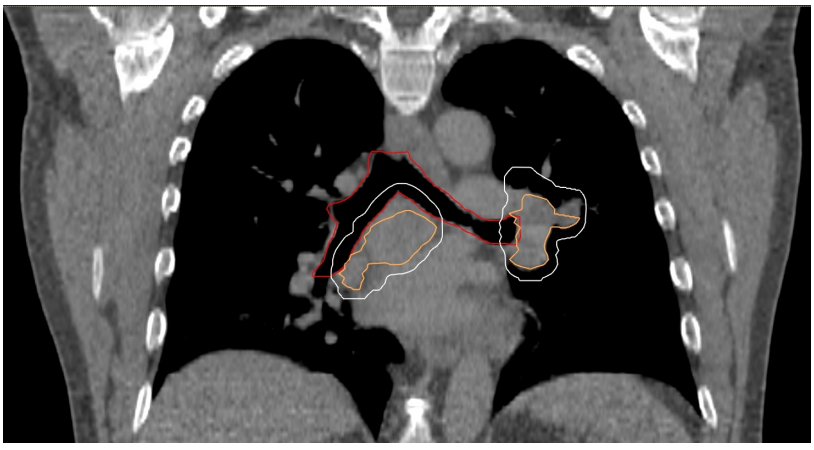

(b) SABR Patient 10 - poor dose escalation achieved.

Figure 4.12: SABR Patients 9 and 10 - tumour location determines level of dose escalation achieved OARs shown in red, PTV_{ITV} in white, and $PTV_{Perfect}$/CTV in orange.

the patients considered by Zhang et al., in the "high" dose group is expected to be minimised. For a conservative approach, the prescribed doses for these two plans could be reduced to 75.2 Gy, to ensure a BED of less than 146 Gy^{-1}.

Three patients (S7, S9 and S10) were limited to a "low dose" for PTV_{ITV} plans, with the remaining 7/10 plans able to achieve at least a "medium" dose. For the experimental PTV plans, this was increased to 8/10 for $PTV_{\text{Low Accuracy}}$, and 9/10 plans for $PTV_{\text{High Accuracy}}$ and PTV_{Perfect}.

As discussed previously, Patient S9 received a "low" dose in each plan, again suggesting that not all patients will be able to receive an optimal SABR treatment. Similarly, two patients (S1 and S5) had PTV_{ITV} BEDs classified as medium-high, suggesting that these patients may not need the more advanced SABR technique requiring use of the MR-linac and real-time tracking.

Patient	BED_{10} (Gy^{-1}) - SABR NSCLC			
	PTV_{ITV}	$PTV_{Low\ Accuracy}$	$PTV_{High\ Accuracy}$	$PTV_{Perfect}$
S1	**117.3**	**130.4**	**145.6**	160.9
S2	**98.2**	**103.0**	**107.1**	**109.5**
S3	**101.3**	**102.6**	**104.5**	**116.8**
S4	**92.7**	**102.1**	**125.3**	**133.8**
S5	**108.3**	**118.5**	**143.1**	187.9
S6	**91.7**	**98.3**	**110.9**	**120.5**
S7	72.3	82.2	**95.1**	**103.4**
S8	**92.6**	**99.5**	**101.2**	**102.9**
S9	64.7	65.9	71.7	77.9
S10	57.5	**87.9**	**88.1**	**91.9**
Median	92.7	100.8	105.8	113.1
Mean	89.7	99.0	109.3	120.5
Minimum	57.5	65.9	71.7	77.9
Maximum	117.3	130.4	145.6	187.9

Table 4.12: BED_{10} (Gy^{-1}) for each early stage SABR PTV. Values in red are below 100 Gy^{-1} threshold. Values in bold are those which fall into "medium" and "medium-high" dose categories.

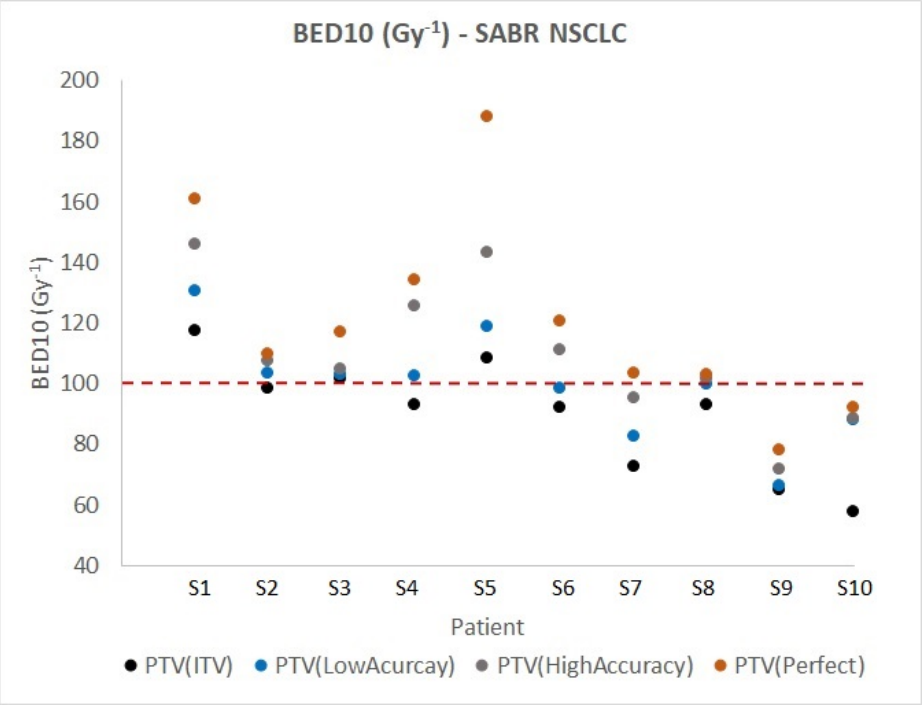

Figure 4.13: SABR - Biologically effective doses

4.5 Discussion

The dose escalation and predicted improvement in patient outcomes that are possible when using reduced CTV to PTV margins due to tracked treatment delivery on an MR-linac was investigated for both locally-advanced conventional radiotherapy, and early-stage stereotactic ablative radiotherapy techniques.

As expected, the experimental PTVs were smaller than for the standard ITV-based approach for all PTVs and both locally-advanced and early-stage patients. This is attributed to the methods used to account for target motion; the ITV approach envelopes the position of the tumour volume at each phase, whereas the experimental PTVs mitigate motion through the use of real-time tracking. LA target volumes are larger, and often more irregularly shaped compared to the early-stage SABR volumes. This determines the level of impact the margin reduction and resulting potential for dose escalation. For the early-stage cohort with smaller CTVs, a reduction in margin size from 5 to 2 mm resulted in a median reduction in PTV volume of 13.9 cm^3 (38.4%), whereas for the larger LA cases, a larger absolute reduction of 58.9 cm^3 occurred, but only a 30.5% reduction. For the LA patients, a general trend of larger increases in predicted two-year disease-free survival was seen for larger tumour volumes, whereas the two SABR patients with the largest tumour volumes were those that did not reach a BED of 100 Gy^{-1} for any PTV. This suggests that initial target volume size may be used alongside OAR and target volume overlap/proximity to potentially preferentially select at planning those who may benefit most from a tracking technique.

The reduction of the PTV volume often resulted in a decrease in the region of overlap of PTV and surrounding dose-limiting organs at risk, thus allowing dose escalation. For two patients in each dataset, the potential dose escalation was limited due to moderate overlap of CTV and OAR.

For the locally-advanced patients, this resulted in a predicted increase in two

year disease-free survival of a median/mean of 3.9/6.8, 8.9/11.8 and 11.7/15.2% for $PTV_{\text{Low Accuracy}}$, $PTV_{\text{High Accuracy}}$, and PTV_{Perfect} respectively. Two patients were able to achieve a large escalation due to minimal overlap of OARs and PTVs.

The SABR modelling suggests that use of the experimental PTVs can increase the number of plans able to reach the minimum suggested biologically effective dose of 100 Gy^{-1}. However, treatment of central lung tumours using SABR has recently been well explored and documented [191–193], including the potential adaptive hypofractionated SABR potentially deliverable on the MR-linac [59]. A current clinical trial (SUNSET) that opened in January 2019 is also investigating optimal dose escalation for central lung tumours for early-stage NSCLC [194]. For this reason the SABR cases will not be further investigated in this thesis.

The clinical delivery of VMAT plans on the MR-linac, when first technically feasible, is likely to be limited to an accuracy similar to the "low accuracy" technique simulated in this thesis. This will limit the usefulness of the technique, resulting in a clinically meaningful benefit for 40% (LA) or 50% (SABR) of central lung tumour patients. However, as the techniques evolve, it is anticipated that the accuracy will increase, approaching the levels simulated by the "high accuracy" technique, which will increase the numbers of patients who would benefit to 80% (LA) and 70% (SABR). Thus, careful patient selection will be required when the technique is first introduced, which has been shown to be possible during the planning stage, based on the distance between, or overlap of, target volumes and OARS.

Other groups have also investigated the predicted effect on PTV size and potential dose escalation based on the use of an MR-linac. Bainbridge et al. [148] considered the differences between treatment on a conventional linac and on an MR-linac. They assumed reductions in; contouring/localisation errors (2-1 mm), differences in tumour motion between planned and fraction(1.2/1.6/1.4-0 mm), and beam penumbra (6.4-8.0 mm). Step and shoot IMRT plans, using nine equidistant, co-planar beams were

produced. They concluded that the use of reduced margins on the MR-linac resulted in a reduction in the dose received by some OARs whilst allowing an isotoxic dose escalation, which resulted in a small increase in mean CTV dose from 79.0 Gy to 81.2 Gy. One advantage of the Bainbridge study is the inclusion during planning of the effects of the magnetic field. This option was unavailable in the TPS used in this study, however it has been shown that once these effects are modelled within a TPS, they can be minimised during optimisation for lung radiotherapy treatments [195]. Thus this is considered to only be a minor limitation of the study. As discussed in Section 2.3, there are several other important differences between the Bainbridge study and this study. The Bainbridge study investigates the use of an MR-linac for lung radiotherapy in terms of better pre-treatment visualisation of the tumour, whereas in this thesis the effects of tracking the tumour in real-time has been investigated. Bainbridge et al. included an estimated baseline drift in tumour position (as no tracking was simulated), and also assumed perfect incidence of the MR imaging and radiotherapy treatment beam isocentres.

4.6 Conclusion

In-silico modelling of an MR-linac radiotherapy technique for treating central lung tumours using a tracking technique, demonstrates a clinically useful benefit over a standard ITV-based treatment approach on a conventional linac. A reduction in the PTV volume increases the separation between the target volume and surrounding organs at risk, which enables dose escalation.

This dose escalation has been shown to be potentially clinically meaningful when modelling outcomes using radiobiological models from previous studies. As plans were produced isotoxically, no increase in the clinically acceptable level of toxicity is to be expected. The patients who would benefit most from the simulated treatment

techniques are easily identifiable at planning, enabling efficient patient selection for clinical departments with limited resources.

The dose escalation achieved during this in-silico modelling will be further investigated to determine the effect of treatment over the entire respiratory cycle, on both the target coverage and organ at risk doses.

Chapter 5

Tracking Based on Baseline Imaging

5.1 The Respiratory Cycle

The process of respiration allows gas exchange in the alveoli within the lungs, exchanging carbon dioxide in the blood with oxygen from the air. Respiration is controlled by the diaphragm, a dome-shaped muscle positioned below the lungs. During inhalation, the diaphragm flattens, expanding the lungs and pulling air into the airways. During exhalation the diaphragm relaxes and reduces the volume of the lungs, forcing air out of the airways. The action of the diaphragm and resulting lung motion may also cause any lung tumours and surrounding healthy structures to move throughout the respiratory cycle, potentially with differential motion.

As discussed previously, an "internal target volume" approach can be used to account for any lung tumour motion, by enveloping all the known positions of the tumour throughout the respiratory cycle, creating an expanded target volume. This is considered the "standard" radiotherapy treatment technique for lung cancer.

The experimental technique investigated in this thesis uses an alternative ap-

proach, using real-time tracking during treatment delivery to translate the treatment beam to ensure the alignment of the primary GTVs. Thus smaller target volumes are able to be used. The plans produced in Chapter 4 were constructed on the mid-ventilation phase of the 4DCT. The tumour may move relative to surrounding tissues, and so it is important to assess the dose throughout the respiratory cycle, i.e. the accumulated dose. The margin reduction used for the experimental plans allows an increase in prescribed dose, which potentially puts the OARs at a greater risk of receiving high doses. As the plans were produced isotoxically, at least one OAR will be at dose tolerance at planning, and so assessing the accumulated dose is particularly important, as even small changes in the relative position of tumour and OAR may result in OARs receiving doses that exceed tolerance.

5.2 Methods - Accumulation over the Respiratory Cycle

The dose was accumulated throughout the respiratory cycle by calculating the dose on each of the ten 4DCT phases and combining them. Each of the phases of the 4DCT represents a tenth of the respiratory cycle.

The tracking technique was simulated by moving the treatment beam so the treatment isocentre always aligned with the primary GTV centre of mass position, as it was at planning for the mid-ventilation phase. This is a simplification of the tracking technique as it assumes that the respiratory cycle is split evenly between these ten defined states, rather than a continuous cycle of motion. This tracking technique could also directly apply to the use of implanted fiducial markers to localise the tumour. The use of ten 4DCT phases has been thoroughly investigated in radiotherapy, and shown to provide a sufficiently accurate representation of motion and its use for accumulation of dose across the respiratory cycle verified [180, 181]. This method also

assumes that the breathing motion throughout treatment is consistent with that at treatment planning simulation. The effect of a change in breathing motion will be investigated later in the thesis.

Two methods of accumulation were performed. Firstly, deformable image registration (DIR) was used to create a deformation map from each phase to the mid-ventilation (planning) phase. This allowed each phase dose to be deformed to the mid-ventilation phase and summed, resulting in the accumulated dose distribution. Deformable image registration is known to have some limitations, particularly in the difficulty of validating the deformation maps. For this reason, a simpler method of mathematically averaging the results for each dose metric (maximum dose to OAR, target coverage, etc.), across the ten 4DCT phases was also performed.

5.2.1 Deformable Image Registration

Deformable image registration is often used in radiotherapy, with the aim of creating a deformation vector field (DVF) that transforms one image to another, whilst balancing image similarity with the plausibility of the estimated DVF, as discussed by Sarrut et al. [158]. A schematic of the basic process for DIR accumulation can be seen in Figure 5.1.

The image similarity measures can be based on image intensities or geometric structures such as known landmarks (surfaces, points) in each image. DIR based on image intensity can use regularisation models with the aim of keeping the deformation map anatomically realistic. DIR based on geometrical measures aims to align the known landmarks or structures, and hence has no information on areas where there are no landmarks, for example the volume of tissue within a contoured organ used to produce the deformation map.

The hybrid intensity-geometry based ANACONDA algorithm used in this study is a module included in the RayStation treatment planning software. The ANACONDA

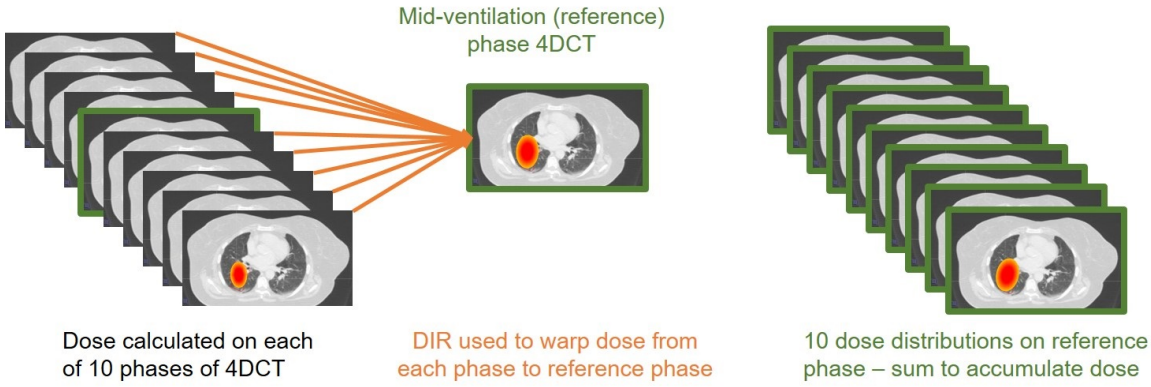

Figure 5.1: Schematic showing the DIR process. A DVF is produced to warp doses from each phase to the mid-ventilation (reference) phase. The ten doses can then be accumulated and compared to the planning dose.

algorithm has been previously discussed by Weistrand et al. [161], and its performance has been validated in lung images [161, 162] and compared to other DIR algorithms in several studies [162, 196]. As ANACONDA is a hybrid intensity-geometry based algorithm, it aims to use image intensity based registration, but using contours or points within the images to "focus" or "control" the resulting deformation maps to ensure results are anatomically realistic. The objective function minimised during the registration is made up of: an image similarity term, a grid regularisation term that aims to keep the deformed grid smooth and invertible, and a penalty term when controlling structures are used [197]. Initially no "focus" or "controlling" regions/points of interest were selected, however the full range of settings were investigated to ensure the optimal parameters were used.

The resulting deformation vector fields were validated firstly by comparing the resulting deformed contours with those manually drawn, using the Dice Similarity Coefficient (DSC). The DSC is a measure of the overlap of volumes, calculated using Equation (5.1) [174], for which a minimum value of 0.8-0.9 [166] has been suggested for adequate similarity. However, it has been shown that although widely used, tissue overlaps cannot accurately be used as a test of registration accuracy [198], and so need to be used with care along with alternative methods of validation.

$$DSC = \frac{2|V_{\text{Manual}} \cap V_{\text{DIR}}|}{V_{\text{Manual}} \cup V_{\text{DIR}}} \tag{5.1}$$

where DSC is equal to the ratio of twice the volume of intersection of the manual volume and the deformable image registration volume to the sum of the two volumes. DSCs range from 0 to 1; volumes which have no overlap will have a DSC of 0, perfectly overlapping volumes will have a DSC of 1.

The Hausdorff distance is a measure of the maximum distance between two structures [176], calculated by taking the maximum value of the smallest distance for every point of a structure to any point of the other structure. The modified Hausdorff distance (average of all calculated distances between two structures) has also been shown to be a useful measure of image similarity [177].

The determinant of the Jacobian was also calculated for the CTV for 5 randomly selected patients. This provides a measure of the local volume change on a voxel-by-voxel basis. A value of 1 indicates local volume preservation, a value greater/less than 1 indicates a local volume expansion/contraction [171].

5.2.2 Dose Metric Averaging

The dose metric averaging method (DMA) was performed by calculating the dose on each phase of the 4DCT. The metric results (minimum/maximum dose to 1 cm^3, etc.) were calculated for each phase and then averaged across the ten phases. This will provide "worst-case" results, and will be a pessimistic simulation of the tracking technique. If one considers the maximum dose to an OAR, if the tissue element that receives the maximum dose is the same on each phase, the average will be a true representation of the accumulated maximum dose. However, in reality, more likely is that the tissue element of OAR receiving the maximum dose will be slightly different

in each phase. Thus the "true" maximum accumulated dose will likely be less (but never more) than the DMA dose. Similarly, when looking at the minimum dose to the target volume, the tissue element receiving the minimum dose is likely to change throughout the respiratory cycle, and so the "true" value of minimum dose is likely to be greater (but never less than) the DMA result.

The DMA method was used as an alternative to the DIR accumulation technique, due to the few assumptions made, and lack of dependence on a difficult to validate deformation vector field.

5.2.3 Tracking Technique

The real-time tracking technique was simulated for the experimental PTVs by aligning the position of the treatment isocentre with that of the primary GTV centre of mass (COM). Thus any rotation or deformation of the GTV was not considered. Practically, this was performed by shifting the treatment beams in 3D for each phase. However, as discussed in Section 2.3.3, the tracking technique may have some associated uncertainties, which were included in the CTV to PTV margin calculations. Tracking uncertainties of 0.2 and 1.2 mm were estimated for $PTV_{\text{High Accuracy}}$ (PTV margin total 2 mm) and $PTV_{\text{Low Accuracy}}$ (PTV margin total 5 mm) respectively.

If assuming a 3D normal distribution of uncertainties, the fraction of errors lying within sphere of radius 0.5σ was calculated to be 13.9%. The fraction of errors within an annulus between 0.5 and 1.5σ is 78.1%, and errors exceeding 1.5σ, 8.0% (see Appendix).

The effect of systematic tracking errors was estimated by altering the isocentre shift to include the uncertainty in each direction (left, right, superior, inferior, anterior and posterior). Thus each plan had 13 dose distributions accumulated over the 10 phases of the respiratory cycle, which were combined using the following weightings;

- Perfect isocentre tracking (weighted by 0.139)

- Isocentre tracking $\pm$ 1σ in each direction (average weighted by 0.781)
- Isocentre tracking $\pm$ 2σ in each direction (average weighted by 0.080).

5.3 Results - Accumulation over Respiratory Cycle

5.3.1 Magnitude of Required Tracking

The change in GTV COM position throughout the respiratory cycle can be seen in Table 5.1 (a) - (d), and the patients with the largest tumour motion are depicted in Figure 5.2. It is worth noting that the patients who underwent audio-visual feedback during image acquisition with the aim of reducing breathing irregularities had a similar range of motion (1.9 - 7.3 mm), compared with those patients who did not (3.0 - 8.6 mm). The largest motion was, as expected, in the superior-inferior direction (1.6 - 8.2 mm).

5.3.2 Deformable Image Registration Results

An example of a resulting deformation vector field can be seen for example in Figure 5.3, where the irregularity and colour of the grid demonstrate the degree of deformation.

The calculated Dice Similarity Coefficients can be seen in Table 5.2. The DSCs calculated for three patients fell below the value of 0.8, the suggested acceptable minimum volume overlap [166]. This may indicate that the DVF resulting from the DIR may be less accurate for these patients.

The determinant of Jacobian results for the resulting deformation vector fields for five patients can be seen in Table 5.3, and an example of a resulting histogram of

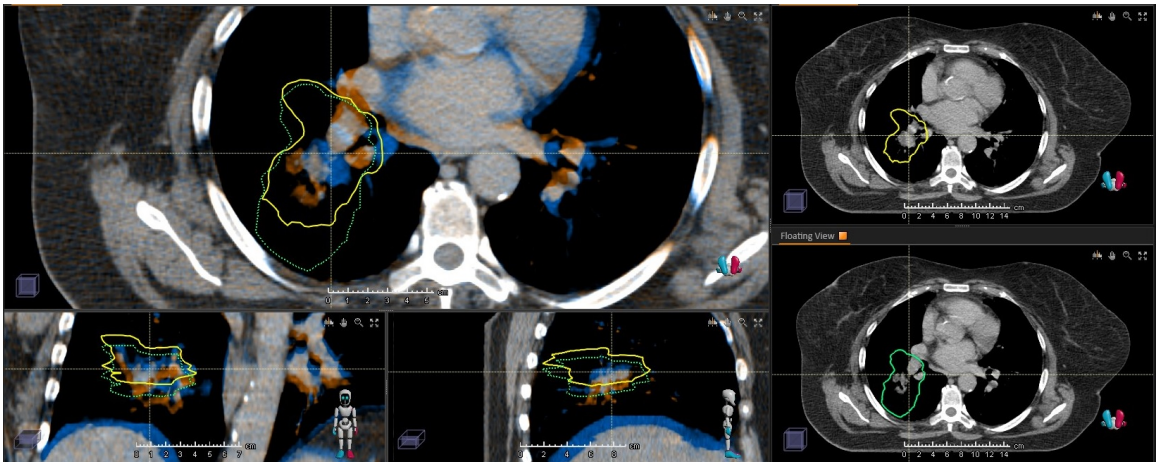

(a) LA-NSCLC Patient 9

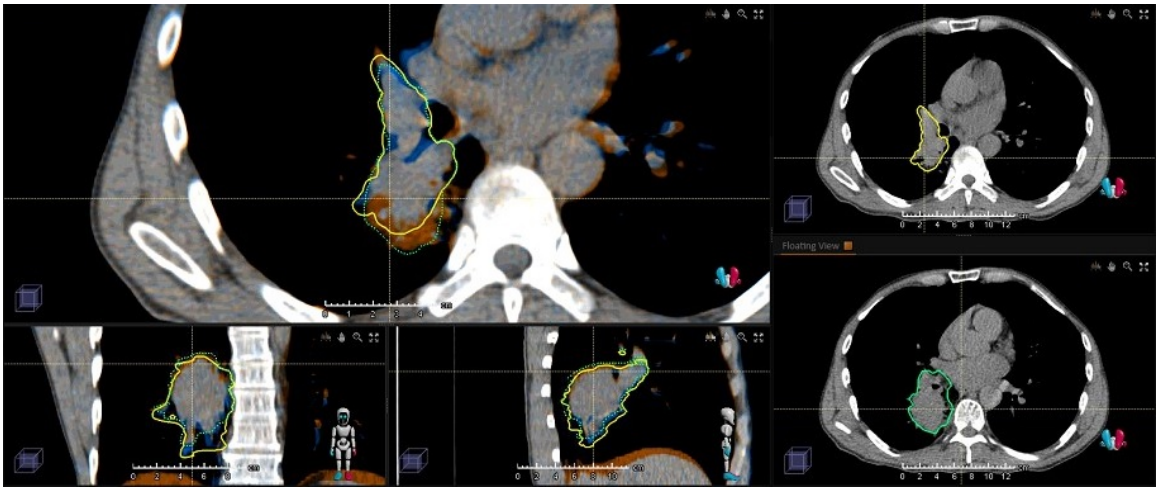

(b) LA-NSCLC Patient 10

Figure 5.2: LA-NSCLC - Patients with the largest tumour centre of mass motion. Mid-ventilation CTV in yellow, phase with largest difference to mid-ventilation CTV in cyan dashed line. The two phases are shown overlaid in blue (mid-ventilation) and orange (alternate phase).

Patient	Mid-ventilation 4DCT phase	Max. 3D motion (mm)	Average 3D motion (mm)	Max. SI motion (mm)
1	60	6.8	3.8	5.6
2	40	5.8	2.1	5.6
3	**70**	**3.4**	**2.0**	**2.7**
4	**70**	**1.9**	**0.8**	**1.6**
5	30	5.2	3.5	4.6
6	**40**	**5.9**	**2.6**	**4.2**
7	80	3.0	1.5	2.3
8	**80**	**2.7**	**1.8**	**2.4**
9	30	8.6	5.0	8.2
10	**20**	**7.3**	**3.5**	**7.2**

Table 5.1: Mid-ventilation 4DCT phase selected for planning, maximum/average of 3D motions between GTV centre of mass on mid-ventilation phase and other 9 4DCT phases, and maximum distance from mid-ventilation phase in superior-inferior direction. Patients highlighted in bold are those which had audio-visual feedback to minimise breathing irregularity during image acquisition as per Hugo et al. [178].

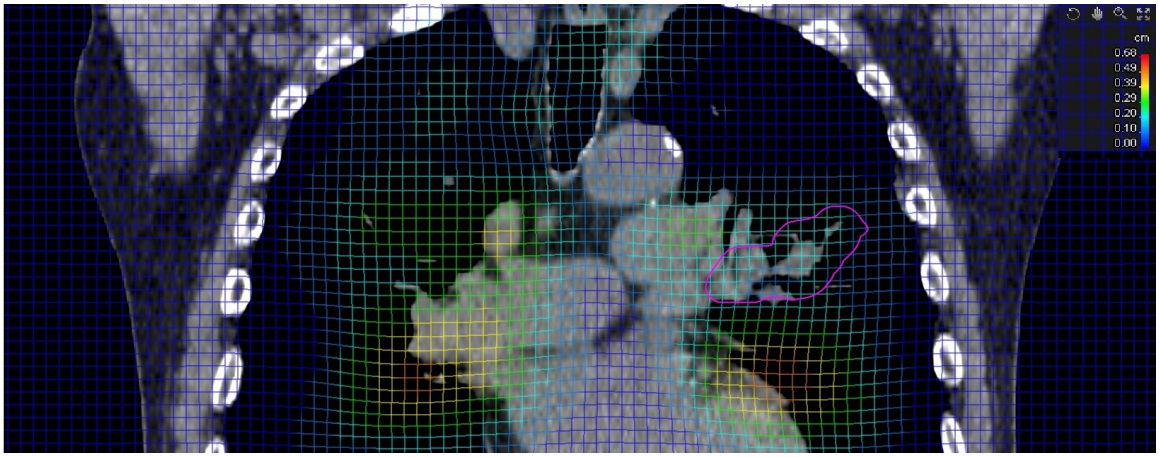

Figure 5.3: Resulting deformable image registration deformation vector field. The irregularity and colour of the grid demonstrate the degree of deformation. GTV delineated in pink.

Patient	Mid-V. GTV volume (cm^3)	Avg. ± SD GTV Volume (cm^3)	Max GTV Volume (cm^3)	Avg. (range) GTV DSC
1	5.9	7.52 ± 0.87	8.9	0.82 (0.76-0.90)
2	9.8	9.83 ± 0.91	11.0	0.78 (0.71-0.81)
3*	10.0	9.71 ± 0.59	10.7	0.82 (0.81-0.85)
4*	17.2	17.29 ± 0.64	18.8	0.96 (0.91-0.98)
5	23.3	27.51 ± 1.97	29.6	0.82 (0.81-0.90)
6*	47.9	52.28 ± 4.09	62.0	0.79 (0.73-0.86)
7	81.6	79.88 ±2.80	84.3	0.88 (0.81-0.95)
8*	60.4	62.00 ± 4.28	67.6	0.85 (0.82-0.88)
9	88.5	91.37 ± 6.78	97.9	0.77 (0.62-0.93)
10*	179.6	177.19 ± 7.75	185.8	0.89 (0.85-0.91)

Table 5.2: GTV values and Dice similarity coefficient results, averaged over all phases within 4DCT. Mid-V. is the mid-ventilation phase results, Avg. is the average (mean), SD is the standard deviation. * identifies patients which had separate tumour and lymph node volumes - values listed here are for tumour only.

Jacobian values can be seen in Figure 5.4. The determinant of Jacobian for the CTV volumes ranged from 0.85 to 1.35 across the 5 patients.

The Hausdorff distance (maximum value across all phases) and the modified Hausdorff distance [177] can be seen in Table 5.4. The poorest result across all patients and phases can be seen in Figure 5.5 where the automated DIR contour in green can be seen to extend inferiorly more than the expert manual delineation in orange. Variation of the metrics across the patients can be seen, confirming the difficulty in validating DIR results.

5.3.3 Accumulation Results

The results for each PTV can be seen in Tables 5.5 (a)-(d). The minimum of the target coverage (minimum dose to 99% of CTV), and the maximum dose to dose-limiting (DL) OARs for each PTV across all patients can be seen in Table 5.6.

5.3.3.1 OAR Accumulation results

The dose to each OAR when accumulated over the respiratory cycle was assessed. The DIR results found that 6 patients had a single OAR breaching tolerance constraints for at least one PTV plan;

- Patient 1 had 3 plans - PTV_{ITV}, $PTV_{\text{Low Accuracy}}$, $PTV_{\text{High Accuracy}}$

Patient	CTV Jacobian		
	Average	Minimum	Maximum
1	1.016	0.907	1.306
2	1.042	0.896	1.345
4	1.004	0.893	1.107
5	1.020	0.878	1.245
10	0.995	0.846	1.098

Table 5.3: CTV voxel Jacobian values for 5 patients. Average (mean) values are across all phases.

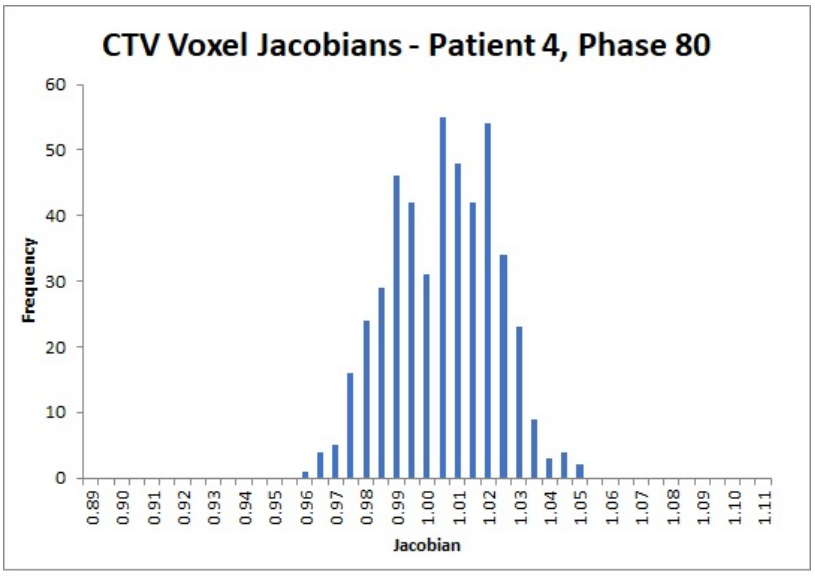

Figure 5.4: Histogram of CTV voxel Jacobian values of DIR deformation vector field for Patient 4, phase 80.

Patient	Hausdorff distance (cm)	
	Maximum	Modified
1	1.08	0.16
2	0.79	0.10
3	0.57	0.09
4	0.35	0.05
5	1.22	0.21
6	1.43	0.14
7	1.05	0.14
8	0.92	0.10
9	0.99	0.12
10	1.86	0.12

Table 5.4: Hausdorff values across all respiratory phases, showing the variation in similarity for deformed and manually delineated GTVs.

Patient	Dose Limiting OAR	DIR Accumulation		DMA Accumulation	
		Min dose to 99% CTV (of planned)	DLOAR Dose (of tolerance	Min dose to 99% CTV (of planned)	DLOAR Dose (of tolerance
1	Heart	100.4%	100.6%	99.4%	100.8%
2	Pulm.Art.	92.7%	102.5%	98.5%	100.7%
3	Aorta	100.4%	100.0%	100.3%	97.6%
4	Oesophagus	99.9%	100.1%	99.9%	100.2%
5	Pulm.Art.	100.3%	99.2%	99.4%	100.0%
6	Heart	100.2%	100.3%	99.6%	100.3%
7	Aorta	99.3%	99.3%	102.3%	99.7%
8	Aorta	99.9%	100.0%	97.4%	99.6%
9	Heart	101.1%	99.2%	99.5%	100.8%
10	Oesophagus	99.8%	99.9%	100.7%	100.0%
Mean		99.4%	100.1%	99.7%	100.0%

(a) PTV_{ITV} accumulation results

Patient	Dose Limiting OAR	DIR Accumulation		DMA Accumulation	
		Min dose to 99% CTV (of planned)	DLOAR Dose (of tolerance	Min dose to 99% CTV (of planned)	DLOAR Dose (of tolerance
1	Heart	99.8%	100.2%	97.6%	100.5%
2	Pulm.Art.	86.5%	99.0%	96.4%	87.1%
3	Trachea	99.5%	100.4%	99.1%	100.5%
4	Oesophagus	99.2%	99.9%	98.7%	100.0%
5	Pulm.Art.	99.0%	99.4%	107.2%	96.2%
6	Heart	99.4%	99.5%	97.7%	99.1%
7	Aorta	98.0%	83.3%	101.4%	100.5%
8	Aorta	98.5%	100.2%	93.9%	99.8%
9	Heart	100.2%	99.1%	83.0%	97.1%
10	Oesophagus	99.4	99.7%	99.6%	99.4%
Mean		98.0%	98.1%	96.6%	98.0%

(b) $PTV_{\text{Low Accuracy}}$ accumulation results

Patient	Dose Limiting OAR	DIR Accumulation		DMA Accumulation	
		Min dose to 99% CTV (of planned)	DLOAR Dose (of tolerance	Min dose to 99% CTV (of planned)	DLOAR Dose (of tolerance
1	Heart	99.0%	100.1%	96.6%	100.5%
2	Pulm.Art.	89.3%	99.5%	98.3%	95.6%
3	Trachea	97.9%	100.0%	98.7%	100.1%
4	Oesophagus	98.6%	99.8%	99.5%	99.9%
5	Pulm.Art.	99.9%	98.9%	109.1%	99.7%
6	Heart	99.2%	98.7%	95.8%	98.5%
7	Aorta	97.4%	82.0%	101.1%	89.5%
8	Aorta	99.3%	100.0%	94.0%	99.5%
9	Heart	99.8%	98.9%	84.7%	100.7%
10	Oesophagus	98.9%	98.6%	100.2%	98.6%
Mean		97.9%	97.7%	97.8%	98.3%

(c) $PTV_{\text{High Accuracy}}$ accumulation results

Patient	Dose Limiting OAR	DIR Accumulation		DMA Accumulation	
		Min dose to 99% CTV (of planned)	DLOAR Dose (of tolerance	Min dose to 99% CTV (of planned)	DLOAR Dose (of tolerance
1	Heart	97.9%	100.0%	94.9%	100.4%
2	Pulm.Art.	87.9%	99.1%	96.8%	98.0%
3	Trachea	98.4%	100.0%	96.8%	100.3%
4	Oesophagus	99.8%	100.0%	99.8%	100.0%
5	Pulm.Art.	95.2%	93.9%	94.0%	92.9%
6	Pulm.Art.	99.3%	100.1%	94.5%	99.1%
7	Aorta	96.2%	98.7%	99.4%	99.3%
8	Trachea	98.9%	100.3%	90.7%	100.0%
9	Heart	95.6%	98.8%	79.0%	100.5%
10	Oesophagus	99.4%	99.4%	99.5%	99.0%
Mean		96.9%	99.0%	94.5%	99.0%

(d) PTV_{Perfect} accumulation results

Table 5.5: Results for DIR and DMA accumulation. Minimum dose to 99% of CTV is shown as a percentage of planning value (on mid-ventilation). Dose Limiting (DL) OAR at planning is listed, with the result this constraint as a percentage of the tolerance (and planning) value. Values exceeding tolerance are highlighted in red.

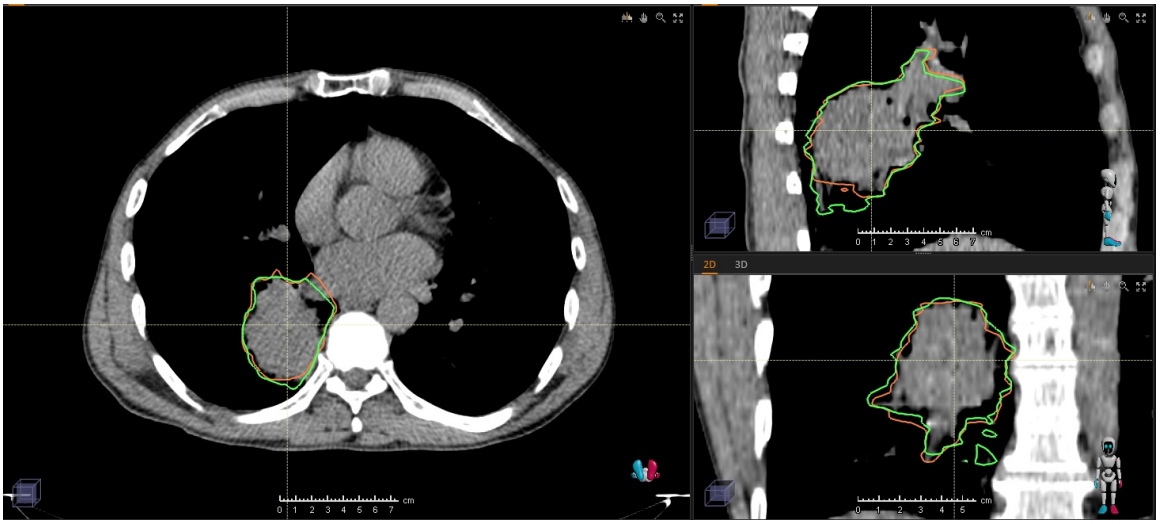

Figure 5.5: Worst-case of Hausdorff distance, which suggested the registration produced a non-smooth deformation. The manual (expert) delineation of the GTV can be seen in orange, the automated DIR delineation, deformed from the mid-ventilation phase can be seen in green.

PTV	DIR Accumulation		DMA Accumulation	
	Min dose to 99% CTV (of planned)	Max DLOAR Dose (of tolerance)	Min dose to 99% CTV (of planned)	DLOAR Dose (of tolerance)
PTV_{ITV}	92.7%	102.5% (4)	97.4%	100.8% (5)
$PTV_{Low\ Accuracy}$	86.5%	100.4% (3)	83.0%	100.5% (3)
$PTV_{High\ Accuracy}$	89.3%	100.1% (1)	84.7%	100.7% (3)
$PTV_{Perfect}$	87.9%	100.3% (2)	79.0%	100.5% (3)

Table 5.6: Minimum/maximum results for PTV_{ITV}, $PTV_{Low\ Accuracy}$, $PTV_{High\ Accuracy}$ and $PTV_{Perfect}$. Number of dose limiting OARs exceeding tolerance shown in brackets.

- Patient 2 had 1 plan - PTV_{ITV}
- Patient 3 had 1 plan - $PTV_{\text{Low Accuracy}}$
- Patient 4 has 1 plan - PTV_{ITV}
- Patient 6 had 2 plans - PTV_{ITV}, PTV_{Perfect}
- Patient 8 had 2 plans - $PTV_{\text{Low Accuracy}}$, PTV_{Perfect}

A total of 10 of 40 plans had an OAR breaching tolerance for the DIR results. However, the degree of overdose was found to be small as can be seen in Table 5.7.

For the DIR technique, the largest dose tolerance breach was 2.5% (1.89 Gy) above tolerance for PTV_{ITV}. The experimental PTVs had smaller breaches of tolerance of 0.4% (0.28 Gy), 0.1% (0.09 Gy) and 0.3% (0.22 Gy) for $PTV_{\text{Low Accuracy}}$, $PTV_{\text{High Accuracy}}$ and PTV_{Perfect} respectively.

Similarly, for the DMA methods, PTV_{ITV} had the largest tolerance violation of 0.8% (0.56 Gy), compared to 0.5% (0.37 Gy), 0.5% (0.33 Gy) and 0.4% (0.27 Gy) for $PTV_{\text{Low Accuracy}}$, $PTV_{\text{High Accuracy}}$ and PTV_{Perfect} respectively as shown in Table 5.8.

The DIR and DMA methods resulted in tolerance violations for the experimental PTVs that were larger than those for the standard plans for only two patients (Patients 3 and 8). These experimental PTV OAR doses were within 0.4 Gy of tolerance, and did not exceed the tolerance violations measured for the standard technique across the whole patient cohort.

It is worth noting that the largest dose tolerance violation received (Patient 2) by a dose-limiting OAR was considerably larger for the standard PTV (2.5%) as shown in Figure 5.5, compared with the experimental PTVs (0.1-0.4%) for the DIR method, although similar for the DMA methods (0.5-0.8%). A similar level of tolerance violation was found for this patient and OAR for the experimental PTVs when tracking was not considered (2.4, 3.1 and 2.4%), but reduced to within tolerance when tracking

Patient	DL OAR	Dose Limiting OAR dose (% of tolerance)			
		PTV_{ITV}	$PTV_{Low\ Accuracy}$	$PTV_{High\ Accuracy}$	$PTV_{Perfect}$
1	Heart D2%	100.6%	100.2%	100.1%	100.0%
2	PA D_{1cc}	102.5%	99.0%	99.5%	99.1%
3	Aorta D_{1cc}	100.0%	100.4%	100.0%	100.0%
4	Oesoph. D_{1cc}	100.1%	99.9%	99.8%	100.0%
6	Heart D2%	100.3%	99.5%	98.7%	100.1%
8	Aorta D_{1cc}	100.0%	100.2%	100.0%	100.3%

(a) DIR - Dose limiting OAR doses as percentage of tolerance values.

Patient	DL OAR	Dose Limiting OAR absolute doses above tolerance (Gy)			
		PTV_{ITV}	$PTV_{Low\ Accuracy}$	$PTV_{High\ Accuracy}$	$PTV_{Perfect}$
1	Heart $D_{2\%}$	0.41	0.11	0.09	0.00
2	PA D_{1cc}	1.89			
3	Aorta D_{1cc}	0.00	0.28	0.01	0.00
4	Oesoph. D_{1cc}	0.06			0.03
6	Heart $D_{2\%}$	0.21			0.07
8	Aorta D_{1cc}	0.00	0.14	0.00	0.22

(b) DIR - Absolute doses exceeding tolerance for dose limiting OARs.

Table 5.7: DIR dose tolerance violations. Values in red indicate the experimental plans that had larger tolerance violations than the PTV_{ITV}

was simulated. However, as previously discussed, the DMA results are "worst-case" results, and so the deviations in DIR results beyond those seen in the DMA results, are attributed to errors within the DIR technique. An increased average Jacobian for the CTV in Patient 2 suggests some unrealistic deformations may be included in the DVF.

The cases where the DIR calculations suggest inferior results than those calculated by the "worst-case" DMA method are attributed to inaccuracies in the image warping performed by the DVF, compared to the "warping" from the use of multiple contours within the DMA approach. It is expected that both DIR and DMA techniques will perform better in regions of high contrast, and poorer in low contrast regions.

Although the number of plans that had an OAR breaching tolerance increased to 14 for the DMA results, the maximum tolerance breach was 0.8%, which again was for PTV_{ITV}, and so these OAR dose breaches are not considered clinically important.

Patient	DL OAR	Dose Limiting OAR dose (% of tolerance)			
		PTV_{ITV}	$PTV_{Low\ Accuracy}$	$PTV_{High\ Accuracy}$	$PTV_{Perfect}$
1	Heart $D_{2\%}$	100.8%	100.5%	100.5%	100.4%
2	PA D_{1cc}	100.7%	87.1%	95.6%	98.0%
3	Aorta D_{1cc}	97.6%	100.5%	100.1%	100.3%
4	Oesoph. D_{1cc}	100.2%	100.0%	99.9%	100.0%
6	Heart $D_{2\%}$	100.3%	99.1%	98.5%	99.1%
8	Aorta D_{1cc}	99.6%	97.3%	98.5%	100.0%

(a) DMA - Dose limiting OAR doses as percentage of tolerance values.

Patient	DL OAR	Dose Limiting OAR excess dose above tolerance (Gy)			
		PTV_{ITV}	$PTV_{Low\ Accuracy}$	$PTV_{High\ Accuracy}$	$PTV_{Perfect}$
1	Heart $D_{2\%}$	0.53	0.33	0.33	0.27
2	PA D_{1cc}	0.56			
3	Aorta D_{1cc}		0.37	0.08	0.20
4	Oesoph. D_{1cc}	0.11	0.03		0.02
6	Heart $D_{2\%}$	0.21			
8	Aorta D_{1cc}				0.03

(b) DMA - Absolute doses exceeding tolerances for dose limiting OARs.

Table 5.8: DMA - Dose tolerance violations. Values in red indicate the experimental plans that had larger tolerance violations than the PTV_{ITV}.

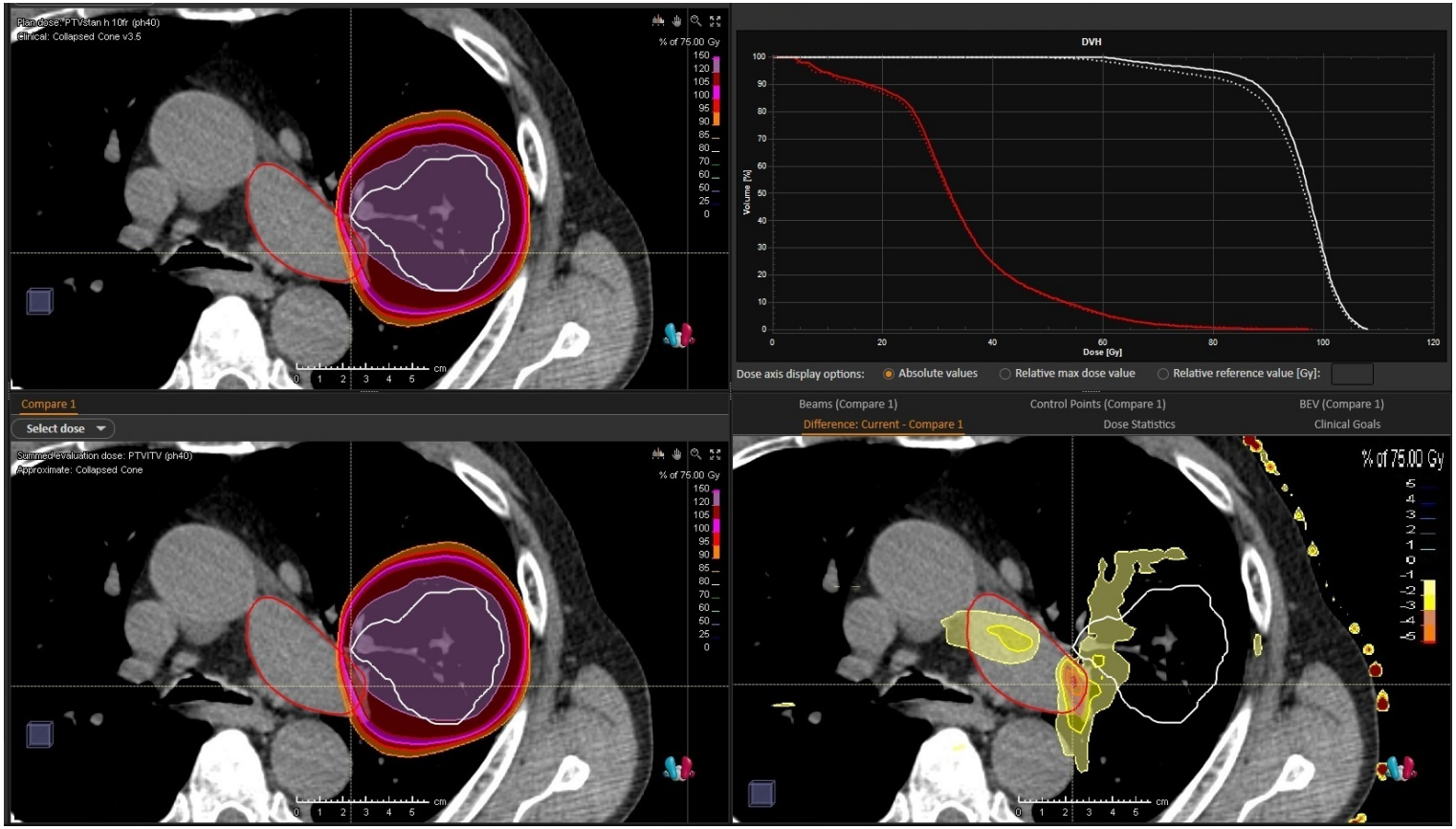

(a) LA-NSCLC Patient 2 axial view

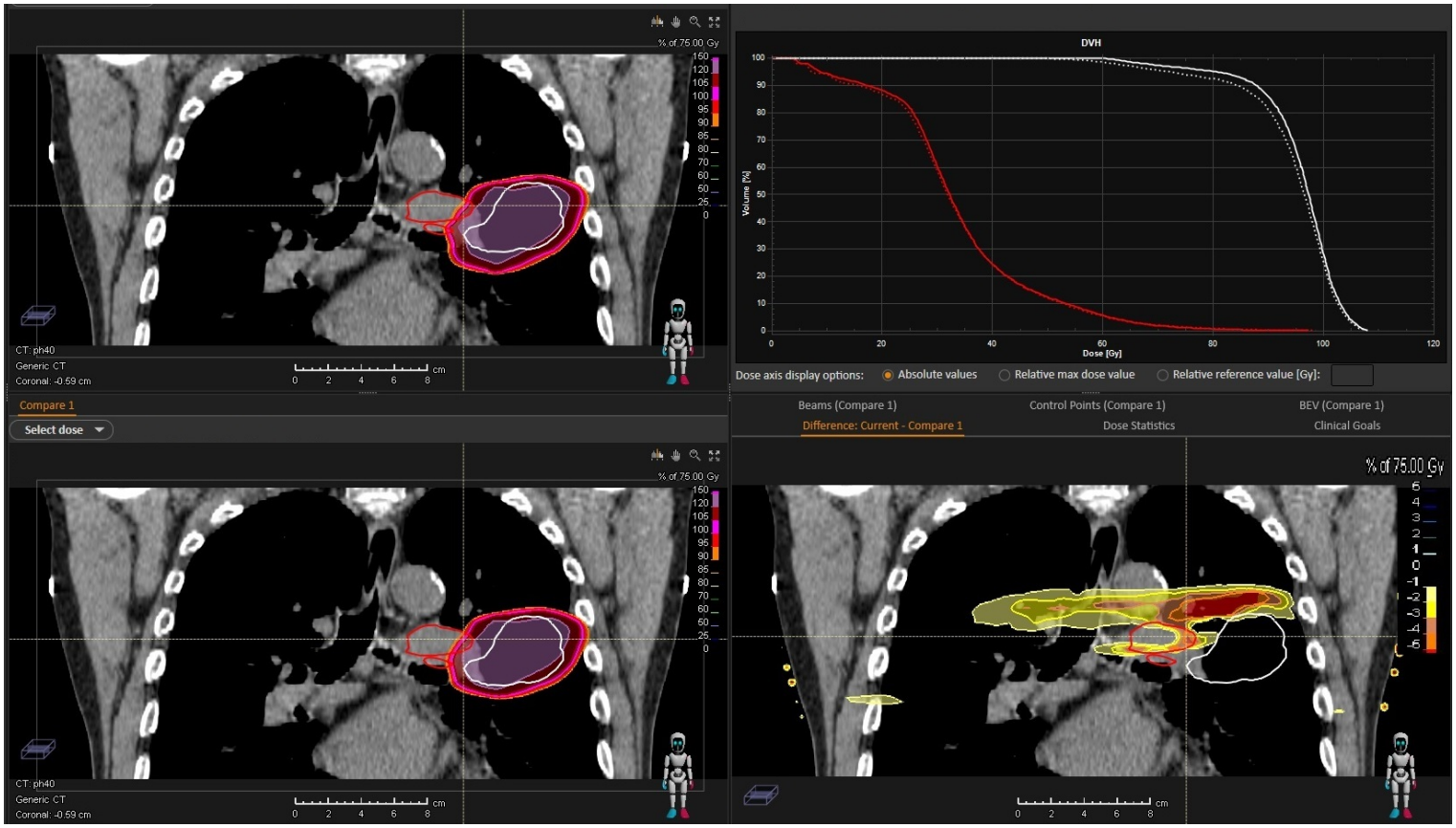

(b) LA-NSCLC Patient 2 coronal view

Figure 5.5: LA-NSCLC - Patient 2 OAR tolerance breach when accumulated over respiratory cycle for PTV_{ITV}. Top Left - Planning coverage. Bottom Left - DIR accumulation over respiratory cycle. Top Right - Dose volume histogram results showing planned dose in solid, and accumulated dose in dashed lines. Bottom Right - Dose difference between planned and accumulated doses (accumulated greater than planned shown). CTV shown in white, OAR in red.

To ensure any overdoses to OAR are not cancelled out by averaging across the tracking uncertainty applied in opposing directions, the doses to the OARs when a single directional tracking uncertainty (rather than the accumulated dose across all directions) were assessed.

For the dose-limiting OARs, a single directional tracking uncertainty for a single patient exceeded the breach of 2.5% seen for PTV_{ITV}, which was for the same patient (patient 2) with a dose of 110% of tolerance (in the superior-inferior direction). One directional tracking uncertainty resulted in additional (non dose-limiting) OAR breaching tolerance, by 2.0% (patient 3, $PTV_{\text{High Accuracy}}$, in the superior direction), although this was at 99.3% of tolerance at planning. To compare these with the variation in doses seen across the respiratory cycle for PTV_{ITV}, for patient 2, the dose calculated to a single phase of respiration was also found to equal 110% of tolerance.

5.3.3.2 Target Coverage Accumulation Results

The target coverage was compared with the planned (mid-ventilation) dose in terms of the minimum dose to 99% of CTV. The results are presented as a percentage of the value at planning; so less than 100% represents a fall in the target coverage when accumulated over the respiratory cycle.

The minimum dose to the target did appear to be compromised by the reduction in margins for the experimental PTVs, particularly for PTV_{Perfect}.

When considering a target coverage of less than 95% of planning value "problematic", each experimental plan had at least two "problematic" accumulated target coverage using the DMA accumulation technique; 2, 2 and 5 plans respectively for $PTV_{\text{Low Accuracy}}$, $PTV_{\text{High Accuracy}}$ and PTV_{Perfect}.

However, for the DIR accumulation results, Patient 2 had poor coverage of target volumes regardless of the PTV used - even for the standard technique, PTV_{ITV}, the minimum dose to 99% of CTV was calculated to be 92.7% of planned dose,

reducing to 86.5, 89.3 and 87.9% of planned dose for $PTV_{\text{Low Accuracy}}$, $PTV_{\text{High Accuracy}}$ and PTV_{Perfect} respectively. When excluding Patient 2 as an outlier, the average of minimum dose to 99% of CTV shows good coverage; 100.1, 99.2, 98.9 and 97.9% of planned dose for PTV_{ITV}, $PTV_{\text{Low Accuracy}}$, $PTV_{\text{High Accuracy}}$ and PTV_{Perfect}. An example of good accumulated coverage can be seen in Figure 5.5.

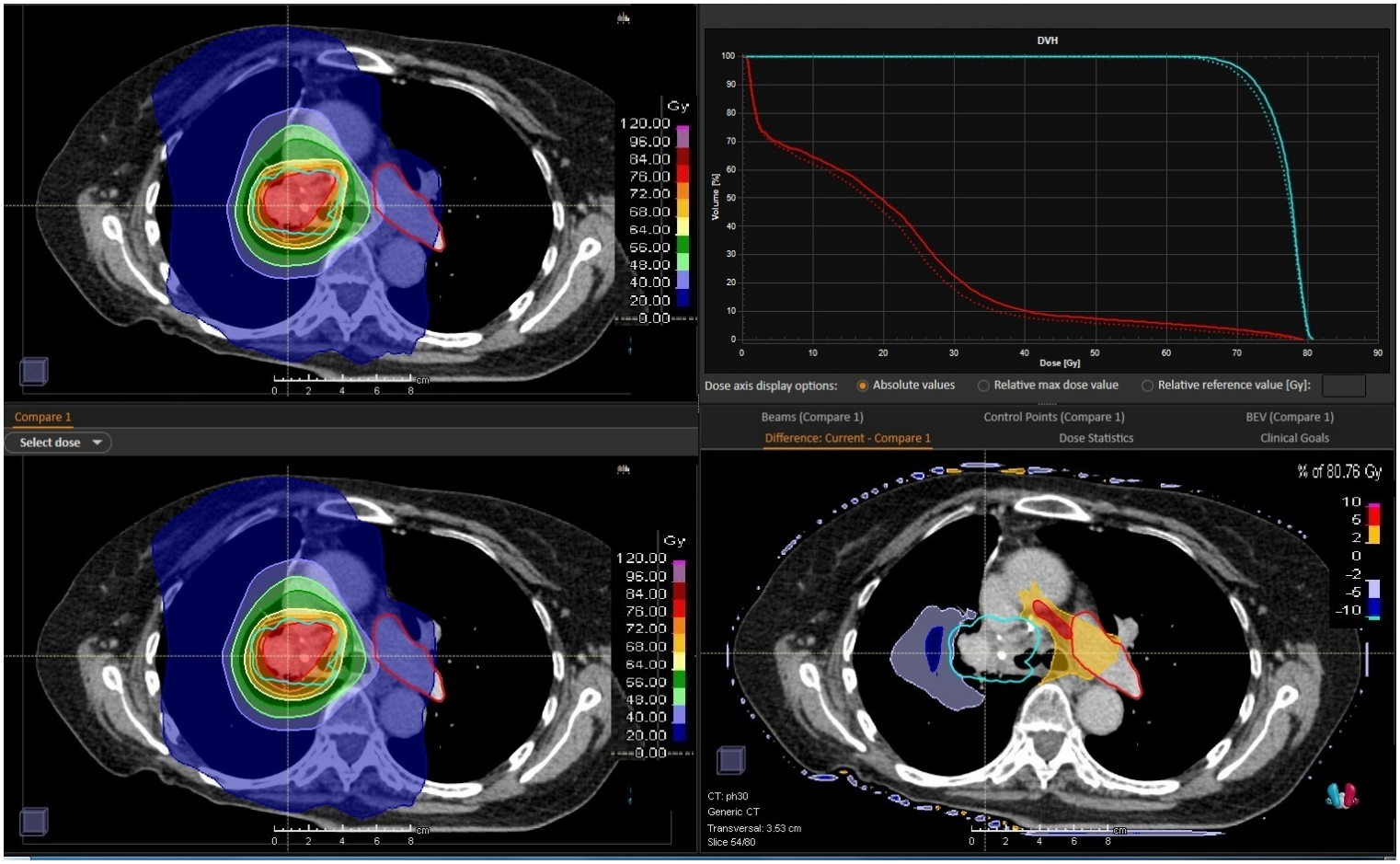

(a) LA-NSCLC Patient 5

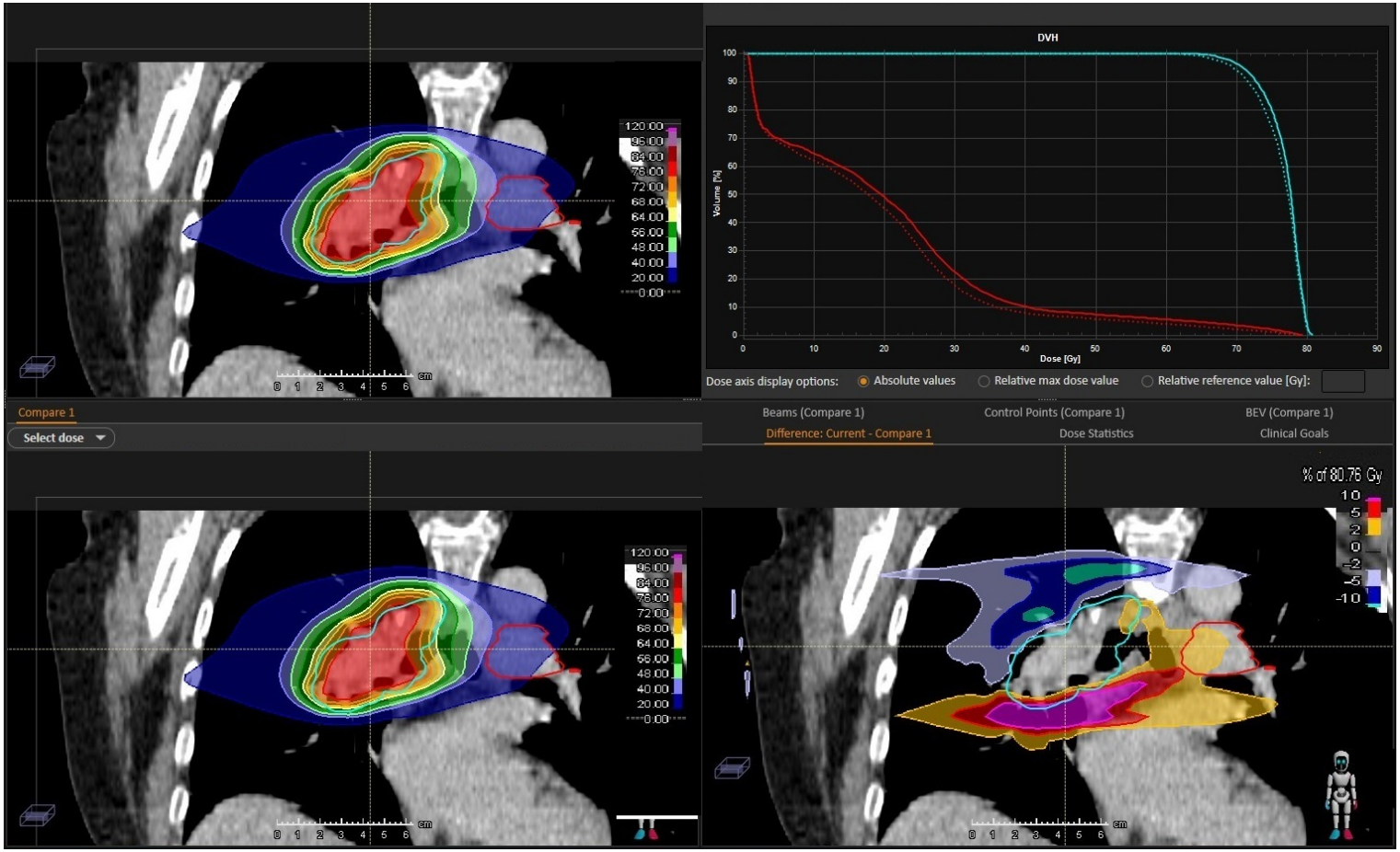

(b) LA-NSCLC Patient 5

Figure 5.5: LA-NSCLC - Patient 5 good coverage when accumulated over respiratory cycle for PTV_{ITV} (coronal view). Top Left - Planning dose distribution. Bottom Left - Dose distribution for DIR accumulation over respiratory cycle. Top Right - Dose volume histogram - planning values in solid, accumulated values in dashed lines. Bottom Right Dose difference between planned and accumulated doses (accumulated less than planned shown). CTV shown in blue, dose-limiting OAR in red.

Although the target coverage was reduced for the experimental PTVs when compared to planned dose, due to the dose escalation possible as a result of the reduced margins, an increase in median/mean absolute dose to CTV was still measured for most experimental PTVs when accumulating the dose over the respiratory cycle, as shown in Tables 5.9 (a) and (b).

Patient 9 had poor target coverage for DMA method for the experimental PTVs (79.0 - 84.7% of planned) particularly compared to the standard approach (99.5% of planned), as demonstrated in Figure 5.5. The poor coverage on the inferior section of the CTV (depicted in orange) can easily be seen in the bottom images, and the large change in dose-volume histogram can be seen.

The poor target coverage calculated for patients 2 and 9 will be thoroughly investigated in Chapter 6.

Patient	DIR - Minimum dose to 99% CTV (Gy)			
	PTV_{ITV}	$PTV_{LowAccuracy}$	$PTV_{High\ Accuracy}$	$PTV_{Perfect}$
1	70.6	71.2	71.1	70.6
2	83.4	80.1	98.2	115.6
3	76.1	77.1	76.1	77.6
4	71.5	72.6	74.4	76.2
5	73.7	73.8	76.6	74.8
6	66.0	69.4	71.2	76.0
7	67.0	66.9	67.9	67.3
8	64.0	65.7	69.2	71.3
9	73.4	88.4	102.5	108.4
10	70.1	72.0	73.3	76.0
Median	71.1	72.3	73.8	76.0
Mean	71.6	73.7	78.0	81.4
P-value		0.19	0.06	0.09

(a) DIR Minimum absolute dose to 99% of CTV

Patient	DMA - Minimum dose to 99% CTV (Gy)			
	PTV_{ITV}	$PTV_{LowAccuracy}$	$PTV_{High\ Accuracy}$	$PTV_{Perfect}$
1	69.9	69.5	69.4	68.5
2	88.7	80.9	108.1	127.2
3	76.0	76.7	76.7	76.4
4	71.5	72.2	75.0	76.2
5	73.1	79.9	83.6	73.8
6	65.6	68.2	68.8	72.3
7	69.1	69.1	70.5	69.6
8	62.4	62.6	65.5	65.3
9	72.2	73.3	87.0	89.6
10	70.7	72.1	74.3	76.1
Median	71.1	72.2	74.6	75.0
Mean	71.9	72.5	77.9	79.5
P-value		0.65	0.08	0.49

(b) DMA Minimum absolute dose to 99% of CTV.

Table 5.9: DIR and DMA Minimum absolute dose to 99% of CTV

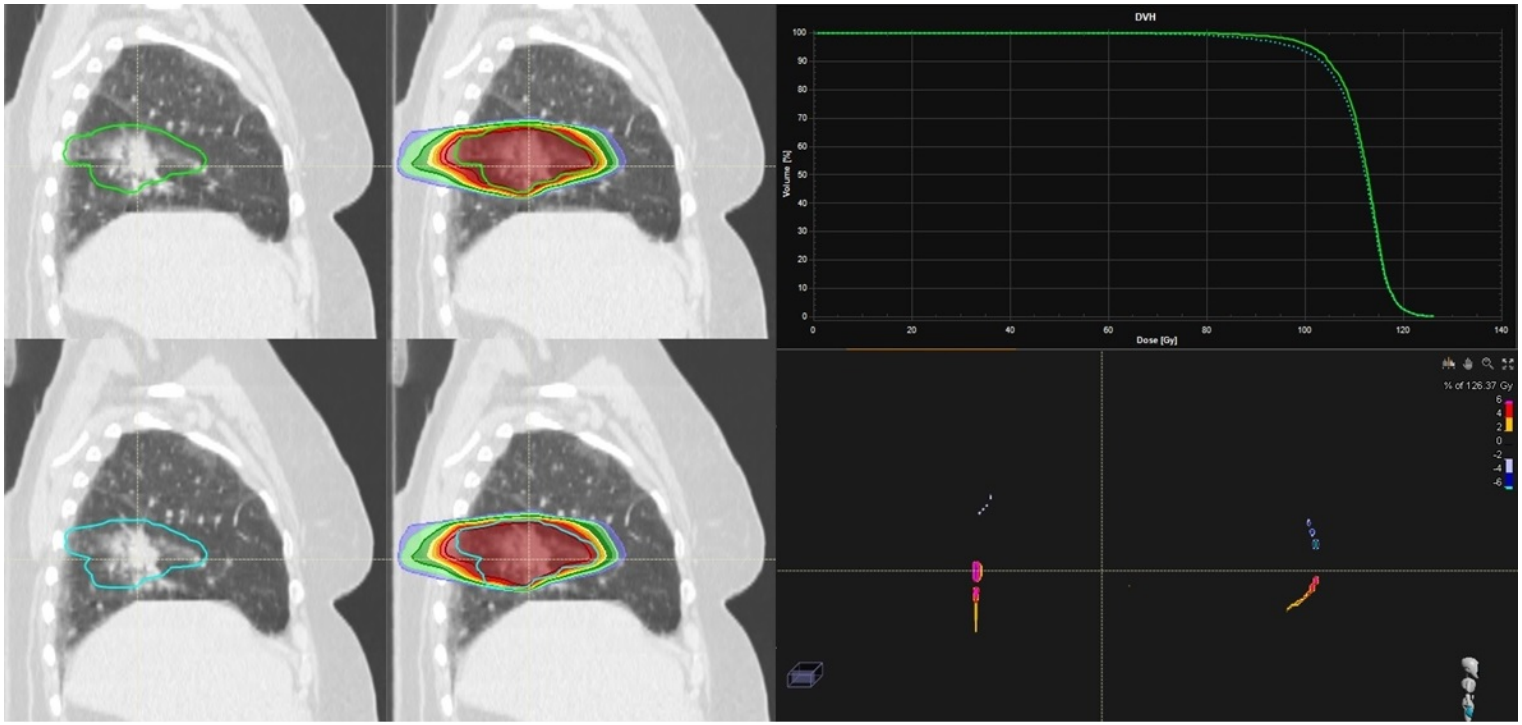

(a) LA-NSCLC Patient 9 phase 20

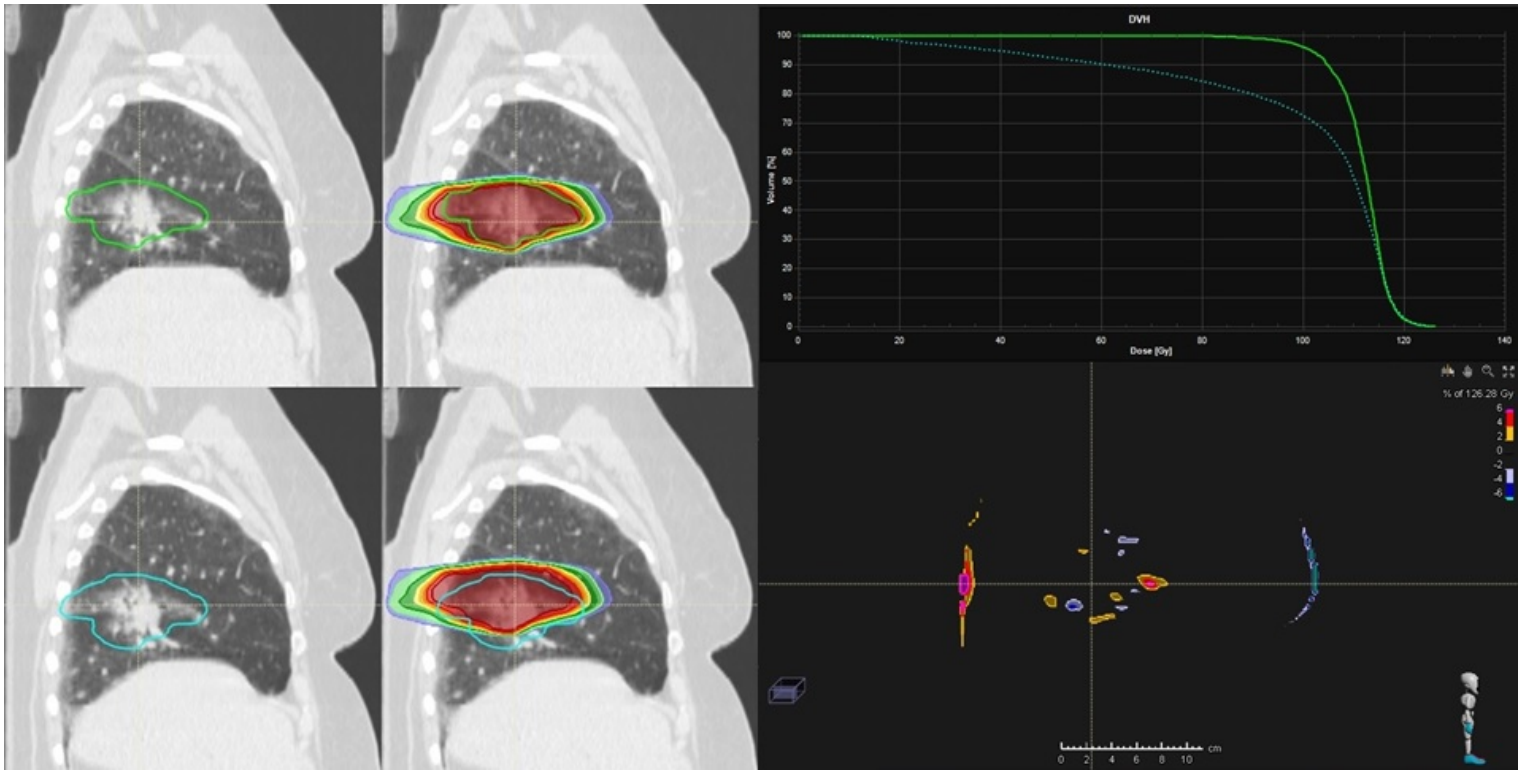

(b) LA-NSCLC Patient 9 phase 0

Figure 5.5: LA-NSCLC - Patient 9 has very poor coverage for some individual phases. $PTV_{Perfect}$ plans depicted. The left images show the CTV volumes on each phase (mid-ventilation in green, other phase in cyan). Middle images show the calculated doses on each phase. Right images show resulting dose volume histograms and dose difference maps. The top row of images is for planned (mid-ventilation), the bottom row is for the phase dose

5.4 Discussion

For all plans simulated, 10 of 40 plans had an OAR breaching tolerance for the DIR methods of accumulation over the respiratory cycle. The largest tolerance violations were measured for the standard ITV plans. As these tolerance violations will be happening in standard practice, which is known to result in acceptable levels of toxicity, the reduced levels of tolerance violations for the experimental PTVs are predicted to result in similar or reduced levels of toxicity, and so are not considered to be clinically relevant.

Similar levels of overdose were observed using the DMA method compared to the DIR method for experimental PTVs. This confirms that less than half of plans will breach OAR dose tolerances by less than 1% of tolerance dose. The DMA results show similar levels of overdose for the standard (0.8%) and experimental PTVs (0.5 - 0.7%), all within 0.5 Gy and so are considered to be of no clinical significance. As previously discussed, these results are considered to be "worst-case". This suggests that the larger deviations seen for the DIR method are caused by the uncertainties in the DIR.

The structures breaching tolerance were always those that were the dose limiting OAR at planning, and the regions of overdose were generally located at regions of overlap between PTV and OAR. Hence the specific sub-volume of OAR that will breach tolerance for under half of cases when considering treatment over the entire respiratory cycle are predictable at the planning stage.

Whilst the data shows no need for concern about OAR doses during respiration for this subset of patients, if one were concerned, on-treatment monitoring may be feasible as only a small, predictable sub-volume of structures in a known location would require monitoring.

Although the accumulated target coverage for the experimental PTVs was slightly reduced compared to the standard technique, due to the isotoxic dose escalation that

was possible due to the reduced margins, the absolute dose delivered to the CTV was ultimately still increased. The "worst-case", DMA median of minimum dose to 99% of the CTV was increased from 71.1 Gy for PTV_{ITV}, to 72.2, 74.6 and 75.0 Gy for $PTV_{Low\ Accuracy}$, $PTV_{High\ Accuracy}$ and $PTV_{Perfect}$ respectively. The isocentre doses are likely to be similar to planned isocentre dose, as the tracking is based upon aligning the beam isocentre with the primary target COM, and so only slight variations would be expected due to changes in radiological path length when the relative tumour position changes and/or deformation of the target occurs.

Two patients (2 and 9) had poor coverage when assessing the accumulation results, the reasons for which will be investigated in the following chapter.

Other authors have investigated the use of dose accumulation methods over the respiratory cycle for lung radiotherapy. However, the majority of studies focus on the dose to the target volume (GTV, ITV, CTV, PTV), whereas only a few consider OAR doses, which were generally performed for SABR cases rather than LA NSCLC [199, 200].

Al-Ward et al. [201] have performed a similar, if more simplistic simulation of a tracking technique compared to an ITV approach, using the MR-linac to deliver IMRT plans for five patients. The OAR doses accumulated across the respiratory cycle using DIR were compared for the tracked and ITV approach for central SABR plans. The target in each plan was prescribed the same dose (rather than an isotoxic technique for dose escalation), and they concluded that the tracking technique was able to reduce the dose to surrounding OARs. The level of reduction was associated with the tumour motion, relative organ at risk motion, and proximity of the OAR to the target. This is analogous to our increase in prescribed dose whilst maintaining the dose to surrounding OARs. However, Al-Ward et al.'s study was an idealised case, with no inclusion of tracking uncertainties and an assumed fixed breathing pattern, and so as they conclude, their results provide a "best case scenario for the tracking

of a moving target".

Another SABR accumulation study by Ehrbar et al. [202] compared several different tracking techniques, including a "single phase tracking" approach similar to that used in this study. The tracking uncertainty was also included in this study as an extension of an alternative "multi-phase tracking" approach, although for a different system based on a prototype of a couch tracking system. Target coverage was assessed, but OAR doses were limited to the investigation of lung doses. The "single phase" (no tracking uncertainties) accumulation resulted in reduced target coverage, and the reduced target volume led to reduced lung dose. However, target coverage was improved when the tracking uncertainties were included (in the "multi-phase" method), although this did limit the dose reduction to the lungs.

No other study is known that combines the 4D accumulation of dose using a tracking technique based on centrally located locally advanced NSCLC treatment delivery on an MR-linac, including tracking uncertainties. The accumulated dose to both target coverage and all important OARs has been considered through the use of both DIR and DMA (worst-case) techniques.

The main limitation of this current study is the assumption that the breathing motion remains constant throughout the treatment delivery. However, this will be considered in Chapter 7, using repeat 4DCT data that was available for 5 of the patients used in this study.

5.5 Conclusion

When dose escalated plans that are produced isotoxically on the mid-ventilation phase of a 4DCT are accumulated over the respiratory cycle, only small OAR tolerance breaches of up to 0.5 Gy occurred. These deviations were located in the isotoxic dose-limiting structure, and generally in areas of overlap between PTV and OAR,

and so are predictable at planning.

When compared to the standard ITV approach, smaller dose tolerance deviations to OARs were calculated, suggesting that the small tolerance breaches may not be a cause for concern.

Whilst a reduction in the target coverage, as compared to planned, was observed for the experimental PTVs, the use of reduced margins allowed an isotoxic dose escalation which resulted in an increase in absolute dose to the target compared to the standard ITV approach. Thus reduced margins and a tracking technique may be beneficial for locally-advanced non-small cell lung cancer patients receiving radiotherapy treatment.

Chapter 6

Potential Technique Pitfalls

The potential challenges specific to the tracking technique and simulations used in this thesis include target rotations and shape changes, deformable image registration accuracy limitations and the use of baseline CT for accumulation across the respiratory cycle. Simulation results from Chapter 5 will be used to highlight the potential results of these limitations.

6.1 Tracking Limitations

The tracking technique involves aligning the primary GTV centre of mass with the treatment beam isocentre, through three-dimensional translations of the treatment beam for each respiratory phase. If 3D translations of the target volume occur, this tracking technique would result in excellent target coverage, with minimal deviations in dose distribution due to any changes in radiological path length resulting from any relative motion of the GTV and surrounding tissues.

However, as well as translations, it is known that tumours also rotate and deform due to forces exerted on them during respiration [203]. As the treatment fields are only translated, this technique is unable to account for rotations and shape changes.

Rotations could potentially be compensated for by rotating the multi-leaf collima-

tors, however this has not be explored in this thesis. Previous studies have assessed the magnitude and resulting dosimetric impact of lung tumour rotations. Wu et al. [204] compared the overlap of GTVs when registering lung tumours using translation only or translation and rotation (as well as the use of deformable image registration) for 30 patients who had previously been treated with SBRT. The inclusion of rotations (or use of DIR) was found to have little impact on the GTV overlaps, and it is suggested that motion correction strategies could be adequate when based solely on 3D translations. The dosimetric consequence of target rotations during SBRT treatments have been investigated for 13 patients [205]. Again, it was concluded that the impact of rotations was small for PTV coverage, concluding that their 3 mm GTV to PTV margins were satisfactory to mitigate any impact from tumour rotations. The impact of rotations will be larger for non-spherical, irregular target volumes.

Shape changes are known to occur throughout the respiratory cycle, and will not be compensated for using the simulated tracking technique. Thus any reductions in target coverage may be due to tumour rotations (although as discussed this is considered unlikely), or target volume shape changes. To assess whether target shape changes are detrimentally affecting the target coverage, both the outlines of the GTVs on different phases once "tracked" (primary GTV COM and beam isocentres are aligned) and the resulting dose distributions on each phase were compared to the mid-ventilation (planning) phase.

An example of the reduced target coverage when accumulated across phases including shape change can be seen in Patient 9's results, in Table 6.1. The GTV volume varied from 78.5 to 97.9 cm^3 across the respiratory cycle, with a volume of 88.5 cm^3 on the mid-ventilation (planning) phase. When simulating the tracking technique, the overlap of the GTV on different phases was increased (average DSC of 0.75 improved to 0.79 when tracked), although for two phases (phase 0 and 90) the overlap was still poor, resulting in DSCs of 0.45 and 0.49 (minimally increased by

tracking from 0.43 and 0.45), compared to a range of 0.76-0.96 for the other phases. Increased Hausdorff distances were also measured for the tracked GTVs of 0.99 cm for these two phases, compared to an average of 0.48 cm for other phases. The poor overlap of these target volumes in phase 0, resulting from the change in target shapes can be seen in Figure 6.1 where the static and tracked alignment of the GTV can be compared, and Figure 6.2 where the 3D GTV volumes can be compared to the mid-ventilation volume. Whilst the alignment of GTVs can be seen to be improved by the tracking, there is still some discrepancy suggesting that deformations are minimising the possible overlap of the GTVs with a three-dimensional shift. The automatic image registration tool was used in RayStation (focussed on the mid-ventilation GTV), to calculate the best alignment of each phase with the mid-ventilation phase, including translations and rotations. This confirmed that only small rotations (up to a maximum of 1.1 degree) were seen for every phase, and the "poor coverage" phases had a similar degree of rotations that the other, "good" coverage phases.

The standard ITV approach resulted in good target coverage which is expected as the shape change (and motion) seen throughout respiration is fully encompassed by the ITV. The ITV had a volume (170.7 cm^3) nearly twice as large as the mid-ventilation GTV (88.5 cm^3). The ITV can be seen with all GTVs in Figure 6.3. The experimental PTVs were created from a single phase GTV, with any motion (but not deformation) accounted for by the tracking technique. Patient 9 had the largest

Duty cycle %	Min dose to 99% of CTV (% of planned value)		
	$PTV_{Low\ Accuracy}$	$PTV_{High\ Accuracy}$	$PTV_{Perfect}$
100% (DIR)	100.2%	99.8%	95.6%
100% (DMA)	83.0%	84.7%	79.0%
90% (DMA)	99.2%	96.2%	89.7%
80% (DMA)	100.2%	97.6%	92.5%

Table 6.1: Patient 9 - Target coverage when gating is simulated to restrict dose delivery to phases where small changes in GTV COM are measured. Doses displayed as a percentage of dose at planning.

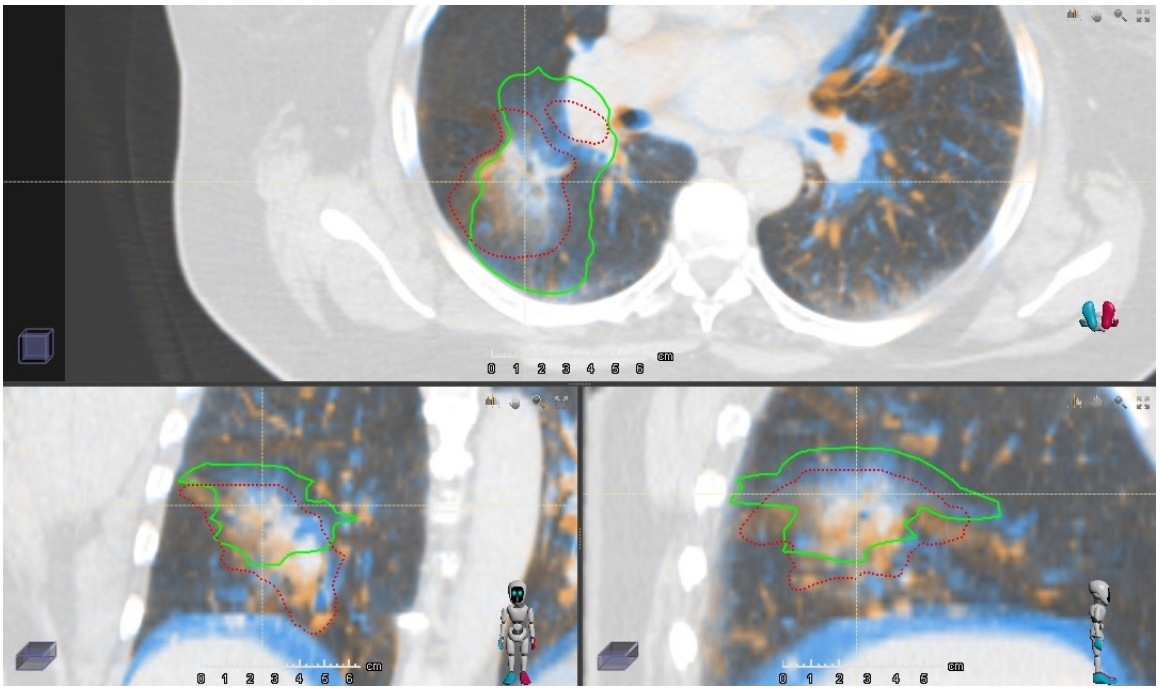

(a) Phase 0 and mid-ventilation (static)

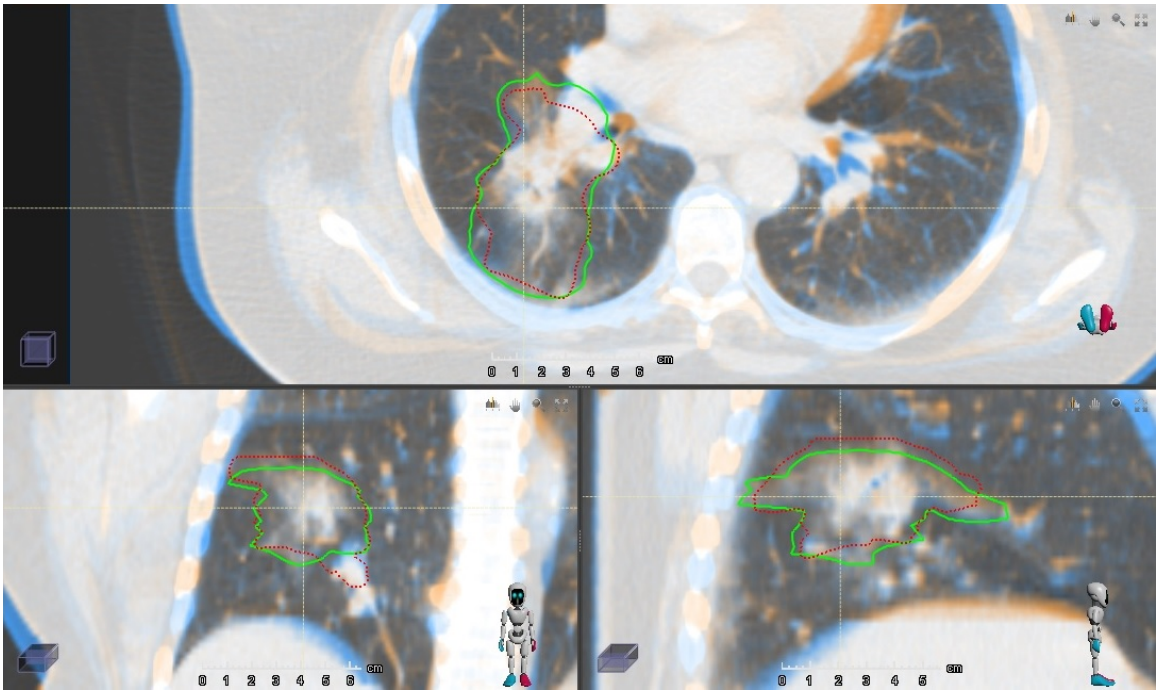

(b) Phase 0 and mid-ventilation (tracked)

Figure 6.1: Registration of mid-ventilation phase and phase 0 for patient 9 - the two phases are shown overlaid in blue (mid-ventilation) and other phase (orange). (a) shows the relative position the GTVs physically occupy on mid-ventilation (green) and phase 0 (red). (b) shows the relative positions of GTVs, when phase 0 scan has been translated to align the GTV centroids. Although alignment of GTVs can be seen to improve with tracking, there is still a significant difference in volume that may be limiting the target coverage for phase 0.

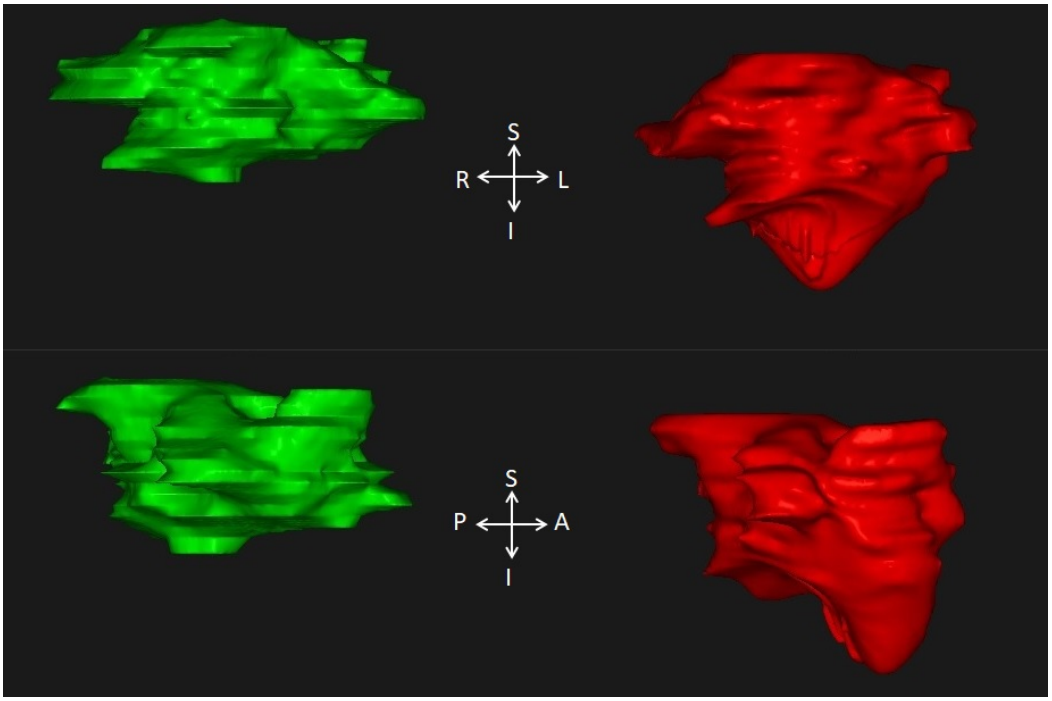

(a) Mid-ventilation GTV (b) Phase 0 GTV

Figure 6.2: Patient 9 3D target shapes of GTV for mid-ventilation and phase 0 (poor coverage). Upper images are sagittal view, lower images are coronal view.

tracking shifts (distances between mid-ventilation and other respiratory phases GTV centre of mass), and so a large reduction of greater than 30% between the target volumes of PTV_{ITV} and $PTV_{Low\ Accuracy}$ was measured. If there was no motion or deformation throughout the respiratory cycle, PTV_{ITV} and $PTV_{Low\ Accuracy}$ would be of equal volume, as they have the same CTV to PTV margins.

The large shape changes seen for phases 0 and 90 resulted in poor target coverage when accumulated using DMA method for the experimental PTVs (79.0 - 84.7% of planned), particularly compared to the standard ITV approach (99.5% of planned). Conversely, the DIR accumulation results suggested reasonable coverage, ranging from 95.6-100.2% of planned (Tables 5.5(a)-(d), Section 5.3.2). The DMA results suggest there may be some problematic reductions in target coverage, but as this is a "worst-case" metric, there may not be a real problem, as suggested by the DIR methods. This patient was further investigated to determine whether the calculated accumulated

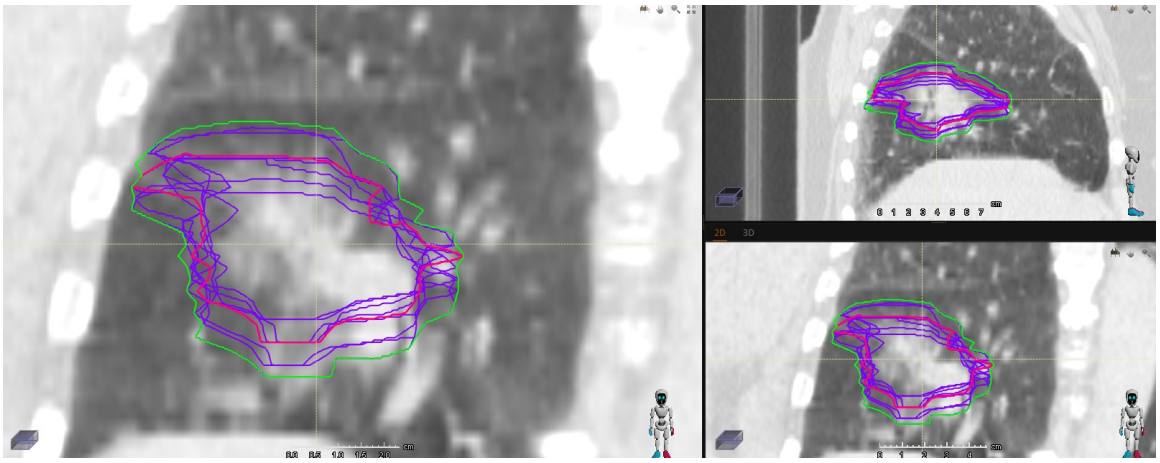

Figure 6.3: Patient 9 GTV contours for all phases - mid-ventilation delineated in pink, all others in purple, ITV in green. The variation in GTV volume over the respiratory cycle can be seen, along with the ITV encompassing all GTV volumes.

target coverage is of concern.

Gating is a technique used in radiotherapy that aims to deliver dose only when the target and/or surrounding avoidance structures are in their optimal positions. A restriction of gating is the increased treatment duration due to delivering dose across only part of respiratory cycle, which can lead to problems with patient toleration of treatment and patient throughput on treatment machines, and so the duty cycle should be as high as possible. I have hypothesised that gating could be used in conjunction with tracking to increase the accumulated target coverage, if a few respiratory phases were resulting in severely reduced coverage, that strongly affected the accumulated dose.

The dose was calculated for each phase (for both DMA and DIR methods) to assess whether any individual phases were having a large impact on the accumulated coverage. An example of phases demonstrating good and poor coverage can be seen in Figure 6.4. The two phases with poor target coverage suggested that a gating approach could improve the target coverage. The exclusion of just one or two phases (so a high duty cycle of 80/90%) greatly improved the target coverage for the experimental PTVs as can be seen in Table 6.1. This effectively removed from

the accumulation the treatment of the targets when large amounts of deformation occurred, and resulted in adequate target coverage.

Both the DMA and DIR accumulation techniques resulted in poor coverage for these two phases. This may suggest that the much poorer accumulated target coverage calculated by the DMA technique compared to the DIR method is a result of the "worst-case" nature of the metric having a large impact on the accumulated results. This can be easily visualised by comparing the target dose coverage on each of the poor coverage phases in Figure 6.5. For one phase the dose is lacking to the inferior aspect of the target volume, whereas for the other phase the dose is lacking to the superior aspect of the target volume. Therefore the "true" dose is likely to be significantly higher than the DMA "worst-case" calculated dose, as the minimum dose when considering these two phases cannot be the average of the minimum dose to each phase as they are clearly in very different sub-volumes of the target. While this indicates issues with the dose metric averaging method under some circumstances, the use of both the DMA and DIR methods together, offers some protection from the limitations of each method when used individually. The issues associated with the DIR technique will now be explored.

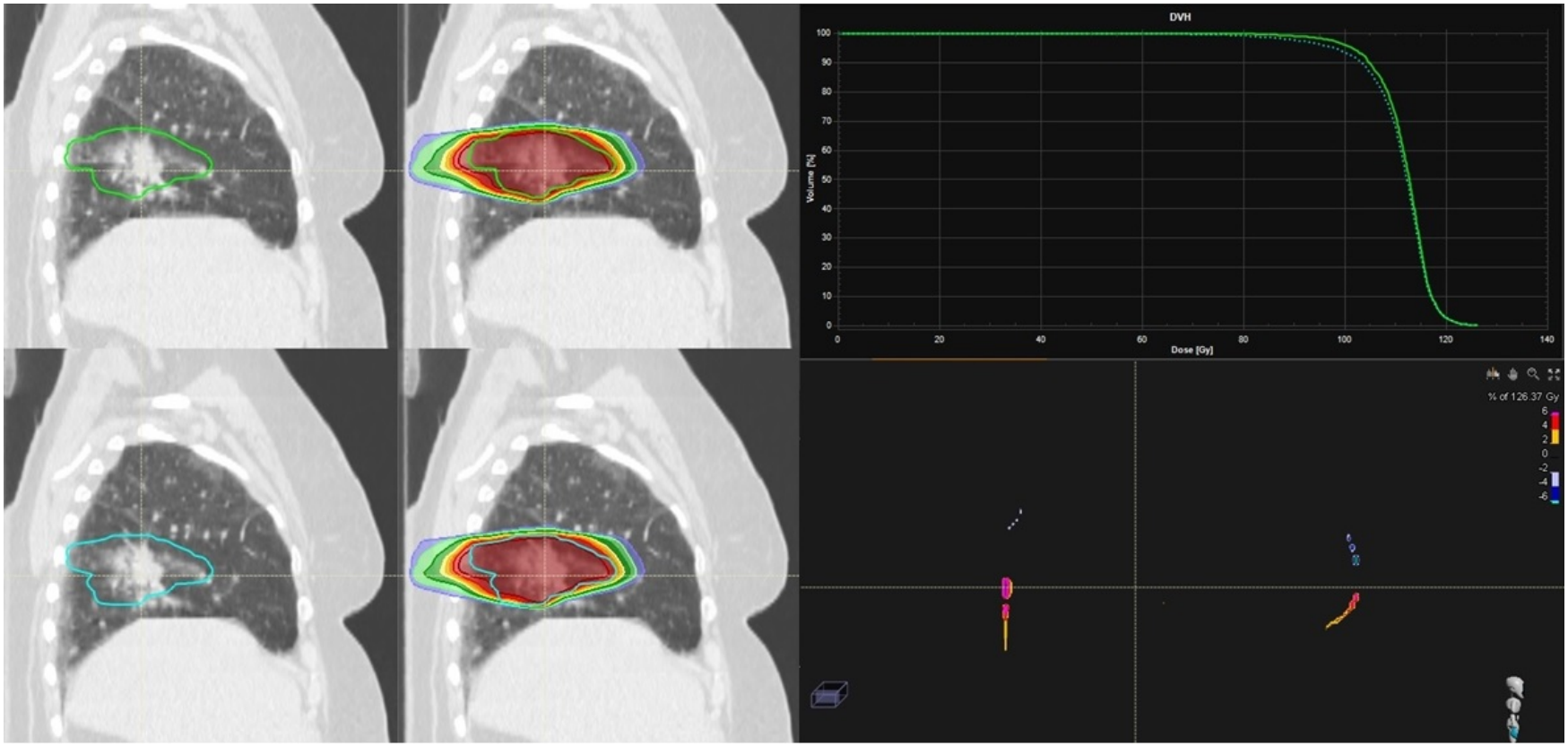

(a) LA-NSCLC Patient 9 Good target coverage

Figure 6.4: LA-NSCLC - Patient 9 has good coverage for some individual phases. $PTV_{Perfect}$ plans depicted. The left images show the CTV volumes on each phase (mid-ventilation in green, alternative phase in cyan). Middle images show the calculated doses on each phase. Right images show resulting dose volume histograms and dose difference maps. The top row of images is for planned (mid-ventilation), the bottom row is for the phase dose.

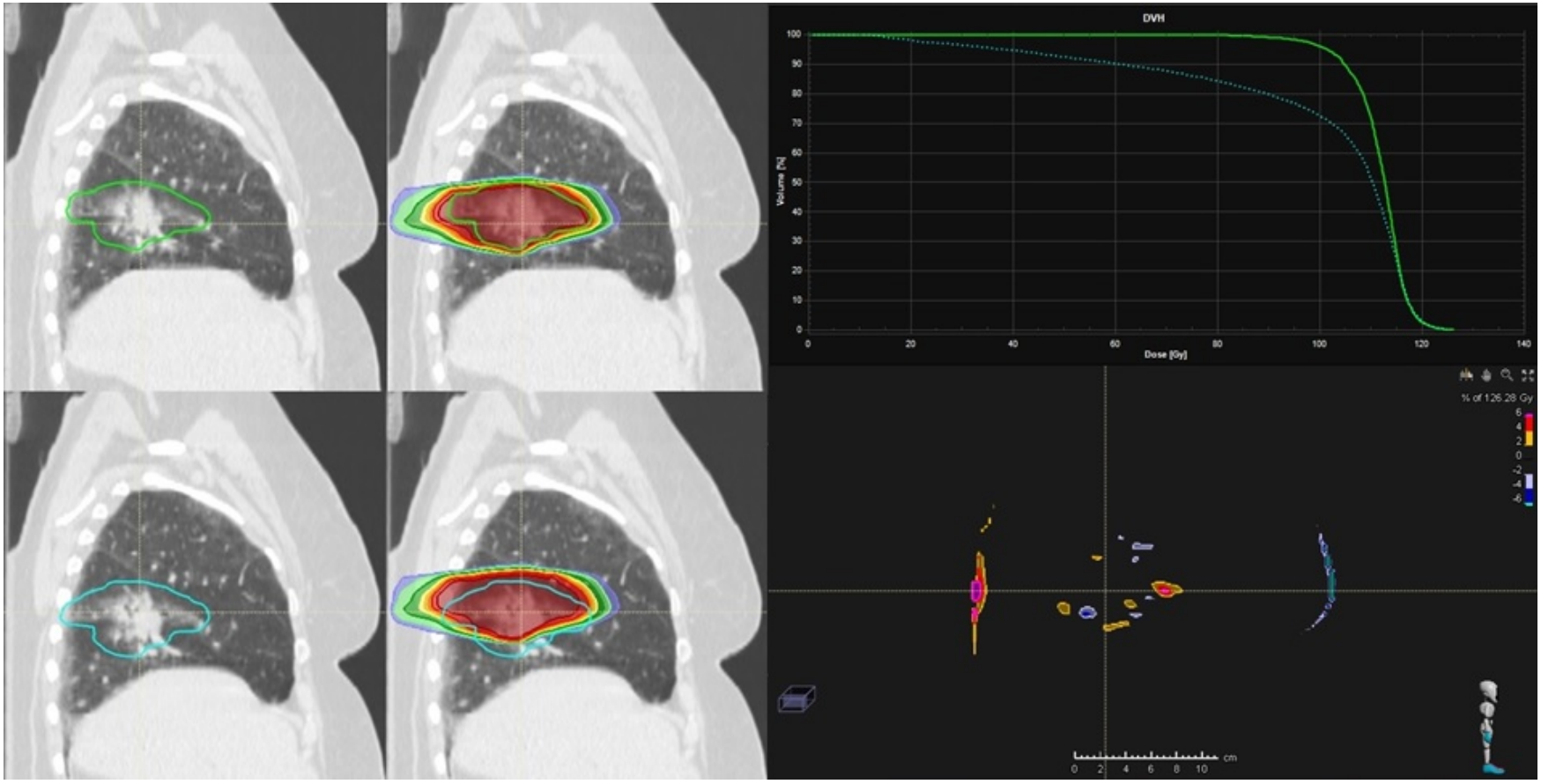

(b) LA-NSCLC Patient 9 Poor target coverage

Figure 6.4: LA-NSCLC - Patient 9 has very poor coverage for some individual phases. $PTV_{Perfect}$ plans depicted. The left images show the CTV volumes on each phase (mid-ventilation in green, alternative phase in cyan). Middle images show the calculated doses on each phase. Right images show resulting dose volume histograms and dose difference maps. The top row of images is for planned (mid-ventilation), the bottom row is for the phase dose.

6.2 DIR Limitations

DIR is known to require careful consideration when implemented for clinical use. Particular care needs to be taken for "black box" software where the user has little knowledge or control over the DIR performed. However, the use of DIR is widespread within the radiotherapy community, and it provides a powerful tool enabling dose accumulation and plan adaption. To ensure the safety of isotoxic radiotherapy treatments, planned on a single respiratory phase, it is useful to assess the accumulation of the dose across the respiratory cycle. This is particularly true in cases of reduced margins, high prescribed doses and when targets are close to surrounding critical structures. For accumulation to be performed, warping of the dose from the individual phases to a reference phase is required. A schematic of the DIR process can be seen in Figure 5.1. The ANACONDA DIR software is a state-of-the-art system enabling dose accumulation, which has been validated in lung studies. The DMA and DIR methods are the only options currently available to perform this accumulation of dose.

The user-defined parameters used within the ANACONDA solution were investigated to ensure the optimal settings were used in this study. For consistent results in terms of the metrics used to validate the DIR, a deformation grid resolution of 0.5 cm/voxel and no controlling ROIs were used. When alternative settings (deformable grid resolutions, control/focus regions and points of interest) were used, the Jacobian determinant values in particular reached levels considered unrealistic, with changes in volume greater than a factor of 2 [206]. As discussed in Section 5.2.1, smoothness of the DVF is important to ensure the deformations are realistic.

Patient 2 provides an example of how DIR results can be limited by errors within the DIR method, as shown in Table 6.2. The coverage appeared acceptable for the DMA accumulation technique, suggesting errors within the DIR process have caused an incorrect accumulation of dose, since the DMA method provides a "worst-case"

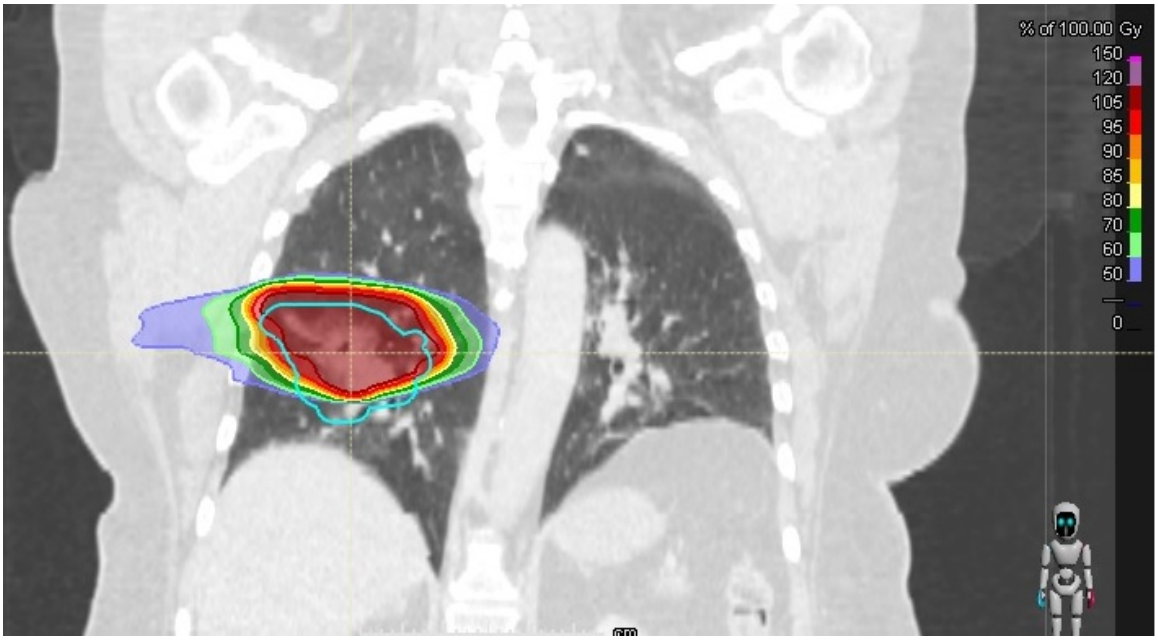

(a) LA-NSCLC Patient 9. Poor inferior coverage of target volume.

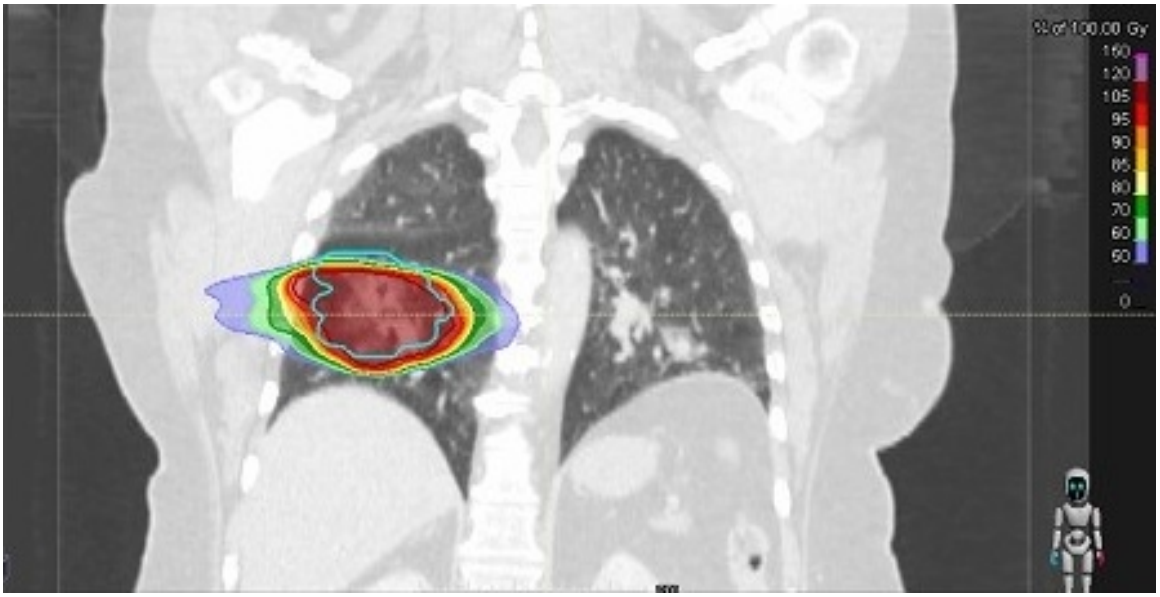

(b) LA-NSCLC Patient 9. Poor superior coverage of target volume.

Figure 6.5: The varying position of underdose to target. Phase GTV in cyan.

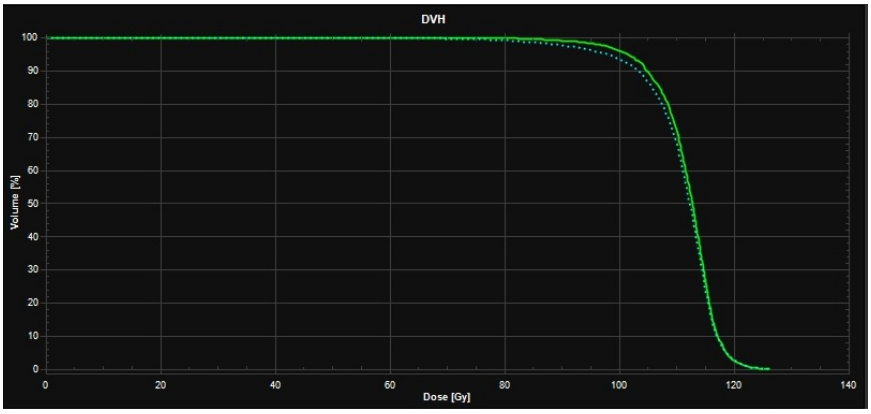

(a) LA-NSCLC DMA - good coverage phase

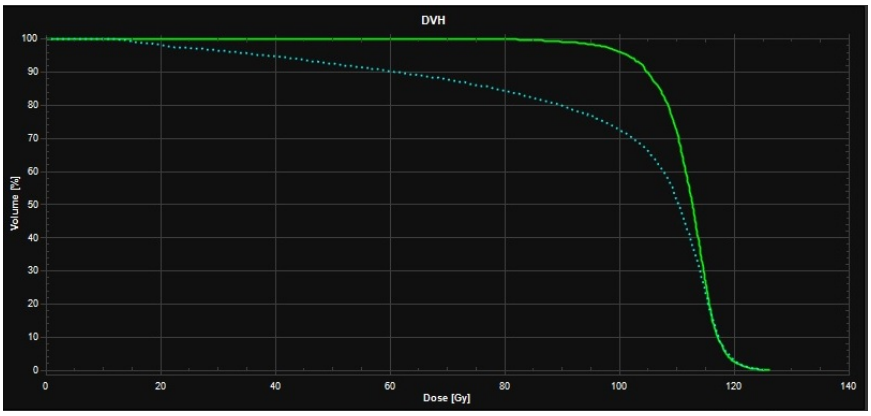

(b) LA-NSCLC DMA - poor coverage phase 1

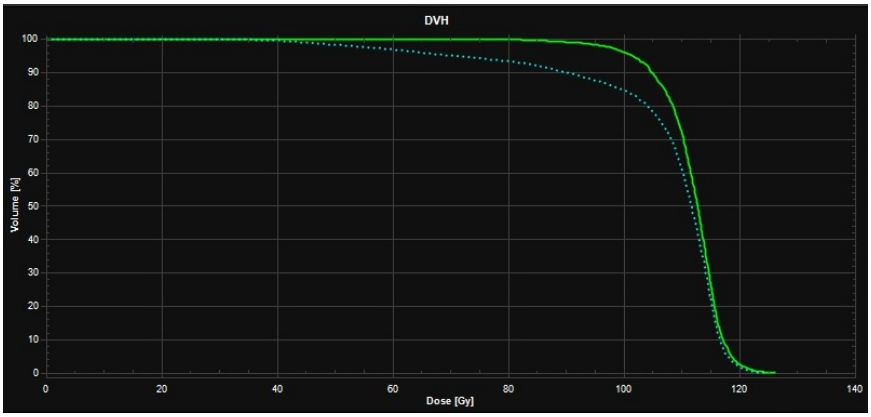

(c) LA-NSCLC DMA - poor coverage phase 2

Figure 6.6: The resulting DVHs for the two poor coverage phases removed by gating, and a contrasting good coverage phase. Planned CTV in solid green, calculated single phase dose in dashed cyan.

estimate. The consequences of the DVF not warping correctly can be visualised by comparing the contours produced by using the DVF to warp the manually drawn contours from an alternate phase to the mid-ventilation phase, with those manually drawn directly on the mid-ventilation phase. An example of the difference in GTV contours can be seen for patient 2 in Figure 6.7, where the mid-ventilation manual GTV contour is shown in orange, is compared with the contour produced by using the DIR to deform the expert manual GTV from an alternative phase to the mid-ventilation phase, shown in green. This demonstrated poorer DIR validation results in terms of GTV DSC (average 0.78 range 0.71-0.81) and larger CTV Jacobian determinants (average 1.042, range 0.896-1.345), suggesting a reasonable expansion of voxels within the CTV volume. However, the Hausdorff distance did not suggest any issues within the DVF of the DIR compared to other patients. The reduction in CTV coverage can be seen in the dose volume histogram (DVH) (a) and localised (b) in Figure 6.8. As expected, the region of underdose was localised to where the target volume is close to the nearby surrounding OAR, which often have the steepest dose gradients. This suggests better DIR, that models the motion at tumour/OAR interfaces may be required [206].

As the "worst-case" results from the DMA methods for patient 2 resulted in reasonable coverage (Table 6.2), errors within the DIR accumulation must be causing the resulting DIR poor coverage. Assessment of the individual phase dose when the GTV COMs are aligned with the beam isocentres and when deformed to the mid-ventilation phase using DIR, showed poor coverage of the manually drawn mid-ventilation GTV contour, for two phases (phases 80 and 10). Conversely, the DMA method resulted in good coverage of manually drawn target volumes on each phase. This suggests errors within the DVFs that are used to warp the dose from each phase to the mid-ventilation phase for the two poor coverage phases. An increase in the Hausdorff distances for the GTV contours produced by the DIR (deformed

from phase 10/80 to the mid-ventilation phase using the DVF) and manually drawn mid-ventilation contour was increased from an average of 0.49 cm for "good coverage" phases, compared to 0.72 cm and 0.79 for the "poor coverage". This again suggests errors within the DVFs.

The use of the complementary DMA and DIR techniques is useful in the assessment of the dose accumulation. If DMA results are acceptable, no further assessment is required, as the true results can only be equal to, or better than DMA results. However, it has been shown that in some circumstances, apparent problems with the DMA technique are due to the "worst-case" nature of the results, rather than true dosimetric issues, and so DIR methods can be a useful tool to further assess any "problematic" cases.

6.3 Limitations of Baseline Accumulation

The assessment performed of the tracking technique on the baseline imaging is an idealised simulation. It assumes that the target shape changes that may occur throughout the respiratory cycle are consistent over the many cycles that the treatment would be delivered. Any changes in respiratory motion of the tumour would be accounted for by the tracking technique, although small deviations, due to a change in relative position and resulting radiological path length changes, may also occur. As previously discussed, any target shape changes will not be accounted for.

To more thoroughly investigate the effects of these potential changes, repeat 4DCT

PTV	DIR target coverage	DMA target coverage
PTV_{ITV}	92.7%	98.5%
$PTV_{Low\ Accuracy}$	86.5%	96.4%
$PTV_{High\ Accuracy}$	89.3%	98.3%
$PTV_{Perfect}$	87.9%	96.8%

Table 6.2: Patient 2 Target coverage results; Minimum dose to 99% of CTV as a percentage of planned dose using both DIR and DMA accumulation techniques.

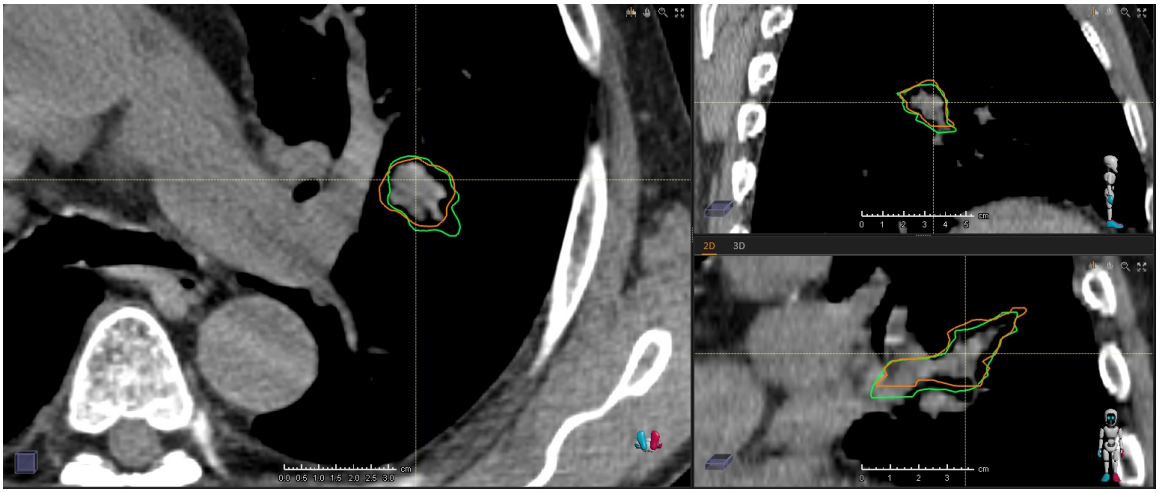

Figure 6.7: Patient 2 GTV contours. DIR contour (green) is produced by using the DVF to warp a manually drawn contour from an alternative phase, to the reference phase, and is compared to GTV manually drawn on the reference phase (orange).

Duty cycle %	Min dose to 99% of CTV (% of planned value)		
	$PTV_{Low\ Accuracy}$	$PTV_{High\ Accuracy}$	$PTV_{Perfect}$
100 %	91.1%	89.7%	87.9%
90%	92.3%	91.6%	89.5%
80%	93.7%	93.6%	90.7%

Table 6.3: Patient 2 - DIR target doses when gating is simulated to restrict dose delivery to phases where small changes in GTV COM are measured. Doses displayed as a percentage of dose at planning. A single scenario simulation (tracking at isocentre, no tracking error included)

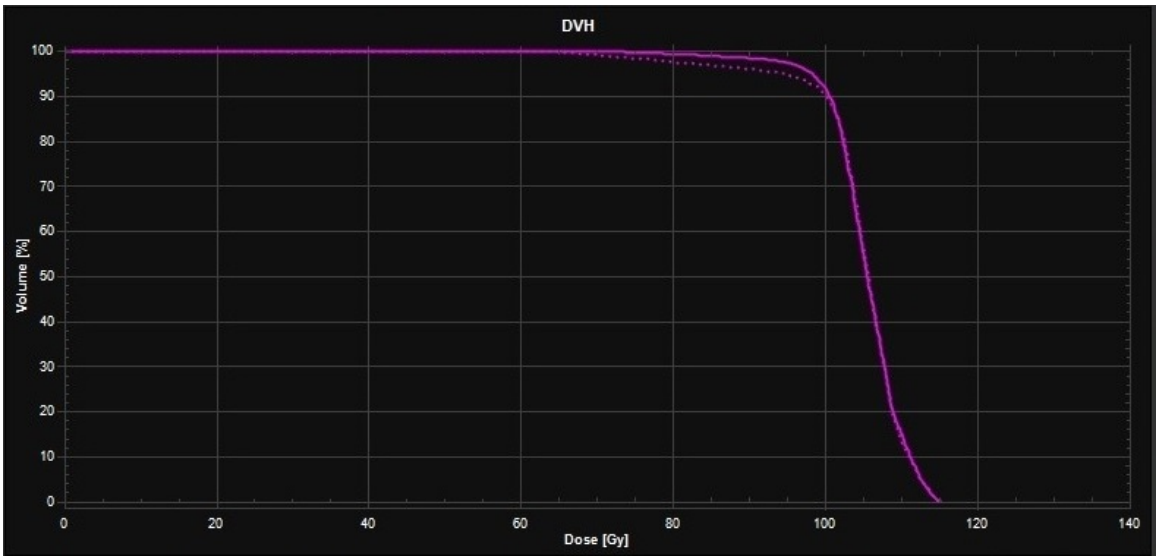

(a) Patient 2 - DVH

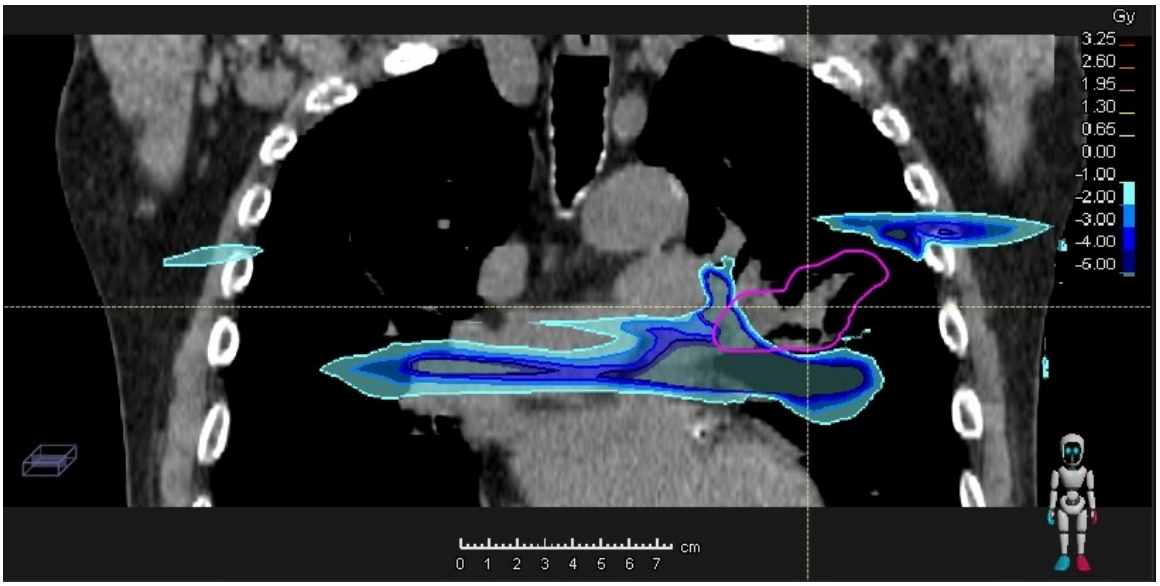

(b) Patient 2 - dose difference map.

Figure 6.8: Patient 2 example of poor target coverage DIR accumulation technique. (a) DVH for planned (solid) and DIR accumulated (dashed) CTV doses. (b) Dose difference map demonstrating the localisation of the region of reduced dose.

images that were available for five patients will be investigated in the following chapter. This will give a more realistic simulation of the treatment that may be delivered at a later time-point than when the planning scan was performed. Even for an MR-linac, where daily planning may be possible, there will still be some time between the planning scan and treatment delivery (for planning, QA etc.), even if it is much reduced compared with conventional radiotherapy techniques, where many weeks between planning and the final treatment delivery can occur.

6.4 Summary

Dose accumulation across the respiratory cycle using both the DIR and DMA methods has been performed. If the "worst-case" DMA results are considered acceptable, no further assessment is required as the "true" results can only be equal to, or better than DMA results. The DIR results may give a more realistic picture of the accumulation in cases where extreme variations in the position of minimum/maximum doses occur, such as patient 9. However, for patient 2, errors in the DIR were found to suggest a reduced target coverage for all plans when compared to the DMA results. Thus it has been found useful to use both accumulation techniques.

The tracking technique simulated will account for target translation, but not rotations or shape change/deformation. For patient 9, shape changes were found to lead to inadequate coverage when considered across the entire respiratory cycle using the "worst-case", DMA methods for the experimental plans. However, using a gating technique with a high duty cycle of 80 or 90% recovered the target coverage to levels similar to the standard ITV approach. The phases that could not receive adequate target coverage using tracking could be identified at planning by comparing the difference in GTV shapes when shifted to align the centres of mass.

When accumulated across the respiratory phase, all ten plans could be delivered

safely, as no excessive OAR tolerance breaches were found beyond those seen for the standard, ITV technique.

Current assessments of the accumulated dose have been performed for the baseline 4DCT. Any changes in the deformation of the target volume between the planning image acquisition and treatment delivery will be investigated through the use of repeat 4DCT data in the following chapter.

Chapter 7

Tracking Based on Repeat Imaging

7.1 Introduction

The MR-linac has the potential to allow daily treatment planning as the patient lies stationary on the treatment couch prior to treatment delivery, minimising any potential anatomical variations. However, daily replanning is time consuming which may limit its usefulness, and may potentially be unnecessary. It took 33 - 44 minutes to plan and deliver the first three- or five-field IMRT daily-planned treatments on the Elekta Unity 1.5 T MR-linac, for spinal metastases [107]. Central lung plans may take substantially longer to plan and deliver due to an increased number of surrounding OARs, and an increase in target motion. This extended time between image acquisition and treatment delivery may result in respiratory changes that may affect the resulting dose distributions. The assessment of doses calculated on repeat imaging will determine whether daily planning is required to ensure adequate target coverage, and safe organ at risk doses.

Changes in the target volume may occur during the treatment course, which may alter the resulting dose distributions. Guckenberger et al. [207] have studied the change in GTV volume during treatment by assessing weekly 3D CT scans for 13

locally advanced NSCLC patients undergoing radiotherapy or radio-chemotherapy. A continuous GTV volume reduction was seen for the majority of patients; when averaged over all patients, a reduction in GTV volume of 1.2% per day was seen. Tumour progression (GTV expansion) was seen in one patient in week one, before the GTV began responding to treatment. The study however concluded that the GTV volume reductions seen did not result in significant changes to the GTV, spinal cord or mean lung doses. The depth of respiration may also change. Often as patients become more accustomed to treatment, they feel more relaxed and their breathing can become slower and deeper.

Previous studies have assessed the reproducibility of repeat CT scans. For example, Moskowitz et al. [208] compared tumour delineations for 32 patients on two CT images acquired within 15 minutes of each other. Patients were removed from the couch and re-setup prior to repeat imaging, and the CT scans were found to be reproducible, so it is likely that only negligible changes would occur in the time between image acquisition and treatment delivery on the MR-linac.

7.2 Methods

The details of 4DCT acquisitions for the baseline and repeat images can be seen in Table 7.1. All delineation of GTVs was performed by an experienced clinician, and all OARs were delineated following a guideline atlas [182]. The 4DCT was not acquired during treatment planning for three patients, and so the number of fractions already delivered when the baseline 4DCT was acquired ranged from 0 to 13. The range of doses that had been delivered at the point of repeat 4DCT acquisition ranged from 8 to 36 Gy. The time/fractions delivered between the baseline and repeat 4DCT ranged from 7 to 22 days/5 to 15 fractions. The five patients were initially selected for use in this study due to the central location of the tumours. The other five patients assessed

in Chapter 5 did not have repeat 4DCT images available for analysis at a later time point. The GTV volumes were compared for the baseline and repeat image sets.

The same methods as described in detail in Chapter 5 were performed on the repeat 4DCT. Briefly, the dose was accumulated across the respiratory cycle using two techniques. Firstly, deformable image registration was used to warp the dose from the repeat 4DCT phases back to the planning phase (mid-ventilation phase on the baseline CT), where the dose was accumulated. The alternative, "worst-case", DMA approach involved calculating the dose on each phase, and taking the calculated metric values, and averaging across the phases and comparing to the planned values.

Any changes in the dose distributions resulting from a change in target shape, or any changes in deformation of the target during respiration due to the later time of image acquisition were investigated. It was hypothesised that an increase in dose deviations compared to baseline accumulation results would be seen for the repeat CT results. The baseline accumulation results include deviations from the planning phase due to respiration only, as each phase assessed was acquired as part of the same 4DCT data set (and at the same time) as the planning phase. Conversely, the repeat image set was acquired 7 - 22 days after the planning phase, and so anatomical as well as respiratory changes may have occurred. Particular attention was given to the OAR doses due to the isotoxic nature of the plans. The experimental plan results were compared to the standard plan results, to determine if any changes seen are

Patient (planned dose/#)	Days between Baseline and Repeat 4DCT	Fraction delivered on day of baseline 4DCT	Fraction delivered on day of repeat 4DCT
3 (2.0 Gy)	15	0	4
4 (1.8 Gy)	7	3	8
6 (2.0 Gy)	22	0	7
8 (2.0 Gy)	7	13	18
10 (2.0 Gy)	18	1	16

Table 7.1: Baseline and repeat 4DCT image details, including dose per fraction of treatment originally delivered to the patient.

likely to be clinically relevant.

7.3 Results

7.3.1 Target Volume Changes

The change in mid-ventilation GTV volume between the baseline and repeat 4DCT imaging can be seen in Table 7.2. The additional therapeutic dose delivered was calculated by multiplying the dose per fraction (1.8 or 2 Gy) by the number of fractions delivered between the baseline and repeat CT imaging. An average decrease in GTV volume of 10.3% was measured between the baseline and repeat images, although there was large variability, with a range of -27.1 to +24.0%. Three patients had a reduction in GTV volume. Patients 4 and 8, who experienced a GTV expansion between baseline and repeat imaging, were the two patients for which the baseline scan was acquired after more than 1 fraction of treatment had been delivered. Patient 8 in particular, had a large increase in GTV volume of 24.0%, with the baseline imaging being acquired on the same day as fraction 13 of treatment was delivered.

Any increase in GTV volume is likely to hinder the target coverage if the treatment plan is not adapted to the new, larger shape. GTV target volume reduction however is expected to result in good target coverage. Both increases and decreases in the target volume may lead to deviations in the dose received by surrounding tissues, as their relative position is likely to change as a result of the GTV volume change.

7.3.2 Accumulation Results

7.3.2.1 Target Coverage Results

The accumulation of doses over the respiratory cycle for the repeat 4DCT imaging can be seen in Table 7.3. Comparisons between baseline and repeat target coverage

Patient	Mid-ventilation (average) GTV volume (cm^3)			Additional therapeutic dose received by repeat CT (Gy)
	Baseline CT	Repeat CT	Difference (%)	
3	10.0 (9.7)	8.3 (8.0)	-1.7 (-17.3%)	8
4	17.2 (17.3)	18.8 (17.3)	1.6 (9.3%)	9
6	47.9 (52.3)	34.9 (30.7)	-13.0 (-27.1%)	14
8	60.4 (62.0)	74.9 (76.1)	14.5 (24.0%)	10
10	179.6 (177.2)	142.2 (137.0)	-37.4 (-20.8%)	30

Table 7.2: Mid-ventilation and average GTV volumes for baseline and repeat CT images.

results are presented in Table 7.4. Patient 8 who had a reasonable increase in GTV volume of 14.5 cm^3 (24%), can be seen to generally have poorer target coverage for each plan assessed using both DMA and DIR accumulation techniques. Patient 4 had consistently good coverage for all PTV plans, ranging from 98.8 ($PTV_{Perfect}$) to 102.2% ($PTV_{Low\ Accuracy}$) for DMA, and was the patient with the smallest change in GTV volume (9.3% reduction).

The absolute doses accumulated over the respiratory cycle for both baseline and repeat CT images can be seen in Table 7.4, with the calculated differences in dose displayed in Table 7.5. For the baseline images, an increase in absolute dose was calculated for each patient and the experimental plan was compared with the standard clinical treatment plan (PTV_{ITV}). However, for the repeat images, two patients had experimental plans that resulted in a reduced absolute dose to the CTV.

The poor target coverage calculated for each PTV for patient 3 was further investigated. There was a period of 15 days between the baseline and repeat imaging, although only 4 fractions of treatment were delivered in this time. A small change in the GTV volume was seen (1.7 cm reduction). However, the relative position of the nodal volume in relation to the primary volume changed from the baseline to the repeat imaging. Whilst the tracking technique (based on the primary GTV centre of mass) resulted in a good alignment of the primary tumour volume, the nodal volumes were not well aligned, as shown in Figure 7.1. Thus, the treatment beam

Patient	Dose Limiting OAR	DIR Accumulation		DMA Accumulation	
		Min dose to 99% CTV (of planned)	DLOAR Dose (of tolerance)	Min dose to 99% CTV (of planned)	DLOAR Dose (of tolerance)
3	Aorta	94.4%	94.5%	93.5%	106.8%
4	Oesophagus	101.9%	102.5%	100.0%	101.3%
6	Heart	98.1%	100.7%	99.6%	99.9%
8	Aorta	97.5%	95.0%	96.5%	105.9%
10	Oesophagus	98.1%	104.0%	95.0%	98.4%
Median		98.1%	100.7%	96.5%	101.3%
Mean		98.0%	99.3%	96.9%	102.6%

(a) Repeat CT PTV_{ITV} results.

Patient	Dose Limiting OAR	DIR Accumulation		DMA Accumulation	
		Min dose to 99% CTV (of planned)	DLOAR Dose (of tolerance)	Min dose to 99% CTV (of planned)	DLOAR Dose (of tolerance)
3	Aorta	92.4%	103.0%	75.7%	105.9%
4	Oesophagus	102.2%	102.8%	100.7%	101.6%
6	Heart	96.4%	100.5%	97.7%	98.5%
8	Aorta	94.1%	101.3%	85.5%	106.9%
10	Oesophagus	93.5%	103.7%	93.8%	96.5%
Median		94.1%	102.8%	93.8%	101.6%
Mean		95.7%	102.3%	90.7%	101.9%

(b) Repeat CT $PTV_{\text{Low Accuracy}}$ results.

Patient	Dose Limiting OAR	DIR Accumulation		DMA Accumulation	
		Min dose to 99% CTV (of planned)	DLOAR Dose (of tolerance)	Min dose to 99% CTV (of planned)	DLOAR Dose (of tolerance)
3	Aorta	86.2%	101.9%	74.6%	104.8%
4	Oesophagus	101.7%	102.8%	100.2%	101.3%
6	Heart	92.0%	100.9%	95.8%	100.5%
8	Aorta	89.7%	100.7%	77.2%	105.4%
10	Oesophagus	88.7%	102.5%	92.8%	97.4%
Median		89.7%	101.9%	92.8%	101.3%
Mean		91.7%	101.7%	88.2%	101.9%

(c) Repeat CT $PTV_{\text{High Accuracy}}$ results.

Patient	Dose Limiting OAR	DIR Accumulation		DMA Accumulation	
		Min dose to 99% CTV (of planned)	DLOAR Dose (of tolerance)	Min dose to 99% CTV (of planned)	DLOAR Dose (of tolerance)
3	Aorta	78.6%	87.3%	68.8%	103.6%
4	Oesophagus	102.0%	100.0%	98.8%	101.9%
6	Heart	90.5%	98.1%	92.1%	101.0%
8	Aorta	88.7%	100.0%	73.6%	104.0%
10	Oesophagus	83.5%	100.0%	90.6%	96.4%
Median		88.7%	100.0%	90.6%	101.9%
Mean		88.7%	97.1%	85.2%	100.7%

(d) Repeat CT PTV_{Perfect} results

Table 7.3: Repeat CT results for DIR and DMA accumulation. Minimum dose to 99% of CTV is shown as a percentage of planning value (on mid-ventilation). Dose Limiting (DL) OAR at planning is listed, with the result this constraint as a percentage of the tolerance (and planning) value. Values exceeding tolerance are highlighted in red.

CT	Number of plans with poor target coverage (Minimum coverage as % of planned)			
	PTV_{ITV}	$PTV_{Low\ Accuracy}$	$PTV_{High\ Accuracy}$	$PTV_{Perfect}$
Baseline (all 10 patients)	0/10 (97.4%)	2/10 (83.0%)	2/10 (84.7%)	5/10 (79.0%)
Baseline (5 repeat patients)	0/5 (97.4%)	1/5 (93.9%)	1/5 (94.0%)	2/5 (90.7%)
Repeat	1/5 (93.5%)	3/5 (75.7%)	3/5 (74.6%)	4/5 (68.8%)

(a) Comparison of baseline and repeat DMA accumulation results. Poor target coverage defined as a minimum dose to 99% of CTV of less than 95% value at planning. The Baseline (5 repeat patients) results are the baseline results but only including the 5 patients used for repeat studies.

Patient	Minimum Absolute Dose to 99% CTV (Gy) for Baseline Accumulation			
	PTV_{ITV}	$PTV_{Low\ Accuracy}$	$PTV_{High\ Accuracy}$	$PTV_{Perfect}$
3	76.0	76.7	76.7	76.4
4	71.5	72.2	75.0	76.2
6	65.6	68.2	68.8	72.3
8	62.4	62.6	65.5	65.3
10	70.7	72.1	74.3	76.1
Median	70.7	72.1	74.3	76.1
Mean	69.2	70.4	72.1	73.3

(b) Minimum absolute dose to 99% of CTV for baseline CT DMA accumulation.

Patient	Minimum Absolute Dose to 99% CTV (Gy) for Repeat Accumulation			
	PTV_{ITV}	$PTV_{Low\ Accuracy}$	$PTV_{High\ Accuracy}$	$PTV_{Perfect}$
3	70.9	58.6	58.0	54.3
4	71.6	73.7	75.6	75.4
6	65.6	68.2	68.8	70.5
8	61.9	57.0	53.8	53.0
10	66.7	67.9	68.8	69.0
Median	66.7	67.9	68.8	69.0
Mean	67.3	65.1	65.0	64.4

(c) Minimum absolute dose to 99% of CTV for repeat CT DMA accumulation.

Table 7.4: Comparison of baseline and repeat accumulated target doses. Values in red are experimental plans which result in a reduced dose compared to the standard technique, PTV_{ITV}.

apertures will be a different shape to the composite target volume, and so will be unable to deliver adequate dose to the entire target volume. This is further depicted by Figure 7.2, which highlights the dose distribution calculated for a single phase, and the nodal regions not covered by the high dose region. The target coverage for cases involving differential primary and nodal motion could potentially be improved by producing plans for, and performing tracking of, the primary and nodal volumes separately.

Similarly for patient 8, poor alignment of the lymph nodes can also been seen when tracking to align the primary tumour is used, as shown in Figure 7.3. A reasonable increase in GTV (14.5 cm^3) is also likely to impact the target coverage. The effect of the increased GTV/change in relative position of the nodal region was minimised for the standard ITV technique as the target volume is created by encompassing any respiratory motion, and hence is larger than the single GTV target volumes, which may mitigate some of the effect of the GTV volume expansion. The experimental techniques use smaller PTV margins and a tracking technique to account for respiratory motion. The tracking approach, based only on 3D translations, will not be able to provide adequate coverage when large GTV expansion is seen, and so replanning may be required to ensure adequate target coverage.

Several studies have investigated the differential motion of the primary tumour and lymph nodes [155, 209, 210]. Respiration was found to cause motion of lymph nodes, which often was not correlated with primary tumour motion. This clearly demonstrates one limitation of a tracking technique aiming to track target volumes comprising primary tumour volumes and separate lymph node volumes using a single translation based on the primary GTV centre of mass (or a single implanted fiducial).

Although changes in the differential motions between primary and nodal target volumes for baseline and repeat imaging were observed, the maximum 3D motion across all phases were very similar; 0.58 and 0.59 cm respectively for patient 8, sug-

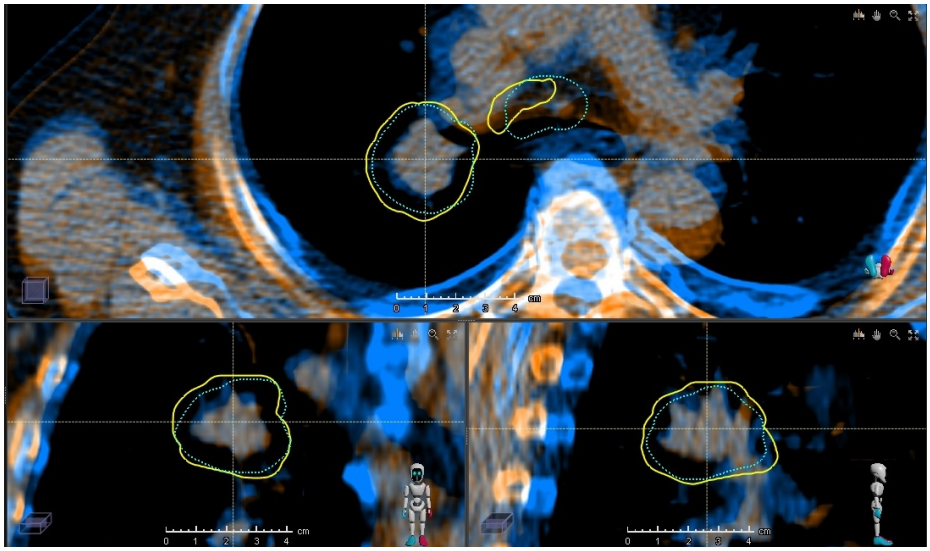

(a) Patient 3, localised to primary CTV.

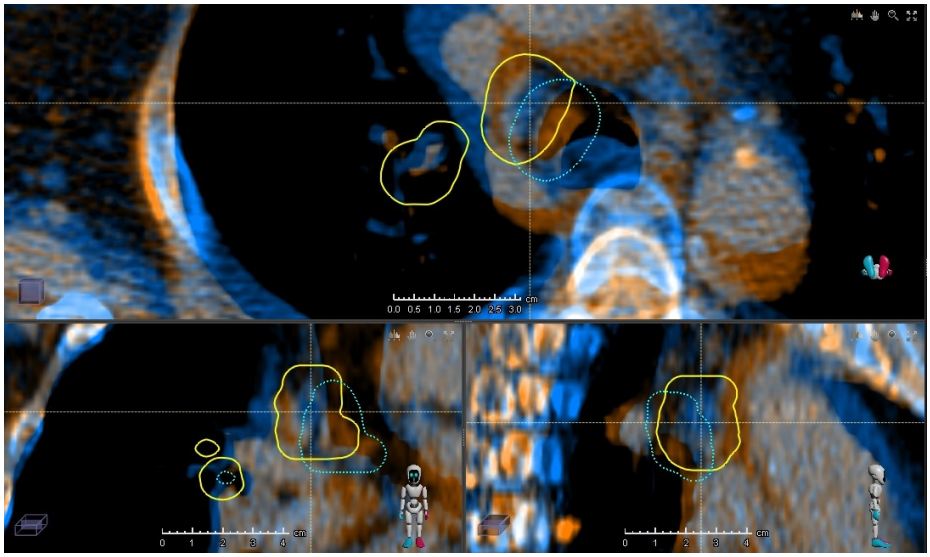

(b) Patient 3, localised to nodal CTV.

Figure 7.1: Different slices of images, showing comparison of planning (baseline) CTV volumes (yellow) and repeat CTV volumes (cyan) for Patient 3. (a) Good alignment of primary CTVs displayed when localised to primary GTV (b) Poor alignment of nodal CTVs displayed when localised to the nodal GTV. Tracking has been performed to align primary tumour. The two phases are shown overlaid in blue (baseline) and orange(repeat).

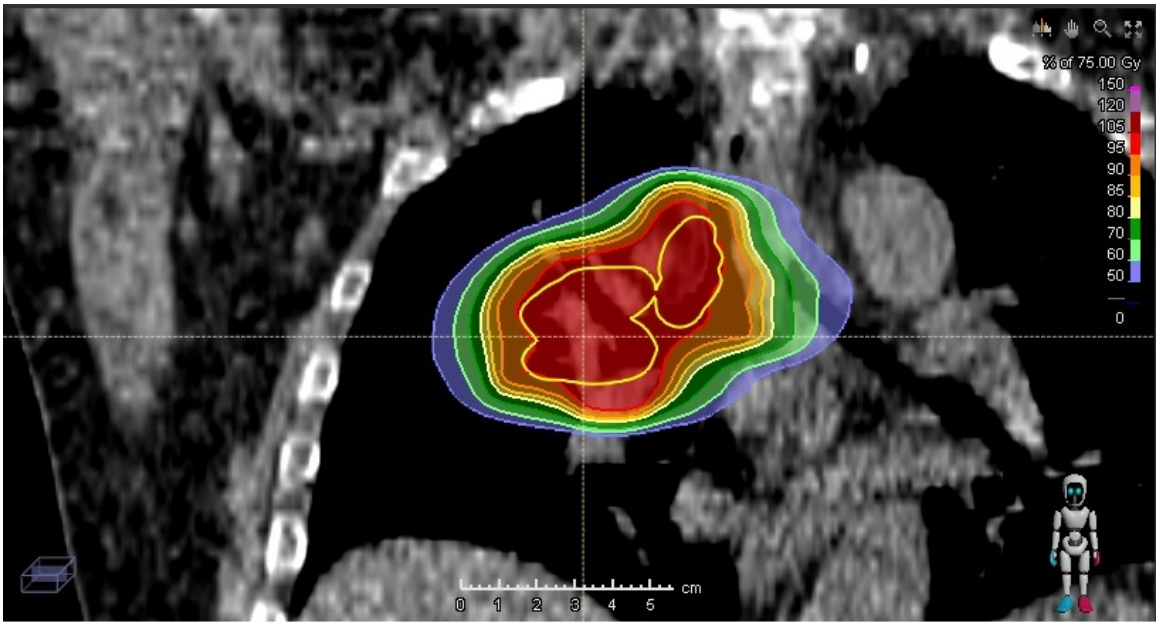

(a) Planned (baseline) dose distribution. CTV in yellow.

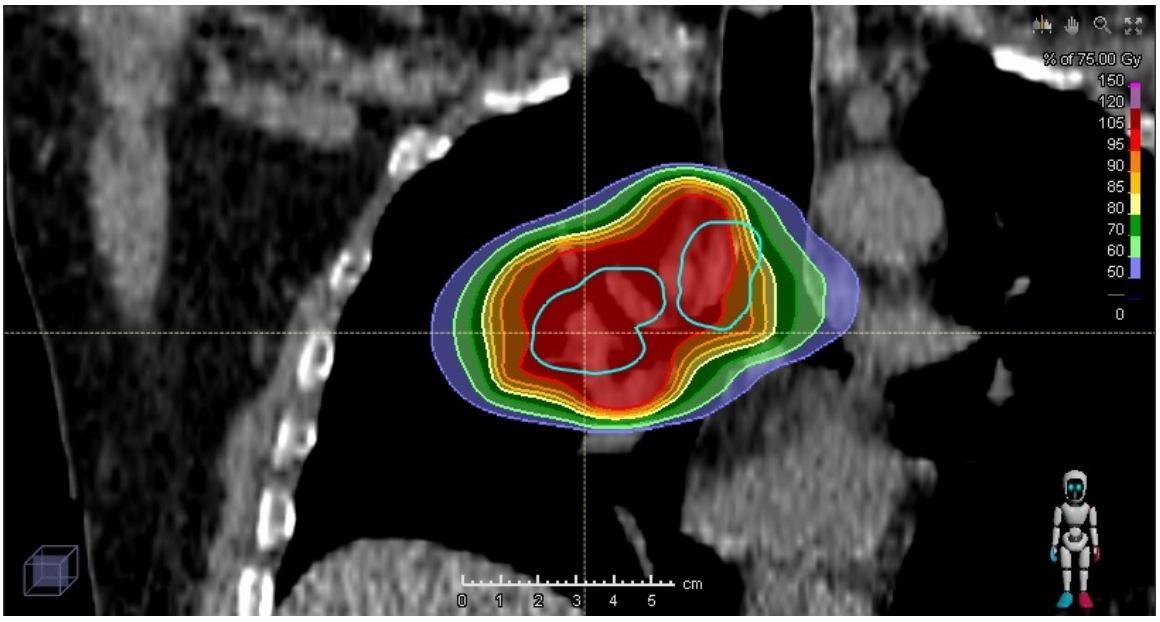

(b) Calculated dose disribution for a single phase on repeat imaging. Repeat CTV in cyan.

Figure 7.2: Patient 3. Dose distributions showing lack of nodal coverage. Planned (baseline) CTV in yellow, repeat CTV in cyan dash.

gesting that it is not the main driver of the poorer repeat target coverage results.

A larger average reduction of absolute dose was measured for experimental PTVs (5.3 - 8.8 Gy) compared to the standard technique (1.9 Gy). Patients 4 and 6 had minimal difference between doses accumulated on the baseline and repeat images across all PTVs, with a maximum reduction of 1.5 Gy.

7.3.2.2 OAR Accumulation Results

The number of plans having dose-limiting OARs breaching planning tolerance, as well as the level of tolerance breach, increased for the repeat accumulation results compared to baseline, can be seen in Table 7.6. However, as was seen for the baseline CT accumulation results, similar levels of tolerance breaches for both the standard PTV_{ITV} approach (6.8%) and experimental PTVs (4.0- 6.9%) were seen. This suggests that the tolerance breaches are not clinically significant, even when reaching ≈107% of tolerance, as these deviations in dose will be occurring during current clinical practice, which is known to result in acceptable toxicity levels.

The accumulated doses to surrounding structures were calculated and compared to planning dose tolerances used at planning. For baseline results, the structures breaching tolerance were only those that were dose limiting OARs and so at tolerance, at planning. For the repeat image set, additional non-dose limiting OARs also breached tolerance, and larger deviations were calculated, as shown in Table 7.7.

Patient	Change in Minimum Absolute Dose to 99% CTV (Gy)			
	PTV_{ITV}	$PTV_{Low\ Accuracy}$	$PTV_{High\ Accuracy}$	$PTV_{Perfect}$
3	-5.1	-18.1	-18.7	-22.1
4	0.1	1.5	0.6	-0.8
6	0.0	0.0	0.0	-1.8
8	-0.5	-5.6	-11.7	-12.3
10	-4.0	-4.2	-5.5	-7.1

Table 7.5: Change in minimum absolute dose to 99% of CTV from baseline to repeat CT DMA accumulation. Negative values indicate an decrease in absolute dose compared to baseline accumulation results.

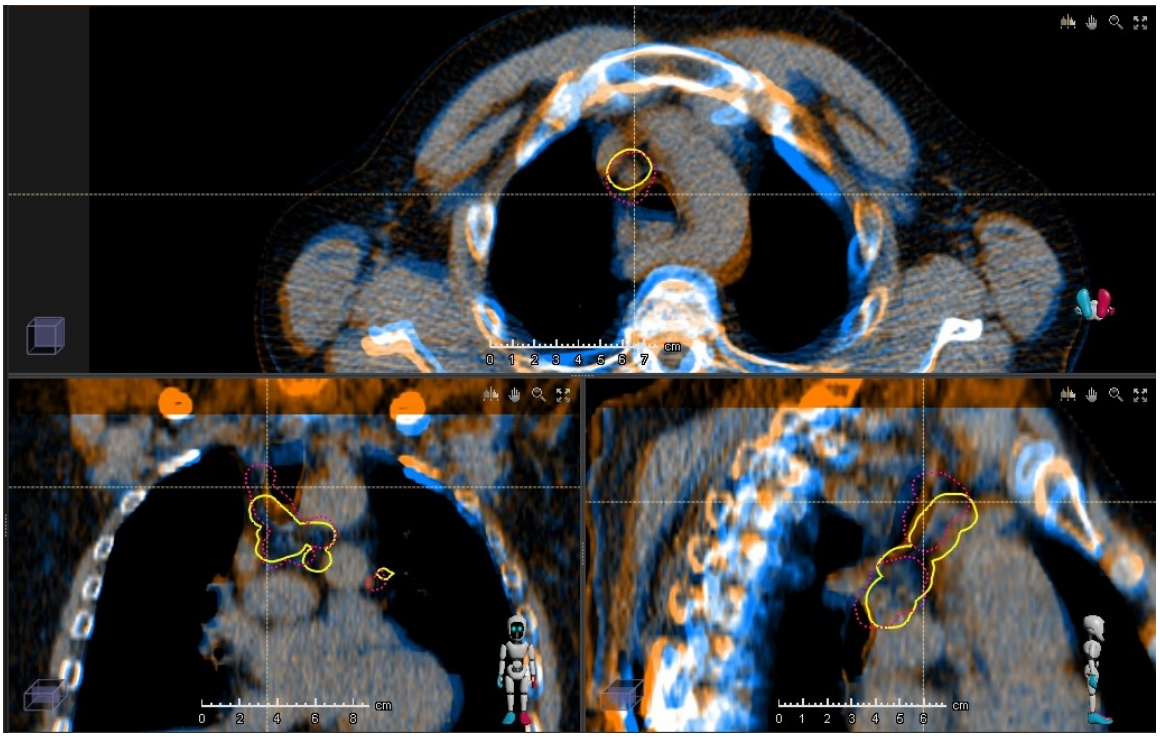

Figure 7.3: Patient 8 comparison of planning (baseline) GTV volumes and repeat GTV volumes. The lymph nodes are delineated in yellow (baseline) and pink (repeat). Tracking has been performed to align primary tumour. The two phases are shown overlaid; baseline (blue) and repeat (orange).

CT	Number of plans with DLOAR breaching tolerance. (Largest breach as % of tolerance.)			
	PTV_{ITV}	$PTV_{Low\ Accuracy}$	$PTV_{High\ Accuracy}$	$PTV_{Perfect}$
Baseline (all 10 patients)	5/10 (100.8%)	3/10 (100.5%)	3/10 (100.7%)	3/10 (100.5%)
Baseline (5 repeat patients)	2/5 (100.3%)	1/5 (100.5%)	1/5 (100.1%)	2/5 (100.3%)
Repeat	3/5 (106.8%)	3/5 (106.9%)	4/5 (105.4%)	4/5 (104.0%)

Table 7.6: DMA accumulation results for the dose limiting organs at risk for baseline and repeat CTs. The Baseline results are listed twice, including all patients, or a subgroup of the five patients investigated with the repeat imaging. Value in red highlights the experimental DLOAR that exceeds tolerance breach measured for standard PTV_{ITV} technique.

However, dose tolerance violations calculated for the standard technique, PTV_{ITV} had very similar levels of tolerance breaches compared to the experimental PTVs, suggesting that the tolerance violations may not be clinically significant, as the dose limits used at planning have been shown to be exceeded over the course of standard treatments to a similar degree to the new, experimental treatment technique.

7.4 Conclusion

This chapter investigates the delivery of plans produced on a single phase on the baseline 4DCT scan, delivered to a repeat scan, including any effects of respiration. As expected, larger dose deviations from planning values were measured for the repeat simulation compared to the baseline simulation of treatment delivery. For some patients, the resulting adequate target coverage and OAR doses show that the use of daily replanning would have been unnecessary. The repeat accumulation results are also directly relevant to tracking techniques performed using implanted fiducial markers.

Two of the five patients had poor target coverage when assessing the DMA (worst-case) results. Patient 8 had a reasonable GTV volume increase of 24%, suggesting that a tracking technique with small margins will be unable to provide adequate target coverage. Patient 3 repeat imaging demonstrated that tracking based on the primary tumour centre of mass does not always provide adequate coverage of nodal target volumes, when the relative position of the primary and lymph nodes change throughout the treatment course.

For both patients 3 and 8, replanning prior to treatment will be required to ensure good target coverage when using tight PTV margins. The increase in GTV volume, and change in relative position of the primary and lymph nodes could be assessed during image-guidance prior to treatment delivery on the MR-linac, or alternatively

PTV	Number of OARs exceeding tolerance	Max. tolerance breach (% of tolerance) (OAR)	Max. tolerance breach (Gy)
PTV_{ITV}	5 (4)	104.0% (Oesophagus)	2.7
$PTV_{Low\ Accuracy}$	6 (4)	103.7% (Oesophagus)	2.5
$PTV_{High\ Accuracy}$	9 (4)	103.2% (102.8%) (Vena Cava) (Oesophagus)	2.4 (1.9)
$PTV_{Perfect}$	11 (4)	103.7% (102.9%) (Vena Cava) (Oesophagus)	2.8 (2.0)

Table 7.7: OARs that exceed planning tolerances when accumulated across the respiratory cycle on the repeat CT image set, for all OARs and all patients, using DIR accumulation. Results limited to dose limiting OAR shown in blue, when different to all OAR results.

using conventional cone-beam imaging and fiducial markers placed in/near the lymph nodes. This would ensure treatment fractions that may result in sub-optimal target coverage will not unknowingly be delivered to patients.

The deviation in target coverage seen for the standard ITV technique was reduced compared with the experimental PTVs investigated. The standard ITV approach is designed to ensure target coverage at all points throughout the respiratory cycle by enveloping the target position in every phase. An unintended consequence of this is the larger planning target volume potentially covering some of the GTV volume expansion or variation in lymph node position. Conversely, the experimental PTVs with reduced margins based on a single phase GTV will not be able to result in adequate coverage, unless the beam apertures are increased for the larger GTV.

An increase in the number of OARs breaching planning tolerances was calculated for the simulation of repeat imaging. However, this is not expected to be clinically relevant, as the magnitude of tolerance violations was similar to the standard ITV simulations. This reinforces the fact that the OAR dose tolerances are planning tolerances, and not accumulated treatment tolerances, as these violations are occurring currently during standard treatments, resulting in acceptable levels of toxicity.

The simulated treatments suggest that the reduced margins used for the experimental PTVs with a tracking technique based on 3D translations, results in a mean minimum tumour dose decrease compared to the standard technique at baseline, and compared to themselves at baseline when the treatment is delivered 7-22 days after planning. Some patients may experience significant target expansion, or a change in the relative position of primary and lymph nodes, which may require replanning to ensure adequate target coverage. However, for three of the five patients, an increase in absolute dose for the experimental plans was measured compared to the standard approach for the repeat image analysis. Whilst the coverage can be reduced compared to their baseline results, this shows that if treatment on "old" treatment plans is required, for some patients it is better to deliver a dose-escalated tracked treatment with reduced margins rather than a standard ITV treatment. For optimal treatment however, up-to-date imaging should be used to re-plan the treatment.

Planning tolerance violations of surrounding critical structures may occur using this tracking technique, although in a similar number of cases and magnitude to that which was seen for the standard clinical ITV technique. Thus, the planning tolerance violations are not considered clinically important, and it is expected that the simulated treatments based on a theoretical margin reduction, with a simple tracking technique could be safely delivered to patients.

Ultimately, the data shows that using reduced margins and a tracking technique is acceptable in terms of normal tissue tolerances, but notably worsens tumour coverage compared to using the standard technique, or up-to-date plans.

It would be useful to also perform the dose accumulation on a repeat data set that was acquired much closer to baseline, ideally with a few minutes to an hour between image acquisitions. This would allow the tracking technique (including any deviations in respiration that may occur) to be fully tested for a daily-planned scenario. Unfortunately, these data were not available during this study.

Chapter 8

Conclusions

Central lung tumours are notoriously difficult to treat with conventional or high dose per fraction radiotherapy regimens due to abutting and overlapping radio-sensitive organs at risk. This thesis has explored the level of isotoxic dose escalation that is possible for central lung tumours using new techniques now technically feasible on the MR-linac. The patients analysed were selected based on the central position, and large respiratory motion, of the primary tumour. Ten locally advanced, non-small cell lung cancer patients were analysed, five of which had repeat imaging data available. Ten early stage patients were also assessed for the potential of dose escalation.

In-silico modelling of a tracking technique based on the primary tumour centroid has been performed, and the resulting dose distributions assessed for both target coverage and dose to surrounding critical structures. The effect of predicted margin reductions when delivered throughout the respiratory cycle has been investigated using dose accumulation, to fully quantify the level of gains that real-time tracked lung radiotherapy on MR-linacs may provide.

Three experimental CTV to PTV margins were investigated; an idealised "perfect" scenario where no errors are considered (CTV=PTV), and a "low accuracy" (5 mm) and "high accuracy" margin (2 mm). The margins were calculated by assessing the

uncertainties in the planning and treatment delivery of a tracked technique on the MR-linac.

A significant reduction in the PTV volume increased the separation between the target volume and surrounding organs at risk. This enabled a statistically significant isotoxic dose escalation of 3.2 - 12.4 Gy for the locally advanced patients, when planned on the mid-ventilation 4DCT phase, compared to the standard clinical ITV approach. This resulted in an improvement in the therapeutic ratio of treatments by increasing the dose to the target volume whilst maintaining clinically acceptable doses to the OARs. The varying PTVs investigated resulted in a predicted mean increase in two year disease-free survival of 6.8, 11.8 and 15.2% compared to the standard technique, implying that the dose escalation achieved may be clinically meaningful. For the early-stage NSCLC patients, an increase in mean prescribed dose of 4.0 - 10.1 Gy led to a predicted mean increase in BED_{10} of 9.3 - 30.8 Gy^{-1}, resulting in an increase from 30% (ITV) to 50/70/80% of patients receiving a BED_{10} of at least 100 Gy^{-1} for experimental PTVs. The patients who would benefit most from this technique are easily identifiable at planning, enabling efficient patient selection for clinical departments with limited resources.

When locally-advanced dose-escalated plans were accumulated over the baseline (planning) respiratory cycle, only small tolerance breaches of up to 0.5 Gy occurred. These deviations were located in the isotoxic dose-limiting structures, and generally in areas of overlap between PTV and OAR, and so are predictable at planning. When comparing to the standard ITV approach, similar levels and frequency of dose tolerance violations were calculated, indicating that the small tolerance breaches are not clinically important. Whilst a reduction in the target coverage as compared to planned was observed for the experimental PTVs, the possible isotoxic dose escalation resulted in an increase in absolute dose to the target compared to the standard ITV approach.

The tracking technique studied accounts for primary target motion, but not rotation or deformation. One patient was found to have poor target coverage when accumulated on the baseline image, attributed to large target volume deformations during respiration, which again was predictable at planning. A gating technique with a high duty cycle of 80 or 90% was found to result in adequate target coverage.

Repeat imaging was also investigated to provide an insight into the resulting variations in dose due to changes in anatomy and/or target rotations/deformations that may occur due to the time between treatment planning and delivery. The simulated treatments show a notable reduction in the mean minimum dose to target for the experimental PTVs compared to at baseline, when the treatment is delivered 7-22 days after planning. This highlights the need for replanning to be performed on up-to-date imaging, rather than continued use of the baseline plan, to ensure optimal target coverage. However, two patients did still receive a higher target absolute dose using the baseline experimental plan when delivered 7 - 22 days after planning image acquisition, than the standard ITV technique using up-to-date imaging. Planning tolerance violations of surrounding critical structures occur for some patients when delivering plans produced on previous images, although in a similar number of cases, and to a similar magnitude than seen for the standard clinical ITV technique. Thus, the planning tolerance violations are not clinically important, and it is expected that the simulated treatments based on a theoretical margin reduction, with a simple tracking technique could be safely delivered to patients.

The use of both DMA and DIR accumulation techniques was found to provide complementary data for the assessment of resulting dose distributions. Practically, if the "worst-case" DMA results are considered acceptable, no further assessment is required as the "true" results can only be equal to, or better than DMA results when assessing maximum or minimum doses. The DIR results may give a more realistic picture of the accumulation in cases where extreme variations in the position

of minimum/maximum doses occur, as seen in a single patient.

The doses received when delivered on the MR-linac using daily on-treatment imaging and replanning are likely to lie somewhere between those calculated for the baseline and repeat simulations. Daily planning on the MR-linac would minimise the effects of any anatomical changes, but changes in deformation due to variations in respiration during the treatment compared to those during the planning scan may still occur. The results of the in-silico modelling performed are directly relevant to tracking treatments based on an implanted fiducial marker, the known motion of which can act as a surrogate for tumour motion.

No other literature is known that explores the isotoxic dose escalation possible for central lung tumours using a tracking technique, which includes accumulated dose over baseline and repeat 4DCT images to incorporate respiratory motion. Current literature is generally limited to tumour doses, often for SABR treatments, whereas this study includes the investigation of tumour and surrounding critical structure doses for locally-advanced NSCLC cases.

Real-time tracking performed on the MR-linac has been shown to be feasible [211, 212], and advantageous compared to tracking based on surrogates, which is limited by the correlation between surrogate and tumour motion, which may change during treatment [213]. Other authors have investigated the use of dose accumulation methods over the respiratory cycle for lung radiotherapy, particular in work aimed to confirm the suitability of the ITV approach throughout respiration [199, 214, 215]. The use of an ITV technique was found to result in only small differences in GTV and the limited OARs assessed: mean lung dose/ipsilateral lung dose, which are confirmed in this thesis for the standard ITV technique. This thesis also includes the assessment of all OARs considered critical structures during planning.

Lung radiotherapy dose escalation achievable on the MR-linac has been investigated by Bainbridge et al. [148]. The dosimetric consequences of creating a daily plan

for ten (non-location specific) locally-advanced NSCLC patients were explored using reduced margins to account for the predicted increase in delineation accuracy and the removal of the inter-fractional uncertainties (by planning each fraction), using an MR-linac specific beam. A small increase in the mean maximum CTV dose of 2.2 Gy was calculated for MR-linac reduced margin plans compared to those for a conventional linac. A similar maximum dose to target was calculated (93.6 Gy) compared to that in this thesis (90.0 Gy), although generally higher doses were calculated by Bainbridge et al., attributed to the patient selection not being limited to those with central tumours which are known to have closer dose-limiting critical structures. No tracking was considered or assessment of the dose accumulated over the respiratory cycle was performed by Bainbridge et al.

Treatment of central lung tumours using SABR has recently been well explored and documented [191–193], including the potential for adaptive hypofractionated SABR being potentially deliverable on the MR-linac [59]. A current clinical trial (SUNSET) is also investigating optimal dose escalation for "ultra-central" lung tumours for early-stage NSCLC [194].

Al-Ward et al. [201] have performed analysis of a similar, if more simplistic simulation of a tracking technique for five SABR patients, using the MR-linac. The reduction in OAR dose when accumulated across the respiratory cycle for tracked, IMRT plans was found to depend upon; tumour motion, relative OAR motion and the proximity of OAR's to the target. The assumption of a constant breathing pattern and no tracking uncertainties limited the usefulness of this study. The reduction in OAR dose resulting from the tracking technique is analogous to the dose escalation calculated in this thesis, which was also found to be dependant upon the proximity of the OAR to the target - specifically the degree of overlap between them. Ehrbar et al. [202] compared several different tracking techniques for VMAT plans, based on a prototype of a couch tracking system for SABR. Tracking uncertainties were

included in this study as an extension of a "multi-phase tracking" approach. Target coverage for twenty patients, selected based on tumour motion exceeding 5 mm was assessed, but OAR doses were limited to the investigation of lung doses. The "single phase" (no tracking uncertainties) accumulation resulted in reduced target coverage, and the reduced target volume led to reduced lung dose. However, target coverage was improved using the "multi-phase" method, which included tracking uncertainties, although this did limit the dose reduction to the lungs.

8.1 Limitations of Study

8.1.1 Dose Calculation

All dose calculations in this thesis were performed in RayStation 7 (RaySearch Laboratories AB, Stockholm, Sweden). RayStation is commonly used in clinical radiotherapy treatments, and both the dose calculation and deformable image registration have been previously validated. However, there are some known limitations to the accuracy of the image registration algorithms and dose calculations [216].

RayStation currently has no feasible way to include MR-linac specific factors relating to the dose calculation. A standard, conventional beam model was used for planning, based on an Elekta Agility 6 MV beam, as provided by RaySearch Laboratories. The limited field size currently available on the MR-linac would not be an issue, as the largest beam aperture was found to be 16.5 cm (for a standard plan), and the lack of lateral shifts in couch position should not be problematic for this patient cohort, as patients were selected based on the central position of the primary tumours. Careful patient set-up would however be required if delivering a plan produced on previous imaging.

The tracking simulations and dose accumulations performed are directly relevant to tracking based on implanted fiducial markers, as treatments can be given on con-

ventional linacs as modelled in RayStation. However, for MR-linac treatments, several MR-linac specific planning considerations were unable to be included. The integration of the MR machinery and conventional linac required some changes to the beam configuration, such as a slight increase in energy, an increase in source to surface distance and multi-leaf collimator leaf width at isocentre as discussed in Chapter 2. These are not expected to have any significant impact on the results of the study. Kalwa et al. [217] studied the difference in plans for oesophagus radiotherapy treatment plans for VMAT plans on a conventional linac and nine-field IMRT plans on an MR-linac. Both plans were able to achieve pre-defined criteria for target volume and organs at risk. Some small differences were calculated for mean doses, which can be attributed to the difference in plan delivery (IMRT rather than VMAT). A lung study comparing nine-field IMRT plans on a conventional linac, with those on an MR-linac resulted in no significant differences when the changes in beam configuration were included [148], and so the results in this thesis are expected to hold for MR-linac plans. It is possible that electron return effects due to delivery of the treatment field in the MR-linac's magnetic field, which are important at interfaces, could change due to variations in the interface positions, if replanning is not performed. However, the interfaces will still be present and so resulting changes are expected to be limited. The effect of tracking treatments delivered on an MR-linac, including the effect of the orthogonal magnetic field of 1.5 T has been briefly investigated by Al-Ward et al. [201], who concluded that there were no discernable deviations in DVH data.

8.1.2 Plan Type

The plans investigated in this thesis were volumetric modulated arc therapy (VMAT) plans, which involves the continuous delivery of radiation whilst the treatment machine rotates around the patient. VMAT plans are known to be more conformal than IMRT/conventional plans, allowing improved target coverage and organ and risk spar-

ing [218]. In this study, the use of VMAT allowed high isotoxic prescribed doses to be used. Current MR-linac treatments are limited to IMRT, but it is expected in the near-future that VMAT will be available. Similar levels of dose escalation were achieved for a cohort of patients when assessing IMRT and VMAT plans, showing the benefit remains for the use of IMRT rather than VMAT plans.

8.1.3 Image Artefacts

Four-dimensional imaging aims to produce a range of 3D images across the respiratory cycle that accurately demonstrate the range of motion of structures. As the 3D images are acquired over a sub-section of the breathing cycle (often 10%, with 10 phases covering the whole cycle), less motion is included compared to an "average" or conventional 3D image which is acquired over the full respiratory cycle. This results in a reduction in blurring of structures often seen in conventional 3D images, which may allow more accurate dose calculations.

However, image artefacts can still be present in the 3D phase image sets as some motion will still be occurring during the shorter phases. Also, any inaccuracies in the binning process, which may result from an irregular breathing pattern may cause artefacts due to reconstruction errors.

An example of image artefacts can be seen in Figure 8.1 for patient 9. An obvious motion artefact at the lung-diaphragm interface can be seen for phase 20 which is unrealistically flat, but not phase 0.

The artefacts commonly seen in 4D image sets do need to be considered during planning, as they may alter the resulting dose distributions. However, this is a limitation for any techniques where the planning is performed on 4D images, and not unique to this technique.

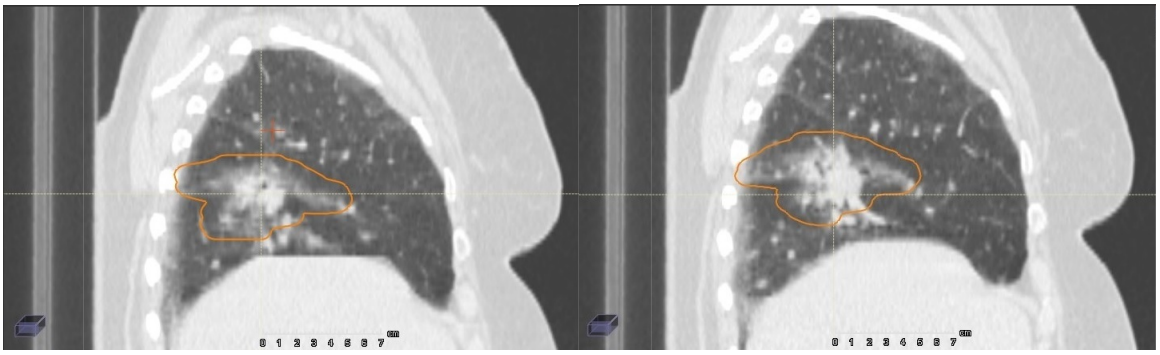

(a) (b)

Figure 8.1: LA-NSCLC - Patient 9. Motion artefact at lung/diaphragm interface seen in (a), phase 20, but not (b), phase 0.

8.1.4 Image Type

The images used were 4DCT images, and no MR images were assessed due to lack of availability. Electron density information that is intrinsic to CT images is used in radiotherapy treatment planning for dose calculation. MR-linacs will require electron density values for planning, whether they be from previous patient-specific imaging, or by creating synthetic CTs by applying electron densities to certain tissue types. This has been investigated by other authors, for the particular case of lung plan adaptation on the MR-linac [219].

MR images are known to have superior image contrast compared to CT, but suffer from distortion etc., as discussed in Chapter 2. The impact of the resulting differences in tumour and organ delineation are expected to be negligible, and is currently being investigated in a clinical trial based at The Christie [139].

8.1.5 Image Acquisition Time Points

The use of baseline images to assess the accumulated doses, whilst slightly optimistic, give an indication of the resulting dose distributions considered across the respiratory cycle for daily plan adaption. The repeat images highlight the changes in delivered doses when plan adaption is not used, and plans based on images that are 7-22 days

old are delivered. This was used to assess whether plan adaption is required when using tight margins and a tracking technique on an MR-linac.

To accurately model daily-adapted treatments on the MR-linacs, image acquisition would ideally more closely follow the expected treatment protocol. Specifically, the time between baseline and repeat image acquisition would be reduced from 7-22 days, to around 30 to 90 minutes, with patients remaining stationary on the treatment couch throughout. These data were unavailable during this study, and so the MR-linac results are expected to lie between baseline and repeat results, but closer to baseline as anatomy changes will be minimised, but some small changes in target deformation may occur due to respiration variations in the time between treatment planning and delivery. While the tracking technique will account for tumour motion, the relative position of surrounding structures (and nodal volumes), as well as target deformations are likely to change.

8.2 Further Work

It was hoped during the project that 4D MR images would be used to simulate an MR-tracking technique on an MR-linac. Unfortunately, these images were not available, and so in time, further work could be performed to confirm the results of this thesis that were based on CT images.

Prior to treating patients clinically with a new treatment technique, a feasibility study and clinical trial will be required to ensure the safety of the technique, and to help determine if the predicted benefits are realised.

The simulation of tracked, VMAT plan delivery on an MR-linac poses a few challenges, that were beyond the scope of this project, but would require investigation prior to clinical use. The combination of tracking and VMAT delivery is particularly difficult when considering intra-fractional motion, and the synchronisation of varying

gantry angle, multi-leaf collimator motion and dose-rate that is performed during VMAT delivery. Three dimensional tracking has been simulated in this study, which includes tracking of "depth", which will be practically difficult to implement. Further work to assess the usefulness of tracking in two dimensions, which can be performed with MLC motion could be investigated.

Large GTV deformations were seen during the respiratory cycle for one patient during baseline dose accumulation, which resulted in a reduced target coverage when accumulated across the entire respiratory cycle. Whilst target coverage was recovered through the use of gating to remove the one/two respiratory phases when large deformations occurred, it may be worth assessing whether use of an alternative target volume for planning may mitigate this problem. For example, as described by Ehrbar et al. [202], the use of a "multi-phase" GTV may be beneficial for some patients. This involves aligning the GTVs (as per tracking technique), then obtaining the sum of the volumes. This is similar to the ITV approach, except the motion is mitigated by the tracking technique. Larger PTVs would result from this more conservative approach, thus reducing the potential for isotoxic dose escalation, but the results may be less affected by deformations.

In the assessment of the repeat images, when tight PTV margins were used one patient was found to suffer with poor target coverage as a result of differential motion of the primary and nodal target volumes. Further work is required to determine whether having two separate plans, allowing tracking of the primary and nodal volumes separately could enable more optimal target coverage. Alternatively, a larger target volume expansion on the nodal volume could be assessed to determine if it would help ensure nodal coverage throughout the respiratory cycle.

Even with recent improvements in MR imaging techniques, 4D image acquisition still takes a minimum of five minutes to acquire [220]. Delineation, treatment planning and plan quality assurance will take further time, further increasing the time between

image acquisition and treatment delivery. When available, the use of repeat imaging data sets acquired 30-90 minutes after baseline would confirm the assumption that daily adapted treatment delivery would provide similar resulting dose distributions to the baseline results analysed in this thesis.

Alternative software that can accurately model the MR-linac treatments, associated magnetic field effects and MR imaging (currently unavailable during this work) could be used to confirm that the findings of this thesis are applicable for MR-linac treatments. Further work is also required to determine whether VMAT treatment delivery is technically feasibly on the MR-linacs, due to current limitations in couch movements, field size, MLC motion etc.

8.2.1 Summary of Further Work

This thesis investigates the potential for isotoxic dose escalation. However, prior to clinical use, further work is required to confirm the findings remain valid when performed on an MR-linac, including the use of MR images and practical constraints due to treatment delivery limitations.

8.3 Summary

For the patient cohort investigated, the use of reduced target margins based on a tracking technique on the MR-linac was found to enable significant isotoxic dose escalation. This resulted in a mean increase in estimated two year disease-free survival of 4.3 - 14.0% compared to the standard ITV approach, depending on the margins used. Clinically acceptable levels of treatment toxicity are expected to be maintained as organ at risk doses were constrained to clinically used tolerances.

When accumulated over the respiratory cycle, an increase in absolute dose was measured for experimental plans compared to standard ITV plans. Small organ at risk

dose tolerance violations occurred, but for the patients analysed, were not clinically significant. Therefore, safe delivery of isotoxically dose escalated radiotherapy plans on an MR-linac can result in increased target dose.

Analysis of repeat imaging acquired 7 - 22 days after baseline imaging has shown that the majority of patients will require replanning during their treatment to ensure optimal target coverage is achieved. For two of the five patients, the delivery of an "old" experimental plan can result in higher target doses than those obtained using standard ITV techniques on an up-to-date image.

In-silico modelling predicts that tracked delivery of isotoxically dose escalated plans will result in a clinically meaningful increase in two-year disease-free survival for central locally-advanced NSCLC, while respecting current normal tissue dose-limits even allowing for movement effects.

Appendix 1.
Calculation of the fraction of errors within an annulus

To assess the suitability of the proposed margins, the predicted error scenarios were simulated during the simulation of treatment delivery. A tracking error of 0 was simulated by translating the relative position of the treatment beams, to ensure they were aligned with the target volume centre of mass. To simulate the error scenarios, further translations in each direction were applied. Thus to calculate the dose whilst considering the errors, each error scenario was weighted during the summation based on the probability of the error scenario occurring.

Tracking errors were assessed at 0, σ and 2σ relative to an origin of the translation required for tracking based on aligning the primary GTV centroids of each phase. For σ and 2σ, the results were averaged across the six dimensions, as depicted in Figure 1. This section describes the calculation of the weightings for each component of the error.

The origin results were assumed to typify results in a shell from 0 to $\frac{1}{2}$ σ; the 1σ results as typifying results in a shell from $\frac{1}{2}$ to $\frac{3}{2}$ σ; and the 2σ results as typifying results from $\frac{3}{2}$ σ outwards.

The σ_{3D} used is a 3D uncertainty, taken from the literature [141].

σ is the one standard deviation uncertainty on position in x, y or z directions considered alone. The total uncertainty in 3D is $\sigma\sqrt{3}$.

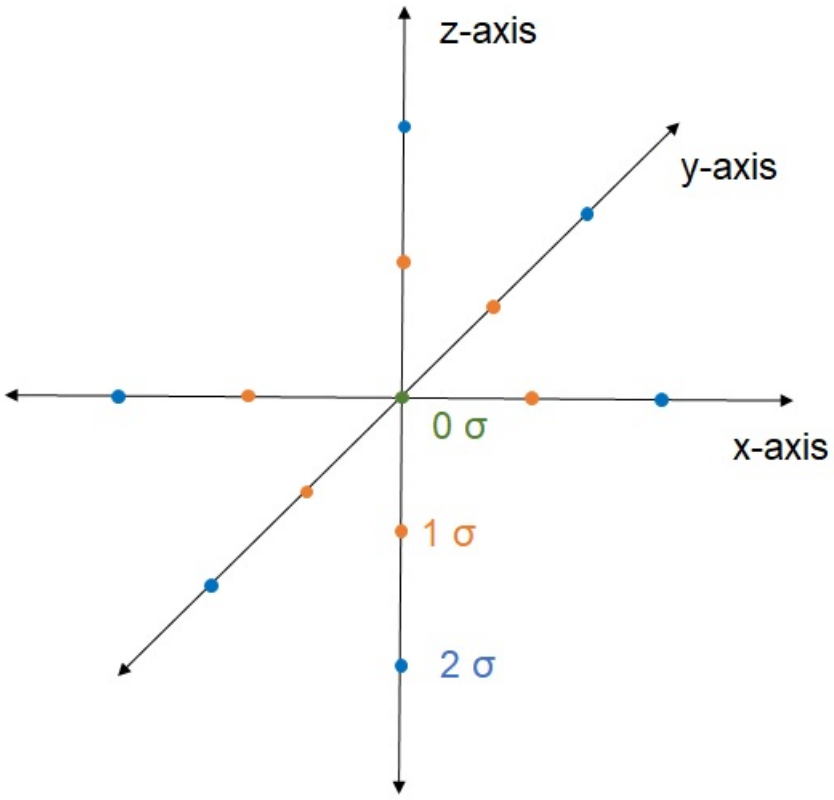

Figure 1: Schematic locations of the tracking errors assessed. Origin is defined as the tracked position calculated from the change in primary tumour GTV centre of mass position.

$$J = \int_{-\infty}^{\infty} \exp\left(\frac{-3x^2}{3*2{\sigma_{3D}}^{\frac{2}{3}}}\right) dx$$

$$\mathrm{J}^2 = \int_{-\infty}^{\infty}\int_{-\infty}^{\infty} \exp\left(\frac{-3(x^2+y^2)}{3*2r^2}\right) dxdy$$

$$\mathrm{J}^2 = \int_{0}^{\infty} 2\pi r \exp\left(\frac{-3r^2}{3*2{\sigma_{3D}}^{\frac{2}{3}}}\right) dr$$

$$\mathrm{J}^2 = -2\pi {\sigma_{3D}}^2 \int_{0}^{\infty} \left(\frac{-2r}{2{\sigma_{3D}}^{\frac{2}{3}}}\right) \exp\left(\frac{-3r^2}{3*2{\sigma_{3D}}^{\frac{2}{3}}}\right) dr$$

$$\mathrm{J}^2 = -2\pi {\sigma_{3D}}^2 \left[\exp(\left(\frac{-3r^2}{3*2{\sigma_{3D}}^{\frac{2}{3}}}\right)\right]_0^{\infty} = 2\pi {\sigma_{3D}}^2$$

$$\therefore J = \sqrt{2\pi}\sigma$$

$$\therefore \int\int\int \exp\left(\frac{-3(x^2+y^2+z^2)}{3*2{\sigma_{3D}}^{\frac{2}{3}}}\right) dxdydz = (\sigma\sqrt{2\sigma})^3$$

$$\text{want to evaluate } \int_a^b 4\pi r^2 \exp\left(\frac{-3r^2}{3*2{\sigma_{3D}}^{\frac{2}{3}}}\right) dr$$

$$= \text{-}4\pi {\sigma_{3D}}^2 \int_a^b r \left(\frac{-2r}{2{\sigma_{3D}}^2}\right) \exp\left(\frac{-3r^2}{3*2{\sigma_{3D}}^{\frac{2}{3}}}\right) dr$$

$$= \text{-}4\pi {\sigma_{3D}}^2 \left[r \exp\left(\frac{-3r^2}{3*2{\sigma_{3D}}^{\frac{2}{3}}}\right)\right]_a^b + 4\pi {\sigma_{3D}}^2 \int_a^b \exp\left(\frac{-3r^2}{3*2{\sigma_{3D}}^{\frac{2}{3}}}\right) dr$$

$$= 4\pi {\sigma_{3D}}^2 \left[-\left[r \exp\left(\frac{-3r^2}{3*2r^2}\right)\right]_a^b + \int_a^b \exp\left(\frac{-3r^2}{3*2{\sigma_{3D}}^{\frac{2}{3}}}\right) dr\right]$$

$$\text{Normalised by: } (\sigma\sqrt{2\pi})^3$$

$$= \left(\frac{-2}{\sigma\sqrt{2\pi}}\right) \left[r \exp(\frac{-3r^2}{3*2\sigma_{3D}})\right]_a^b + 2N_a^b$$

Where N is the normal distribution integrated between a and b.

Case 1 (3D annulus from 0 to $\sigma/2$): a=0, b=$\left(\frac{\sqrt{3}\sigma}{2}\right)$

$$
\begin{aligned}
&= \frac{-2\sqrt{3}}{\sigma\sqrt{2\pi}} \frac{\sigma}{2} \exp\left(\frac{-\sqrt{3}}{8}\right) + 2(0.8069 - 0.5) \\
&= \left(\frac{\sqrt{3}}{\sqrt{2\pi}}\right) \exp\left(\frac{-\sqrt{3}}{8}\right) + 2 * 0.3069 \\
&= 0.139
\end{aligned}
$$

Case 2 (3D annulus from $\sigma/2$ to $3\sigma/2$): a=$\left(\frac{\sqrt{3}\sigma}{2}\right), b = \frac{3\sqrt{3}\sigma}{2}\Big)$

$$
\begin{aligned}
&= \left(\frac{-2}{\sigma\sqrt{2\pi}}\right) \left[\left(\frac{3\sqrt{3}\sigma}{2}\right) \exp\left(\frac{-3*9}{8}\right) - \frac{\sqrt{3}\sigma}{2} \exp(\frac{3}{8})\right] \\
&\quad + 2(0.8953 \text{ - } 0.8069) \\
&= \left(\frac{-\sqrt{3}}{(\sqrt{2\pi}}\right) \left[3 \exp(\frac{-3*9}{8}) - \exp(\frac{3}{8})\right] + 0.3768 \\
&= \left(\frac{-\sqrt{3}}{(\sqrt{2\pi}}\right) (-0.5846) + 0.4834 = 0.781
\end{aligned}
$$

Case 3 (3D annulus from $3\sigma/2$ to ∞: a=$\left(\frac{3\sqrt{3}}{\sigma}2\right), b = \infty$

$$
\begin{aligned}
&= \left(\frac{-\sqrt{3}}{\sigma\sqrt{2\pi}}\right) \left[(\frac{-3\sigma}{2}) \exp\left(\frac{-3*9}{8}\right)\right] + 2N^{\infty}_{3\sqrt{3}/2} \\
&= \left(\frac{3\sqrt{3}}{\sqrt{2\pi}}\right) \exp\left(\frac{-3*9}{8}\right) + 2(1 - 0.9953) \\
&= 0.080
\end{aligned}
$$

Thus, the probability of tracking error lying between 0 and 0.5 σ is 13.9%, 0.5 and 1.5 σ is 78.1%, and beyond 1.5σ is 8% for 3D errors.

Appendix 2.
Candidates work:

- Chapter 1: Literature search.
- Chapter 2: Literature search, margin calculations.
- Chapter 3: Bifurcation point positioning and analysis, MatLab code generation, application of MatLab code on both bifurcation points and airway contours, airway contouring.
- Chapter 4: All OARs required and not already available were contoured following an atlas, PTV creation using margins previously calculated (Chapter 2), creation of isotoxic treatment plans, assessment of prescribed doses, calculation of predicted outcomes based on radiobiological models.
- Chapter 5: Calculation of required tracking translations, application of "tracking", calculation of resulting dose distributions, accumulation of dose distributions across error scenarios/respiratory phases within treatment planning system (TPS). Deformable image registration was performed within the treatment planning system, and used to accumulate the dose, calculation of "Dose Metric Averaging" technique results. All data analysis.
- Chapter 6: Investigations in the limitations of the technique, including simulation of the gating technique
- Chapter 7: As per Chapter 5, all in-silico modelling within TPS and analysis.
- Thesis written.

Assistance given:

- Throughout the DPhil, discussion with project supervisors, transfer/confirmation examiners and others within the group helped to progress the project.

- Previous researchers had anonymised and collated 5 locally-advanced and 10 early-stage patients in a planning system. As part of the clinical treatments, GTVs, CTVs and some OARs had been contoured by trained Radiation Oncologists / treatment planners from Oxford University Hospitals (generally on a single phase).

- Data from Hugo et al. [178] was used which included 4DCT data sets and some contours of GTVs, CTVs and some OARs.

- As discussed, a previous study by Partridge et al was used to predict the effect of isotoxic dose escalation on two-year disease-free survival (LA) [66].

Bibliography

[1] Cancer Research UK. Lung Cancer Statistics https://www.cancerresearchuk.org/health-professional/cancer-statistics/statistics-by-cancer-type/lung-cancer, Accessed 31-07-19.

[2] C R Smittenaar, K A Petersen, K Stewart, and N Moitt. Cancer incidence and mortality projections in the UK until 2035. *Br. J. Cancer*, 115(1147-1155), 2016.

[3] The Royal College of Physicians. Lung cancer clinical outcomes publication 2017. *Lung Cancer Clin. Outcomes Publ. 2017*, 2017(November), 2017.

[4] S Walters, C Maringe, M Coleman, M Peake, J Butler, N Young, S Bergström, L Hanna, E Jakobsen, K Kölbeck, S Sundstrøm, G Engholm, A Gavin, M Gjerstorff, J Hatcher, T Johannesen, K M Linklater, C E McGahan, J Steward, E Tracey, D Turner, M.A Richards, and B Rachet. Lung cancer survival and stage at diagnosis in Australia, Canada, Denmark, Norway, Sweden and the UK: a population-based study, 2004-2007. *Thorax*, 68(6):551–64, jun 2013.

[5] Cancer Research UK. Lung Cancer Survival https://www.cancerresearchuk.org/about-cancer/lung-cancer/survival, Accessed 31-07-19.

[6] P. Goldstraw, J. Crowley, K. Chansky, D. J. Giroux, P. A. Groome, R. Rami-Porta, P. E. Postmus, V. Rusch, and L. Sobin. The IASLC Lung Cancer Staging

Project: Proposals for the Revision of the TNM Stage Groupings in the Forthcoming (Seventh) Edition of the TNM Classification of Malignant Tumours. Technical report, 2007.

[7] M M Oken, R H Creech, D C Tormey, J Horton, T E Davis, E T McFadden, and P P Carbone. Toxicity and response criteria of the Eastern Cooperative Oncology Group. *Am. J. Clin. Oncol.*, 5(6):649–55, dec 1982.

[8] National Cancer Registration and Analysis Service. Chemotherapy, Radiotherapy and Surgical Tumour Resections in England 2013-2015. Technical report, 2018.

[9] J Vansteenkiste, L Crinò, C Dooms, J Y Douillard, C Faivre-Finn, E Lim, G Rocco, S Senan, P Van Schil, G Veronesi, R Stahel, S Peters, E Felip, and Panel Members. 2nd ESMO Consensus Conference on Lung Cancer: early-stage non-small-cell lung cancer consensus on diagnosis, treatment and follow-up. *Ann. Onocology*, 25:1462–1474, 2014.

[10] M Beasley, D Driver, and J Dobbs. Complications of radiotherapy: improving the therapeutic index. *Cancer Imaging*, 5:78–84, 2005.

[11] H J Dobbs, R P Parker, N J Hodson, P Hobday, and J E Husband. *Radiother. Oncol.*, 1:133–141.

[12] R P Parker, P A Hobday, and K J Cassell. The direct use of CT numbers in radiotherapy dosage calculations for inhomogeneous media. *Phys. Med. Biol.*, 24(4):802–809, 1979.

[13] G S Mageras, A Pevsner, E.D Yorke, K E Rosenzweig, E C Ford, A Hertanto, S M Larson, D M Lovelock, Y E Erdi, S A Nehmeh, J L Humm, and C C Ling. Measurement of Lung Tumor Motion using Respiration-Correlated CT. *Int. J. Radiat. Oncol. Biol. Phys.*, 60(3):933–941, 2004.

[14] J Unkelbach and U Oelfke. Inclusion of organ movements in IMRT treatment planning via inverse planning based on probability distributions. *Phys. Med. Biol.*, 49:4005–4029, 2004.

[15] P J Keall, S Joshi, S S Vedam, J V Siebers, V R Kini, and R Mohan. Four-dimensional radiotherapy planning for DMLC-based respiratory motion tracking. *Med. Phys.*, 32(4):942–951, 2005.

[16] E M Leter, F Cademartiri, P C Levendag, T Flohr, H Stam, and P J Nowak. Four-dimensional multislice computed tomography of respiratory lung tumour motion in conformal radiotherapy. *Int. J. Radiat. Oncol. Biol. Phys.*, 62(3):888–892, 2005.

[17] E Rietzel, G T Y Chen, N C Choi, and C G Willet. Four-dimensional computed tomography: Image formation and clinical protocol. *Int. J. Radiat. Oncol. Biol. Phys.*, 61(4):1535–1550, 2005.

[18] P Metcalfe, G P Liney, L Holloway, A Walker, M Barton, G P Delaney, S Vinod, and W Tomé. The Potential for an Enhanced Role For MRI in Radiation-therapy Treatment Planning. *Technol. Cancer Res. Treat.*, 12(5), 2013.

[19] D Thorwarth. Functional imaging for radiotherapy treatment planning: current status and future directions-a review. *Br. J. Radiol.*, 88:20150056, 2015.

[20] W De Wever, S Stroobants, J Coolen, and J A Verschakelen. Integrated PET/CT in the staging of nonsmall cell lung cancer: technical aspects and clinical integration. *Eur. Respir. J.*, 33:201–212, 2009.

[21] D R Baldwin. Imaging in lung cancer: recent advances in PET-CT and screen. *Thorax*, 66(275-277), 2011.

[22] M Kara Bucci, Alison Bevan, and Mack Roach. Advances in radiation therapy: conventional to 3D, to IMRT, to 4D, and beyond. *CA. Cancer J. Clin.*, 55(2):117–134, 2005.

[23] S G Chun, C Hu, H Choy, R U Komaki, R D Timmerman, S E Schild, J A Bogart, M C Dobelbower, W R Bosch, J M Galvin, V S Kavadi, S Narayan, P Iyengar, C G Robinson, R Wynn, A Raben, M Augspurger, R M MacRae, R Paulus, and J D Bradley. Comparison of 3-D Conformal and Intensity Modulated Radiation Therapy Outcomes for Locally Advanced Non-Small Cell Lung Cancer in NRG Oncology/RTOG 0617. *Int. J. Radiat. Oncol.*, 93(3):S1–S2, nov 2015.

[24] J Boyle, B Ackerson, L Gu, and C R Kelsey. Dosimetric advantages of intensity modulated radiation therapy in locally advanced lung cancer. *Adv. Radiat. Oncol.*, 2:6–11, 2017.

[25] J L Bedford, N Hansen, H A Mcnair, A H Aitken, J E C Brock, A P Warrington, and M Brada. Treatment of lung cancer using volumetric modulated arc therapy and image guidance: A case study. *Acta Oncol. (Madr).*, 47(7):1438–1443, 2008.

[26] T. Landberg, J. Chavaudra, J. Dobbs, G. Hanks, K.-A. Johansson, T. Möller, and J. Purdy. Report 50. *J. Int. Comm. Radiat. Units Meas.*, os26(1), sep 1993.

[27] T Landberg, J Chavaudra, J Dobbs, J-P Gerard, G Hanks, J-C Horiot, K-A. Johansson, T Möller, J Purdy, N Suntharalingam, and H Svensson. Report 62. *J. Int. Comm. Radiat. Units Meas.*, os32(1), nov 1999.

[28] J W H Wolthaus, J-J Sonke, M B. van Herk, J S A Belderbos, M M G Rossi, J V Lebesque, and E M F Damen. Comparison of different strategies to use

four-dimensional computed tomography in treatment planning for lung cancer patients. *Int. J. Radiat. Oncol. Biol. Phys.*, 70(4):1229–1238, 2008.

[29] V. Gregoire, T. R. Mackie, W. De Neve, M. Gospodarowiez, J. A. Purdy, M. van Herk, and A. Niemierko. Report 83. *J. ICRU*, 10(1), apr 2010.

[30] A L Boyer, L Antonuk, A Fenster, M Van Herk, H Meertens, P Munro, L E Reinstein, and J Wong. A review of electronic portal imaging devices (EPIDs). *Med. Phys.*, 19(1):1–16, jan 1992.

[31] S Lavertu, L-M Girouard, and J Pouliot. Observation study of electronic portal images for off-line verification. *Radiother. Oncol.*, 54(1):47–55, jan 2000.

[32] D A Jaffray, D G Drake, M Moreau, A A Martinez, and J W Wong. A radiographic and tomographic imaging system integrated into a medical linear accelerator for localization of bone and soft-tissue targets. *Int. J. Radiat. Oncol.*, 45(3):773–789, oct 1999.

[33] D A Jaffray, J H Siewerdsen, J W Wong, and A A Martinez. Flat-Panel Cone-Beam Computed Tomography for Image-Guided Radiation Therapy. *Int. J. Radiat. Oncol. Biol. Phys.*, 53(5):1137–1349, 2002.

[34] U Oelfke, T Tücking, S Nill, A Seeber, B Hesse, P Huber, and C Thilmann. Linac-integrated kV-cone beam CT: Technical features and first applications. *Med. Dosim.*, 31(1):62–70, mar 2006.

[35] B Sorcini and A Tilikidis. Clinical application of image-guided radiotherapy, IGRT (on the Varian OBI platform). *Cancer Radiother.*, 10:252–257, 2006.

[36] J-P Bissonnette, T G Purdie, J A Higgins, W Li, and A Bezjak. Cone-Beam Computed Tomographic Image Guidance for Lung Cancer Radiation Therapy. *Int. J. Radiat. Oncol.*, 73(3):927–934, 2009.

[37] G Altorjai, I Fotina, M Stock, Di Georg, and K Dieckmann. Cone-beam CT-based Delineation of Stereotactic Lung Targets: The Influence of Image Modality and Target Size on Interobserver Variability. *Int. J. Radiat. Oncol. Biol. Phys.*, 82(2):e265–e272, 2012.

[38] S Thengumpallil, K Smith, P Monnin, J Bourhis, F Bochud, and R Moeckli. Difference in performance between 3D and 4D CBCT for lung imaging: a dose and image quality analysis. *J. Appl. Clin. Med. Phys.*, 17(6):97–106, 2016.

[39] H Yan, L Cervino, X Jia, and S B Jiang. A comprehensive study on the relationship between the image quality and imaging dose in low-dose cone beam CT. *Phys. Med. Biol.*, 57(7):2063, apr 2012.

[40] P J Keall, G S Mageras, J M Balter, R S Emery, K M Forster, S B Jiang, J M Kapatoes, D A Low, M J Murphy, B R Murray, C R Ramsey, M B Van Herk, S S Vedam, J W Wong, and E Yorke. The management of respiratory motion in radiation oncology report of AAPM Task Group 76. *Med. Phys.*, 33(10):3874–3900, 2006.

[41] G Li, De Citrin, K Camphausen, B Mueller, C Burman, B Mychalczak, R W Miller, and Y Song. Advances in 4D Medical Imaging and 4D Radiation Therapy. *Technol. Cancer Res. Treat.*, 7(1):67–81, feb 2008.

[42] G D Hugo and M Rosu. Advances in 4D Radiation Therapy for Managing Respiration: Part I – 4D Imaging. *Z. Med. Phys.*, 22(4):258, 2012.

[43] S S Korreman. Image-guided radiotherapy and motion management in lung cancer. *Br. J. Radiol.*, 88(1051):20150100, 2015.

[44] S A Yoganathan, K J Maria Das, Arpita Agarwal, and Shaleen Kumar. Magnitude, Impact, and Management of Respiration-induced Target Motion in Radio-

therapy Treatment: A Comprehensive Review. *J. Med. Phys.*, 42(3):101–115, 2017.

[45] U Nestle, D De Ruysscher, U Ricardi, X Geets, J Belderbos, C Pöttgen, R Dziadiuszko, S Peeters, Y Lievens, C Hurkmans, B Slotman, S Ramella, C Faivre-Finn, F McDonald, F Manapov, P M Putora, C LePéchoux, and P Van Houtte. ESTRO ACROP guidelines for target volume definition in the treatment of locally advanced non-small cell lung cancer. *Radiother. Oncol.*, 127(1):1–5, apr 2018.

[46] A Shah, P A Kupelian, B J Waghorn, T R Willoughby, J M Rineer, R R Mañon, M A Vollenweider, and S L Meeks. Real-time tumor tracking in the lung using an electromagnetic tracking system. *Int. J. Radiat. Oncol. Biol. Phys.*, 86(3):477–483, 2013.

[47] C-C Shieh, P J Keall, Z Kuncic, C-Y Huang, and I Feain. Markerless tumor tracking using short kilovoltage imaging arcs for lung image-guided radiotherapy. *Phys. Med. Biol.*, 60(24):9437–9454, 2015.

[48] T Shiinoki, S Kawamura, T Uehara, Y Yuasa, K Fujimoto, M Koike, T Sera, Y Emoto, H Hanazawa, and K Shibuya. Evaluation of a combined respiratory-gating system comprising the TrueBeam linear accelerator and a new real-time tumor-tracking radiotherapy system: a preliminary study. *J. Appl. Clin. Med. Phys.*, 17(4):202–213, 2016.

[49] M Josipovic, M C Aznar, and G F Persson. Deep inspiration breath hold radiotherapy of lung cancer: The good, the bad and the ugly case. *Acta Oncol. (Madr).*, 53(10):1446–1448, 2014.

[50] R B Venkat, A Sawant, Y Suh, R George, and P J Keall. Development and preliminary evaluation of a prototype audiovisual biofeedback device incorpo-

rating a patient-specific guiding waveform. *Phys. Med. Biol.*, 53:N197–N208, 2008.

[51] G Bouilhol, M Ayadi, S Rit, S Thengumpallil, J Schaerer, J Vandemeulebroucke, L Claude, and D Sarrut. Is abdominal compression useful in lung stereotactic body radiation therapy? A 4DCT and dosimetric lobe-dependent study. *Phys. Medica*, 29(4):333–340, 2013.

[52] J D Goldstein, Y R Lawrence, S Appel, E Landau, M A Ben-David, T Rabin, M Benayun, Se Dubinski, N Weizman, D Alezra, H Gnessin, A M Goldstein, K Baidun, M J Segel, N Peled, and Z Symon. Clinical Investigation Continuous Positive Airway Pressure for Motion Management in Stereotactic Body Radiation Therapy to the Lung: A Controlled Pilot Study Radiation Oncology. *Radiat. Oncol. Biol.*, 93(2):391–399, 2015.

[53] V Murthy, Z Master, P Adurkar, I Mallick, U Mahantshetty, G Bakshi, H Tongaonkar, and S Shrivastava. 'Plan of the day' adaptive radiotherapy for bladder cancer using helical tomotherapy. *Radiother. Oncol.*, 99(1):55–60, 2011.

[54] X. A Li, F Liu, A Tai, E Ahunbay, G Chen, T Kelly, C Lawton, and B Erickson. Development of an online adaptive solution to account for inter- and intrafractional variations. *Radiother. Oncol.*, 100(3):370–374, 2011.

[55] J McKenna, M J Parkes, C Snowden, J Prentis, N S West, C Walker, and M S Iqbal. Mitigating respiratory motion in radiotherapy: rapid, shallow, noninvasive mechanical ventilation for internal thoracic targets. *Int. J. Radiat. Oncol.*, 103(4):1004–1010, mar 2018.

[56] The Royal College of Radiologists. Radiotherapy dose fractionation Second edition,

https://www.rcr.ac.uk/system/files/publication/field_publication_files/bfco163_dose_fractionation_2nd_ed_march2017.pdf, 2016.

[57] R Timmerman, R McGarry, C Yiannoutsos, L Papiez, K Tudor, J DeLuca, M Ewing, R Abdulrahman, C DesRosiers, M Williams, and J Fletcher. Excessive toxicity when treating central tumors in a phase II study of stereotactic body radiation therapy for medically inoperable early-stage lung cancer. *J. Clin. Oncol.*, 24(30):4833–4839, 2006.

[58] UK SABR Consortium. Stereotactic Ablative Body Radiation Therapy (SABR): A Resource, https://sabr.org.uk/wp-content/uploads/2016/04/UKSABRConsortiumGuidelinesv51.pdf, 2016.

[59] L E Henke, J R Olsen, J A Contreras, A Curcuru, T A DeWees, O L Green, J Michalski, S Mutic, M C Roach, J D Bradley, P J Parikh, R Kashani, and C G Robinson. Stereotactic MR-guided Online Adaptive Radiation Therapy (SMART) for Ultra-Central Thorax Malignancies: Results of a Phase I Trial. *Adv. Radiat. Oncol.*, pages 1–9, 2018.

[60] W Weder, D Moghanaki, B Stiles, S Siva, and G Rocco. The great debate flashes: surgery versus stereotactic body radiotherapy as the primary treatment of early-stage lung cancer. *Eur J Cardiothorac Surg*, 53:295–305, 2018.

[61] M P Snee, L Mcparland, F Collinson, C M Lowe, A Striha, D R Baldwin, B Naidu, D Sebag-Montefiore, W M Gregory, J Bestall, J Hewison, S Hinsley, and K Franks. The SABRTooth feasibility trial protocol: a study to determine the feasibility and acceptability of conducting a phase III randomised controlled trial comparing stereotactic ablative radiotherapy (SABR) with surgery in patients with peripheral stage I non. *Pilot Feasibility Stud.*, 2(5), 2016.

[62] H. C. Fernando and R. Timmerman. JoLT-Ca Sublobar Resection (SR) Versus Stereotactic Ablative Radiotherapy (SAbR) for Lung Cancer (STABLE-MATES), https://clinicaltrials.gov/ct2/show/NCT0246802, 2018.

[63] T G Purdie, K N Franks, A Bezjak, J Higgins, D A Jaffray, J P Bissonnette, V Sarkar, C Shi, P Rassiah, S Stathakis, and N Papanikolaou. *Int. J. Radiat. Oncol. Biol. Phys.*, 69(3):S705, 2007.

[64] M Machtay, S Swann, R Komaki, R Byhardt, R Paulus, W Sause, K Albain, B Movsas, and W J Curran. Higher BED is Associated with Improved Local-regional Control and Survival for NSCLC Treated with Chemoradiotherapy: An RTOG Analysis. *Int. J. Radiat. Oncol. Biol. Phys.*, 63(2):S40, 2005.

[65] Z-H Wang, C Yan, Z-Y Zhang, C-P Zhang, H-S Hu, J Kirwan, and W M Mendenhall. Radiation-induced volume changes in parotid and submandibular glands in patients with head and neck cancer receiving postoperative radiotherapy: a longitudinal study. *Laryngoscope*, 119(10):1966–1974, 2009.

[66] M Partridge, M Ramos, A Sardaro, and M Brada. Dose escalation for non-small cell lung cancer: Analysis and modelling of published literature. *Radiother. Oncol.*, 99(1):6–11, 2011.

[67] J Ramroth, D J Cutter, S C Darby, G S Higgins, P McGale, M Partridge, and C W Taylor. Dose and Fractionation in Radiation Therapy of Curative Intent for Non-Small Cell Lung Cancer: Meta-Analysis of Randomized Trials. *Int. J. Radiat. Oncol. Biol. Phys.*, 96(4):736–747, 2016.

[68] L Kestin, I Grills, M Guckenberger, J Belderbos, A J Hope, M Werner-Wasik, J-J Sonke, J-P Bissonnette, Y Xiao, and D Yan. Dose-response relationship with clinical outcome for lung stereotactic body radiotherapy (SBRT) delivered via online image guidance. *Radiother. Oncol.*, 110(3):499–504, mar 2014.

[69] H Onishi, H Shirato, Y Nagata, Ma Hiraoka, M Fujino, K Gomi, Yu Niibe, K Karasawa, K Hayakawa, Y Takai, T Kimura, A Takeda, A Ouchi, M Hareyama, M Kokubo, R Hara, J Itami, K Yamada, and T Araki. Hypofractionated stereotactic radiotherapy (HypoFXSRT) for stage I non-small cell lung cancer: updated results of 257 patients in a Japanese multi-institutional study. *J. Thorac. Oncol.*, 2(7 Suppl 3):S94–S100, jul 2007.

[70] M Guckenberger, J Wulf, G Mueller, T Krieger, K Baier, M Gabor, A Richter, J Wilbert, and M Flentje. Dose–Response Relationship for Image-Guided Stereotactic Body Radiotherapy of Pulmonary Tumors: Relevance of 4D Dose Calculation. *Int. J. Radiat. Oncol. Biol. Phys.*, 74(1):47–54, may 2009.

[71] S Vivekanandan, D B Landau, N Counsell, D R Warren, A Khwanda, S D Rosen, E Parsons, Y Ngai, L Farrelly, L Hughes, M A Hawkins, and J D Fenwick. The impact of cardiac radiation dosimetry on survival following radiotherapy for non-small cell lung cancer. *Int. J. Radiat. Oncol.*, 99(1):51–60, 2017.

[72] B W Raaymakers, A J E Raaijmakers, A N T J Kotte, Jette D, and J J W Lagendijk. Integrating a MRI scanner with a 6 MV radiotherapy accelerator: dose deposition in a transverse magnetic field. *Phys. Med. Biol.*, 49:4109, 2004.

[73] B Fallone, B Murray, S Rathee, T Stanescu, S Steciw, S Vidakovic, E Blosser, and D Tymofichuk. First MR Images Obtained During Megavoltage Photon Irradiation From An Integrated Linac-MR System. *Med. Phys.*, 36(6):2745, 2009.

[74] S Mutic and J F Dempsey. The ViewRay System: Magnetic Resonance-Guided and Controlled Radiotherapy. *Semin. Radiat. Oncol.*, 24(3):196–199, 2014.

[75] P J Keall, M Barton, and S Crozier. The Australian Magnetic Resonance Imaging-Linac Program. *Semin. Radiat. Oncol.*, 24:203–206, 2014.

[76] H Aoyama, H Shirato, T Nishioka, S Hashimoto, K Tsuchiya, K Kagei, R Onimaru, Y Watanabe, and K Miyasaka. Magnetic Resonance Imaging System for Three-Dimensional Conformal Radiotherapy and Its Impact on Gross Tumor Volume Delination of Central Nervous System Tumors. *Int. J. Radiat. Oncol. Biol. Phys.*, 50(3):821–87, 2001.

[77] A R Yeung, C E Vargas, A Falchook, D Louis, K Olivier, S Keole, D Yeung, N P Mendenhall, and L Zuofeng. Dose-Volume Differences for Computed Tomography and Magnetic Resonance Imaging Segmentation and Planning for Proton Prostate Cancer Therapy. *Radiat. Oncol. Biol.*, 72(5):1426–1433, 2008.

[78] R Chuter, R Prestwich, D Bird, A Scarsbrook, J Sykes, D Wilson, and R Speight. The use of deformable image registration to integrate diagnostic MRI into the radiotherapy planning pathway for head and neck cancer. *Radiother. Oncol.*, 122(2):229–235, 2017.

[79] C E Noel, P J Parikh, C R Spencer, O L Green, Y Hu, S Mutic, and J R Olsen. Comparison of onboard low-field magnetic resonance imaging versus onboard computed tomography for anatomy visualization in radiotherapy. *Acta Oncol. (Madr).*, 54(9):1474–1482, 2015.

[80] H Bainbridge, A Salem, R H N Tijssen, M Dubec, A Wetscherek, C Es, J Belderbos, C Faivre-Finn, and F Mcdonald. Magnetic resonance imaging in precision radiation therapy for lung cancer; on behalf of the lung tumour site group of the international Atlantic MR-Linac Consortium. *Transl Lung Cancer Res*, 6(6):689–707, 2017.

[81] S Acharya, B W Fischer-Valuck, R Kashani, P Parikh, D Yang, T Zhao, O Green, O Wooten, H H Li, Y Hu, V Rodriguez, L Olsen, C Robinson, J Michalski, S Mutic, and J Olsen. Online Magnetic Resonance Image Guided Adaptive Radiation Therapy: First Clinical Applications Radiation Oncology. *Int. J. Radiat. Oncol. Biol. Phys.*, 94(2):394–403, 2016.

[82] P A Bottomley. Turning Up the Heat on MRI. *J. Am. Coll. Radiol.*, 5(7):853–855, 2008.

[83] BMJ. How does it work? Magnetic resonance imaging. *BMJ*, 324:324, 2002.

[84] E M Purcell, H C Torrey, and R V Pound. Resonance Absorption by Nuclear Magnetic Moments in a Solid. *Phys. R*, 69(1-2):37–38, 1945.

[85] F Bloch. Nuclear Induction. *Phys. Rev.*, 70(7-8):460–474, 1946.

[86] M J Menten, A Wetscherek, and M F Fast. MRI-guided lung SBRT: Present and future developments. *Phys. Medica*, 2016.

[87] H Chandarana, H Wang, R. H N Tijssen, and I J. Das. Emerging Role of MRI in Radiation Therapy. *J. Magn. Reson. Imaging*, pages 1–11, 2018.

[88] M A Schmidt and G S Payne. Radiotherapy planning using MRI. *Phys. Med. Biol.*, 59:R323–361, 2015.

[89] S J Doran, L Charles-Edwards, S A Reinsberg, and M O Leach. A complete distortion correction for MR images: I. Gradient warp correction. *Phys. Med. Biol.*, 50(7):1343–1361, 2005.

[90] D Wang, W Strugnell, G Cowin, D M Doddrell, and R Slaughter. Geometric distortion in clinical MRI systems: Part II: Correction using a 3D phantom. *Magn. Reson. Imaging*, 22(9):1223–1232, 2004.

[91] D Wang and D M Doddrell. Geometric Distortion in Structural Magnetic Resonance Imaging. *Curr. Med. Imaging Rev.*, 1:49–60, 2005.

[92] L N Baldwin, K Wachowicz, S D Thomas, R Rivest, and B G Fallone. Characterization , prediction , and correction of geometric distortion in 3 T MR images. *Med. Phys.*, 34(2):388–399, 2007.

[93] A Janke, H Zhao, G J Cowin, G J Galloway, and D M Doddrell. Use of spherical harmonic deconvolution methods to compensate for nonlinear gradient effects on MRI images. *Magn. Reson. Med.*, 52(1):115–122, 2004.

[94] D Wang, D M Doddrell, and G Cowin. A novel phantom and method for comprehensive 3-dimensional measurement and correction of geometric distortion in magnetic resonance imaging. *Magn. Reson. Imaging*, 22(4):529–542, 2004.

[95] Z Caramanos, V S Fonov, S J Francis, S Narayanan, G B Pike, D L Collins, and D L Arnold. Gradient distortions in MRI: Characterizing and correcting for their effects on SIENA-generated measures of brain volume change. *Neuroimage*, 49(2):1601–1611, 2010.

[96] N Maikusa, F Yamashita, K Tanaka, O Abe, A Kawaguchi, H Kabasawa, S Chiba, A Kasahara, N Kobayashi, T Yuasa, N Sato, H Matsuda, and T Iwatsubo. Improved volumetric measurement of brain structure with a distortion correction procedure using an ADNI phantom. *Med. Phys.*, 40(6), 2013.

[97] S A Reinsberg, S J Doran, E M Charles-Edwards, and M O Leach. A complete distortion correction for MR images: II. Rectification of static-field inhomogeneities by similarity-based profile mapping. *Phys. Med. Biol.*, 50(11):2651–2661, 2005.

[98] T Stanescu, K Wachowicz, and D. A Jaffray. Characterization of tissue magnetic susceptibility-induced distortions for MRIgRT. *Med. Phys.*, 39(12):7185–7193, 2012.

[99] J M Wild, H Marshall, M Bock, L R Schad, P M Jakob, M Puderbach, F Molinari, E J R Van Beek, and J Biederer. MRI of the lung (1/3): methods. *Insights Imaging*, 3:345–353, 2012.

[100] C J Muller, R Loffler, M Deimling, M Peller, and M Reiser. MR lung imaging at 0.2 T with T1-weighted true FISP: native and oxygen-enhanced. *J Magn Reson Imaging*, 14(2):164–168, 2001.

[101] M K Stam, S P M Crijns, B A Zonnenberg, M M Barendrecht, M van Vulpen, J J W Lagendijk, and B W Raaymakers. Navigators for motion detection during real-time MRI-guided radiotherapy. *Phys. Med. Biol.*, 57(21):6797–6805, 2012.

[102] J Biederer, M Beer, W Hirsch, J Wild, M Fabel, M Puderbach, E J R Van Beek, Academic Radiology, Royal Hallamshire, and Hospital Sheffield. MRI of the lung (2/3). Why ... when ... how? *Insights Imaging*, 3:355–371, 2012.

[103] C Hintze, J Biederer, H Wenz, R Eberhardt, and H Kauczor. MRT zum staging des lungenkarzinoms. *Radiologe*, 46:251–259, 2006.

[104] Clinicaltrials.gov. Hyperpolarized Xenon Gas MR Imaging in NSCLC Radiotherapy, 2019.

[105] I Arivarasan, C Anuradha, S Subramanian, A Anantharaman, and V Ramasubramanian. Magnetic resonance image guidance in external beam radiation therapy planning and delivery. *Japanese J. Radiol.*, pages 1–10, 2017.

[106] A J E Raaijmakers, B Hardemark, B W Raaymakers, Raaijmakers C P J, and J J W Lagendijk. Dose optimization for the MRI-accelerator: IMRT in the presence of a magnetic field. *Phys. Med. Biol.*, 52:7045–7054, 2007.

[107] B W Raaymakers, I M Jürgenliemk-Schulz, G H Bol, M Glitzner, A N T J Kotte, B Van Asselen, J CJ De Boer, J J Bluemink, S L Hackett, M A Moerland, S J Woodings, J W H Wolthaus, H M Van Zijp, M E P Philippens, R Tijssen, J G M Kok, E N De Groot-Van Breugel, I Kiekebosch, L T C Meijers, C N Nomden, G G Sikkes, P A H Doornaert, W S C Eppinga, N Kasperts, L G W Kerkmeijer, J H A Tersteeg, K J Brown, B Pais, P Woodhead, and J J W Lagendijk. First patients treated with a 1.5 T MRI-Linac: Clinical proof of concept of a high-precision, high-field MRI guided radiotherapy treatment. *Phys. Med. Biol.*, 62(23):L41–L50, 2017.

[108] R W Chuter, P Whitehurst, A Choudhury, M Van Herk, and A McWilliam. Technical Note: Investigating the impact of field size on patient selection for the 1.5T MR-Linac. *Med. Phys.*, 44(11):5667–5671, 2017.

[109] D Schmidhalter, M K Fix, M Wyss, N Schaer, P Munro, S Scheib, P. Kunz, and P. Manser. Evaluation of a new six degrees of freedom couch for radiation therapy. *Med. Phys.*, 40(11), 2013.

[110] C Ménard and U van der Heide. Introduction: Systems for Magnetic Resonance Image Guided Radiation Therapy. *Semin. Radiat. Oncol.*, 24(3):192, 2014.

[111] K Wachowicz, N De Zanche, E Yip, V Volotovskyy, and B G Fallone. CNR considerations for rapid real-time MRI tumor tracking in radiotherapy hybrid devices: Effects of B0field strength. *Med. Phys.*, 43(8):4903–4914, 2016.

[112] J J W Lagendijk, B W Raaymakers, and M van Vulpen. The Magnetic Resonance Imaging-Linac System. *Semin. Radiat. Oncol.*, 24(3):207–209, 2014.

[113] B G Fallone. The Rotating Biplanar Linac-Magnetic Resonance Imaging System. *Semin. Radiat. Oncol.*, 24(3):200–202, 2014.

[114] S Y Tari, K Wachowicz, and G B Fallone. A non-axial superconducting magnet design for optimized patient access and minimal SAD for use in a Linac-MR hybrid: Proof of concept. *Phys. Med. Biol.*, 62(8):N147–N160, 2017.

[115] N Roberts, B Oborn, U Jelen, B Dong, J Begg, A George, S J Alnaghy, T Causer, T Alharthi, L Holloway, and P Metcalfe. Modelling the x-ray source for the Australian MRI-Linac. *J. Phys. Conf. Ser.*, 1154:012025, 2019.

[116] Y Hu, O L Green, D Feng, D. Du, O H Wooten, H H Li, L. Santanam, P J Parikh, J R Olsen, and S. Mutic. Image Performance Characterization of an MRI-Guided Radiation Therapy System. *Radiat. Oncol. Biol.*, 87(2):S13, oct 2013.

[117] J Lamb, Mi Cao, A Kishan, N Agazaryan, D H Thomas, N Shaverdian, Y Yang, S Ray, D A Low, A Raldow, M L Steinberg, and P Lee. Online Adaptive Radiation Therapy: Implementation of a New Process of Care. *Cureus*, 9(8):1618, 2017.

[118] H D Suit. Editorial: What's the optimum choice? *Int. J. Radiat. Oncol. Biol. Phys.*, 12:171–1712, 1986.

[119] J Laughlin and A Kutcher. Choice of Optimum Megavoltage for Accelerators for Photon Beam Treatment. *Radiat. Oncol. Biol. Phys*, 12(9):1551–1557, 1986.

[120] J S Ginn, N Agazaryan, M Cao, U Baharom, D A Low, Y Yang, Y Gao, P Hu, P Lee, and J M Lamb. Characterization of spatial distortion in a 0.35 T MRI-guided radiotherapy system. *Phys. Med. Biol.*, 62(11):4525–4540, 2017.

[121] C W Wee, H J An, H-C Kang, H J Kim, and H-G Wu. Variability of Gross Tumor Volume Delineation for Stereotactic Body Radiotherapy of the Lung With Tri-60 Co Magnetic Resonance Image-Guided Radiotherapy System (ViewRay): A Comparative Study With Magnetic Resonance-and Computed Tomography-Based Target Del. *Technol. Cancer Res. Treat.*, 17:1–7, 2018.

[122] D L Saenz, Y Yan, N Christensen, M A Henzler, L J Forrest, J E Bayouth, and B R Paliwal. Characterization of a 0.35T MR system for phantom image quality stability and in vivo assessment of motion quantification. *J. Appl. Clin. Med. Phys.*, 16(6):30–40, 2015.

[123] Viewray INC. ViewRay Specification, https://viewray.com/wp-content/uploads/2018/06/L-0011ViewRaySystemSummarySpecifications_RevC.pdf, accessed 31-07-19, 2013.

[124] J J W Lagendijk, B W Raaymakers, A J E Raaijmakers, J Overweg, K J Brown, E M Kerkhof, R W Van Der Put, B Hårdemark, M Van Vulpen, and U A Van Der Heide. MRI/linac integration. *Radiother. Oncol.*, 86:25–29, 2008.

[125] R Canzeri. Elekta Unity, world's first high-field MR-linac, receives CE mark, https://www.elekta.com/meta/press-all.html?id=000DC1B6E1EEAF5F, accessed 31-07-19, 2018.

[126] B W Raaymakers, J. J.W. Lagendijk, J. Overweg, J. G.M. Kok, A. J.E. Raaijmakers, E. M. Kerkhof, R. W. Van Der Put, I. Meijsing, S. P.M. Crijns, F. Benedosso, M. Van Vulpen, C. H.W. De Graaff, J. Allen, and K. J. Brown. Integrating a 1.5 T MRI scanner with a 6 MV accelerator: Proof of concept. *Phys. Med. Biol.*, 54(12):229, 2009.

[127] S J Woodings, J J Bluemink, J H W De Vries, Y Niatsetski, B Van Veelen, J Schillings, J G M Kok, J W H Wolthaus, S L Hackett, B Van Asselen, H M

Van Zijp, S Pencea, D A Roberts, J J W Lagendijk, and B W Raaymakers. Beam characterisation of the 1.5 T MRI-linac. *Phys. Med. Biol.*, 63(8), 2018.

[128] T Tadic and B G Fallone. Design and optimization of a novel bored biplanar permanent-magnet assembly for hybrid magnetic resonance imaging systems. *IEEE Trans. Magn.*, 46(12):4052–4058, 2010.

[129] C. Kirkby, B. Murray, S. Rathee, and B. G. Fallone. Lung dosimetry in a linac-MRI radiotherapy unit with a longitudinal magnetic field. *Med. Phys.*, 37(9):4722–4732, 2010.

[130] J M Edmund and T Nyholm. A review of substitute CT generation for MRI-only radiation therapy. *Radiat. Oncol.*, 12(1):28, 2017.

[131] N Burgos, F Guerreiro, J Mcclelland, B Presles, M Modat, S Nill, D Dearnaley, N Desouza, U Oelfke, A-C Knopf, S Ourselin, and M J Cardoso. Iterative framework for the joint segmentation and CT synthesis of MR images: application to MRI-only radiotherapy treatment planning. *Phys. Med. Biol.*, 62:4237–4253, 2017.

[132] F Guerreiro, N Burgos, A Dunlop, K Wong, I Petkar, C Nutting, K Harrington, S Bhide, K Newbold, D Dearnaley, N M Desouza, V A Morgan, J Mcclelland, S Nill, M J Cardoso, S Ourselin, U Oelfke, and A C Knopf. Evaluation of a multi-atlas CT synthesis approach for MRI-only radiotherapy treatment planning. *Phys. Medica*, 35:7–17, 2017.

[133] H Wang, H Chandarana, K T Block, T Vahle, M Fenchel, and I J Das. Dosimetric evaluation of synthetic CT for magnetic resonance-only based radiotherapy planning of lung cancer. *Radiat. Oncol.*, 12(1):108, 2017.

[134] A Johansson, M Karlsson, and T Nyholm. CT substitute derived from MRI sequences with ultrashort echo time. *Med. Phys.*, 38(5):2708–2714, 2011.

[135] The Royal College of Radiologists, Institute of Physics and Engineering in Medicine, and Society and College of Radiographers. *On target: ensuring geometric accuracy in radiotherapy*. London: The Royal College of Radiologists, 2008.

[136] M Van Herk, P Remeijer, C Rasch, and J V Lebesque. The probability of correct target dosage: Dose-population histograms for deriving treatment margins in radiotherapy. *Int. J. Radiat. Oncol. Biol. Phys.*, 47(4):1121–1135, 2000.

[137] G Ecclestone, J-P Bissonnette, and E Heath. Experimental validation of the van Herk margin formula for lung radiation therapy. *Med. Phys.*, 40(11):111721, 2013.

[138] D C P Cobben, H C.J de Boer, R H Tijssen, E G G M Rutten, M van Vulpen, J Peerlings, E G C Troost, A L Hoffmann, and A L H M W van Lier. Emerging role of MRI for radiation treatment planning in lung cancer. *Technol. Cancer Res. Treat.*, pages 1–14, 2015.

[139] S Falk. Magnetic Resonance Imaging (MRI) for the Delineation of Organs At Risk (OAR) and Target Volumes in Lung Cancer Patients, https://clinicaltrials.gov/ct2/show/NCT03048760, accessed 31-07-19.

[140] T Bjerre, S Crijns, P M af Rosenschöld, M Aznar, L Specht, R Larsen, and P Keall. Three-dimensional MRI-linac intra-fraction guidance using multiple orthogonal cine-MRI planes. *Phys. Med. Biol.*, 58(14):4943–4950, 2013.

[141] M Seregni, D Paganelli, D Lee, P B Greer, G Baroni, Keall P J, and M Riboldi. Motion prediction in MRI-guided radiotherapy based on interleaved orthogonal cine-MRI. *Phys. Med. Biol.*, 61:872–887, 2016.

[142] T Ravkilde, P J Keall, K Højbjerre, W Fledelius, E Worm, and Per R Poulsen. Geometric accuracy of dynamic MLC tracking with an implantable wired electromagnetic transponder. *Acta Oncol. (Madr).*, 50(6):944–951, 2011.

[143] S P M Crijns, B W Raaymakers, and J J W Lagendijk. Proof of concept of MRI-guided tracked radiation delivery: tracking one-dimensional motion. *Phys. Med. Biol.*, 57:7863–7872, 2012.

[144] J Yun, E Yip, K Wachowicz, S Rathee, M Mackenzie, D Robinson, and B. G. Fallone. Evaluation of a lung tumor autocontouring algorithm for intrafractional tumor tracking using low-field MRI: A phantom study. *Med. Phys.*, 39(3):1481, 2012.

[145] E Yip, J Yun, Z Gabos, S Baker, D Yee, K Wachowicz, S Rathee, and B G Fallone. Evaluating performance of a user-trained MR lung tumor autocontouring algorithm in the context of intra- and interobserver variations. *Med. Phys.*, 45(1):307–313, 2018.

[146] J J Gordon and J V Siebers. Convolution method and CTV-to-PTV margins for finite fractions and small systematic errors. *Phys. Med. Biol.*, 52(7):1967–1990, 2007.

[147] Hans C J De Boer and Ben J M Heijmen. A protocol for the reduction of systematic patient setup errors with minimal portal imaging workload. *Int. J. Radiat. Oncol. Biol. Phys.*, 50(5):1350–1365, aug 2001.

[148] H E Bainbridge, M J Menten, M F Fast, S Nill, U Oelfke, and F Mcdonald. Treating locally advanced lung cancer with a 1 . 5 T MR-Linac – Effects of the magnetic field and irradiation geometry on conventionally fractionated and isotoxic dose-escalated radiotherapy. *Radiother. Oncol.*, pages 1–6, 2017.

[149] S S Korreman. Motion in radiotherapy: photon therapy. *Phys. Med. Biol.*, 57:161, 2012.

[150] Y Seppenwoolde, H Shirato, K Kitamura, S Shimizu, M Van Herk, J V Lebesque, and K Miyasaka. Precise and real-time measurement of 3D tumor motion in lung due to breathing and heartbeat, measured during radiotherapy. *Int. J. Radiat. Oncol. Biol. Phys.*, 53(4):822–834, 2002.

[151] S C Erridge, Y Seppenwoolde, S H Muller, M Van Herk, K De Jaeger, J S A Belderbos, L J Boersma, and J V Lebesque. Portal imaging to assess set-up errors, tumor motion and tumor shrinkage during conformal radiotherapy of non-small cell lung cancer. *Radiother. Oncol.*, 66:75–85, 2003.

[152] J W H Wolthaus, C Schneider, J J Sonke, M van Herk, J S A Belderbos, M M G Rossi, J V Lebesque, and E M F Damen. Mid-ventilation CT scan construction from four-dimensional respiration-correlated CT scans for radiotherapy planning of lung cancer patients. *Int. J. Radiat. Oncol. Biol. Phys.*, 65(5):1560–1571, 2006.

[153] M Imura, K Yamazaki, H Shirato, R Onimaru, M Fujino, S Shimizu, T Harada, S Ogura, H Dosaka-Akita, K Miyasaka, and M Nishimura. Insertion and fixation of fiducial markers for setup and tracking of lung tumors in radiotherapy. *Int. J. Radiat. Oncol. Biol. Phys.*, 63(5):1442–1447, 2005.

[154] M Nakamura, Y Ishihara, Y Matsuo, Y Iizuka, N Ueki, H Iramina, H Hirashima, and T Mizowaki. Quantification of the kV X-ray imaging dose during real-time tumor tracking and from three- and four-dimensional cone-beam computed tomography in lung cancer patients using a Monte Carlo simulation. *J. Radiat. Res.*, 59(2):173–181, 2018.

[155] E E Schaake, M M G Rossi, W A Buikhuisen, J A Burgers, A A J Smit, J S A Belderbos, and J J Sonke. Differential motion between mediastinal lymph nodes and primary tumor in radically irradiated lung cancer patients. *Int. J. Radiat. Oncol. Biol. Phys.*, 90(4):959–966, 2014.

[156] N Jan, G D Hugo, N Mukhopadhyay, and E Weiss. Respiratory motion variability of primary tumors and lymph nodes during radiotherapy of locally advanced non-small-cell lung cancers. *Radiat. Oncol.*, 10(1):133, 2015.

[157] D A Jaffray, P E Lindsay, K K Brock, J O Deasy, and W A Tomé. Accurate Accumulation of Dose for Improved Understanding of Radiation Effects in Normal Tissue. *Int. J. Radiat. Oncol. Biol. Phys.*, 76(3 SUPPL.), 2010.

[158] D Sarrut, T Baudier, M Ayadi, R Tanguy, and S Rit. Deformable image registration applied to lung SBRT: Usefulness and limitations. *Phys. Medica*, 44(August):108–112, 2017.

[159] K K Brock. Results of a Multi-Institution Deformable Registration Accuracy Study (MIDRAS). *Int. J. Radiat. Oncol. Biol. Phys.*, 76(2):583–596, 2010.

[160] K Nie, C Chuang, N Kirby, S Braunstein, and J Pouliot. Site-specific deformable imaging registration algorithm selection using patient-based simulated deformations. *Med. Phys.*, 40(4):0419111–04191110, 2013.

[161] O Weistrand and S Svensson. The ANACONDA algorithm for deformable image registration in radiotherapy. *Med. Phys.*, 42(1):40–53, 2015.

[162] N Kadoya, Y Nakajima, M Saito, Y Miyabe, M Kurooka, S Kito, Y Fujita, M Sasaki, K Arai, K Tani, M Yagi, A Wakita, N Tohyama, and K Jingu. Multi-institutional Validation Study of Commercially Available Deformable Image Registration Software for Thoracic Images. *Int. J. Radiat. Oncol. Biol. Phys.*, 96(2):422–431, 2016.

[163] M Velec, J L Moseley, S Svensson, B Hårdemark, D A Jaffray, and K K Brock. Validation of biomechanical deformable image registration in the abdomen, thorax and pelvis in a commercial radiotherapy treatment planning system. *Med. Phys.*, 2017.

[164] S Moriya, H Tachibana, N Kitamura, A Sawant, and M Sato. Dose warping performance in deformable image registration in lung. *Phys. Medica*, 37:16–23, 2017.

[165] N Mogadas, T Sothmann, T Knopp, T Gauer, C Petersen, and R Werner. Influence of deformable image registration on 4D dose simulation for extracranial SBRT: A multi-registration framework study. *Radiother. Oncol.*, 2018.

[166] K K Brock, S Mutic, T R McNutt, H Li, and M L Kessler. Use of image registration and fusion algorithms and techniques in radiotherapy: Report of the AAPM Radiation Therapy Committee Task Group No. 132: Report. *Med. Phys.*, 44(7):e43–e76, 2017.

[167] M. Weckesser, L. Stegger, K. U. Juergens, D. Wormanns, W. Heindel, and O. Schober. Correlation between respiration-induced thoracic expansion and a shift of central structures. *Eur. Radiol.*, 16(7):1614–1620, 2006.

[168] A Modh, A Rimner, E Williams, A Foster, M Shah, W Shi, Z Zhang, D Y Gelblum, K E Rosenzweig, E D Yorke, Jackson, and A J Wu. Local control and toxicity in a large cohort of central lung tumors treated with stereotactic body radiation therapy. *Int. J. Radiat. Oncol. Biol. Phys.*, 90(5):1168–1176, 2014.

[169] H S Park, E M Harder BS, B R Mancini, R H Decker, E M Harder, B R Mancini, and R H Decker. Central versus Peripheral Tumor Location: Influence on Survival, Local Control, and Toxicity Following Stereotactic Body Radiotherapy

for Primary Non–Small-Cell Lung Cancer. *J. Thorac. Oncol.*, 10(5):832–837, 2015.

[170] J M Haseltine, A Rimner, D Y Gelblum, A Modh, K E Rosenzweig, A Jackson, E D Yorke, and A J Wu. Fatal complications after stereotactic body radiation therapy for central lung tumors abutting the proximal bronchial tree. *Pract. Radiat. Oncol.*, 6(2):e27–e33, 2016.

[171] K Murphy, B Van Ginneken, J M Reinhardt, S Kabus, K Ding, Xi Deng, K Cao, K Du, G E Christensen, Vi Garcia, T Vercauteren, N Ayache, O Commowick, G Malandain, B Glocker, N Paragios, N Navab, V Gorbunova, J Sporring, M De Bruijne, X H Senior, M P Heinrich, J A Schnabel, M Jenkinson, C Lorenz, M Modat, J R Mcclelland, S Ourselin, S E A Muenzing, M A Viergever, D De Nigris, D L Collins, T Arbel, M Peroni, R Li, G C Sharp, A Schmidt-Richberg, J Ehrhardt, R Werner, D Smeets, D Loeckx, G Song, N Tustison, B Avants, J C Gee, M Staring, S Klein, B C Stoel, M Urschler, M Werlberger, J Vandemeulebroucke, S Rit, D Sarrut, and J P W Pluim. Evaluation of Registration Methods on Thoracic CT: The EMPIRE10 Challenge. *IEEE Trans. Med. Imaging*, 30(11):1901–1920, 2011.

[172] R Castillo, E Castillo, R Guerra, V E Johnson, T McPhail, A K Garg, and T Guerrero. A framework for evaluation of deformable image registration spatial accuracy using large landmark point sets. *Phys. Med. Biol.*, 54(7):1849–1870, 2009.

[173] C W Stevens, R F Munden, K M Forster, J F Kelly, Z Liao, G Starkschall, S Tucker, and R Komaki. Respiratory-driven lung tumor motion is independent of tumor size, tumor location, and pulmonary function. *Int. J. Radiat. Oncol. Biol. Phys.*, 51(1):62–68, 2001.

[174] L R Dice. Measures of the Amount of Ecologic Association Between Species. *Ecology*, 26(3):297–302, 1945.

[175] M Ezhil, B Choi, G Starkschall, M. K Bucci, S Vedam, and P Balter. Comparison of Rigid and Adaptive Methods of Propagating Gross Tumor Volume Through Respiratory Phases of Four-Dimensional Computed Tomography Image Data Set. *Int. J. Radiat. Oncol. Biol. Phys.*, 71(1):290–296, 2008.

[176] D P Huttenlocher, G A Klanderman, and W J Rucklidge. Comparing images using the Hausdroff distance. *IEEE Trans. Pattern Anal. Mach. Intell.*, 15(9):850–863, 1993.

[177] M.-P. Dubuisson and A.K. Jain. A modified Hausdorff distance for object matching. *Proc. 12th Int. Conf. Pattern Recognit.*, 1(1):566–568, 1994.

[178] G D Hugo, El Weiss, W C Sleeman, S Balik, P J Keall, J Lu, and J F Williamson. A longitudinal four-dimensional computed tomography and cone beam computed tomography dataset for image-guided radiation therapy research in lung cancer:. *Med. Phys.*, 44(2):762–771, 2017.

[179] R W M Underberg, F J Lagerwaard, J P Cuijpers, B J Slotman, J R Van Sornsen De Koste, and S Senan. Four-dimensional CT scans for treatment planning in stereotactic radiotherapy for stage I lung cancer. *Int. J. Radiat. Oncol. Biol. Phys.*, 60(4):1283–1290, 2004.

[180] A Richter, J Wilbert, and M Flentje. Dosimetric evaluation of intrafractional tumor motion by means of a robot driven phantom. *Med. Phys.*, 38(10):5280–5289, 2011.

[181] M C Aznar, G F Persson, I M Kofoed, D E. Nygaard, and S S Korreman. Irregular breathing during 4DCT scanning of lung cancer patients: Is the mid-ventilation approach robust? *Phys. Medica*, 30(1):69–75, 2014.

[182] F Kong, T Ritter, and D Quint. Consideration of dose limits for organs at risk of thoracic radiotherapy. *Int. J. Radiat. Oncol.*, 1(5):1–16, 2010.

[183] D B Landau, L Hughes, A Baker, A T Bates, M C Bayne, N Counsell, A Garcia-Alonso, S V Harden, J D Hicks, S R Hughes, M C Illsley, I Khan, V Laurence, Z Malik, H Mayles, W P M Mayles, E Miles, N Mohammed, Y Ngai, E Parsons, J Spicer, P Wells, D Wilkinson, and J D Fenwick. IDEAL-CRT: A Phase 1/2 Trial of Isotoxic Dose-Escalated Radiation Therapy and Concurrent Chemotherapy in Patients With Stage II/III Non-Small Cell Lung Cancer. *Int. J. Radiat. Oncol. Biol. Phys.*, 95(5):1367–1377, 2016.

[184] A van Baardwijk, G Bosmans, S M Bentzen, L Boersma, A Dekker, R Wanders, B G Wouters, P Lambin, and D De Ruysscher. Radiation Dose Prescription for Non-Small-Cell Lung Cancer According to Normal Tissue Dose Constraints: An In Silico Clinical Trial. *Int. J. Radiat. Oncol. Biol. Phys.*, 71(4):1103–1110, 2008.

[185] S. Adebahr, S. Collette, E. Shash, M. Lambrecht, C. Le Pechoux, C. Faivre-Finn, D. De Ruysscher, H. Peulen, J. Belderbos, R. Dziadziuszko, C. Fink, M. Guckenberger, C. Hurkmans, and U. Nestle. LungTech, an EORTC Phase II trial of stereotactic body radiotherapy for centrally located lung tumours: A clinical perspective. *Br. J. Radiol.*, 88(1051):20150036, 2015.

[186] F J Lagerwaard, C J A Haasbeek, E F Smit, B J Slotman, and S Senan. Outcomes of Risk-Adapted Fractionated Stereotactic Radiotherapy for Stage I Non-Small-Cell Lung Cancer. *Int. J. Radiat. Oncol. Biol. Phys.*, 70(3):685–692, 2008.

[187] J Y Chang, A Bezjak, and F Mornex. Stereotactic Ablative Radiotherapy for Centrally Located Early-Stage Non-Small-Cell Lung Cancer: What We Have

Learned on behalf of the IASLC Advanced Radiation Technology Committee. *J. Thorac. Oncol.*, 10(4):577–585, 2014.

[188] M Taremi, A Hope, M Dahele, S Pearson, S Fung, T Purdie, A Brade, J Cho, A Sun, J P Bissonnette, and A Bezjak. Stereotactic body radiotherapy for medically inoperable lung cancer: Prospective, single-center study of 108 consecutive patients. *Int. J. Radiat. Oncol. Biol. Phys.*, 82(2):967–973, 2012.

[189] J Zhang, F Yang, B Li, H Li, J Liu, W Huang, D Wang, Y Yi, and J Wang. Which is the optimal biologically effective dose of stereotactic body radiotherapy for stage i non-small-cell lung cancer? A meta-analysis. *Int. J. Radiat. Oncol. Biol. Phys.*, 81(4):305–316, 2011.

[190] S M Parker, R A Siochi, S Wen, and M D Mattes. Impact of Tumor Size on Local Control and Pneumonitis After Stereotactic Body Radiation Therapy for Lung Tumors. *Pract. Radiat. Oncol.*, 9(1):e90–e97, jan 2018.

[191] C J.A. Haasbeek, F J Lagerwaard, B J Slotman, and S Senan. Outcomes of stereotactic ablative radiotherapy for centrally located early-stage lung cancer. *J. Thorac. Oncol.*, 6(12):2036–2043, 2011.

[192] T Kimura, Y Nagata, H Harada, S Hayashi, Y Matsuo, T Takanaka, M Kokubo, K Takayama, H Onishi, K Hirakawa, Y Shioyama, and T Ehara. Phase I study of stereotactic body radiation therapy for centrally located stage IA non-small cell lung cancer (JROSG10-1). *Int. J. Clin. Oncol.*, 22(5):849–856, 2017.

[193] D H Murrell, J M Laba, A Erickson, B Millman, DA Palma, and A V Louie. Stereotactic ablative radiotherapy for ultra-central lung tumors: Prioritize target coverage or organs at risk? *Radiat. Oncol.*, 13(1), 2018.

[194] M Giuliani, A S. Mathew, H Bahig, S V. Bratman, E Filion, D Glick, A V. Louie, S Raman, A Swaminath, A Warner, V Yau, and D Palma. SUNSET:

Stereotactic Radiation for Ultracentral Non–Small-Cell Lung Cancer—A Safety and Efficacy Trial. *Clin. Lung Cancer*, 19(4):e529–e532, jul 2018.

[195] M J Menten, M F. Fast, S Nill, C P. Kamerling, F McDonald, and U Oelfke. Lung stereotactic body radiotherapy with an MR-linac – Quantifying the impact of the magnetic field and real-time tumor tracking. *Radiother. Oncol.*, 119(3):461–466, 2016.

[196] G Loi, M Fusella, E Lanzi, E Cagni, C Garibaldi, G Iacoviello, F Lucio, E Menghi, R Miceli, L C Orlandini, A Roggio, F Rosica, M Stasi, L Strigari, S Strolin, and C Fiandra. Performance of commercially available deformable image registration platforms for contour propagation using patient-based computational phantoms: A multi-institutional study: A. *Med. Phys.*, 45(2):748–757, dec 2018.

[197] RayStation. Deformable Registration in Raystation (White Paper), 2017.

[198] T Rohlfing. Image similarity and tissue overlaps as surrogates for image registration accuracy: Widely used but unreliable. *IEEE Trans. Med. Imaging*, 31(2):153–163, 2012.

[199] M Guckenberger, J Wilbert, T Krieger, A Richter, K Baier, J Meyer, and M Flentje. Four-Dimensional Treatment Planning for Stereotactic Body Radiotherapy. *Int. J. Radiat. Oncol. Biol. Phys.*, 69(1):276–285, 2007.

[200] G Valdes, C Lee, S Tenn, P Lee, C Robinson, K Iwamoto, D Low, and J M Lamb. The relative accuracy of 4D dose accumulation for lung radiotherapy using rigid dose projection versus dose recalculation on every breathing phase. *Med. Phys.*, 44(3):1120–1127, 2017.

[201] S M Al-Ward, A Kim, C Mccann, M Ruschin, P Cheung, A Sahgal, and B M Keller. The development of a 4D treatment planning methodology to simulate

the tracking of central lung tumors in an MRI-linac. *J. Appl. Clin. Med. Phys.*, 19(1):145–155, 2018.

[202] S Klöck, M Guckenberger, A Jöhl, O Riesterer, S Tanadini-Lang, A Tartas, Luisa S Stark, and S Ehrbar. ITV, mid-ventilation, gating or couch tracking – A comparison of respiratory motion-management techniques based on 4D dose calculations. *Radiother. Oncol.*, 124(1):80–88, jul 2017.

[203] M Kandi, T B Nyeng, D Sloth Møller, M Ma Knap, L Hoffmann, A Ahmed Khalil, and Marianne Ingerslev Holt. Difference in target definition using three different methods to include respiratory motion in radiotherapy of lung cancer. *Acta Oncol. (Madr).*, 56(11):1604–1609, 2017.

[204] J Wu, P Lei, R Shekhar, H Li, M Suntharalingam, and W D D'Souza. Do Tumors in the Lung Deform During Normal Respiration? An Image Registration Investigation. *Int. J. Radiat. Oncol. Biol. Phys.*, 75(1):268–275, 2009.

[205] A. Menna, S. Chiesa, A.R. Alitto, L. Azario, G.C. Mattiucci, S. Teodoli, N. Dinapoli, L. De Filippo, M. Balducci, and V. Valentini. Is there a true dosimetric improvement in lung SBRT using a 6-Degree of Freedom couch in IGRT era? *Radiother. Oncol.*, 119(EP-1798):S842, 2016.

[206] B W Papiez, M P Heinrich, J Fehrenbach, L Risser, and J A Schnabel. An implicit sliding-motion preserving regularisation via bilateral filtering for deformable image registration. *Med. Image Anal.*, 18(8):1299–1311, dec 2014.

[207] M Guckenberger, J Wilbert, A Richter, K Baier, and M Flentje. Potential of adaptive radiotherapy to escalate the radiation dose in combined radiochemotherapy for locally advanced non-small cell lung cancer. *Int. J. Radiat. Oncol. Biol. Phys.*, 79(3):901–908, 2011.

[208] C S Moskowitz, L H. Schwartz, L P. James, G J. Riely, R A. Lefkowitz, M G. Kris, Y Qin, P Guo, M S. Ginsberg, and B Zhao. Evaluating Variability in Tumor Measurements from Same-day Repeat CT Scans of Patients with Non–Small Cell Lung Cancer. *Radiology*, 252(1):263–272, 2009.

[209] E D Donnelly, P J Parikh, W Lu, Ti Zhao, K Lechleiter, M Nystrom, J P Hubenschmidt, D A Low, and J D Bradley. Assessment of Intrafraction Mediastinal and Hilar Lymph Node Movement and Comparison to Lung Tumor Motion Using Four-Dimensional CT. *Int. J. Radiat. Oncol. Biol. Phys.*, 69(2):580–588, 2007.

[210] M L Schmidt, L Hoffmann, M M Knap, T R Rasmussen, B H Folkersen, J Toftegaard, D S Møller, and P R Poulsen. Cardiac and respiration induced motion of mediastinal lymph node targets in lung cancer patients throughout the radiotherapy treatment course. *Radiother. Oncol.*, 121(1):52–58, 2016.

[211] J Yun, K Wachowicz, M Mackenzie, S Rathee, D Robinson, and B G Fallone. First demonstration of intrafractional tumor-tracked irradiation using 2D phantom MR images on a prototype linac-MR. *Med. Phys.*, 40(5):051718, 2013.

[212] M F Fast, C P Kamerling, P Ziegenhein, M J Menten, J L Bedford, S Nill, and U Oelfke. Assessment of MLC tracking performance during hypofractionated prostate radiotherapy using real-time dose reconstruction. *Phys. Med. Biol.*, 61(4):1546–1562, 2016.

[213] K Malinowski, T J McAvoy, R George, S Dietrich, and W D D'Souza. Incidence of changes in respiration-induced tumor motion and its relationship with respiratory surrogates during individual treatment fractions. *Int. J. Radiat. Oncol. Biol. Phys.*, 82(5):1665–1673, 2012.

[214] M A Admiraal, D Schuring, and C W Hurkmans. Dose calculations accounting for breathing motion in stereotactic lung radiotherapy based on 4D-CT and the internal target volume. *Radiother. Oncol.*, 86(1):55–60, 2008.

[215] V Mexner, Jo W H Wolthaus, M van Herk, E M F Damen, and J J Sonke. Effects of Respiration-Induced Density Variations on Dose Distributions in Radiotherapy of Lung Cancer. *Int. J. Radiat. Oncol. Biol. Phys.*, 74(4):1266–1275, 2009.

[216] B Mzenda, K V Mugabe, R Sims, G Godwin, and D Loria. Modeling and dosimetric performance evaluation of the RayStation treatment planning system. *J. Appl. Clin. Med. Phys.*, 15(5):29–46, 2014.

[217] P Kalwa, D Mönnich, C Gani, M Nachbar, D Zips, and D Thorwarth. Comparison of treatment plans for a high-field MRI-linac and a conventional linac for esophageal cancer. *Strahlentherapie und Onkol.*, 2018.

[218] Y Li, J Wang, L Tan, B Hui, X Ma, Y Yan, C Xue, X Shi, E K Drokow, and J Ren. Dosimetric comparison between IMRT and VMAT inirradiation for peripheral and central lung cancer. *Oncol. Lett.*, 15(3):3735–3745, 2018.

[219] J N Freedman, H Bainbridge, S Nill, D J Collins, M Kachelriess, M O Leach, F McDonald, U Oelfke, and A Wetscherek. Synthetic 4D-CT of the thorax for treatment plan adaptation on MR-guided radiotherapy systems. *Phys. Med. Biol.*, 64(115005):1–12, 2019.

[220] N J Mickevicius and E S Paulson. Investigation of undersampling and reconstruction algorithm dependence on respiratory correlated 4D-MRI for online MR-guided radiation therapy. *Phys. Med. Biol.*, 62:2910 – 2921, 2017.